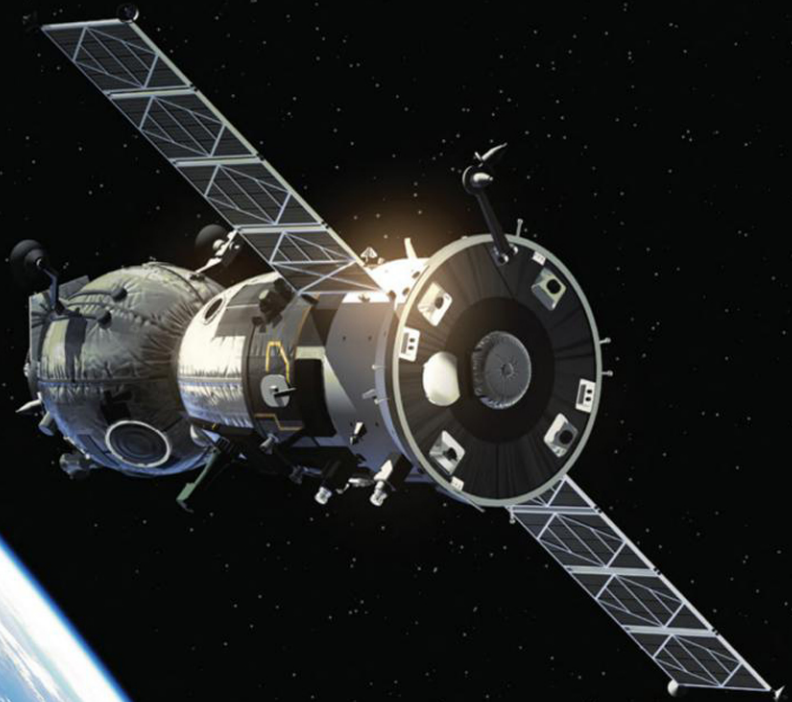


Spacecraft Collision Avoidance Technology

ZHANG RONGZHI & YANG KAIZHONG





Spacecraft Collision Avoidance Technology



Spacecraft Collision Avoidance Technology

Zhang Rongzhi

Researcher, State Key Laboratory of Astronautic Dynamics,
Xi'an Satellite Control Center,
Xi'an, P.R. China

Yang Kaizhong

Researcher, State Key Laboratory of Astronautic Dynamics,
Xi'an Satellite Control Center,
Xi'an, P.R. China



ACADEMIC PRESS

An imprint of Elsevier

Academic Press is an imprint of Elsevier
125 London Wall, London EC2Y 5AS, United Kingdom
525 B Street, Suite 1650, San Diego, CA 92101, United States
50 Hampshire Street, 5th Floor, Cambridge, MA 02139, United States
The Boulevard, Langford Lane, Kidlington, Oxford OX5 1GB, United Kingdom

Copyright © 2020 National Defence Industry Press. Published by Elsevier. All rights reserved.

No part of this publication may be reproduced or transmitted in any form or by any means, electronic or mechanical, including photocopying, recording, or any information storage and retrieval system, without permission in writing from the publisher. Details on how to seek permission, further information about the Publisher's permissions policies and our arrangements with organizations such as the Copyright Clearance Center and the Copyright Licensing Agency, can be found at our website: www.elsevier.com/permissions.

This book and the individual contributions contained in it are protected under copyright by the Publisher (other than as may be noted herein).

Notices

Knowledge and best practice in this field are constantly changing. As new research and experience broaden our understanding, changes in research methods, professional practices, or medical treatment may become necessary.

Practitioners and researchers must always rely on their own experience and knowledge in evaluating and using any information, methods, compounds, or experiments described herein. In using such information or methods they should be mindful of their own safety and the safety of others, including parties for whom they have a professional responsibility.

To the fullest extent of the law, neither the Publisher nor the authors, contributors, or editors, assume any liability for any injury and/or damage to persons or property as a matter of products liability, negligence or otherwise, or from any use or operation of any methods, products, instructions, or ideas contained in the material herein.

British Library Cataloguing-in-Publication Data

A catalogue record for this book is available from the British Library

Library of Congress Cataloguing-in-Publication Data

A catalog record for this book is available from the Library of Congress

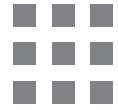
ISBN: 978-0-12-818011-2

For information on all Academic Press publications
visit our website at <https://www.elsevier.com/books-and-journals>

Publisher: Matthew Deans
Acquisitions Editor: Glyn Jones
Editorial Project Manager: Ana Claudia Garcia
Production Project Manager: Sruthi Satheesh
Cover Designer: Christian Billow

Typeset by MPS Limited, Chennai, India





Contents

1.	Outline of spacecraft collision warning	1
1.1	Distribution and characteristics of space objects	1
1.2	Characteristics and hazards of space debris	3
1.3	Collision warning of spacecraft	6
2.	Basics of orbital calculation for spacecraft collision avoidance	11
2.1	Basic definitions and transformation in astronomy	11
2.2	Space object orbit: basic definitions and transformation	21
3.	Space object detection technology	35
3.1	Overview	35
3.2	Radar measurement technology	37
3.3	Electro-optical detection technology	48
3.4	Public correction models for measurement data	64
3.5	Relationship between detection network and orbit accuracy	70
4.	Space environment and object orbit	73
4.1	Atmospheric effect on space object orbit	73
4.2	Atmospheric density model	75
4.3	Systematic error and random error of atmospheric density models	106
4.4	Prediction confidence level of space environment parameters influenced atmospheric density	109
4.5	Calculation strategy of atmospheric perturbation for spacecraft collision avoidance warning calculation	115
5.	Spacecraft collision warning orbit calculation method	123
5.1	Precise orbital calculation method	124
5.2	Cataloged orbit calculation method	131

6. Spacecraft collision warning and avoidance strategy	155
6.1 Collision warning calculation	156
6.2 The method of spacecraft avoidance	172
6.3 Collision warning strategy for spacecraft safety operation and case studies	177
References	187
Index	193

Outline of spacecraft collision warning

1.1 Distribution and characteristics of space objects

Since the launch of the first satellite in 1957, the total number of space object has reached the order of 10 millions, and the gross mass is up to 10,000 tons, according to statistical analysis. Up to February 24, 2016, the number of space objects whose diameter is about subsquare-decimeter and can be tracked on the ground is 17,552 in total [from NASA public two-line element (TLE) data, excluding classified satellites of the United States and its allies]. All the space objects, whose diameters are less than subsquare-decimeter fall into the category of space debris. Of the objects larger than subsquare-decimeter, the number of active spacecraft with intact shape is less than 2000, and other 15,000 objects are also space debris, or space junk. It can be seen that space debris constitutes the majority of space objects and the number is still growing. Fig. 1–1 shows the progressive increment of space objects tracked from the ground since 1957 to the present. As depicted in the figure, the number of space objects, especially that of space debris, is increasing at an astonishing speed, in particular, after critical space collisions such as the collision of the US satellite and the Russian satellite on February 11, 2009.

Although active spacecraft are not the major component of space objects, they play an increasingly important role in today's information society and are deployed into various orbits according to different applications. Fig. 1–2 shows the distribution of spacecraft in space around the Earth. From Fig. 1–2 the space over the altitude of 36,000 and below 2000 km above the equator is the main operation region for spacecraft.

Table 1–1 is the distribution of 1303 active spacecraft in terms of orbital altitude and inclination.

In terms of orbital altitude, spacecraft at an altitude of greater than 30,000 km account for 38.14% of all, and most of them are communications satellites in GEO; spacecraft at an altitude between 30,000 and 2000 km account for 8.29%, and most of them are GNSS satellite; spacecraft at an altitude between 2000 and 500 km account for 47.35%, and most of them are resource survey and experimental satellites; spacecraft at an altitude below 500 km account for 6.22%, and most of them are satellites for special experiments.

In terms of orbital inclination, there are 455 satellites with an inclination less than 5 degrees, accounting for 34.92%, and most of them are GEO satellites; there are 64 satellites with an inclination between 5 and 40 degrees, accounting for 4.91%, and most of them are relay and mission satellites; there are 297 satellites with an inclination between 40 and 80 degrees,

2 Spacecraft Collision Avoidance Technology

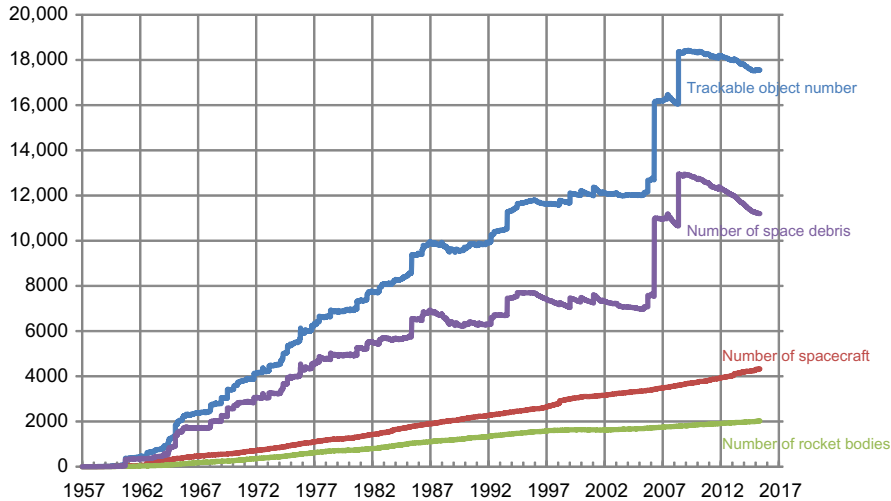


FIGURE 1–1 Increment of trackable space objects.

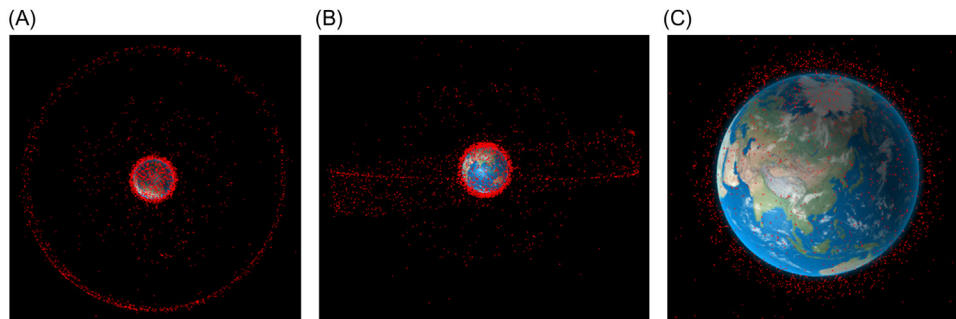


FIGURE 1–2 Distribution of spacecraft (including defunct satellites) from various views: (A) view of Earth from North Pole, (B) view of Earth from Equator, and (C) view of Earth in the vicinity of Earth.

accounting for 22.79%, and most of them are GNSS and communications satellites; there are 468 satellites with an inclination between 80 and 120 degrees, accounting for 35.92%, and most of them are imaging, reconnaissance, and resource survey satellites. From this the orbital space of GEO satellites at an altitude of 36,000 km and with an inclination around 0 degrees, that of GNSS satellites at an altitude of 20,000 km and with an inclination between 40 and 80 degrees and that of sun-synchronous satellites at an altitude between 500 and 2000 km and with an inclination of around 90 degrees are the dominant regions for space activities.

A large amount of space junks are created when space activities are carried out. Till 2016, the number of space debris tracked and cataloged reaches 15,729. [Table 1–2](#) shows the

Table 1–1 Distribution of active spacecraft in different orbits (%).

H_p (km)	i (degrees)					Total
	$i < 5$	$5 \leq i < 40$	$40 \leq i < 80$	$80 \leq i < 120$	$120 \leq i$	
$H_p \geq 30,000$	33.69	3.38	0.69	0.31	0.08	38.15
$2000 \leq H_p < 30,000$	1.07	0.15	7.06	0.00	0.00	8.28
$500 \leq H_p < 2000$	0.08	1.23	11.74	33.15	1.15	47.35
$H_p < 500$	0.08	0.15	3.30	2.46	0.23	6.22
Total	34.92	4.91	22.79	35.92	1.46	100

Table 1–2 Distribution of space debris in different orbits (%).

H_p (km)	i (degrees)					Total
	$i < 5$	$5 \leq i < 40$	$40 \leq i < 80$	$80 \leq i < 120$	$120 \leq i$	
$H_p \geq 30,000$	0.19	1.75	0.03	0.01	0.00	1.98
$2000 \leq H_p < 30,000$	1.09	7.40	6.71	0.62	0.09	15.91
$500 \leq H_p < 2000$	0.02	1.26	21.98	53.65	0.13	77.04
$H_p < 500$	4.18	0.03	0.24	0.62	0.00	5.07
Total	5.48	10.44	28.96	54.90	0.22	100

orbital distribution of the debris that is mainly distributed in the orbital space with an altitude below 2000 km. Table 1–3 shows the volume rate in different orbital space. It can be seen that, compared with other regions, the volume rate of detected space debris per $(100 \text{ km})^3$ is more than 0.01 in LEO at an altitude between 300 and 2000 km and is obviously higher than that of space debris in MEO and GEO. The volume rate of detected space debris per $(100 \text{ km})^3$ is more than 0.7, especially in the space above South Pole and North Pole at an altitude between 600 and 900 km where on-orbit satellites concentrate. Hence, this region is the most threatening place where space debris may collide with spacecraft and collision warning is urgent.

1.2 Characteristics and hazards of space debris

At 00:55 (Beijing Time) on February 11, 2009, the collision of the US Iridium 33 and Russia Cosmos 2251 satellite about 790 km above Siberia (North Pole) marked the first collision of intact satellites in the history. It is confirmed that more than 1200 detectable debris were generated in this collision. Fig. 1–3 depicts the distribution of orbit debris created in the collision. All the debris will reside in space for a long time.

In fact, five collisions on satellites by space debris causing catastrophic loss were confirmed before this one (see Table 1–4). In December 1991, a Russia defunct navigation satellite Cosmos 1934 was hit by a piece of space debris from the same series of satellite Cosmos 926.

Table 1–3 Distribution of space debris in main orbital regions.

Orbital altitude (km)	Entire region		Special regions	
	Number of space objects moving through the region	Space volume rate (number of space debris/100 km ³)	Number of space objects moving through the region	Space volume rate (number of space debris/100 km ³)
200–300	363	0.00658	15	0.00451
300–400	764	0.01333	78	0.02274
400–500	1327	0.02248	375	0.10613
500–600	2628	0.04319	1265	0.34777
600–700	4447	0.07121	2763	0.73812
700–800	6552	0.10202	4614	1.19827
800–900	7305	0.11076	5185	1.30956
900–1000	5906	0.08724	3586	0.88115
1000–1100	4450	0.06388	2250	0.53809
1100–1200	3566	0.04988	1390	0.32364
1200–1300	3190	0.04354	1085	0.24605
1300–1400	3112	0.04119	994	0.21962
1400–1500	3791	0.04907	1646	0.35444
18,000–22,000	1967	0.00005	61	0.00003
35,000–37,000	2067	0.00005	2066	0.00291

Note: As for certain regions at an altitude between 35,000 and 37,000 km, the area with latitude within ± 5 degrees will be selected; as for certain regions at other altitudes, the area with high latitude (above 70 or below -70 degrees) will be selected.

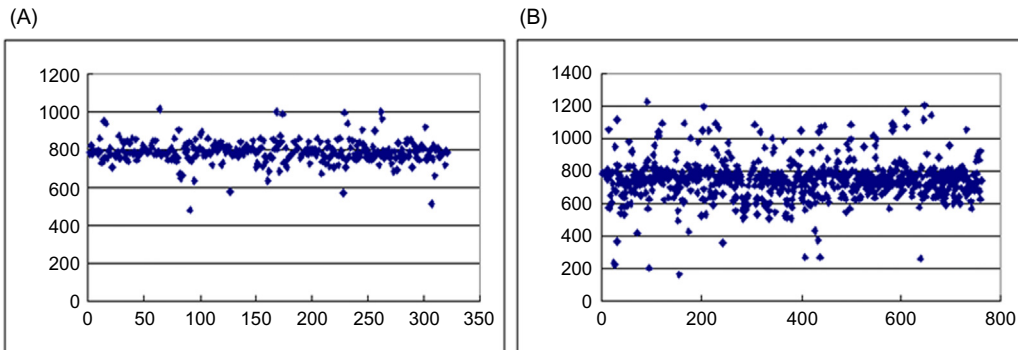


FIGURE 1–3 Space debris distribution created in the United States–Russian Satellite Collision in 2009: (A) the orbit altitude distribution of debris from Iridium 33 and (B) the orbit altitude distribution of debris from Cosmos 2251.

On July 24, 1996, the French ELINT satellite CERIES launched on July 7, 1995, was hit by the debris of an Ariane rocket launched in 1986. Although the rocket debris did not hit the body of the satellite, it broke down the gravity gradient stabilization boom which caused the satellite attitude control failure. These are only observed and documented collisions.

Table 1–4 The confirmed spacecraft collision events in history.

Number	Time	Site	Space object 1	Space object 2
1	1991-12	Above Siberian	Satellite Cosmos 1934 (Russia)	Satellite Cosmos 926 (Russia)
2	1996-07-24	—	Satellite Cerise (France)	Rocket debris Ariane (ESA)
3	2005-01-17	885 km above the South Pole	Rocket Thor Burner 2A	Debris from the upper stage of CZ-4 (China)
4	2009-02-10	790 km Above Siberian	Satellite Iridium 33 (United States)	Satellite Cosmos 2251 (Russia)
5	2013-05-24	Above Indian Ocean	Satellite Pegasus (Ecuador)	Rocket fuel tank (the Soviet Union)

Besides, the sudden failure or degradation of active spacecraft (satellites or rockets) is frequently observed. Due to the limitation of observation ability and device accuracy, although it could not be confirmed that those events were caused by debris impact, the undetected impacts by small debris are likely to be the primary reason. According to postevent estimation, there are several other satellites and rocket bodies impacted. In 1997 the defunct satellite NOAA 7 was collided by unknown space debris; in 2002 the defunct satellite Cosmos 539 was collided by unknown space debris; in 2007 the on-orbit active meteorological satellite-8 was collided by unknown space debris. Each collision not only caused direct damage to the spacecraft but also produced a large amount of space debris residing in space for a long time and further deteriorating the space environment. Fig. 1–1 shows the increment of fragments since 1957, where each collision incident would eventually cause an abrupt increase of new debris, and the probability of spacecraft collision would increase in turn. With the increase of collisions the situation may drop into a malicious cascade, which would eventually threaten the security of long-term operation of spacecraft. According to the space debris evolution model of a relative institution, if current population and increasing trend of space debris are not controlled, the space will be too crowded to be normally utilized in just about 200 years.

The huge destruction on spacecraft by the impact of space debris is caused mainly by the relative velocity. To remain in orbit without decaying, all space objects will fly at a velocity of approximately 10 km/s. Since the flight directions of both objects are different during the impact, the mean relative impact velocity will usually be greater than 10 km/s. Assuming that the relative velocity is 10 km/s, the generated kinetic energy will be enormous. According to the equation that kinetic energy equals to mass multiplied by the square of velocity, the kinetic energy generated by the collision between a 10-g debris and a spacecraft equals to that by the crash between two cars running at a speed of 100 km/h on the highway. The consequence will be catastrophic. According to ground simulations and current manufacturing status of space material, it is acknowledged that the number of space debris with a diameter smaller than 1 cm is enormous and hard to be tracked; thus protection from these tiny debris can only rely on the progress on spacecraft material to minimize the damage of space debris on spacecraft. The number of space debris with a diameter between 1 and 10 cm is on the order of 100,000. The international community is expected to achieve

complete monitoring of this kind of debris in the next two to three decades. The possible technical approach may be the combination of spacecraft self-protection and monitoring and avoidance by the ground in the future. There are 10,000–20,000 pieces of space debris with a diameter larger than 10 cm currently tracked by the international community, through which collision warning and collision avoidance can be achieved. The tracking capabilities are not enough to monitor all the critical objects of nearly 10 cm in diameter, and the orbits of these objects cannot be precisely determined by all the available global observing resources currently. Yet it is a feasible way and already in practice to mitigate the collision risk for on-orbit spacecraft through the collision prediction by tracking space objects with a diameter larger than 10 cm via the global tracking stations. Apparently, this technical approach is not the optimal due to the insufficiency of the global monitoring resources and the inadequacy of the current prediction accuracy. However, with the joint effort of the international society, solutions will become more and more mature.

1.3 Collision warning of spacecraft

Space debris avoidance has almost been a routine activity for capable space powers to ensure the security of their spacecraft or space station. International Space Station (ISS) executed several orbital and altitude maneuvers to avoid space debris every year. According to statistical data, from 2008 to 2014, ISS altogether executed 14 collision avoidance maneuvers (see Table 1–5) due to the collision threat of space object. From Table 1–5, ISS respectively

Table 1–5 Statistical data of collision avoidance maneuver of ISS in recent years.

Avoidance time	Avoidance object	Action
2008-08-27	Debris from satellite Cosmos 2421 (Russia)	Collision avoidance maneuver
2009-03-22	Upper stage (China)	Collision avoidance maneuver
2009-07-18	Upper stage (Russia)	Collision avoidance maneuver
2010-10-26	Debris from satellite UARS (United States)	Collision avoidance maneuver
2011-04-02	Debris from satellite Cosmos 2251 (Russia)	Collision avoidance maneuver
2011-06-28	Breakdown debris from proton rocket	Astronauts entered into the Soyuz spaceship to hide
2011-09-29	Rocket body debris from Tsyklon (Russia)	Collision avoidance maneuver
2012-01-13	Debris from satellite Iridium 33 (United States)	Collision avoidance maneuver
2012-01-28	Debris from satellite FY-1C (China)	Collision avoidance maneuver
2012-03-24	Debris from satellite Cosmos 2251 (Russia)	Astronauts entered into the Soyuz spaceship to hide
2014-03-16	Debris from satellite Meteor 2-5 (Russia)	Collision avoidance maneuver
2014-04-03	Rocket body form Ariane (ESA)	Collision avoidance maneuver
2014-10-27	Debris from satellite Cosmos 2251 (Russia)	Collision avoidance maneuver
2014-11-12	Debris form remote sensing satellite 12 (China) and ATV-5 (ESA)	Collision avoidance maneuver

executed one maneuver in 2008, two maneuvers in 2009, one maneuver in 2010, three maneuvers in 2011, three maneuvers in 2012, and four maneuvers in 2014. It is obvious that the increasing number of avoidance frequency shows the worsening of the operation environment of spacecraft.

However, current limited tracking resources and accuracy of orbital dynamics prediction models lead to the unfavorable credibility of collision avoidance. With the increasing number of space debris, spacecraft are encountering more and more enormous collision threats and risks during on-orbit operation. In 2015 from October 1 to 10, the United States notified 21 collision warning events of LEO satellites of China (Table 1–6). These events were confirmed to be false alarms afterward. If avoidance maneuvers were executed according to these false alarm notices, more fuel would have been consumed and the designed lifetime of the spacecraft would have been greatly reduced. If avoidance maneuvers were frequently executed, the normal applications would have been interrupted, and the efficiency of the spacecraft would have been reduced. Therefore reducing false alarms and improving the credibility of early warning is prerequisite for engineering implementation of spacecraft collision warning and avoidance.

Table 1–6 Collision warning events of LEO satellites notified by the United States to China (2015-10-01T00:00:00–2015-10-10T00:00:00).

Number	Satellites of China (NORAD code)	Space object (NORAD code)	Time of closest approach (Beijing time)	Miss distance (m)	R direction (m)	T direction (m)	N direction (m)
1	37,167	30,694	10-01 06:57:54	703	– 127	339	603
2	38,038	30,954	10-02 00:28:04	652	– 189	– 181	598
3	37,931	30,721	10-03 16:07:10	221	– 9	– 211	– 67
4	36,415	29,928	10-04 00:26:10	627	– 25	223	– 586
5	28,890	35,076	10-04 10:08:46	486	133	456	105
6	31,490	35,336	10-04 17:36:32	927	– 77	– 813	440
7	39,455	29,875	10-04 19:01:04	189	– 190	– 4	– 5
8	39,209	1722	10-05 07:19:04	615	86	– 498	– 351
9	39,358	40,467	10-05 19:56:12	157	– 104	23	117
10	40,701	15,592	10-06 02:29:22	380	– 97	– 12	– 368
11	40,701	15,592	10-06 02:29:23	354	– 88	– 8	– 343
12	29,506	33,409	10-06 10:21:29	758	58	752	– 79
13	28,737	30,192	10-06 14:16:14	849	– 145	323	– 773
14	40,701	15,592	10-08 14:17:50	903	– 108	11	– 897
15	40,701	15,592	10-08 14:17:51	948	– 116	8	– 941
16	27,431	82,030	10-08 22:57:53	115	82	– 3	82
17	37,930	9986	10-09 05:09:14	540	190	– 133	– 488
18	33,433	39,888	10-09 11:42:27	669	162	58	– 648
19	27,431	39,603	10-09 14:21:40	630	165	1	609
20	38,861	21,423	10-09 20:40:47	308	34	4	– 307
21	38,861	15,495	10-09 23:49:13	391	– 97	344	160

The direct reason for the high false alarm rate of spacecraft collision warning is the insufficient prediction accuracy of orbital positions of both spacecraft and the dangerous space object. Assuming that the prediction accuracy of both orbital positions in 24 hours is within the magnitude of meter, the collision warning on spacecraft within meter level in 24 hours can be 100% credible. However, at present, the quasi–real-time orbit determination accuracy of spacecraft measured using cooperative equipment can reach the order of meters or even centimeters, whereas the ultimate accuracy of the dangerous space object measured by noncooperative equipment can only reach the order of 10 m. However, as an active spacecraft collision warning, alarms should generally be sent at least 24 hours ahead. Hence, after the quasi–real-time orbit determination, orbital position in 24 hours will be propagated using orbit dynamics extrapolation method, and collision warning will be performed. Considering the accuracy of the orbital dynamics model, especially the influence of errors in atmospheric density model, even though no error exists in quasi–real-time orbit determination, the accuracy of predicted orbital positions for 24 hours is hard to surpass the order of 100 m. Within two big error spheres with diameter of 100 m, the collision possibility of two objects with diameter of a few meters or even less is very low. Limited by the global space object–detection resources, current space object catalog system worldwide can only maintain the accuracy of quasi–real-time orbit determination for all space objects at the magnitude of kilometers and the accuracy of extrapolation predicted orbital positions for 24 hours at the magnitude of 10 km, which will lead to the collision warning based on common space object catalog orbital system without any credibility.

In view of current ability, two types of collision warnings are defined in the collision warning strategy in this book, that is, colorless warning and colorful warning. A colorless warning is based on normal catalog system for space object monitor task without special requirement on accuracy or any additional tracking task. It can be carried out by using measurement data from devices or only TLE from an open source on the internet. Any universities, organizations, or individuals in the world can carry out colorless warning if they are interested. This kind of collision warning cannot be used as the basis for spacecraft avoidance due to relatively higher false alarm rate and lower credibility, whereas it can be used to filter dangerous events, select dangerous objects, and schedule detection devices to execute important observations. Colorless warning is a kind of collision warning based on normal catalog system without extra observation cost. Colorful warning is a kind of collision warning based on selected conjunction candidates by colorless warning. Since colorful warning is used to determine whether or not to perform collision avoidance, it requires real-time assessment and high orbit prediction accuracy of space object. Therefore intensive observations on conjunction candidates need to be scheduled. In general, colorful warning can be divided as yellow and red warnings in terms of phase and requirement on orbit prediction accuracy. Red warning is the precondition for spacecraft collision avoidance and yellow warning lays the foundation for red warning and is necessary for further reducing false alarm rate, concentrating detection devices on conjunction candidates, and improving the credibility of red warning. In colorful warning, especially in the phase of red warning, all-time and all-weather stable detection device is necessary to ensure the stability of data collection, and precise orbit determination system is used to perform orbit determination and prediction calculation to ensure the high credibility of conjunction point prediction.

The foundation of spacecraft collision warning system with no false dismissal, low false alarm rate, and high credibility depends on enormous space object–detection network, accurate orbit determination and prediction, reasonable detection and calculation resource scheduling strategy, and efficient management commanding system. Space object catalog and orbit determination system is used to continually screen numerous colorless warning messages with possible collision risks in order to ensure no false dismissal within the space surveillance capacity; the reasonable resource scheduling strategy is used to screen yellow warning messages with possible collision risks and eliminate most of the false alarms; precise orbit determination and prediction system is used to recognize important dangerous red events and schedule spacecraft to perform collision avoidance maneuver. This is the main task of the whole collision warning process.

This work involves fundamental technologies of space object orbit calculation, detection data acquisition technology, precise orbit calculation theory, the space environment of space object flight, overall planning, and other technological theories. The above fundamental technologies, theories, and models will be successively introduced in the upcoming chapters in this book. It is expected that this book can help readers acquire a thorough, objective, and detailed understanding of spacecraft collision avoidance technologies.

Basics of orbital calculation for spacecraft collision avoidance

The warning of spacecraft collision avoidance is essentially a warning of the risk of close approach between two space objects, the position information of which is obtained through collaborative and noncooperative orbit measurement and prediction. Due to different measurements of two high-dynamic moving objects and different sources of measurement information from different countries of international cooperation, it is especially important to adopt a unified benchmark frame. In addition, the precise orbit calculation of space objects should be carried out in space inertial system, and the measurement of space objects is usually obtained on the basis of the fixed TT&C stations in Earth's fixed coordinate system. The transformation of celestial spheres and various coordinates of the Earth are involved. This chapter gives a brief introduction to the definition of time and coordinate system and the transformation between the systems, as well as basics of orbital dynamics.

2.1 Basic definitions and transformation in astronomy

2.1.1 Basic concepts in astronomy

The basic idea of astronomy is the basis of the inertial coordinate system of celestial sphere that we are talking about. Fig. 2–1 is the reference ellipsoid for the celestial sphere; it shows the horizontal plane, meridian plane, equator, ecliptic, equinox, and hour angle, and the definitions are shown as follows:

Reference ellipsoid: A rotating ellipsoid is often defined that approximates the figure of the Earth. This rotating ellipsoid is called the reference ellipsoid. Reference ellipsoid's center O coincides with the Earth's center of mass, and the rotation axis of the ellipsoid points toward the conventional international origin P .

Horizontal plane: It is defined as the tangent plane $A-a_1 \dots a_n$ with its tangent point A at the reference ellipsoid.

Meridian plane: It is defined as the plane PA passing through any point A on the surface and the North and South Poles.

Equator: Equatorial plane is the plane passing through the Earth's center of mass and perpendicular to the rotation axis. And equator is the intersection of the surface with the equatorial plane.

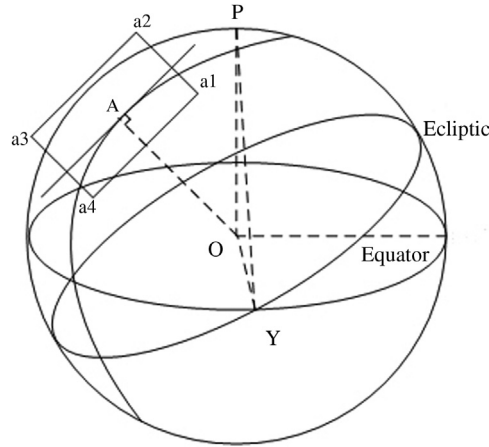


FIGURE 2-1 Space frames and basic planes.

Ecliptic: The Earth rotates around the Sun. An observer on the Earth viewing the Sun will note that the Sun orbits around the Earth. The trajectory of the apparent diurnal movement of the center of the Sun is referred to as ecliptic.

Vernal equinox: The ecliptic and the equator intersect at two points. The point γ where the Sun moves from the southern hemisphere into the northern hemisphere is the ascending node, also known as the vernal equinox. The direction from the center of the Earth toward the vernal equinox is the direction toward the vernal equinox. It is often used as a basic direction in astronomy.

Hour angle: O is the center of the Earth, P is the North Pole, and S is the observing station. PSG is the meridian passing S, X denotes any celestial body, PXT is a large arc passing X, and γ TG is the equator. Then the arc GT is called the hour angle of celestial X. For the vernal equinox γ , G γ is the hour angle of the vernal equinox.

Precession: The vernal equinox is not fixed among the stars, and actually it moves slowly along the ecliptic westwards. This phenomenon is called precession. Precession is caused due to the gravitation of the moon, sun, and planets. Earth's rotation axis revolves around the ecliptic pole, with a precession angle of 23.5 degrees, opposite to the Earth's rotation direction, and a period of 26,000 years. This is called lunisolar precession. It makes vernal equinox moving westward about $50''.37$ along the ecliptic each year. In addition, the gravity of planets will cause the rotation of the Earth's orbital plane. This will also cause movement of the vernal equinox (but does not cause the Earth's axis precession). This is called planetary precession. It makes equinox moving $0''.13$ along the equator each year.

Nutation: The orbital planes of the moon and the sun do not coincide with the equatorial plane of the Earth. They are sometimes above the equatorial plane and sometimes under the equatorial plane. In addition, the Moon–Earth or Sun–Earth distance is also changing. These factors yield the changing moment of the precession of the Earth's axis. This further

makes the Earth's axis precession extremely complex. Precession trajectory can be seen as tiny swaying in the vicinity of the average position for a short period. The tiny swaying is called nutation. Nutation's half amplitude is about $9''.2$, with a period of about 18.6 years.

Nutation is denoted by "longitude nutation" and "obliquity nutation." The precise formula is very complicated, if you want to be accurate to $0''.0001$, the formula will contain more than 100 items. Therefore in practical applications the formula is not directly used. Instead, Jet Propulsion Laboratory provides "sun–moon–planet ephemeris and nutation" data for calculations.

When only the effect of precession is considered, the vernal equinox and equator are referred to as the mean vernal equinox and mean equator. When the influence of precession and nutation are considered together, they are called the instantaneous vernal equinox and instantaneous equator, or true vernal equinox and true equator.

Pole shift: The Earth's poles are the intersection of the Earth's rotation axis with the surface. Subject to complex motions of oceanic currents, tides, and Earth mantles, the instantaneous rotating axis of the Earth will wander within 1 as, which makes the Earth's poles not strictly fixed points on the surface.

The shift of the Earth's poles on the surface is referred to as pole shift. The position of the instantaneous pole at any time can be represented by X_p and Y_p , Origin of the coordinate system is the conventional international origin P_0 (CIO), X -axis prime Greenwich meridian, and Y -axis the meridian at 90-degree-west longitude. The polar change of 2012–14 is shown in Fig. 2–2. It is shown that the variety rule of polar anniversary is obvious during the period of 3 years. The range of changes is within 10 m, and there is a significant systematic bias for P_0 .

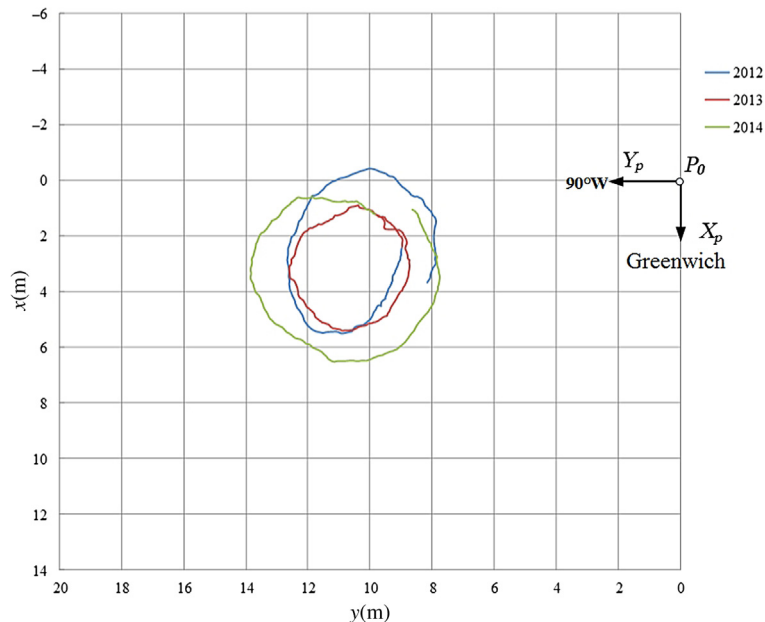


FIGURE 2–2 Polar shift from 2012 to 2014.

Pole shift is a completely different geophysical phenomenon with precession and nutation. Precession and nutation reflect the direction change of the Earth's rotation axis in stellar space, but the relative position within the Earth's interior does not change. Thus precession and nutation only cause changes in celestial coordinate but do not cause a change in the Earth's surface latitude and longitude. In contrast the pole shift shows no change in the direction of Earth's rotation axis in stellar space, but its relative position within the Earth's interior does change. This leads to changes of polar positions on the Earth's surface and eventually causes changes of the longitude and latitude on the Earth's surface. As the topocentric coordinates are defined within Earth-fixed coordinate systems, the pole shift correction shall be applied when the topocentric coordinates interact with the celestial sphere. In addition, the precession and nutation can be modeled very well, and the actual observations are consistent with the theoretical models. The formula will usually produce satisfactory precision of values. In contrast the normalized amplitude of the pole shift on the surface is hard to coincide with the theoretical value, though the value is only about the order of tens of meters. Thus high precision pole shift values are based on actual observations. Currently, the shift value (X_p , Y_p) is accurately measured and published by the International Earth Rotation and Reference Systems Service (IERS), so as to obtain accurate prediction value and precise solution value.

In addition, China's International GNSS Monitoring and Assessment System (referred IGMAS) has been approved by the 10th Annual Meeting of the International Conference on Geomatics (ICG-10) in November 2015. The Mission of IGMAS is to provide a global real-time tracking network with full-arc and multicoverage for BDS/GLONASS/Galileo navigation satellites, as well as an information platform with the abilities of data collection, storage, analysis, management, publishing, and other functions, so as to monitor and evaluate the operation and key indicators of GNSS and to generate products such as high-quality navigation satellite ephemeris, clock, Earth's pole shift parameters, tracking station coordinate and velocity, global ionospheric delay model, and GNSS-integrity products. Since 2016, global users can go to <http://en.beidou.gov.cn/> for pole-shift parameters [103].

2.1.2 Time systems and major transformation formula

In orbit calculation, time is an independent variable. Yet different time systems are applied for calculating different physics quantities. Time system is defined with the starting point and the unit of measurement of time intervals.

2.1.2.1 Sidereal time

The time when the vernal equinox passages over the observer is the zero hour of the local sidereal time. The local sidereal time is defined as the hour angle of the vernal equinox. As can be seen from the definition of sidereal time, the change rate of sidereal time is that of the apparent diurnal motion of the vernal equinox. The apparent diurnal motion rate of vernal equinox is the composition of the Earth's rotation rate and rate of the equinox itself.

We know that the vernal equinox displacement rate is subject to precession and nutation effects. When precession and nutation is considered, the obtained sidereal time is called true sidereal time, denoted as θ_g .

2.1.2.2 Solar time

The solar time includes true solar time and mean solar time.

True solar time: The time when the apparent Sun passages over the observer's meridian is the zero hour, then the hour angle of the apparent Sun is the local true solar time.

Since the ecliptic and the equator do not coincide, and the Earth's orbit around the Sun is not a circle, the true solar time changes irregularly. Thus mean solar time is defined as follows.

First a fictitious point is introduced in the ecliptic which moves with the mean angular velocity of the Sun and passes the perigee apogee at the same time as the Sun. Then another fictitious point is introduced in the equator which moves at the same speed as the fictitious point in the ecliptic and returns to the vernal equinox at the same time as the point in the ecliptic. This second point is called the mean sun. The relationship is given next:

Mean solar time = hour angle of mean sun + 12 hours or

Mean solar time = hour angle of mean vernal equinox—right ascension of mean sun + 12 hours.

2.1.2.3 Universal time

Greenwich mean solar time is called Universal Time.

Since the mean Sun is a fictitious point, and is not subject to observation, Universal Time is in fact determined by observing the diurnal motion of stars and obtained via sidereal time. Universal Time reflects the Earth's rotation. Due to the uneven nature of the Earth's rotation and changes in the Earth's meridian caused by pole shift, the Universal time is not uniform. Depending on the adjustments to Universal Time, three variations of Universal Time are defined.

UT0: Universal Time determined by direct observation of the stars is called UT0.

Due to the pole shift, the local meridians also change. So the UT0 corresponds to the position of the observer. UT1 is obtained after pole shift correction.

$UT1 = UT0 + \text{pole shift correction}$.

As the Earth's rotation presents long-term, periodic, and irregular changes, UT1 also has the above features. After seasonal periodic correction, we get UT2:

$UT2 = UT1 - \text{periodic items}$.

2.1.2.4 Ephemeris time

The start point of ephemeris time is defined as the epoch when the Sun's geometric mean longitude is $279^{\circ}41'48''04$, relative to the instantaneous mean vernal equinox. The standard second is defined as the second length on January 0 12:00 (ET) of the tropical year 1900 (or the fraction $1/31, 556$, and 925.9747 of the tropical year).

Ephemeris time is a uniform timescale within the solar barycentric framework, and it is the independent variable in Newtonian equations of motion for calculating the ephemerides of the Sun, Moon, planets, and satellites.

Definition of ephemeris time depends on the system of astronomical constants adopted. The ephemeris time is obtained by observations of the positions of the Moon. The ephemeris time relying on modified Brown lunar ephemeris during 1960–67 is referred to as ET0. Apart from the modified Brown lunar ephemeris, another ephemeris time relying on astronomical constants system of the year 1964 during 1968–71 is called ET1. The lunar ephemeris was refined after 1972 when the new series in lunar motion were researched, and the ephemeris time relying on the refined lunar ephemeris is called ET2. Ephemeris time used herein is ET2, referred to as ET for short.

2.1.2.5 Atomic time

The current major International Atomic Time system, TAI, is determined by the International Time Bureau (BIH). Take 0:00 on January 1, 1972 (UT2) as the starting point of TAI. The length of a second is defined as 9,192,631,770 periods of the radiation corresponding to the transition between the two hyperfine levels of the ground state of the Cesium 133 atoms.

2.1.2.6 Coordinated universal time

As can be seen from the definitions of Universal Time and Atomic Time, Universal Time represents the Earth's rotation, yet the change is not uniform. While the change in Atomic Time is more uniform than Universal time, its definition has no connection with the Earth's rotation. Thus the atomic time does not reflect the Earth's rotation. To this end, Coordinated Universal Time, UTC, is introduced to basically synchronize with the Earth's rotation. Epoch of UTC is the same with the epoch of Universal Time, and the duration of a second is the same as the definition of an atomic second. UTC is the standard time signal for tracking stations to synchronize time.

Actually, the definition of UTC changed several times in history. With an intent to make UTC as close as possible to UT2, frequency compensation was adopted prior to January 1, 1972 to make the UTC second very close to the UT second. When $|\text{UTC}-\text{UT2}|$ is greater than 0.1 second, the specified date is forced to a time jump of 0.1 second. After January 1, 1972, the length of second in UTC is equal to the second of atomic time. When $|\text{UTC}-\text{UT1}|$ is greater than 0.9 second, a time jump is forced on 0:00 January 1 (UTC) or 0:00 July 1 (UTC). Each jump is 1 second, which is also called leap second.

2.1.2.7 GPS time

GPS time (GPST) is an atomic timescale used in global positioning system, of which the zero is at 0:00:00 on January 6, 1980. At the starting epoch, GPS and UTC aligned exactly, and the two time systems give the identical time. Due to the presence of UTC leap second and the continuity of GPST, there will always be a difference of an integer number (n) of seconds between UTC and GPST, where n is the accumulative number of seconds to UTC in this

duration. Yet at 0:00:00 January 6, 1980, the difference between UTC and TAI is 19 seconds, so the difference between GPST and TAI is always 19 seconds, namely

$$TAI - GPST = 19 \text{ seconds}$$

Theoretically, TAI and GPST are both atomic timescale and have no time jumps; thus there is a strictly fixed difference of 19 seconds between them. Yet TAI and GPST are maintained by different atomic clocks, and the difference C_0 between TAI and GPST is measured and published by specialized institutions. Current monitoring indicates that the value C_0 is usually kept within 10 ns. For spacecraft collision warning computation, this difference can be completely ignored. However, as GPS is widely used in time alignment and onboard GPS timing, UTC–GPST difference cannot be totally ignored.

2.1.2.8 BeiDou time

With the improvement of China BeiDou Navigation Satellite System, BeiDou time is also widely used as well as GPST. Similarly, BeiDou time is an atomic timescale, of which the zero is at 0:00:00 on January 1, 2006 (UTC). The second duration of TAI is adopted in BeiDou time with no leap second. The longest time duration of BeiDou time is a week (defined by 604,800 seconds), which is referred to as WN and SOW. TAI and BDT can be transformed as follows:

$$TAI - BDT = 33 \text{ seconds}$$

By UTC (NTSC), BDT can be contacted with the international UTC. The deviation between BDT and UTC is kept within 100 ns (1 second). The leap second information of BDT from UTC is broadcasted in navigation message [102].

2.1.2.9 Time system conversion

For conversion from UT1 to Greenwich mean sidereal time, $\bar{\theta}_g$, the following formula is used:

$$\bar{\theta}_g = 18^h.6973746 + 879000^h.0513367T_U + 0^s.093104T_U^2 - 6.2^s \times 10^{-6}T_U^3 \quad (2.1)$$

where T_U is the Julian centuries since 12:00 January 1, 2000 (UT1) (JD = 2451545.0).

For conversion from Gregorian date to Julian Date, assume that the year, month, day, hour, minute, and second in the Gregorian calendar are, respectively, Y, M, D, h, m, and s. Then

$$J = D - 32075 + [1461 \times (Y + 4800 + [(M - 14)/12])/4] + [367 \times (M - 2 - [(M - 14)/12] \times 12)/12] - [3 \times [(Y + 4900 + [(M - 14)/12]/100)/4] \quad (2.2)$$

where $[X]$ represents the integral part of X .

The corresponding Julian date:

$$JD = J - 0.5 + h/24 + m/1440 + s/86,400 \quad (2.3)$$

2.1.3 Coordinate systems and major transformation formula

In orbit calculation, we have to, in a precise way, deal with a variety of observations and orbit ephemeris conversion in different coordinate systems. Meanwhile, many quantities in dynamic models for orbital calculation are defined in a specific coordinate system. A variety of coordinate systems are therefore to be introduced to facilitate the processing and calculation.

A coordinate system is defined by three elements: origin, the basic plane, and the primary direction in the plane (usually the direction of X -axis in the Cartesian coordinate system).

2.1.3.1 2000.0 inertial coordinate system

The origin is at the center of mass of the Earth, the fundamental plane is the mean equator of J2000.0, and the X -axis is aligned with the mean equinox of J2000.0. Z -axis is the normal direction of the fundamental plane and is aligned with the North Pole. Y -axis and X , Z axes make up a right-handed system.

In the 2000.0 inertial coordinate system the position vector is denoted with \vec{r} , and the velocity vector is denoted with $\dot{\vec{r}}$.

2.1.3.2 Instantaneous mean equatorial coordinate system

The origin is at the center of mass of the Earth, the fundamental plane is the mean equator at the instant of observation, and the X -axis is aligned with the mean equinox of the observation instant. Z -axis is the normal direction of the fundamental plane and is aligned with the North Pole. Y -axis and X , Z axes satisfy the right-handed rule.

In this coordinate system the position vector is denoted with \vec{r}_m . The velocity vector is denoted with $\dot{\vec{r}}_m$.

2.1.3.3 Instantaneous true equatorial coordinates system

The origin is at the center of mass of the Earth, the fundamental plane is the true equator at the instant of observation, and the X -axis is aligned with the true equinox of the observation instant. Z -axis is the normal direction of the fundamental plane and is aligned with the North Pole. Y -axis and X , Z axes satisfy the right-handed rule.

In this coordinate system the position vector is denoted with \vec{r}_t , and the velocity vector with $\dot{\vec{r}}_t$.

2.1.3.4 Quasi Earth-fixed coordinate system

The origin is at the center of mass of the Earth, the fundamental plane is the instantaneous equator of the Earth, and the X -axis is aligned with the Greenwich Meridian. Z -axis is aligned with the instantaneous North Pole of the Earth's rotation axis. Due to the pole shift effect,

the Z -axis' intersection with the Earth surface changes with time. X , Y , and Z axes make up a right-handed system.

This coordinate system is fixed to the Earth and rotates with the Earth. In this coordinate system the position vector is denoted with \vec{r}'_b , and the velocity vector with $\dot{\vec{r}}'_b$.

2.1.3.5 International Terrestrial Reference System

International Terrestrial Reference System (ITRS) is the most accurate and widely used conventional terrestrial coordinate system. In accordance with IUGG resolutions, ITRS is defined by the IERS. The core of its definition of spatial coordinates O-XYZ is as follows: O is the center of mass of the Earth, Z -axis points to the Celestial Intermediate Origin (CIO), X -axis is aligned with the Greenwich meridian, and Y -axis, perpendicular to X , Z -axes, satisfies a right-handed rule. Only such an invisible reference system definition is not enough to determine the position of a point on the surface of the Earth. In addition to the ITRS reference system definition a group of reference stations are used, and these stations are called IERS reference stations. The stations' coordinates (X , Y , and Z), their velocity (ΔX , ΔY , and ΔZ)/year, and the earth orientation parameters published by IERS all together constitute the International Terrestrial Reference Frame (ITRF). With this frame of reference, you can measure the difference between any point on Earth or in space and the reference points to calculate the coordinates of the measured point in the ITRS. The precise pole motion parameters are also available to calculate the point's coordinates in the celestial coordinate systems.

2.1.3.6 Earth-fixed coordinate system

In order to keep fixed point's coordinates constant, it is necessary to construct a coordinate system completely fixed with the Earth body itself. A variety of Earth-fixed coordinate systems can be defined according to different applications. In order to facilitate the conversion between celestial coordinates and terrestrial coordinates, space object orbital calculation usually adopts CGCS2000 (China Geodesic Coordinate System 2000) or WGS-84 (World Geodesic System 1984) Earth-fixed coordinate systems, which are coincident with the ITRF. This coordinate system is fixed to the Earth and rotates with the Earth. In this coordinate system the position vector is denoted with \vec{r}_b , and the velocity vector with $\dot{\vec{r}}_b$.

As the GPS coordinate reference system, WGS-84 coordinate system is a US-defined global geocentric coordinate system. It is widely adopted in the world with the popularity of GPS navigation and positioning technology. The coordinate system definition is almost consistent with ITRS. The coordinates of IERS reference stations in this frame have a difference of less than 1 cm relative to the defined ITRF coordinates in three axes.

CGCS2000 is also known as 2000 China Geodetic Coordinate System. The origin and the three axes are consistent with ITRS reference system, and the ellipsoid geometry parameters $a = 6,378,137.0$ and $f = 1: 298.257222101$. At the reference epoch of 2000, CGCS2000 can be considered coincident with the ITRF and WGS-84 at the centimeter level.

2.1.3.7 Geodetic system

The topocentric coordinates of the observer, as well as the satellite ground track, are often expressed in geodetic coordinate system. The coordinate system uses the geodetic reference ellipsoid as a reference surface, and the observer's position is denoted in geodetic longitude λ , geodetic latitude φ , and the height h , which is defined as follows:

The longitude is measured as the angle between the observer's (or celestial bodies') geodetic meridian plane and the prime meridian plane. It is measured eastward from the prime meridian plane.

The geodetic latitude is the angle between the normal to the reference ellipsoid at the observer and the equatorial plane. It is measured from the equator, with northward as positive and southward as negative.

The height is defined as the distance along the normal direction from the observer to the reference ellipsoid. It is measured from the reference ellipsoid, with outward as positive and inward as negative.

2.1.3.8 Topocentric coordinate system

The origin is the center of the tracking station, that is, the rotating center of the tracking antenna. The local horizon at the station center is the fundamental plane. The primary direction is directing northward from the origin.

For station Cartesian coordinates, X -axis directs eastward in the fundamental plane, Y -axis directs toward the primary direction, and Z -axis is perpendicular to the fundamental plane pointing upward.

For station spherical coordinate system, range ρ is the distance from the center to the satellite, azimuth A is the angle measured clockwise from the primary direction to the satellite position vector's projection upon the fundamental plane, and elevation E is the angle between the satellite position vector and the fundamental plane.

In this coordinate system the position vector is denoted with ρ , and the velocity vector with $\dot{\rho}$.

2.1.3.9 Satellite coordinate system

Coordinate origin is the satellite's center of mass. Z -axis points from the satellite center of mass to the center of the Earth (i.e., r direction), Y -axis directs opposite of the normal to the orbital plane, and X -axis directs toward the motion direction and is perpendicular to Z -axis within the orbital plane. X -, Y -, and Z -axes satisfy the right-handed rule.

2.1.3.10 **UNW** and **RTN** coordinate system

2.1.3.10.1 **UNW** coordinate system

UNW coordinate system is defined by the followings. The origin is the center of mass of a space object. **U** direction is of the direction of the velocity vector. **N** direction is perpendicular to **U** direction and points toward the orbit normal direction. **W** direction constitutes right-hand system with **U** and **N** directions. The vectors of **UNW** coordinate system are defined in J2000.0 inertial coordinate system as **U**, **N**, **W**, then there is

$$\mathbf{U} = \frac{\mathbf{v}}{|\mathbf{v}|} \quad \mathbf{W} = \frac{\mathbf{v} \times \mathbf{r}}{|\mathbf{v} \times \mathbf{r}|} \quad \mathbf{N} = \mathbf{W} \times \mathbf{U}$$

where \mathbf{v} and \mathbf{r} are, respectively, the position and velocity vector in J2000.0 inertial coordinate system.

2.1.3.10.2 RTN coordinate system

RTN coordinate system is defined by the followings. The origin is the satellite's center of mass. **R** radial axis coincides with direction from the center of the Earth to the satellite center of mass. **T** transverse axis points toward the movement direction in the orbital plane and is perpendicular to the **R**-axis. **N**-axis is the normal to the orbital plane and constitutes the right-hand system with **R**- and **T**-axes. The vectors of **RTN** coordinate system are defined in J2000 inertial coordinate system as **R**, **T**, **N**, then there is

$$\mathbf{R} = \frac{\mathbf{r}}{|\mathbf{r}|} \quad \mathbf{N} = \frac{\mathbf{r} \times \mathbf{v}}{|\mathbf{r} \times \mathbf{v}|} \quad \mathbf{T} = \mathbf{N} \times \mathbf{R}$$

2.1.3.11 Coordinate transformation

Ephemeris calculation is the prerequisite for satellite orbital determination and prediction. And the integrator in this calculation requires continuous time frame of high stability and inertial coordinate system with no rotation, so that the satellite position can be integrated. This is why we select atomic time TAI and 2000.0 inertial coordinate frames adopted by BIH for integration of orbital ephemeris calculation. Yet all observations for satellite tracking are defined in Earth's fixed coordinate system and conventional UTC. So space-time frame transformations are the basics of orbital calculation. We shall be very familiar with the definitions of abovementioned time and coordinate systems and use such parameters as time, pole motion, precession and nutation, to compute the transformation from one frame to another.

2.2 Space object orbit: basic definitions and transformation

The trajectory of any object flying in the space can be expressed by its position and velocity at any epoch, t , in inertial J2000 coordinate system. Space objects herein are referred to those orbiting the Earth; they move in elliptic orbits at the first cosmic velocity, according to Kepler theorem. At time t , three parameters depicting the shape and size of the ellipse are mainly dependent on the object's velocity. And the orientation of the ellipse in J2000 inertial system and the three parameters depicting the object's elliptic motion together give the exact position of the object in J2000 inertial system. These six parameters are also known as six orbital elements, which depict analytically the space object's position and velocity in space. Thus the space object's trajectory can be expressed in inertial coordinate system or in orbital elements to depict its position and velocity in space. These two expressions can be conversed precisely with mathematical formulas and can be solved with numerical and analytical approaches, respectively, so as to obtain the space object's trajectory at any time t .

2.2.1 Space object's two-body motion in space

Space object in motion is subject to a variety of forces. Among these forces the gravity of the Earth to the satellite is the most important and absolutely the dominant force. Meanwhile, the space object can be treated as a point of mass as its mass and size is so small relative to the Earth. Earth's gravitational force upon the space object can fall into two parts: centric gravitation and other gravitation. The centric gravitation indicates that the Earth is assumed to be a sphere with uniform mass distribution, and the Earth is considered a point of mass with all its mass concentrated in the barycenter. In this case the space object is moving mainly under the influence of the Earth's gravity, and its equation of motion can be written as:

$$\frac{d^2\vec{r}}{dt^2} = -\mu \frac{\vec{r}}{r^2} + \vec{F} \quad (2.4)$$

where \vec{r} is the object's radial vector; $\mu = G(M + m)$, G is the universal gravitational constant, M is the mass of the Earth, and m represents the mass of the object; the first item $-\mu(\vec{r}/r^2)$ is the gravity of the center of the Earth; \vec{F} is the sum of all perturbations except for the gravity, including the Earth nonspherical perturbations, atmospheric drag, solar radiation pressure, and sun and moon gravity. It is noted that in Eq. (2.4), the length is measured in the unit of the Earth's radius.

If you ignore other perturbations, and only consider the gravity, the motion equation becomes:

$$\frac{d^2\vec{r}}{dt^2} = -\mu \frac{\vec{r}}{r^2} \quad (2.5)$$

In celestial mechanics the motion described by the equation is called the two-body problem (or two-body motion). And two-body problem has analytical solution, see Refs. [4,9].

2.2.2 Integration of two-body problem

Analytical solutions of two-body problem equations have the following integrals:

1. Area integration

$$\vec{r} \times \dot{\vec{r}} = \vec{h} \quad (2.6)$$

2. Energy integration

$$\dot{\vec{r}} \cdot \dot{\vec{r}} = \frac{2\mu}{r} + c \quad (2.7)$$

3. Laplace integration

$$\dot{\vec{r}} \cdot \vec{h} = \mu \frac{\vec{r}}{r} + \vec{e} \quad (2.8)$$

where \vec{h} and \vec{e} are integral vectors, c is constant of the integration, and they satisfy the following relationship:

$$\begin{aligned}\vec{h} \cdot \vec{e} &= 0 \\ \vec{e} \cdot \vec{e} - c(\vec{h} - \vec{h}) &= \mu^2\end{aligned}$$

From the above integrations, it is easy to derive the orbital equation:

$$r = \frac{h^2/\mu}{1 + e \cos \angle(\vec{e}, \vec{r})} \quad (2.9)$$

This is a conic equation. For space object orbiting the Earth, its velocity is less than the second cosmic velocity; then, its orbit is elliptical, namely $0 \leq e < 1$.

The trajectory of space object in the two-body motion is transformed into a depiction of ellipse. Thus the motion equation can be expressed with the six elements $a, e, i, \Omega, \omega, M$, see Fig. 2–3.

In the figure, O' is the center of the ellipse; O is a focus of the ellipse, namely the Earth's core; a is the semimajor axis of the ellipse; e is the eccentricity, $e = \sqrt{a^2 - b^2}/a$; i is the angle between the ellipse and the point W where the satellite intersects the equator when flying from south to north; Ω is the angle in equatorial plane between W and the vernal equinox; ω is the angle in ellipse between the perigee P and W ; f is the angle in the elliptical plane

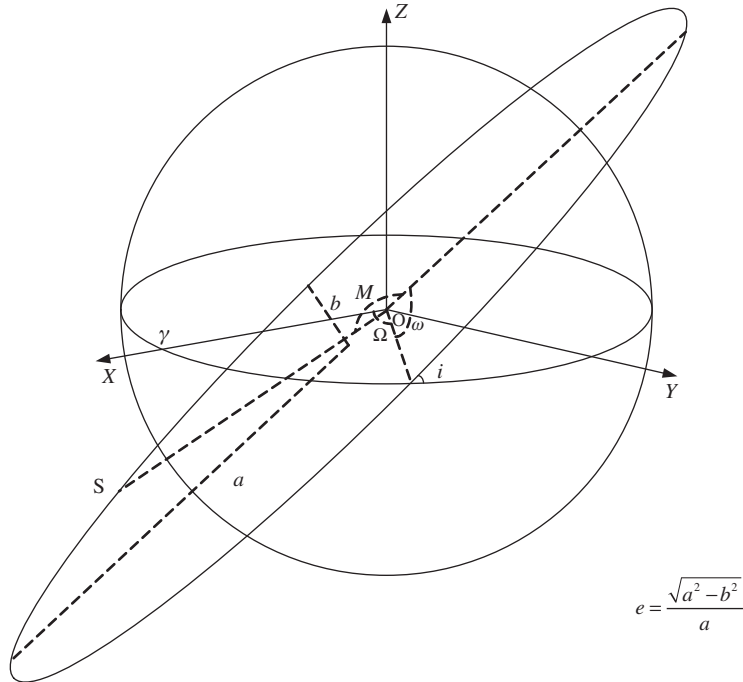


FIGURE 2–3 Six orbital elements of space object motion.

between the line SO and the line PO, namely the true anomaly; and E is the angle in the elliptical plane between the line SO' and the line PO', namely the eccentric anomaly (see Ref. [4]).

The six elements $(a, e, i, \Omega, \omega, M)$ depicting the space object trajectory are also called orbital elements of space object.

The last element f of the orbit elements is usually replaced with the mean anomaly M in order to reflect clearly the movement rule of space objects. The Kepler equation can be obtained based on the area integral and vis-viva equation:

$$E - e \sin E = M \quad (2.10)$$

where E can be obtained from the following formula:

$$r = a(1 - e \cos E) \quad (2.11)$$

M is an element depicting satellite's location in the orbit.

$$M = n(t - \tau) \quad (2.12)$$

where

$$n = \sqrt{\frac{\mu}{a^3}} \quad (2.13)$$

n is usually referred as mean motion and τ as the epoch of the perigee passage. The orbital equation and energy integration are:

$$r = \frac{a(1 - e^2)}{1 + e \cos f} \quad (2.14)$$

$$v^2 = \mu \left(\frac{2}{r} - \frac{1}{a} \right) \quad (2.15)$$

In celestial mechanics, Eq. (2.15) is often called vis-viva equation.

Here the conversion relationship between the true anomaly f and eccentric anomaly E is

$$\begin{aligned} r \sin f &= a\sqrt{1 - e^2} \sin E \\ r \cos f &= a(\cos E - e) \end{aligned} \quad (2.16)$$

$$\begin{aligned} f &= E + 2tg^{-1} \left[\frac{e \sin E}{1 + \sqrt{1 - e^2} - e \cos E} \right] \\ E &= f + 2tg^{-1} \left[\frac{e \sin f}{1 + \sqrt{1 - e^2} + e \cos f} \right] \end{aligned} \quad (2.17)$$

Under the assumption of the two-body problem, for space object flying around the Earth, if the epoch T_0 and the six orbital elements are determined, only M is a time variable theoretically among the six elements at any time T .

$$\begin{aligned} M_t &= M_{t_0} + n \times t \\ n &= \sqrt{\frac{GM}{a^3}} \end{aligned} \quad (2.18)$$

where n is the angular velocity of the satellite motion. That is, the velocity can be obtained if the satellite position at any time T is available.

2.2.3 Basic conversion of orbital elements for space objects

2.2.3.1 Interchange between orbital elements and position/velocity in Cartesian system

The position/velocity $(x, y, z, \dot{x}, \dot{y}, \dot{z})$ of space object in J2000 inertial system at time, t , has a unique correspondence conversion relationship with the six orbital elements $(a, e, i, \Omega, \omega, E)$:

$$\begin{aligned} \begin{bmatrix} x \\ y \\ z \end{bmatrix} &= a(\cos E - e)\hat{P} + a\sqrt{1-e^2} \sin E\hat{Q} \\ \begin{bmatrix} \dot{x} \\ \dot{y} \\ \dot{z} \end{bmatrix} &= -\sin E \frac{\sqrt{\mu a}}{r} \hat{P} + \cos E \frac{\sqrt{\mu a(1-e^2)}}{r} \hat{Q} \\ \hat{P} &= \begin{bmatrix} \cos \Omega \cos \omega - \sin \Omega \sin \omega \sin i \\ \sin \Omega \cos \omega - \cos \Omega \sin \omega \cos i \\ \sin \omega \sin i \end{bmatrix} \\ \hat{Q} &= \begin{bmatrix} -\cos \Omega \sin \omega - \sin \Omega \cos \omega \cos i \\ -\sin \Omega \sin \omega + \cos \Omega \cos \omega \cos i \\ \cos \omega \sin i \end{bmatrix} \\ r &= \sqrt{x^2 + y^2 + z^2} \end{aligned} \quad (2.19)$$

2.2.3.2 Partial derivative of elements with respect to coordinates and velocity

Define

$$\vec{N}_1 = \begin{pmatrix} 1 \\ 0 \\ 0 \end{pmatrix} \quad \vec{N}_2 = \begin{pmatrix} 0 \\ 1 \\ 0 \end{pmatrix} \quad \vec{N}_3 = \begin{pmatrix} 0 \\ 0 \\ 1 \end{pmatrix},$$

$$\begin{aligned}\bar{e} &= \dot{\bar{r}} \times \bar{h} - \mu \frac{\bar{r}}{r} \\ \bar{R} &= \begin{pmatrix} \sin i \sin \Omega \\ -\sin i \cos \Omega \\ \cos i \end{pmatrix} = \frac{\bar{h}}{h} \\ \bar{A} &= \frac{\bar{N}_3 \times \bar{h}}{|\bar{N}_3 \times \bar{h}|}, \quad \bar{B} = \frac{\bar{h} \times \bar{A}}{|\bar{h} \times \bar{A}|}\end{aligned}$$

where $\bar{h} = \bar{r} \times \dot{\bar{r}}$, $h = |\bar{h}|$

1. The partial derivative of a with respect to $\bar{r}, \dot{\bar{r}}$

$$\frac{\partial a}{\partial \bar{r}} = \frac{2a^2 \bar{r}}{r^3}, \quad \frac{\partial a}{\partial \dot{\bar{r}}} = \frac{2a^2 \dot{\bar{r}}}{\mu} \quad (2.20)$$

2. The partial derivative of i with respect to $\bar{r}, \dot{\bar{r}}$

$$\begin{aligned}-\sin i \frac{\partial i}{\partial \bar{r}} &= \frac{\dot{\bar{r}} \times \bar{N}_3}{h} - \frac{(\bar{N}_3 \cdot \bar{h})}{h^3} (\dot{\bar{r}} \times \bar{h}), \\ -\sin i \frac{\partial i}{\partial \dot{\bar{r}}} &= \frac{\bar{N}_3 \times \bar{r}}{h} - \frac{(\bar{N}_3 \cdot \bar{h})}{h^3} (\bar{h} \times \bar{r})\end{aligned} \quad (2.21)$$

3. The partial derivative of Ω with respect to $\bar{r}, \dot{\bar{r}}$

$$\begin{aligned}\frac{\partial \Omega}{\partial \bar{r}} &= \frac{\cos^2 \Omega}{(\bar{N}_2 \cdot \bar{h})^2} (\dot{\bar{r}} \times \bar{N}_1 - \dot{\bar{r}} \times \bar{N}_2); \\ \frac{\partial \Omega}{\partial \dot{\bar{r}}} &= \frac{\cos^2 \Omega}{(\bar{N}_2 \cdot \bar{h})^2} (\bar{N}_1 \times \bar{r} - \bar{N}_2 \times \bar{r})\end{aligned} \quad (2.22)$$

4. The partial derivative of e with respect to $\bar{r}, \dot{\bar{r}}$

$$\begin{aligned}\mu^2 e \frac{\partial e}{\partial \bar{r}} &= \left(\dot{\bar{r}} \times (\bar{e} \times \dot{\bar{r}}) - \mu \left(\frac{\bar{e}}{r} - \frac{(\bar{e} \cdot \bar{r})}{r^3} \bar{r} \right) \right) \\ \mu^2 e \frac{\partial e}{\partial \dot{\bar{r}}} &= (\bar{h} \times \bar{e}) + (\bar{e} \times \dot{\bar{r}}) \times \bar{r}\end{aligned} \quad (2.23)$$

5. The partial derivative of ω with respect to \vec{r} , $\dot{\vec{r}}$

$$\begin{aligned}\frac{\partial \omega}{\partial \vec{r}} &= \frac{\mu \vec{e} \cdot \vec{A}}{\vec{e} \cdot \vec{e}} \frac{\partial \xi}{\partial \vec{r}} - \frac{\mu \vec{e} \cdot \vec{B}}{\vec{e} \cdot \vec{e}} \frac{\partial \eta}{\partial \vec{r}} \\ \frac{\partial \omega}{\partial \dot{\vec{r}}} &= \frac{\mu \vec{e} \cdot \vec{A}}{\vec{e} \cdot \vec{e}} \frac{\partial \xi}{\partial \dot{\vec{r}}} - \frac{\mu \vec{e} \cdot \vec{B}}{\vec{e} \cdot \vec{e}} \frac{\partial \eta}{\partial \dot{\vec{r}}}\end{aligned}\quad (2.24)$$

where

$$\begin{aligned}\frac{\partial \xi}{\partial \vec{r}} &= \dot{\vec{r}} \times \vec{C} - \mu \left(\frac{\vec{B}}{r} - \frac{(\vec{B} \cdot \vec{r})}{r^3} \right) \vec{r} \\ \frac{\partial \xi}{\partial \dot{\vec{r}}} &= \vec{h} \times \vec{B} + \vec{C} \times \vec{r} \\ \frac{\partial \eta}{\partial \vec{r}} &= \dot{\vec{r}} \times \vec{D} - \mu \left(\frac{\vec{A}}{r} - \frac{(\vec{A} \cdot \vec{r})}{r^3} \right) \vec{r} \\ \frac{\partial \eta}{\partial \dot{\vec{r}}} &= \vec{h} \times \vec{A} + \vec{D} \times \vec{r}\end{aligned}\quad (2.25)$$

where $\vec{C} = \vec{B} \times \dot{\vec{r}} + \vec{A} \times \vec{G} + \vec{F}^* \times \vec{N}_3$

$$\vec{C} = \vec{B} \times \dot{\vec{r}} + \vec{A} \times \vec{G} + \vec{F}^* \times \vec{N}_3 \quad \vec{D} = \vec{A} \times \dot{\vec{r}} + \vec{F} \times \vec{N}_3$$

6. The partial derivative of M with respect to \vec{r} , $\dot{\vec{r}}$

$$\begin{aligned}\frac{\partial M}{\partial \vec{r}} &= \left(\frac{e \cos E}{e^2} - 1 \right) \left(\frac{\dot{\vec{r}}}{na^2} - \frac{\vec{r} \cdot \dot{\vec{r}} \vec{r}}{na r} \right) - \frac{e \sin E \dot{\vec{r}} \cdot \dot{\vec{r}} \vec{r}}{e^2 \mu r} \\ \frac{\partial M}{\partial \dot{\vec{r}}} &= \left(\frac{e \cos E}{e^2} - 1 \right) \left(\frac{\vec{r}}{na^2} - \frac{\vec{r} \cdot \dot{\vec{r}} \dot{\vec{r}}}{na \mu} \right) - \frac{e \sin E 2r \dot{\vec{r}}}{e^2 \mu}\end{aligned}\quad (2.26)$$

where $e \sin E = (\vec{r} \cdot \dot{\vec{r}}/na^2)$, $e \cos E = 1 - (r/a)$, $e^2 = (e \sin E)^2 + (e \cos E)^2$.

2.2.3.3 Partial derivative of coordinates and velocity with respect to elements

For Kepler elements, there are:

$$\begin{aligned}\Delta \vec{r} &= \frac{1}{a} \left[\vec{r} - \frac{3}{2} \dot{\vec{r}}(t - t_0) \right] \Delta a + (H\vec{r} + K\dot{\vec{r}}) \Delta e + \frac{\dot{\vec{r}}}{n} \Delta M_0 \\ &\quad + (\vec{\Omega} \times \vec{r}) \Delta i + (\vec{N} \times \vec{r}) \Delta \Omega + (\vec{R} \times \vec{r}) \Delta \omega \\ \Delta \vec{r} &= \frac{3}{2a} \left[\frac{\mu}{r^3} \vec{r}(t - t_0) - \frac{1}{3} \dot{\vec{r}} \right] \Delta a + (H'\vec{r} + K'\dot{\vec{r}}) \Delta e + \frac{\mu \vec{r}}{nr^3} \Delta M_0 \\ &\quad + (\vec{\Omega} \times \dot{\vec{r}}) \Delta i + (\vec{N} \times \dot{\vec{r}}) \Delta \Omega + (\vec{R} \times \dot{\vec{r}}) \Delta \omega\end{aligned}\quad (2.27)$$

where

$$\begin{aligned}
H &= -\frac{a}{p}(\cos E + e), \quad K = \frac{p+r}{np} \sin E \\
I &= -\frac{1}{\sqrt{1-e^2}} \sin E \\
J &= \frac{1}{n\sqrt{1-e^2}} \left(\frac{e}{1+\sqrt{1-e^2}} - 2 \cos E + e \cos^2 E \right) \\
H' &= -\frac{na^2}{rp} \left[1 - \frac{a}{r} \left(1 + \frac{p}{r} \right) \right] \sin E, \quad K' = \frac{a}{p} \cos E \\
I' &= \frac{na^2}{r^2\sqrt{1-e^2}} \left[-\frac{e}{1+\sqrt{1-e^2}} + \frac{a}{r} \sqrt{1-e^2} \cos E + e \cos^2 E \right] \\
J' &= \frac{1}{\sqrt{1-e^2}} \sin E
\end{aligned} \tag{2.28}$$

where n is mean motion, and $p = a(1 - e^2)$

$$\vec{\Omega} = \begin{pmatrix} \cos \Omega \\ \sin \Omega \\ 0 \end{pmatrix}, \quad \vec{N} = \begin{pmatrix} 0 \\ 0 \\ 1 \end{pmatrix}, \quad \vec{R} = \begin{pmatrix} \sin \Omega \sin i \\ -\cos \Omega \sin i \\ \cos i \end{pmatrix} \tag{2.29}$$

For derivation of these formulas, see Ref. [3].

2.2.3.4 Partial derivative of acceleration with respect to position/velocity in two-body motion of space object

From Eq. (2.5), we have two-body motion's acceleration:

$$\vec{a}_{TB} = -\frac{GM_E}{r^3} \vec{r} \tag{2.30}$$

The acceleration in two-body problem can also be expressed in potential function. Namely Eq. (2.30) satisfies the following relationship:

$$\nabla \times \vec{f} = 0$$

where $\nabla \times \vec{f}$ denotes the curl of \vec{f} .

Therefore the gravitational field is a conservative force field. For a conservative force field, there is potential function:

$$V = \int_{\infty}^r \vec{f} d\vec{r}$$

Such that:

$$\vec{f} = \text{grad } v$$

where $\text{grad } v$ denotes the gradient of v .

If \vec{f} is taken as the force upon unit mass, $\text{grad } v$ is the acceleration under gravity. For the two-body problem, its potential function is:

$$V_0 = \frac{GM_E}{r} \quad (2.31)$$

In the two-body problem the satellite acceleration is:

$$\vec{a}_{TB} = \text{grad } V_0 = \begin{bmatrix} \frac{\partial V_0}{\partial x} \\ \frac{\partial V_0}{\partial y} \\ \frac{\partial V_0}{\partial z} \end{bmatrix} \quad (2.32)$$

The partial derivative of the satellite position vector is:

$$\frac{\partial \vec{a}_{TB}}{\partial \vec{r}} = \begin{pmatrix} \frac{\partial \vec{a}_{TB1}}{\partial x} & \frac{\partial \vec{a}_{TB1}}{\partial y} & \frac{\partial \vec{a}_{TB1}}{\partial z} \\ \frac{\partial \vec{a}_{TB2}}{\partial x} & \frac{\partial \vec{a}_{TB2}}{\partial y} & \frac{\partial \vec{a}_{TB2}}{\partial z} \\ \frac{\partial \vec{a}_{TB3}}{\partial x} & \frac{\partial \vec{a}_{TB3}}{\partial y} & \frac{\partial \vec{a}_{TB3}}{\partial z} \end{pmatrix} = \frac{GM_E}{r^3} \begin{pmatrix} 3\frac{x^2}{r^2} - 1 & 3\frac{xy}{r^2} & 3\frac{xz}{r^2} \\ & 3\frac{y^2}{r^2} - 1 & 3\frac{yz}{r^2} \\ & & 3\frac{z^2}{r^2} - 1 \end{pmatrix} \quad (2.33)$$

Partial derivative with respect to GM:

$$\frac{\partial \vec{a}_{TB}}{\partial GM_E} = -\frac{\vec{r}}{r^3} \quad (2.34)$$

2.2.4 Orbital perturbations of space object

Space object in motion is by no means as simple as a two-body problem. It is affected by many forces. Even if we take the Earth as a mass point, the Earth's gravitational force upon the space object can fall into two parts: (1) the Earth is assumed to be a sphere with uniform mass distribution, and the Earth is considered as a point of mass with all its mass concentrated in the barycenter, which is the force in the two-body problem and (2) the Earth is in fact not a strict sphere with uniform mass distribution, the nonspherical force upon the

satellite shall also be considered, which is referred to the zonal and tesseral harmonic perturbation force. In addition, the space object in motion is also subject to such forces as atmospheric drag, N -body problem force, solar radiation pressure, Earth's radiation pressure, relativistic effects, attitude control force, and so on, which can be expressed uniformly by:

$$\ddot{\vec{r}} = \vec{f}_{TB} + \vec{f}_{NB} + \vec{f}_{NS} + \vec{f}_{TD} + \vec{f}_{RL} + \vec{f}_{SR} + \vec{f}_{AL} + \vec{f}_{DG} + \vec{f}_{TH} \quad (2.35)$$

where \vec{r} is the position vector of the space object in the inertial coordinate system.

$$\vec{r} = x\vec{i} + y\vec{j} + z\vec{k}$$

The right part of formula (2.35) indicates the force on unit mass of space object. where \vec{f}_{TB} denotes the force of two-body problem, namely the Earth is assumed to be a sphere with uniform mass distribution, and both the Earth and the space object are considered as points of mass. \vec{f}_{TB} is the Earth's gravitational force upon the space object. \vec{f}_{NB} denotes the gravitation force of the Moon, the Sun, and other planets except the Earth upon the space object. \vec{f}_{NS} denotes the gravitation force of the nonspherical part of the Earth upon the space object. \vec{f}_{TD} denotes change of the gravitation force of the Earth upon the space object caused by the Earth tide (including solid tide, sea tide, and atmospheric tide). \vec{f}_{RL} denotes influence of relativistic effects on motion of the space object. \vec{f}_{SR} denotes pressure of solar radiation upon the space object. \vec{f}_{AL} denotes the force of the Earth infrared radiation and the Earth reflecting the Sun's ray upon the space object. \vec{f}_{DG} denotes the drag of the Earth atmosphere upon the space object. \vec{f}_{TH} denotes the other force upon the space object, such as the dynamic for control of the space object attitude.

If the analytical solution of formula (2.35) can be obtained, and as long as the motion status \vec{r}_0 and $\dot{\vec{r}}_0$ of the space object at some original time t_0 are known, the motion status \vec{r} and $\dot{\vec{r}}$ of the space object at any time of $t \geq t_0$ can be obtained. Generally speaking, the expressions of the above forces are very complicated. The precise analytical solution of formula (2.35) is not yet obtained except the two-body problem, and only some approximate solutions can be obtained in the case of approximate suppose. As for catalogue orbit determination with precision of 100 m, the one-order approximate resolution is effective. As for precise warning of spacecraft collision, the calculation precision of space object orbit is required to be within meters and even better; here it is difficult to obtain the analytical solution of formula (2.35).

Along with the development of computers and application math the numerical integration method can be used to solve the numerical integration problem perfectly. In the numerical integration approach, the position, velocity, and acceleration of the space object in orbit are the uniform expressions of the numerical integration equation. So formula (2.35) can be written as the expression of acceleration:

$$\vec{a} = \vec{a}_{TB} + \vec{a}_{NB} + \vec{a}_{NS} + \vec{a}_{TD} + \vec{a}_{RL} + \vec{a}_{SR} + \vec{a}_{AL} + \vec{a}_{DG} + \vec{a}_{TH} \quad (2.36)$$

In formula (2.35), effect of each perturbation force upon orbit of the space object is different. The magnitude of perturbation force is discussed further in order to describe clearly the primary and secondary relationship among perturbation forces. If the force of the two-body problem is taken as 1, the force of the Earth's zonal and tesseral harmonic terms is in the order of 10^{-3} , the atmospheric drag for low Earth orbit satellites may be up to the magnitude of 10^{-5} , the attitude control force is in the order of 10^{-6} for space object in use and frequent attitude maneuvering, the force of N -body force is in the magnitude of 10^{-7} , the solar and Earth radiation pressure is around the magnitude of 10^{-8} , and the influence of relativistic effects should be in the magnitude of 10^{-9} . Typically except for the two-body problem force, all the other forces upon the space object are collectively referred to as flight perturbation forces for space object or perturbations in short. Large perturbations are up to the magnitude of 10^{-3} , and some are as small as 10^{-9} . With further research in orbital dynamics and continuous improvement of measurement accuracy, more perturbations are discovered and refined in a smaller magnitude. The perturbations will change explicitly for different satellite orbits. Tables 2–1 to 2–3 give the perturbation upon the position accuracy in 24 hours for space objects in three different orbits at 340, 780, and 36,000 km, respectively. As shown in Table 2–1 for orbital calculation error below the altitude of 340 km, only assuming the atmospheric drag model error is 5% (actually, there is no such model in the world with an error of less than 5%) and the atmospheric drag perturbation is considered, the 24-hour orbital calculation error is up to the magnitude of several kilometers. Even if all other perturbations are ignored, the influence for low Earth orbit satellite is only tens of meters in 24-hour orbit calculation error. Of course, with the increase in satellite orbit height, Tables 2–2 and 2–3 show that the effects of atmospheric perturbation are gradually reduced, while the perturbations of solar and lunar gravitational forces and solar radiation pressure are gradually

Table 2–1 Various perturbations on a LEO satellite orbit (orbital altitude of 340 km).

Items	Perturbation (within 24 h)							
	1	2	3	4	5	6	7	8
The sun and moon tides		Y	Y	Y	Y	Y	Y	Y
Atmospheric drag	Y	5% error	Y	Y	Y	Y	Y	Y
Earth reflection	Y	Y		Y	Y	Y	Y	Y
relativity	Y	Y	Y		Y	Y	Y	Y
N -body problem	Y	Y	Y	Y		Y	Y	Y
Solar radiation pressure	Y	Y	Y	Y	Y		Y	Y
Solar gravity	Y	Y	Y	Y	Y	Y		Y
Moon's gravity	Y	Y	Y	Y	Y	Y	Y	
Forecast 1 day error								
Position central error	3.528	64,114.0	0	2.662	0.0017	6.944	13.418	39.619
The maximum radial	0.159	872.4	0	0.027	0.0013	1.945	0.689	0.926
The maximum tangential	3.513	64,109.6	0	2.662	0.0016	6.944	13.417	23.011
Normal maximum	0.832	19.4	0	0.001	0.0010	0.003	0.049	33.295

Note: "Y" means this perturbation is considered, and blank means the opposite.

Table 2–2 Various perturbations on resource satellite orbit (orbital altitude of 780 km).

Items	Perturbation (within 24 h)							
	1	2	3	4	5	6	7	8
The solar and lunar tides		Y	Y	Y	Y	Y	Y	Y
Atmospheric drag	Y		Y	Y	Y	Y	Y	Y
Earth reflection	Y	Y		Y	Y	Y	Y	Y
Relativity	Y	Y	Y		Y	Y	Y	Y
<i>N</i> -body problem	Y	Y	Y	Y		Y	Y	Y
Solar radiation pressure	Y	Y	Y	Y	Y		Y	Y
Solar gravity	Y	Y	Y	Y	Y	Y		Y
Moon's gravity	Y	Y	Y	Y	Y	Y	Y	
Forecast 1 day error								
Position central error	1.646	27.733	0	2.382	0.0014	8.970	32.516	64.440
The maximum radial	0.132	0.484	0	0.027	0.0011	2.187	0.932	2.028
The maximum tangential	1.590	27.732	0	2.382	0.0014	8.970	29.543	62.023
Normal maximum	0.702	0.009	0	0.012	0.0009	0.277	14.333	27.339

Note: "Y" means this perturbation is considered, and blank means the opposite.

Table 2–3 Various perturbations on the geostationary satellite orbit (orbital altitude 36,000 km).

Items	Perturbation (within 24 h)							
	1	2	3	4	5	6	7	8
The solar and lunar tides		Y	Y	Y	Y	Y	Y	Y
Atmospheric drag	Y		Y	Y	Y	Y	Y	Y
Earth reflection	Y	Y		Y	Y	Y	Y	Y
Relativity	Y	Y	Y		Y	Y	Y	Y
<i>N</i> -body problem	Y	Y	Y	Y		Y	Y	Y
Solar radiation pressure	Y	Y	Y	Y	Y		Y	Y
Solar gravity	Y	Y	Y	Y	Y	Y		Y
Moon's gravity	Y	Y	Y	Y	Y	Y	Y	
Forecast 1 day error								
Position central error	0.118	0	0	23.1	0.007	234.2	1754	6429
The maximum radial	0.045	0	0	5.68	0.006	98.5	1224	3699
The maximum tangential	0.176	0	0	35.93	0.01	401.8	2922	1.09E4
Normal maximum	0.059	0	0	0.005	0.003	5.6	493.6	1552

Note: "Y" means this perturbation is considered, and blank means the opposite.

increasing. As for the LEO, it is obvious that the atmosphere drag is the primary orbit perturbation force besides the gravity force. Modeling precision of the atmosphere drag is minimum relative to other perturbations, which results in active international research of this field.

In formula (2.36) the theoretical research of the first seven perturbation acceleration is relatively perfect, whose precise formula is presented in Ref. [1], and which is not discussed any more. The dynamics model of the eighth atmosphere perturbation will be discussed further in Chapter 4, Space environment and object orbit. The ninth item is the cruise attitude control force perturbation of the space object in operation, which is relative to the attitude data. In the noncooperative measurement mode the operation attitude data cannot be obtained by telemetry of the space object. In orbit calculation the data can only be considered together with the atmosphere density correction factor, so the perturbation force and uncertainty of the atmosphere model will be discussed together in Chapter 4, Space environment and object orbit.

Space object detection technology

3.1 Overview

Space object detection is to detect the object entering the monitored space region in time with certain technical equipment or means. According to the position of platforms on which the observation equipment is deployed, there are two kinds of detection equipment, ground-based and space-based equipment. The former is located on the surface of the Earth, while the latter is located in space.

3.1.1 Ground-based detection

Ground-based detection uses equipment installed on the surface of the Earth to measure the position of the space object. There are two kinds of means: radio detection and electro-optical detection [46].

3.1.1.1 *Radio detection technology*

Radio detection includes mechanical tracking radar, phased array radar, and electromagnetic fence. Ground-based radio detection is an important way to detect space objects due to its all-weather and all-day work mode without the influence of the weather and its ability of detecting multiple objects and discovering new objects. But with the increase of the distance, the requirements on transmission power are getting higher and higher. As a result, radio detection is primarily used to monitor space objects in low orbits. The detection of objects at long range and in higher orbit requires antennae with higher transmitting power and larger size, which will lead to low benefit–cost ratio.

1. Mechanical tracking radar

Mechanical tracking radar adopts a mechanical way to control the direction of the beam. The space object can only be detected and measured by this type of radar when it enters the range of the antenna beam. Hence, this type of radars is mainly for object tracking and imaging. Since this kind of radar cannot scan electronically and its beam is very narrow, its ability of observing multiple objects is limited and it is usually used for tracking the single object with a field of view less than 1 degree.

2. Phased array radar

Phased array radar adopts an electronic way to control the direction of the beam and it can simultaneously monitor multiple objects in different directions. Hence, it is usually used for tracking and search tasks. This type of radar can track multiple objects simultaneously due to its wide field of view.

3. Electromagnetic fence

Electromagnetic wave emitted from the radar antenna of the electromagnetic fence is not a narrow beam, but a thin planar field. When the space object penetrating the planar field, the reflected electromagnetic waves are received by the receiver, and the correlation of successive penetrating data can be used to determine the space object.

This kind of radar detects space object usually in three operating modes, tracking mode, beam pointing mode, and mixed mode (stare-and-chase). In tracking mode the radar continuously tracks one space object, so as to obtain successive data such as angle measurement, ranging, range rate, phase, and amplitude of radar echoes. These data will further be used to calculate the object orbital elements. Beam pointing mode means that the radar antenna is fixed in one direction and only receives the radar echoes data through its field of view. This method can provide statistical information such as the number and size of space objects, but it cannot obtain a continuous tracking data. The mixed mode means that the radar begins operating in beam pointing mode and switches to the tracking mode as soon as the object crosses the beam. Thus continuous tracking data can be obtained. Once the required data is collected, the radar will again return to the beam pointing mode.

This kind of radar can work in both monostatic structure (the receiver and the transmitter are collocated in one antenna) and bistatic structure (the receiver and the transmitter are separated by a distance in different antennae).

3.1.1.2 *Electro-optical detection technology*

Ground-based electro-optical measurement is a monitor method of space objects with electro-optical telescope facilities. Electro-optical telescope facilities are an electrically enhanced telescope, which integrates telescope and electro-optical monitoring equipment.

As the most traditional approach, electro-optical detection is featured with mature technology, low cost of construction and operation, and better performance for objects in medium/high Earth orbit. However, due to atmospheric absorption and unavailability of ultraviolet and infrared bands, only the visible light telescope can be used for measurement. In addition, optical telescope is affected by the day and night, terrain, and weather conditions. It is reasonable that one object is unobservable for one electro-optical facility, even if the object is geometrically visible in clear weather. There is a possibility of more than 30% that the object may still be affected by daylight and shadow effects.

A major role of optical measurement in space object monitoring is to provide high-precision measurement data of space objects and to measure space object at a long distance (deep space), which supplements the limitations of short distance for radar observations.

Ground-based detection, as the primary approach, contributes a primary source to space object detection data. Without the limitation of volume and mass, ground observation equipment may obtain higher spatial resolution with large aperture antenna and obtain a long-distance observation ability of space objects with higher transmission power, which cannot be realized with other detection means. Yet the ground-based detection also has the following two disadvantages. First, ground stations cannot achieve seamless coverage of space

domains or time domains and the construction of more stations is constrained by political and geographical factors. Second, among current detection means, radar has active detection ability; however, it is limited by the detection range; electro-optical approach has long detection range; however, it cannot meet requirements on all-weather and all-time.

3.1.2 Space-based detection

Space-based detection uses detection equipment installed on space-based platforms to detect space objects. Space-based detection has higher resolution, due to the closer distance between detection position and space object, as well as the absence of atmospheric interference (e.g., extinction and absorption). However, its cost is usually higher than that of ground-based detection and it is necessary to realize a balance between the performance and the cost for space-based detection. Space-based measurements can be divided into optical measurement and radar measurement in terms of measurement method for space objects.

Currently, ground-based detection is the primary means for space object surveillance, while space-based detection plays a complementary role. In ground-based detection, surveillance of LEO objects adopts radio detection as its primary means and electro-optical detection as the complementary one. Surveillance of MEO/HEO objects is usually dependent on optical detection.

3.2 Radar measurement technology

At present, the main detection equipment for LEO objects is ground-based radar monitoring system. Among the space catalog library of LEO space objects with size of larger than 10 cm tracked by the United States Space Command (USSPACECOM), the contribution of radar equipment accounted for 99.8%. Since ground-based radar can realize higher spatial resolution with large aperture antenna and longer detection range with large transmission power without the limitation of volume, mass, and weather conditions, it is preferentially selected to detect space objects in LEO.

Currently, ground-based surveillance radars mainly adopt the following three detection methods: precision tracking mode, phased array scanning mode, and fence surveillance mode. Radars working in precision tracking mode need to be guided by orbit prediction information and mainly perform precise tracking, orbit determination, and even imaging of specific single object, such as GLOBUS 11 in the United States and TIRA in Germany. Radars working in phased array scanning mode can track multiple objects in a flexible way. For instance, ANFPS85 phased array radar in US Eglin Air Force Base can simultaneously track 200 objects in LEO. On the other hand, it can also form a “virtual” beam barrier to achieve universal measurement functions. For instance, GRAVES radar in France can provide a virtual fence with azimuth coverage of 180 degrees in phased array scanning mode. Radars working in fence surveillance mode can provide one or several “seamless” electronic fences via beam dwelling or beam scanning in space, so as to get the position and velocity of space

objects traversing the beam fence. Compared with phased array radar and optical telescope, radar working in fence surveillance mode has favorable advantages of larger update rate and acquisition number of space objects.

3.2.1 Radar measurement elements

Tracking radars usually refer to those that can continuously and automatically track the object, precisely measure, and output its coordinate position parameters (such as azimuth A , the elevation angle E , range R , and the radial velocity V).

3.2.1.1 Radar object angle measurement and tracking methods

The angle measurement of the radar can be realized with the direction of the transmission (and receiving) antenna. When the received signals are maximum, the pointing direction of the antenna is the angle of the object. The larger the antenna aperture is, the narrower its beam is, the better the directional feature of its beam is and then the higher the angle measurement accuracy is. However, in general, the angle measurement accuracy of the approach of using beam maximum value is relatively low.

The direction of echo wave can also be obtained by measuring the phase difference of signals from two separate receiving antennas, which is the working theory of angle measurement in interferometer and the foundation of phase comparison monopulse angular measurement. Similarly, the echo wave direction of the object can also be obtained by measuring the amplitude difference of signals from two separate receiving antennas (or of two tilted beams from one antenna), which lays the foundation of angle measurement in lobe switching, conical scanning, and amplitude comparison monopulse angle measurement. Since the phase difference and amplitude difference contain the object angle position, the tracking radar can perform continuous automatic tracking.

3.2.1.2 Radar object range measurement and tracking methods

When the pulse radar works, a stream of high-frequency signal with certain invariable pulse repeat period is transmitted by the transmitter via antenna. If there is an object within the propagating direction of the transmitted waves, the scatter phenomenon will appear and partial waves will be reflected to the receiving antenna. Hence, the time spent on the round trip between the radar and the object can be used to calculate the distance R from the object to radar. As for radar in single station, the relation between the distance R and the delay time t_R of echo waves relative to the transmitted signal is shown in the following equation:

$$t_R = \frac{2R}{c} \quad (3.1)$$

$$R = \frac{1}{2} ct_R \quad (3.2)$$

where c is the propagation speed of radio waves in the homogeneous medium.

Hence, the distance R from the object to radar can be obtained through accurate measurement of the delay, which is the approach for the pulse radar to execute range measurement.

3.2.1.3 Object velocity measurement and tracking

The following two approaches are commonly used for radars to carry out velocity measurement:

1. Through continuous measurement of the distance to the object, the variation ratio of distance can be obtained as well as the radial velocity of the object. This method is relatively simple without velocity ambiguity. However, the velocity measurement accuracy is relatively low due to the influence of range measurement accuracy.
2. The velocity of the object can be obtained with the Doppler frequency shift of the echo waves. Assuming the object is moving at speed of v in the radial direction with respect to the radar, compared the transmitted frequency f_0 , there exists Doppler frequency shift f_d in the received echo frequency f_r , and

$$f_d = f_r - f_0 = \frac{-2vf_0}{c+v} \approx \left(\frac{-2v}{c}\right)f_0 \quad (3.3)$$

where c is the speed of light. Assume that the velocity of the object is far less than the speed of light. In addition, when the object is moving away from the radar, the Doppler frequency is negative and, otherwise, it is positive. Therefore the radial velocity of the object can be obtained by measuring the Doppler frequency.

As for radar with high pulse repeat frequency, the accuracy of velocity measurement of this approach is relatively high without velocity measurement ambiguity. However, this approach still has the problem of range measurement ambiguity. As for radar with medium or low pulse repeat frequency, the Doppler frequency shift of the echo waves can be used to execute velocity measurement; however, this approach has the problem of both velocity measurement ambiguity and range measurement ambiguity. As for the continuous echo waves, this is the optimal velocity measurement method with higher accuracy and without the velocity measurement ambiguity; however, there exist some problems in range measurement.

Apparently, all the velocity measurement approaches require certain continuous observation time of the object. Theoretical analysis shows that the longer the observation time of the object is, the higher the obtained velocity measurement accuracy is.

3.2.2 Radar measurement data modeling

In the measurement data of radar, in general, there are three types of error: systematic, random, and gross. The system error keeps invariable or changes slowly following certain rules during the sampling process, is predictable to some extent, and usually can be partially corrected through proper calibration and compensation technology around the measurement;

random error is introduced by various uncertain perturbations or random factors, it cannot be corrected through calibration or compensation and however can be reduced through filter technology; and gross error is the result of negligent operation, equipment failure, or abnormal changes. This section will focus on the systematic error and random error in each radar measurement data.

3.2.2.1 Ranging error

The ranging error occurs during the measurement of the object slant distance and can be divided into tracking errors relative to radar (such as zero distance offset, thermal noise, multipath); conversion errors relative to radar (such as distance quantization and Doppler coupling); errors relative to object (such as dynamic lag and distance); and propagation errors (such as troposphere refraction). In view of types of errors, they can be divided into system error and random error.

- Ranging random error

Ranging random errors include receiving loop thermal noise error, pulse front edge jitter error, servo noise error, quantization error, pulse width variation error, and multipath error.

- Thermal noise error

Thermal noise error is related to the effective bandwidth and effective signal noise ratio of the signal. Assuming the pulse width of the transmitted wave of one monopulse radar is $0.8 \mu\text{s}$, the slope of range normalization error is 1.8, the pulse repeat frequency is 585.5 Hz, range servo bandwidth is 10 Hz, and the signal-to-noise (S/N) ratio is set to be 12 dB. Then the thermal noise error of the receiving system is 2.2 m.

- Jitter error

The pulse front edge jitter of transmitted waves will bring perturbation error to measurement data. For example, if the amplitude of the transmitted pulse front edge jitter is $\pm 10 \text{ ns}$, and the jitter is assumed to be uniform distribution, then the generated ranging random error is about 1 m.

- Servo noise error

As for pulse radar ranging system, the magnitude of servo noise error is usually 0.5–1 m.

- Quantization error

Since the code in measurement data is limited by bit, quantization error will exist in the measurement data. For example, if the distance measurement data uses a binary code output of 22 bits, the minimum quantization unit is 1.953125 m. Hence, the quantization error can be up to 0.7 m.

- Transmit pulse width variation error

If the pulse width of the transmitted waves varies within $\pm 10 \text{ ns}$ and follows the uniform distribution, the generated ranging error is less than 1 m.

- Multipath error

Echo waves reflected through multipath effect will lead to the multipath error during ranging measurement. If the emission factor is 0.3, the pulse width of the transmitted waves is 0.8 μs , the relative side lobe gain is 25 dB, then the multipath errors is in the order of up to 1 m.

- Ranging system error

System error is a major part of the ranging errors in ranging systems, which may include zero value error, delay error, wave refraction error, and dynamic lag error.

- Zero error

The distance of zero is the major determinate error item when the radar performs tracking and measurement, and this error must be calibrated. In general, the method of standard range marker shall be established within the radar facilities to simulate the space object. The range marker shall be as far as possible from the radar. The distance between the corner reflector on top of the range marker and the center of radar can be obtained through measurement data with high accuracy. The calibration of zero value by the use of range reference pole or marker is limited the selection of the range marker position. Generally, the zero error residuals after calibration should be less than 2 m.

- Delay error

Whether in pulse radar receiver or transponder, certain time will be spent in the transmitting or receiving of signals. The delay in receiving system can be obtained by calibration. And the error after calibration should be less than 2 m.

- Refractive error

Refractive error will be introduced when the wave propagates in the atmosphere and ionosphere. Refractive error correction model may be used in this case, and the residual error after correction should be less 1 m.

- Dynamic lag error

When the variable accelerated motion of the object leads to servo lead or lag, it will eventually introduce data errors in ranging. Ranging error due to dynamic lag can be described by the following equation:

$$\Delta R = K_v^{-1} \ddot{R} \quad (3.4)$$

From Eq. (3.4), it can be seen that the more tremendously the distance changes, the greater the dynamic lag error is.

3.2.2.2 Angle measurement error

Angle measurement error refers to measurement error generated during the measurement of angle coordinate of radar. Angle measurement errors includes tracking errors relative to radar (such as thermal noise, multipath, gust, wind, and gravity torsion moment), conversion errors relative to radar (such as shafting orthogonal, horizontal error zero, and data quantization), errors relative to object (such as dynamic lag and angular glint), and propagation

errors (such as refraction errors). In view of types of errors, they can be divided into system error and random error.

- Angle random error

The receiving system thermal noise error is the main component of angle measurement random errors.

- Receiving system thermal noise error

The thermal noise entering the receiving system of radar causes the output error of the angle error detector, which is especially important in the case of low S/N ratio and will lead to the tremendous disturbance on the angle of the antenna.

- Gust disturbance error

There are two kinds of winds, steady wind and gust. Gust is the component of fluctuation in the vicinity of the steady wind and will generate variable moment on the antenna. Gust disturbance error includes two parts, antenna deformation error and the servo zero drift error. When the wind reaches Grade 8, set the antenna aerodynamic constant to be $0.25 \text{ kgm}/(\text{m/s})^2$, the antenna elasticity coefficient to be 10^{-4} mil/kgm and the gust rms amplitude to be 2.5 m/s , then calculation shows that the gust can cause antenna deformation error of 0.0025 mil .

- Servo noise error

Since the servo system and the mechanical transmission system are not ideal, the noise generated is servo noise. Due to the nonlinearity of system components, the instability of the servo system, mechanical noise, and echo error, the servo noise error is very difficult to be calculated; however, it can be quantitatively estimated through the practical measurement.

- Code disk error

After the angle of the radar is outputted, errors can also be generated during numerical read process. Code disk error includes the quantization error and nonlinearity error. For 18-bit code disk the quantization error is $\sigma_g = 6000 \times 12^{-18}(\sqrt{12})^{-1} = 0.007 \text{ mil}$. The nonlinearity error of the code disk σ_f is determined via quantitative estimations. In general, the reference value of σ_f for an 18-bit code disk is 0.02 mil .

- Multipath error

During the tracking process with low elevation angle, waves between the radar and the object may be transmitted through two paths, the direct path between the radar and the object and the path via the reflection by the ground. When the elevation is low enough, the tracking on an object will be severely influenced.

- Angle measurement systematic error

The angle measurement systematic errors of mechanical radars include zero error, shafting error, gravity sag error, radio wave refraction error, and dynamic lag error.

- Zero error

In engineering, when the aiming axis is in horizontal direction and toward the direction of true north, it is considered to be the zero of the azimuth and the

elevation. In theory, the reading of the radar encoder should be zero; however, there is often an initial reading in code wheel in fact and that is the zero error. After calibration the residual value of zero error should normally be less than 0.05 mil.

- Shafting error

Shafting errors are equipment systematic errors such as the nonhorizontal error of the base, nonorthogonal error of azimuth and elevation axes, nonvertical error of optical axis, and unmatched error of electro-optical axis.

The calibration of the base nonhorizontal error is to determine the tilt amplitude β and the maximum tilt direction A_M of the antenna base. The imaging level meter is usually used for calibration. The nonorthogonal of the azimuth and the elevation axes means the elevation axis is not vertical to the azimuth axis. It can only generate azimuth angle error and cannot be adjusted after assembly. The electrical axis shall be vertical to the elevation axis, otherwise it will generate the elevation error. Both the electrical axis in azimuth and that in elevation shall be correctly calibrated. Since the adjustment of electrical axis and the orientation of coordinates are not convenient, in actual application, optical telescope mounted in the antenna is usually used as the media. During the assembly the optical axis shall be adjusted to be consistent with the electrical axis and to be vertical to the elevation axis. If the optical axis is not matched with the electrical axis, the azimuth error and the elevation error will occur. After calibration, each residual of the abovementioned errors must be less than 0.05 mil.

- Refractive error

Refractive errors can be divided into troposphere refraction and ionosphere refraction. Wave refraction usually generates the elevation error. Ionosphere refraction error depends on the working frequency of radar to a great extent.

If the wave refraction error is relatively large, it will have significant impact on the orbit determination of the space object and shall be corrected with the practical space environment parameters.

- Dynamic lag error

Dynamic lag is the index to evaluate the rapidity of the servo system. Dynamic lag error occurs because the velocity, acceleration, or high-order derivative cannot be tracked by the tracking system in coordinates of radar. Assuming the object angular velocity and angular acceleration are, respectively, $\dot{\theta}$ and $\ddot{\theta}$, then the dynamic lag error approximately satisfies the following relationship:

$$\Delta\theta = K_{\dot{\theta}}^{-1}\dot{\theta} + K_{\ddot{\theta}}^{-1}\ddot{\theta} \quad (3.5)$$

where $K_{\dot{\theta}}^{-1}$ and $K_{\ddot{\theta}}^{-1}$ are angular velocity error coefficient and angular acceleration error coefficient of the servo system, respectively. In space TT&C engineering the residual of the corrected dynamic lag error should be less than 0.07 mil.

- Antenna gravity sag error

The electrical axis offset will be generated by the structure distortion of radar under the function of gravity. In general, the larger the size of the antenna is, the severer the

distortion is. In the engineering of data processing, the corrected residual should be less than 0.05 mil.

3.2.2.3 Velocity measurement error

Doppler velocity measurement of pulse radars uses the Doppler effect of relative motion of object to obtain the change rate of range; hence, the accuracy of velocity measurement depends on the measurement accuracy of Doppler frequency. In the process of measuring the Doppler frequency shift, random and systematic errors will also be generated.

- Velocity measurement random error

Random errors of the velocity measurement system in pulse radars are generated mainly by thermal noise, multipath, object modulation, and quantization data processing.

- Thermal noise error

Assuming the velocity measurement subsystem of the monopulse radar has an equivalent noise bandwidth of 10 Hz, a filter bandwidth of 40 Hz, the error slope of the loop discriminator is taken as 1.2. If the S/N ratio = 12 dB, the thermal noise error is about 0.3 m/s. If the S/N is 20 dB, the thermal noise error is reduced to 0.01 m/s.

- Quantization error

If 20-bit codes of binary system are used to record Doppler frequency, the quantization error of the speed is less than 0.01 m/s.

- Speed measurement systematic error

The system error of velocity measurement system of the pulse radar mainly includes equipment zero error, zero variation error of frequency discriminator, radio wave refraction error, and dynamic lag errors. Wherein the equipment zero error and wave refraction error are identical with [Section 3.1.2](#).

- Zero value error of discriminator

Discriminator's zero value can be calibrated, but the change in temperature will cause the change of zero value. This error should be controlled within 0.01 m/s.

- Dynamic lag error

This velocity measurement error caused by the dynamic lag is

$$\Delta V = K_a^{-1} \ddot{R} \quad (3.6)$$

where K_a is the acceleration error coefficient of the velocity measurement system.

3.2.2.4 Mathematical model of systematic errors

Define the error of monopulse radar observation data $\Delta X(X = R, A, E, \dot{R})$ to be the difference between the measured data X_e and the true value of the observed object X_0 , that is, $\Delta X = X_e - X_0$. Based on the analysis of various typical errors in pulse radar tracking process, we can establish error correction models for ranging, angle measurement, and range rate data.

$$\Delta X = \Delta X_f + \Delta X_p + \varepsilon_X \quad (3.7)$$

where ΔX_f represents the measurement data errors due to equipment fixed deviation and shafting bias (referred to as equipment systematic error); ΔX_p denotes nonrandom errors that are generated in tracking process and can be modeled (referred to as process errors); and ε_X represents the composite influence of various unmodeled minor errors and random errors.

During the tracking process of pulse radars, the equipment systematic errors mainly consist of zero value, shafting error, and delay error of transponders. For range and angle measurement data, the mathematical model of equipment systematic error is as follows:

$$\begin{cases} \Delta R_f = R_0 + R_\tau \\ \Delta A_f = A_0 + (\beta \sin(A - A_M) + \delta) \tan E + (\lambda_{\text{optical/mechanical}} + \lambda_{A-\text{optical}})(\sec E - 1) \\ \Delta E_f = E_0 + \beta \cos(A - A_M) + k_g \cos E + \lambda_{E-\text{optical}} \end{cases} \quad (3.8)$$

where R_0 , A_0 , and E_0 are ranging and angle measurement zero value; R_τ is transponder delay error; β is the tilt amplitude of the base; A_M is the maximum tilt azimuth of the base; $\lambda_{A-\text{optical}}$ and $\lambda_{E-\text{optical}}$ are the deviation quantities of optical axis azimuth and elevation, respectively; δ is the nonorthogonal quantity of the azimuth and elevation axes; $\lambda_{\text{optical/mechanical}}$ is the optical/mechanical axis deviation quantity; and k_g is the radar antenna gravity sag factor.

The errors introduced during tracking process mainly include radio wave refraction error, timing error, and radio wave propagation time error. For range and angle measurement data, mathematical model for process errors is as follows:

$$\begin{cases} \Delta R_p = \Delta R_N + \Delta t \cdot \dot{R} + \frac{\Delta R}{c} \cdot \dot{R} \\ \Delta A_p = \Delta t \cdot \dot{A} + \frac{\Delta R}{c} \cdot \dot{A} \\ \Delta E_p = \Delta E_N + \Delta t \cdot \dot{E} + \frac{\Delta R}{c} \cdot \dot{E} \end{cases} \quad (3.9)$$

where ΔR_N and ΔE_N are the ranging and angle measurement errors, respectively, due to radio wave refraction; Δt is timing error; and $\Delta R/c$ is radio wave propagation time error.

3.2.3 Typical space surveillance radar

Radar designs are different according to different functional requirements in space target tracking and measurement. The commonly used detection and identification radars in the world are three kinds of ground-based radars: mechanical scanning and tracking radar that relies heavily on guidance, search radar with search and discovery function, and electromagnetic fence, which is mainly used to find targets, especially small ones.

3.2.3.1 Mechanical scanning tracking radar

The radar, which uses mechanical movement of the entire antenna system or a part of the system to achieve beam scanning, is called mechanical scanning tracking radar. The advantage of mechanical scanning is simple. The main disadvantages are that the mechanical inertia is great, the scanning speed is not high, it is difficult to quickly capture an object, and only a single object can be tracked and measured.

In order to achieve all-round track, the mechanical scanning tracking radars are typically mounted on an antenna base with two-dimensional mechanical rotation (azimuth, elevation). In order to ensure dynamic performance of the antenna operation and accuracy of the angle measurement, the antenna base of tracking radar has relatively complex mechanical and electrical requirements. Its servo system is a typical application of automatic control theory. The antenna can be controlled to track the operation object with the angle error signal between the radar antenna and object and perform real-time accurate measurement of the position of the mechanical axis of the radar.

The single pulse precision tracking radars are mechanical scanning tracking radars, which are deployed on American British Indies in Antigua and Ascension Island near the equator. Antigua Island is equipped with AN/FPQ-14 monopulse tracking radar. Operating frequency is 5400–5900 MHz; operating distance is 1480 km; operating antenna has Cassegrain circular parabolic diameter of 8.8 m. Ascension Island deployed two radars, and the main radar is AN/FPQ-15 monopulse precision tracking radar. Its frequency is 5400–5900 MHz, and parabolic diameter is 8.5 m. Another is AN/FPQ-18 monopulse precision tracking radar. And its frequency is 5400–5900 MHz, and the operating distance is 1100 km.

3.2.3.2 Phased array radar

Phased array radar is a phased array antenna (PAA) radar and an electronic scanning radar. If antenna uses electronic approaches to realize the steering or scanning of antenna beam in space, this kind of antenna is called electronic scanning antenna or electronically scanned array antenna. In line with the beam scanning method, electronic scanning antenna can be categorized into phase scanning and frequency scanning antennas. Both can be included in the concept of PAA.

PAA is composed of multiple antenna elements (radiating elements) arranged in certain order on a plane or curved surface, as well as signal power distribution/summing network components. If the elements of PAA are distributed on a plane, it is called planar PAA. If they are distributed on a curved surface, the antenna is called curved surface array antenna. A phase shifter is set on each antenna to change the phase relationship between the antenna element signals. The variation of signal amplitude between antenna elements is achieved by unequal power distribution/summing network or attenuator. Under the control of beam steering computers, the phase and amplitude relations between antenna elements can be changed, so as to obtain the antenna aperture illumination function corresponding to the required antenna pattern, and to quickly change the direction and shape of the antenna beam.

PAA has the following features. It can simultaneously search, detect and track multiple objects from different directions and at different heights, and simultaneously perform multi-object search, tracking, acquisition, identification, guiding, control, and victories evaluation. It can reasonably manage and control the main lobe gain, which is conducive to the realization of adaptive side lobe suppression against various disturbances. Its fast scanning capability shortens the time required for object signal detection, admission, and information transmission and enables the radar with high response speed. The antenna array of phased array radars is composed of many elements. Even if one or more of the array elements cannot transmit or receive, the performance of the radar as a whole will not be degraded. Therefore the radar is highly reliable.

The US equipment dedicated for space target tracking is the large phased array radar AN/FPS-85 in Florida. The radar was put to use in 1967. It is the first phased array radar used for space surveillance. The transmitting array is a square with a side length of 30 m. The working frequency is 442 MHz, the effective receiving beam width is 0.8 degree, the azimuth angle in the searching space is 102 degrees, the elevation angle is 105 degrees, and the detection range is up to 4000 km. It can simultaneously track over 200 targets and perform over 10,000 detections against thousands of space targets.

3.2.3.3 *Space fence*

The space fence radar system originated from the concept of continuous wave multistatic radars. A powerful transmitter generates a large fan-shaped energy beam, commonly referred to as space “fence.” When space objects pass through the fence, the reflected radar signals will be received by multiple receiving stations by the use of a large antenna, which will work as interferometers to determine the object arrival angle and angular velocity. The space object’s position is determined by observations from several stations. The object’s orbit will be calculated if it passes through the fence for several times.

US Navy Space Surveillance System (NAVSPASUR) was built in 1961. As a large radio interferometer, it has nine radar stations distributed across the southern United States, forming a large circle with inclination of 33.57 degrees relative to the equator. The fence has three transmitting stations and six receiving stations, with its space monitoring fence at roughly the level of the 33rd parallel north, crossing a longitude range of 42.5 degrees from 77.50 to 120 degrees west longitude. Such a large monitor screen can detect space debris with inclination of greater than 33 degrees. 88% of low and medium Earth orbit debris with 10 cm or larger in diameter can be detected in its everyday tracking. For a duration of 10 days, 170,000 observations will be finished, which accounts for 95% of low and medium Earth orbit debris of 10 cm in diameter or larger.

US space fence can track objects at heights of up to 24,000 km, and its average transmit power is up to 767 kW. The length of the antenna array is very long in the north–south direction. Transmit beam width is only 0.02 degree in the north–south direction. Such a narrow beam means that the overall gain of the transmit antenna can theoretically reach 70 dB or more. In order to enhance the effectiveness of the fence, it is under upgrade. Upgrading is focused on the following two aspects:

1. The frequency is raised to S-band, in order to detect space debris of 10 cm or less in diameter.
2. Bistatic design and determination with only one pass of data.

US Air Force next-generation “space fence” project contract was signed in June 2014. The project is the core of the US military to enhance space situational awareness capabilities, trying to track smaller objects. The new “space fence” will use world’s largest S-band (2–4 GHz) phased array radar, focusing on uninstructed detection and tracking of hundreds of thousands of objects in low and medium Earth orbits. The first site of the new “space fence” is located at Kwajalein Atoll in the Pacific Marshall Islands. Compared with the old system, the new “space fence” has large improvement in coverage, object library capacity, detection accuracy, and timeliness. The project will work to enhance the detection of space objects to a new level.

3.3 Electro-optical detection technology

3.3.1 Principles of electro-optical detection

Space object observing can be achieved by a variety of methods of radio, radar, and optical measurements, wherein the optical measurement method has characteristics of high accuracy and low cost, especially with a dominant position in the high-orbit space observation objects. Optical observation techniques have advantages such as low operating costs, far detection distance, stealth satellite detection, high accuracy, and environment friendly; the optical telescope has shortcomings, including easy influence by the weather and only working in the clear night, and the low-orbit object observation is only suitable for twilight observation. With the development of optoelectronic components and image processing technology, the optical measurement rose to a new level, and the optical observation technology is quickly becoming a primary observation mean of high-orbit space objects.

3.3.1.1 *The optical structure of electro-optical telescopes*

There are three typical structures of telescope optical system: refractive structure, reflective structure, and catadioptric structure.

1. Refractive structure

Refracting telescope is one of the first telescopes designed and used by human. In 1608–09, Hans Lipperhey, Jacob Metius, and Zacharias Janssen independently invented the refracting telescope. Galileo Galilei, an Italian scientist, first developed a telescope system composed of objective lens and eyepiece, which magnified 30 times, and discovered the craters on the Moon and four major moons of the Jupiter using the system. Refracting electro-optical telescope has the following characteristics: (1) larger field of view of surveillance, (2) stable quality of star images, and (3) little effects of scattering light. Because of these characteristics, it is usually used in astrometry, stellar

astronomy, and optical observation. But the shortcoming is that diameter of refracting telescope cannot be bigger.

2. Reflective structure

According to the position of the focus, telescopes with reflective structure can be divided into five types: main focus, Newton focus, Cassegrain focus, Nasmyth focus and coude focus. Most horizontal reflective telescopes will use Cassegrain focus, one or two Nasmyth focus; and equatorial reflector telescope will use Cassegrain focus and coude focus. Reflective structure has characteristics such as no color aberration, small loss of near-ultraviolet and near-infrared light, and the clear aperture. The current excellent telescopes in mainstream of the world are all reflecting telescopes.

3. Catadioptric structure

Refracting telescope has large field of view, but its aperture cannot be bigger; the aperture of reflecting telescope can be bigger and its clarity is good, but the field of view is small. So the catadioptric telescope comes into being, namely, that both the refraction and reflection phenomenon exist in optical system. Schmidt telescope is the most commonly used. Its primary mirror is a spherical mirror and its corrector is a wave-shaped lens. Generally, the aperture of the primary mirror is about 1.5 times the correction mirror. And the corrector's aperture is used to be its equivalent aperture, because the light shall first pass through the corrector, and then only corrected light is required. World's largest Schmidt telescope having primary mirror diameter of 2 m, 1.34m diameter mirror to correct the field of view reaches 3.4 degrees.

3.3.1.2 Optical telescope's mount structure

There are three sorts of optical telescope mounts used for space objects' observation: equatorial, altitude–azimuth, and altitude–altitude, as discussed in the following:

1. Equatorial mount

Equatorial structure has two mutually perpendicular axes of rotation. One is called pole axis that is parallel to celestial pole and pointing at the North Pole. The other is perpendicular to the polar axis and called declination axis. Rotation about the polar and declination axes can make the telescope point to different hour angles and declination, as shown in Fig. 3–1A. The advantages of the equatorial mount include the following aspects. First, the apparent motion of celestial bodies can be compensated easily by uniform rotation of ascension axis; second, tracking area covers all zenith spot, and there is no blind zenith spot. Yet it has the disadvantage of having blind spot in pole area, complex mechanical structure, complicated installation, and high cost. This mount structure is usually not used for space object observation equipment.

2. Altitude–azimuth mount

Alt–az mount has two mutually perpendicular axes. The azimuth axis (also called vertical axis) is perpendicular to the geoid and the horizontal axis (also called elevation axis) is parallel to the geoid. Visual axis rotating around the vertical and the horizontal axes enables the telescope to a different azimuth and elevation, as shown in Fig. 3–1B.

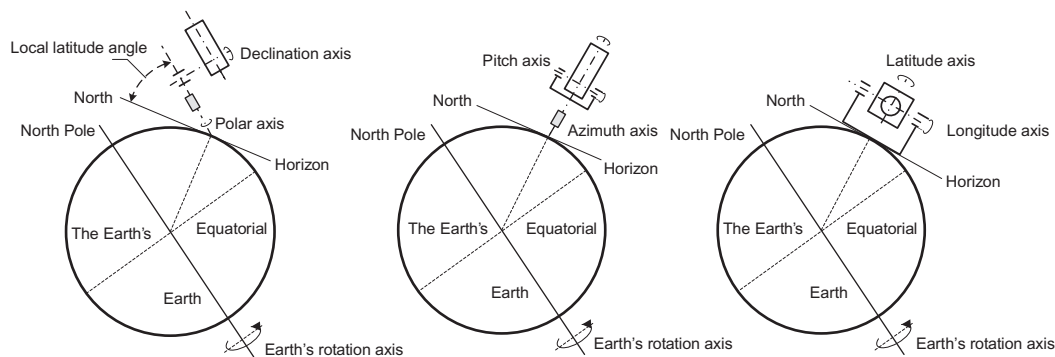


FIGURE 3-1 Electric-optical telescope basic structural patterns: (A) equatorial, (B) altitude–azimuth, and (C) altitude–altitude.

The alt–az mount has the advantages of better mechanical structure, small slewing radius, good tracking performance, and easy field installation. The disadvantage is its tracking blind spot in zenith. Due to the limitation of telescope rotation velocity and acceleration, it is impossible for any alt–az telescope to achieve an instant fast change of 180 degrees in azimuth when the space object is passing the zenith. Thus the blind spot is formed around the zenith area, which is called blind tracking spot.

3. Altitude–altitude mount

Alt–alt mount also has two mutually perpendicular axes of rotation. The longitude axis is parallel to the north–south direction, and the other perpendicular to the longitude axis is called latitude axis. The apparent axis' rotation around the longitude and the latitude axes enables the telescope point to different space areas, as shown in Fig. 3–1C. Alt–alt mount has two advantages: (1) it has no blind spot in zenith, which is the best observation area. (2) When the zero position of the latitude and longitude is set in the zenith, the longitude and latitude axes work within the range of (–90 degrees, +90 degrees), which can cover any moving object in the space. In contrast, the alt–az mount will have to work in the range of 360 degrees to achieve the same result. In this case the reliability of the device is improved. It has the disadvantage of large slewing radius and complicated field installation.

3.3.2 Electric-optical telescopes measurement data types and positioning

3.3.2.1 Measurement data

1. Measurement data and positioning

Electric-optical telescope has two positioning methods, shafting positioning and celestial positioning. The two methods have different approaches for space object measurement. When the electric-optical telescope adopts celestial positioning mode for tracking and observation, it uses the relative position images of the object in the same

frame of the field of view with respect to the stars obtained through TV measurement system, so as to calculate the precise position of the object, and then guide the shafting positioning TV system to track the object. Shafting positioning measurement system mainly uses television shafting precision positioning to complete the object tracking and high-precision measurements.

When the electric-optical telescope adopts different positioning modes for space object tacking, the measured data have different types. Measurement data by Alt–az shafting positioning include azimuth A and elevation h ; measurement data by celestial positioning include right ascension α and declination δ .

2. Measurement data conversion

The following paragraph describes the method of converting the two measurements. Assuming the longitude and latitude of the tracking site are Λ and ϕ ; the local sidereal time is θ ; and the observed object's range, azimuth, and elevation are ρ , A , and h , respectively, then:

The position vector $\vec{\rho}$ of the space object with respect to the site's alt–az coordinate system is as follows:

$$\vec{\rho} = \rho \cosh \sin A \hat{i} + \rho \cosh \cos A \hat{j} + \rho \sinh \hat{k} \quad (3.10)$$

where $\hat{i}, \hat{j}, \hat{k}$ is the site's basic vector. The transformation matrix from the site alt–az coordinates to geocentric equatorial coordinates is as follows:

$$\mathbf{Q}_{xX} = \begin{bmatrix} -\sin \theta & -\sin \phi \cos \theta & \cos \phi \cos \theta \\ \cos \theta & -\sin \phi \sin \theta & \cos \phi \sin \theta \\ 0 & \cos \phi & \sin \phi \end{bmatrix} \quad (3.11)$$

Therefore the position vector of the space object in the topocentric equatorial Cartesian coordinate system, $\vec{\rho}_X$ is as follows:

$$\vec{\rho}_X = \mathbf{Q}_{xX} \vec{\rho} = \begin{bmatrix} -\sin \theta & -\sin \phi \cos \theta & \cos \phi \cos \theta \\ \cos \theta & -\sin \phi \sin \theta & \cos \phi \sin \theta \\ 0 & \cos \phi & \sin \phi \end{bmatrix} \begin{bmatrix} \rho \cosh \sin A \\ \rho \cosh \cos A \\ \rho \sinh \end{bmatrix} [\hat{I}, \hat{J}, \hat{K}] \quad (3.12)$$

The relation between the observation vector in topocentric equatorial Cartesian coordinates and the observed right ascension α and declination δ is:

$$\vec{\rho}_X = \rho \cos \delta \cos \alpha \hat{i} + \rho \cos \delta \sin \alpha \hat{j} + \rho \sin \delta \hat{k} \quad (3.13)$$

By comparing the above two equations, we obtain the relation between right ascension α , declination δ , and azimuth A and elevation h :

$$\begin{aligned} \sin \delta &= \rho \cos h \cos A \cos \phi + \rho \sin h \sin \phi \\ \cos \delta \cos \alpha &= -\sin \theta \cos h \sin A - \sin \phi \cos \theta \cos h \cos A + \cos \phi \cos \theta \sin h \\ \cos \delta \sin \alpha &= \cos \theta \cos h \sin A - \sin \phi \sin \theta \cos h \cos A + \cos \phi \sin \theta \sin h \end{aligned} \quad (3.14)$$

3.3.2.2 Working mechanism and features of positioning

1. Working mechanism and features of shafting positioning

When the shafting positioning mode is adopted by the electro-optical telescope, once the object enters the field of view of the optical system, the servo system will capture, lock, and track the object, keeping the object always within the field of view of the optical system. TV measurement system will record the object's bias relative to the center of the field of view, or miss distance. Meanwhile, angle measuring device begins to measure the azimuth and elevation of the center of the field of view, which, together with the miss distance, will be synthesized into the actual angular position of the object.

Characteristics of shaft positioning include shaft positioning accuracy that depends basically on the shafting precision of the telescope, so shaft machining precision of the telescope is high, resulting in higher development costs of the telescope, and due to the influence of atmospheric refraction correction error, measurement accuracy will be affected during low elevation observation; the tracked objects by shaft positioning has no problem of prolonged star image, and the fast and slow objects does not need to be tracked in different ways; shafting positioning calculation is simple, requirement for real-time processing of computer is not high, which will help improve the sampling frequency of the measured data.

2. Working principle and characteristics of astronomical positioning

Celestial positioning gives the position information of space objects by comparing the relative position of the space object with respect to reference stars in CCD image. This positioning approach is achieved by establishing the mapping relationship between the ideal and the measured coordinates of the reference stars. The working procedures of the celestial positioning include establishing measured star patterns, calculating mass center of the star images, fast matching algorithm of star patterns, ideal coordinates of reference stars, CCD image processing models, normalization of electro-optical telescope pointing, and space object's position.

The main characteristics of the celestial positioning are as follows: (1) accuracy of celestial positioning is not subject to telescope shafting error and atmospheric refraction correction error, thus the positioning precision of the celestial positioning is higher than the shaft positioning; (2) this positioning approach requires larger field of view, and at least three reference stars are required in the field of view; and (3) celestial positioning requires higher level of computer real-time processing. Millions of star data shall be stored in the computer, and reference stars shall be found in very short time according to the telescope pointing and positions in CCD images, so as to output the positioning results of the space objects.

3.3.3 Measurement models of electro-optical telescope

In the tracking of space objects by electro-optical telescopes, the telescope is controlled to point toward the preset space area, and "stares" at the space object spot. In working mode of shafting positioning, the telescope collects the images and extracts the miss distance of the

objects. The miss distance will then be integrated with the telescope encoder data, and the final position information will be output after comprehensive error correction. In working mode of celestial positioning, the collected images are recorded in real time, where calculation is done, in consulting with the reference star library, to give the position information of the space objects. The following section discusses the measurement models in the working modes of shafting positioning and celestial positioning.

3.3.3.1 Measurement model of shafting positioning

The common positioning mode in an electro-optical telescope system is shafting positioning, which is a method of absolute positioning. By assuming Telescope Imaging CCD center coordinates is (x_0, y_0) , the centroid position space object image is (x_s, y_s) , CCD image scale is (S_x, S_y) , photoelectric telescope pointing to (A_0, E_0) , combined with the objects of object amount and the telescope pointing information, calculate the spatial orientation of the object A_s and the pitch angle E_s are as follows:

$$\begin{cases} E_s = E_0 \pm (y_s - y_0) \times S_y \\ A_s = A_0 \pm (x_s - x_0) \times S_x / \cos E_s \end{cases} \quad (3.15)$$

where the selection of plus or negative signs depends on the incremental direction of the azimuth and elevation in the CCD image.

The conversion relation between alt–az coordinates (A_s, E_s) and alt–alt coordinates (L, B) is as follows:

$$\begin{cases} E_s = \arcsin(\cos L \cos B) \\ A_s = \arctan(\sin L \operatorname{ctg} B) \end{cases} \quad (3.16)$$

3.3.3.2 Measurement model of celestial positioning

Modern astronomical positioning method was first proposed by John and Jean and then developed by Chris, Dustin, and so on. Celestial positioning gives the position information of space objects by comparing the relative position of the space object with respect to reference stars in CCD image. This positioning approach is achieved by establishing the mapping relationship between the ideal coordinates (ξ, η) and the measured coordinates (X, Y) of the reference stars.

1. Star image matching

Star pattern matching is one of the vital steps to achieve high-precision celestial positioning, including the selected catalog, the establishment of a database of star pattern recognition, calculation of star image centroid, and star pattern matching algorithm.

a. Selection of star catalog

The accuracy of star catalog is far higher than the accuracy of the observing equipment. The selected star catalogs shall contain sufficient and evenly distributed

reference stars in whole space. Common used catalogs include TRC, Tycho-1, and Tycho-2.

b. Establishment of star pattern recognition database

The number of stars in the catalog library is huge. For example, there are about 900,000 entries of stars brighter than 11 Mag in Tycho-2 catalog. If all stars in Tycho-2 catalog are selected as candidates to calculate, much time is required for computing. This is not conducive to the rapid realization of star pattern recognition, not alone to the star pattern calculation. In fact, this is not necessary in actual application. In engineering practice a subcatalog of the stars is selected, which usually consists of stars within the extreme detection of the electro-optical telescope. In addition, some stars whose angular distance is less than certain value are deleted from the subcatalog, so as to further reduce the retrieval time of the reference stars, to increase the real-time performance of celestial positioning, and to further reduce measurement error of reference stars' coordinates.

c. Calculation of star image's centroid

Star image's centroid is obtained by the processing of observed CCD image, as the CCD field of view is large for space object optical observation equipment, and the data processing has high real-time requirements, commonly used centroid calculation method is two-dimensional modified moment method.

d. Fast matching algorithm of star patterns

Commonly used star pattern matching algorithms include triangle matching algorithm, polygon angular distance matching algorithm, and grid algorithm. Among them triangle algorithm is the most adopted in engineering applications due to its simple structure and less computing.

2. CCD image processing model

Due to the telescope aberrations, CCD installation deviation error, and other factors, the relationship between the ideal and the actual coordinates cannot be accurately derived. Thus this relationship is usually expressed in polynomial, that is, CCD image processing models. CCD image processing models used in space object observations include two-constant model, four-constant model, six-constant model, eight-constant model, ten-constant model, twelve-constant model, and twenty-constant model, which is used to establish the relationship between the measured coordinates and the ideal ones.

There is a one-to-one correspondence between the ideal coordinates (ξ_i, η_i) and the equatorial coordinates (α_i, δ_i) of the reference star. The formula for calculation is:

$$\begin{cases} \xi_i = \frac{\cos \delta_i \sin (\alpha_i - \alpha_0)}{\sin \delta_i \sin \delta_0 + \cos \delta_i \cos \delta_0 \cos (\alpha_i - \alpha_0)} \\ \eta_i = \frac{\sin \delta_i \cos \delta_0 - \cos \delta_i \sin \delta_0 \cos (\alpha_i - \alpha_0)}{\sin \delta_i \sin \delta_0 + \cos \delta_i \cos \delta_0 \cos (\alpha_i - \alpha_0)} \end{cases} \quad (3.17)$$

where (α_0, δ_0) is the correspondent right ascension and declination of the CCD image center.

a. Two-constant model

Generally, one reference star is required in this model, the CCD image's scales in the x and y directions are assumed to be identical, and the angle θ between the ideal coordinates (ξ_i, η_i) and measured coordinates (x_i, y_i) are known.

$$\begin{cases} \xi_i = a + \cos \theta x_i + \sin \theta y_i \\ \eta_i = d - \sin \theta x_i + \cos \theta y_i \end{cases} \quad (3.18)$$

b. Four-constant model

Generally, two reference stars are required in this model, and the scales in both directions are assumed to be identical.

$$\begin{cases} \xi_i = a + b x_i + c y_i \\ \eta_i = d - e x_i + f y_i \end{cases} \quad (3.19)$$

c. Six-constant model

Three or more reference stars are required in this model.

$$\begin{cases} \xi_i = a + b x_i + c y_i \\ \eta_i = d - c x_i + b y_i \end{cases} \quad (3.20)$$

The abovementioned three models primarily consider the first-order linear effect, while eight- or ten-constant models take into account the nonlinear difference and require multiple unknown variables. Thus more reference stars are required. It should be noted that the final positioning accuracy of space objects obtained by using higher order CCD image processing models is not necessarily better than the one obtained by using lower order models. Because measurement error of each of the reference stars will be integrated into the final measurement results. It is easy to verify that the more the unknown variables to be solved, the lower the accuracy of the solution is, in the case of the same conditional equations and of the same random errors of known quantities. Besides, higher order CCD image processing models require more computer processing overloading. Therefore we only select sufficient reference stars within certain range of the space object image and use lower order CCD image processing models. In this way the processing time requirements and expected accuracy can both be met.

3. Calculation steps in real-time celestial positioning

- a.** Read the telescope's encoder data in the L axis and B axis, and translate the pointing information into the celestial coordinates of the telescope's pointing (right ascension and declination).
- b.** Around the telescope pointing (right ascension and declination) neighboring, quickly retrieve star catalog and find the reference stars within the CCD field of view.
- c.** According to the telescope pointing and CCD camera's scale, calculate the equatorial coordinates of each measured star image.

- d. Match the theoretical equatorial coordinates with the measured equatorial coordinates, and obtain the measured coordinates of the reference stars.
- e. Obtain the measured coordinates of the space objects by CCD image processing.
- f. Establish CCD image processing model by the use of reference stars.
- g. Calculate the space objects' right ascension and declination by the use of CCD image processing model and measured coordinates of space objects.

3.3.4 Measurement errors and compensation techniques of telescopes

Measurement error of electro-optical telescope systems refers to deviation of measured angular values from their true values in space object measurement. Overall, the factors affecting the measurement accuracy of the telescope can be divided into static and dynamic measurement error sources. When the telescope is in stationary state, the measurement errors usually result from such factors as manufacturing process, installation, and adjustment. When the telescope is tracking moving objects, the measurement errors are usually larger, due to mechanical deformation and random factors. The static measurement error sources include vertical axis tilt errors, the horizontal axis tilt errors, sighting axis error, zero difference, directional difference, errors caused by optical system geometric distortion, and atmospheric refraction error. The sources of dynamic measurement errors include tracking motion error, CCD miss output lag error, the error caused by atmospheric jitter, sighting axis swing error, and other random errors. According to the nature of the error, the previously mentioned errors fall into system errors and random errors. The vast majority of system errors can be adjusted or corrected, but residual errors still exist after correction. Random errors cannot be corrected due to its randomness. Their impact can be decreased by smoothing of measured data.

3.3.4.1 *Static errors*

1. Shafting error

During tracking the shaft must meet certain conditions, such as vertical axis must be perpendicular to the horizontal, and the horizontal axis must be perpendicular to the vertical axis. Due to constraints of manufacturing process, assembly and adjustment in use and other factors, the instrument's three axes, in fact, do not fully meet the abovementioned three conditions. Therefore there are objective measurement errors caused by inaccurate axes. This type of errors is called shafting error. It consists of vertical axis tilt error, horizontal axis tilt error, and sighting axis error. These errors include two parts: one is a constant systematic error caused due to the adjustment and the other part is the amount of change in the instrument movement, namely, random errors.

2. Encoder error

Elevation and azimuth shaft angle encoders are precision angular measurement parts of electro-optical telescope. Encoder error here refers to the installation and adjustment error due to the nonalignment with the optical axis after the encoders are installed on

horizontal and vertical axes. Namely, the error includes the horizontal axis encoder's zero difference and the vertical axis azimuth encoder's directional difference. They affect the authenticity of the measured values, thus affecting the measurement accuracy, and shall be corrected.

3. TV static miss distance measurement error

TV miss distance refers to the offset of the object image point from the origin of the object screen coordinate system. TV miss distance measurement error includes quantization error in the CCD sensor, interpolation error, tail error, and the optical system's focal length error. The number of scanning lines of the CCD camera is subject to the resolution limits of the imaging object surface, and the spacing between the scanning lines is the smallest unit used to measure the size of the object image point. Thus the angular resolution of the camera limits the measurement accuracy of the system.

4. TV miss distance pure lag error

When the television camera works, the image information stored in the object surface is read out by raster scanning, pixel by pixel from top to bottom and left to right. There is a lag of one frame from the beginning of the timing sampling to the sending out of the miss distance. Things may differ if there are other lag factors. For instance, inertia of the television camera itself may generate the signal transmission lag, causing the change of time lag of the miss distance. The measurement data of TV tracking synthesizes the encoder data and TV miss distance. Due to the pure time lag of the TV miss distance, errors will eventually exist in the synthesized data.

5. Impact of atmosphere refraction

In observing space objects with precision electro-optical telescopes, the observed direction of the object differs from its real direction due to the atmospheric refraction. And this type of directional error is called refraction. The true height equals to the observed height deducted by the atmosphere refraction. The smaller the star's elevation is, the greater the refraction is. The change of atmosphere pressure will lead to different atmosphere refraction. Atmosphere refraction is an important factor affecting the measurement accuracy of space objects. Current theoretical formula for atmosphere refraction is based on the assumptions that the atmosphere density changes with its distance from the ground and with other ambient environment changes. Precise observation requires further precise correction of atmosphere refraction.

6. Other static errors

Other static errors include errors caused by inconsistent coordinates, nonalignment error between the optical axis of the optical system and the electro-optical axis of the CCD plane, as well as nonalignment error between the horizontal and vertical axes of CCD plane and the optical system.

3.3.4.2 *Dynamic errors*

1. Instrument tracking motion error

When electro-optical telescope is tracking motion objects, rotation of the turret will inevitably bring about structural deformation, displacement of instrument, or shaft

bending, which will thereby generate dynamic error increment. And these errors are random, including base adjustment error, the vertical axis swing error, the vertical axis photoelectric encoder measurement error, the vertical axis photoelectric encoder zero error, the vertical axis photoelectric encoder coupling error, horizontal axis swing error, the horizontal axis optical encoder measurement error, the horizontal axis optical encoder zero error, the horizontal axis optical encoder coupling error, sighting axis up-down placement error, error of collimation error (swing of sighting axis azimuth), and swing error of sighting axis elevation angle.

2. Nonsynchronized time sampling error

In real-time dynamic TV measurement systems, the object position is measured mostly by counters in row and field directions. Nonsynchronized sampling error is caused by the inconsistency between the time of the object image point scanning by the electron beam and the time of system sampling. TV measurement system is a real-time sampling system, where a variety of data, such as time information, object point information, and position of the instrument (i.e., center position of camera tube object surface), must be collected in a unified time. Generally, the leading edge of frame synchronization pulse is taken as the sampling pulse to collect the previous frame of data. This type of sampling is called frame-end sampling or frame-terminal sampling. In the dynamic measurement system, the object image points keep moving in the camera tube object surface. The moving distance of the point within one pulse interval is the nonsynchronization sampling error of the dynamic measurement.

3. Boresight swing error of optical systems

Reasons for boresight swing of optical systems include (1) optical elements in motion (such as dimming variable density disk and the focus lens). (2) Optical system barrel or optical parts distortion or slight displacement due to thermal deformation, which is caused by one side radiation by sunlight or different thermal expansion coefficients of metal materials. (3) Barrel structure deformation caused by its weight redistribution when the barrel is in elevation motion. (4) Horizontal axis random swing in horizontal plane due to the gap between the bearings.

4. Errors caused by atmospheric jitter

Atmospheric jitter can cause diffusion of object image points and further affect the position extraction of the object in CCD surface. Impact of atmospheric jitter on the electro-optical telescope TV measurement system includes three aspects: random fluctuation of image point position, random fluctuation of optical density in the image, which may result in larger image or irregular diffusion circle in comparison with situation without atmospheric jitter effect. Atmospheric jitter is still a complex issue, as it is heavily affected by the natural meteorological conditions, as well as by locations, seasons, and other environmental factors. Generally, we select an empirical value as the random error rms value caused by the atmospheric jitter.

5. Other errors

In addition to the major errors affecting the measurement accuracy, there are other potential minor factors, including changes of the foundation due to ambient temperature

vibration, stability of counter pulse, random interference by ambient electrical field, magnetic field, and thermal noises.

3.3.4.3 Angle measurement error model

When a single telescope is used to measure the space object, it can only give the radial angle of the object relative to the telescope, that is, the included angle between each axis of the measurement coordinate system and the line connecting the main point of the optical system and the space object. The angle measurement errors come from various sources for different telescope structures. Here we only take alt-az tracking telescope as an example to analyze the sources of the angle measurement errors and their calculation.

Telescope angle measurement error refers to the difference between the actual angular position and the measured angular position of the measured space object at a certain moment.

As shown in Fig. 3-2, O denotes the tracking/observing station, OP is the visual axis orientation of the device, and OM is the apparent direction of the object, then σ_φ represents the error angle of the measurement for this telescope. Its components in the horizontal direction and the height direction is $\delta_{\varphi A}$ and $\delta_{\varphi E}$, respectively.

$$\delta_{\varphi A} = \delta_A \cos E, \quad \delta_{\varphi E} = \delta_E$$

where δ_A denotes the azimuth angle measurement error, and δ_E denotes elevation angle measurement error. $\sigma_{\varphi A}$ and $\sigma_{\varphi E}$ are further composed of multiple errors.

$$\begin{aligned} \sigma_{\varphi A} &= \sqrt{\sum_{i=1}^{i=n} (K_i K'_i \delta_{Ai})^2} \\ \sigma_{\varphi E} &= \sqrt{\sum_{j=1}^{j=m} (K_j K'_j \delta_{Ej})^2} \end{aligned} \quad (3.21)$$

where δ_{Ai} and δ_{Ej} denote the limit values for the i th item of azimuth error and j th item of elevation error, respectively; K_i , K_j , K'_i , and K'_j represent the probability coefficients and error transfer coefficients for the i th item and j th item, respectively.

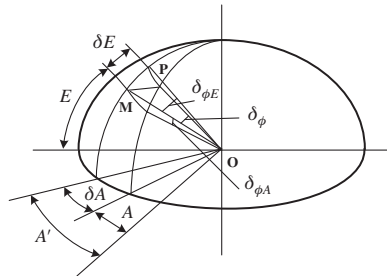


FIGURE 3-2 Angle measurement error diagram.

The mean square error of the angle measurement error is:

$$\sigma_\phi = \sqrt{\sigma_{\phi_A}^2 + \sigma_{\phi_E}^2} = \sqrt{\sum_{i=1}^{i=n} (K_i K'_i \delta_{Ai})^2 + \sum_{j=1}^{j=m} (K_j K'_j \delta_{Ej})^2} = \sqrt{\sum_{i=1}^{i=n} (K'_i \sigma_{Ai})^2 + \sum_{j=1}^{j=m} (K'_j \sigma_{Ej})^2} \quad (3.22)$$

For tracking optical measurement device, the angle measurement error σ_φ consists of static error and dynamic error.

$$\sigma_\phi = \sqrt{\sigma_A^2 + \sigma_E^2} \quad \begin{aligned} \sigma_A &= \sqrt{\sigma_{AS}^2 + \sigma_{AD}^2} \\ \sigma_E &= \sqrt{\sigma_{ES}^2 + \sigma_{ED}^2} \end{aligned} \quad (3.23)$$

where σ_{AS} , σ_{ES} , σ_{AD} , and σ_{ED} denote the static and dynamic errors of the azimuth (elevation) angle, respectively.

Device's dynamic error results from the dynamic loads in motion when the device is tracking space objects. As it is difficult to estimate, empirical formula is generally adopted to calculate the error.

$$\begin{aligned} \sigma_{AD} &= K_A \sigma_{AS} \\ \sigma_{ED} &= K_E \sigma_{ES} \end{aligned}$$

K_A and K_E are dynamic error coefficients, which generally range from 1.15 to 1.5.

$$\begin{cases} \sigma_{AS} = \sqrt{[(1/2) \cdot \text{tg } E \cdot \sigma_V]^2 + [(1/\sqrt{2}) \cdot \text{tg } E \cdot \sigma_i]^2 + (\sigma_C / \cos E)^2 + \sigma_R^2 + (\sigma_P / \cos E)^2} \\ \sigma_{ES} = \sqrt{[(1/2) \sigma_V]^2 + \sigma_{CV}^2 + \sigma_R^2 + \sigma_P^2} \end{cases} \quad (3.24)$$

In abovementioned formulas, E is elevation angle of the equipment; σ_V is vertical axis error, that is, the vertical axis' deviation from the local plumb line.

$$\sigma_V = \sqrt{\sigma_{V1}^2 + \sigma_{V2}^2 + \sigma_{V3}^2}$$

σ_{V1} is the vertical axis leveling error, $\sigma_{V1} = \tau/10\sqrt{2}$, τ is leveling bubble grid values. σ_{V2} is the vertical axis swing (for ball bearing shaft, it is the vertical axis swing of the thrust bearing in flat rail). $\sigma_{V2} = K' \Delta h \rho / \sqrt{2} D$, Δh represents the end surface roughness of the thrust bearing. K' is the load deformation coefficient; usually $K' = 0.4-0.96$, ρ is 2×10^5 . D is the thrust bearing's median diameter, and σ_{V3} is the random swing of the vertical axis. For ball bearing shaft, it depends on the component of more than three times of ball size error, the out-of-roundness and the roughness of thrust bearing ring. σ_i is horizontal axis error, that is, non-perpendicularity between the horizontal axis and vertical axis. $\sigma_i = \sqrt{\sigma_{i1}^2 + \sigma_{i2}^2 + \sigma_{i3}^2}$ σ_{i1} represents the nonperpendicularity of the horizontal axis with respect to the vertical axis, and σ_{i2} the system swing of the horizontal axis within the vertical plane. For the ball bearing shaft, there is the following equation: $\sigma_{i2} = K'' \Delta D \rho \sqrt{2} / L$, ΔD is the out-of-roundness of the journal; L is the distance between two fulcrums of the horizontal axis; and K'' is load

deformation coefficient, where $K'' = 0.4-0.96$. σ_{B3} represents the random swing of the horizontal axis within the vertical plane. For the ball bearing shaft, there is the following equation: $\sigma_{B3} = 2(\Delta d + \Delta P)\rho/(3L)$, Δd is the ball size error. ΔP is the out-of-roundness of the ball. σ_C is the boresight error, that is, the nonperpendicularity of the boresight axis and horizontal axis within their plane. $\sigma_C = \sqrt{\sigma_{C1}^2 + \sigma_{C2}^2 + \sigma_{C3}^2 + \sigma_{C4}^2 + \sigma_{C5}^2}$, σ_{C1} is collimation error, which depends on its measurement error; σ_{C2} is boresight system swing resulting from the horizontal axis deformation. σ_{C3} is the system swing of boresight axis within its plane with horizontal axis; σ_{C4} is the random swing of boresight axis within its plane with horizontal axis; σ_{C5} is the boresight axis deviation due to the variation of optical elements and cross hair. σ_{CV} is swing of the boresight axis within the cross section perpendicular to the horizontal axis. σ_R is goniometer error, namely, the error of goniometer in azimuth and elevation directions. $\sigma_R = \sqrt{\sigma_{R1}^2 + \sigma_{R2}^2 + \sigma_{R3}^2 + \sigma_{R4}^2}$, σ_{R1} is the goniometer zero error; σ_{R2} is goniometer measurement error; σ_{R3} is the coupling transmission error of goniometer; and σ_{R4} is zero error caused by coupling torsional deformation of the goniometer. σ_P is the miss distance measurement error, namely, the interpretation error of the object position in the film or CCD. When a film recorder is adopted, the miss distance measurement error is $\sigma_P = \sqrt{\sigma_{P1}^2 + \sigma_{P2}^2 + \sigma_{P3}^2}$, σ_{P1} is focusing error; and σ_{P2} is the position measurement error of interpretative instrument. σ_{P3} is aiming error. When CCD is adopted in measurement, the miss distance measurement error is $\sigma_P = \sqrt{\sigma_{P1}^2 + \sigma_{P2}^2 + \sigma_{P3}^2 + \sigma_{P4}^2}$, σ_{P1} is focusing error; σ_{P2} is centroid extraction origin error; $\sigma_{P2} = \Delta''/(2\sqrt{3})$, Δ'' is angular resolution of CCD pixels. $\Delta'' = (\Delta/f) \times 2 \times 10^{-5}$, σ_{P3} is centroid extraction object position error; $\sigma_{P3} = \Delta''/(2\sqrt{3})$, σ_{P4} is coordinate rotation error during CCD installation.

3.3.4.4 Error compensation technology

In order to measure the position of the target accurately, it is necessary to determine the shafting error and reading system error of the telescope system accurately. Error calculation and compensation is completed by taking pictures for multiple stars. Common error composition techniques include least square systematic error correction and spherical harmonic systematic error correction. Among them, the least square systematic error correction method mainly considers several systematic errors that have a great impact on angular measurement accuracy, such as shafting error, directional difference, and zero difference. The parameters in the correction function are few in number and cannot be changed, so it is difficult to achieve a comprehensive correction of the systematic error. However, the spherical harmonic systematic error correction method does not specifically consider the physical meaning of each parameter and only selects the number of parameters according to the fitting degree of the system error curve. Therefore in the systematic error correction of electro-optical tracking system, as long as the parameters are reasonably selected, the systematic error correction method of spherical harmonic function will have higher accuracy than the least square systematic error correction method. The spherical harmonic systematic error correction method is introduced next.

Systematic error, as a quantity related with telescope position status, is a function of position. We use A and E to represent the azimuth and elevation angles and use functions f_A and f_B to indicate the deviation. Then

$$\begin{aligned}\Delta A &= f_A(A, E) \\ \Delta E &= f_B(A, E)\end{aligned}\quad (3.25)$$

f_A and f_B are pointing correction functions, which are continuous functions on the sphere. For spherically distributed stars, if the observed positions A_0 and E_0 of the stars are measured and the calculated positions A_C and E_C are obtained via ephemeris, then we can obtain the pointing deviation of the telescope in each direction:

$$\begin{aligned}\Delta A &= A_0 - A_C \\ \Delta E &= E_0 - E_C\end{aligned}$$

After fitting of the discrete values distributed on the semisphere, we will get the correction function $f_A(A, E)$, $f_B(A, E)$, which can be represented by spherical harmonic functions. Telescope pointing systematic errors at different elevation angles are complex functions of the elevation change. Thus the harmonic functions shall be fitted with high-order terms. Select a spheric harmonic function with harmonic terms of up to four orders and each order is linear, which is expressed as follows:

$$F(\theta, \lambda) = \sum_{n=0}^{\infty} \left\{ A_n^0 P_n(\cos \theta) + \sum_{m=1}^n [A_n^m \cos m\lambda + B_n^m \sin m\lambda] P_n^m(\cos \theta) \right\} \quad (3.26)$$

where $P_n(\cos \theta)$ is Legendre polynomials:

$$P_n(\cos \theta) = \frac{1}{2^n \times n!} \times \frac{d^n}{d(\cos \theta)^n} (\cos^2 \theta - 1)^n \quad (3.27)$$

$P_n^m(\cos \theta)$ is associated Legendre polynomials

$$P_n^m(\cos \theta) = (-1)^m (1 - \cos^2 \theta)^{m/2} \times \frac{d^m}{d(\cos \theta)^m} P_n(\cos \theta) \quad (3.28)$$

By simplifying $F(\theta, \lambda)$ and making relevant truncating, we will obtain the systematic error correction function of the telescope in azimuth and elevation directions:

$$\begin{aligned}f_A(A, E) \sin E - \Delta A \sin \theta &= A_0 + A_1 \cos E + A_2 \cos A \sin E + A_3 \sin A \sin E + A_4 \cos^2 E + \\ &A_5 \cos A \sin E \cos E + A_6 \sin A \sin E \cos E + A_7 \cos^3 E + \\ &A_8 \cos A \sin E \cos^2 E + A_9 \sin A \sin E \cos^2 E + A_{10} \cos^4 E + \\ &A_{11} \cos A \sin E \cos^3 E + A_{12} \sin A \sin E \cos^3 E \\ f_A(A, E) \sin E = \Delta E &= B_0 + B_1 \cos E + B_2 \cos A \sin E + B_3 \sin A \sin E + B_4 \cos^2 E + \\ &B_5 \cos A \sin E \cos E + B_6 \sin A \sin E \cos E + B_7 \cos^3 E + \\ &B_8 \cos A \sin E \cos^2 E + B_9 \sin A \sin E \cos^2 E + B_{10} \cos^4 E + \\ &B_{11} \cos A \sin E \cos^3 E + B_{12} \sin A \sin E \cos^3 E\end{aligned}\quad (3.29)$$

where A_i and B_i are coefficients ($i = 0, 1, 2, 3, \dots, 12$).

Measurement of 30 plus stars evenly distributed in azimuth and elevation directions will give their theoretical and observed values of the stars at the given observing time.

The observed values of the 30 plus stars constitute a set of nonlinear equations.

$$\begin{aligned} AX_A &= L_A \\ AX_B &= L_B \end{aligned} \quad (3.30)$$

where

$$A = \begin{bmatrix} a_{1,1} & a_{1,2} & \vdots & a_{1,13} \\ a_{2,1} & a_{2,2} & \vdots & a_{2,13} \\ \vdots & \vdots & \vdots & \vdots \\ a_{N,1} & a_{N,2} & \vdots & a_{N,13} \end{bmatrix}$$

$$X_A = \begin{bmatrix} A_0 \\ A_1 \\ \vdots \\ A_{13} \end{bmatrix} \quad L_A = \begin{bmatrix} \Delta A_0 \\ \Delta A_1 \\ \vdots \\ A \Delta_{13} \end{bmatrix}$$

$$X_B = \begin{bmatrix} B_0 \\ B_1 \\ \vdots \\ B_{13} \end{bmatrix} \quad L_B = \begin{bmatrix} \Delta E_0 \\ \Delta E_1 \\ \vdots \\ A E_{13} \end{bmatrix}$$

Each element in matrix A is defined as:

$$\begin{aligned} a_{i,1} &= 1, a_{i,2} = \cos E_i, \\ a_{i,3} &= \cos A_i \sin E_i, a_{i,4} = \sin A_i \sin E_i, a_{i,5} = \cos^2 E_i, a_{i,6} = \cos A_i \cos E_i \sin E_i, \\ a_{i,7} &= \sin A_i \cos E_i \sin E_i, a_{i,8} = \cos^3 E_i, a_{i,9} = \cos A_i \sin E_i \cos^2 E_i, a_{i,10} = \sin A_i \sin E_i \cos^2 E_i, \\ a_{i,11} &= \cos^4 E_i, a_{i,12} = \cos A_i \sin E_i \cos^3 E_i, a_{i,13} = \sin A_i \sin E_i \cos^3 E_i \text{ where } i = 1, 2, \dots, N, \text{ and } \\ &N \text{ is the measured number of stars.} \end{aligned}$$

$$\text{Solving equations } \begin{cases} AX_A = L_A \\ AX_B = L_B \end{cases}$$

we will obtain the coefficients X_A, X_B of function $f_A(A, E), f_B(A, E)$; then we can get the mean square error of the observed values.

In the usage of observed data the star data shall be preprocessed so as to discard those star data with gross errors. The mean square error of the observed values is:

$$\delta_0 = \sqrt{\frac{\sum_{i=1}^M V_{A_i}^2 + \sum_{i=1}^M V_{E_i}^2}{M - t}} \quad (3.31)$$

where V_{Ai} and V_{Ei} are residuals to calculate azimuth and elevation. M is the number of available stars after the gross error is excluded. t is the number of unknowns, $t = 13$.

$$\begin{aligned} V_{Ai} &= f_A(A_i, E_i) / \sin E_i - \Delta A_i \\ V_{Ei} &= f_E(A_i, E_i) - \Delta B_i \end{aligned} \quad (3.32)$$

Telescope systematic error correction with spherical harmonics has been proven to be effective in practice. In telescope observation the pointing error with spherical harmonic correction may reach about 2 arcs (in measuring stellar).

3.4 Public correction models for measurement data

“Measurement model” is analytic expressions to establish observing geometry between observing sites and space objects, as well as mathematical models for observed data systematic error correction, which will give the partial derivatives of the observed quantities with respect to each relevant parameter. Measurement data itself is not very precise, and the data inevitably has random and systematic errors.

3.4.1 The partial derivatives of each measurement element with respect to the space object position

Measurement data types mainly include range measurement, angle measurement, and range rate measurement. For radar measurement the observed quantities are t , ρ , A , E , and $\dot{\rho}$; for optical measurement the observed quantities are astronomical longitude λ and latitude φ . The abovementioned types of observed data can be calculated by the use of space objects’ state vectors $\rightarrow r$ and $\dot{\rightarrow} r$. If the theoretically calculated value of the measurement data is denoted with C , then we have

$$C = G(t, \rightarrow r, \dot{\rightarrow} r, \rightarrow R) \quad (3.33)$$

where $\rightarrow r$ and $\dot{\rightarrow} r$ are motion status vectors of the space objects, and $\rightarrow R$ is the observing site’s position vector.

Taking into account the systematic error of the observation data, the above formula becomes:

$$C = G(t, \rightarrow r, \dot{\rightarrow} r, \rightarrow R) + \Delta C + \Delta C_c + \Delta \dot{C}_c T \quad (3.34)$$

where ΔC is the sum of systematic errors being considered.

$$\Delta C = \Delta C_{TR} + \Delta C_{IO} + \Delta C_{RL} + \Delta C_{RT} + \Delta C_{OF} + \Delta C_{EC} \quad (3.35)$$

where ΔC_{TR} is the tropospheric refraction correction; ΔC_{IO} is the ionospheric refraction correction; ΔC_{RL} is the impact of general relativistic effect upon the light time-of-flight, and the

resulted range correction; ΔC_{RT} is the range measurement correction due to the sun's gravitational potential effect and Lorentz effect of the geocentric station coordinates; ΔC_{OF} is the offset correction of space object transmit antenna with respect to the object centroid; and ΔC_{EC} is the eccentricity correction of the observing site.

The last two systematic errors in Eq. (3.34) are referred to herein as the offset error. where $\Delta \hat{C}_c$ is part of the offset error that changes linearly with time. For arc-related parameters, time T commences from the start time of the arcs; for nonarc-related parameters, time T starts from the epoch of the motion state vector of the object.

The following gives correction approaches for tropospheric refraction error, ionospheric error, general relativistic effect error, and vertical deflection.

3.4.2 Tropospheric refraction error correction

Troposphere is the lowest level of the atmosphere with a height of 60 km or less, high atmospheric density, and complex components. It is a mixture of a variety of gases (nitrogen, oxygen, hydrogen, carbon dioxide, and other neutral plasma) and water vapor. The boundary of the troposphere differs depending on temperature and vertical temperature gradients. Its height continues to drop from the equator to the poles, but also in the immediate vicinity of the equator there is a small discontinuity.

When the electromagnetic wave propagates through troposphere, its velocity will change and its path will also bend, and this is the tropospheric refraction effect. When the radio passes through troposphere, the resulted distance will deviate, and this is referred to as tropospheric refraction error. In the zenith direction, distance refraction error caused by troposphere may be up to 2–3 m. At elevation of 3 degrees the error is up to 30–40 m.

There are many tropospheric refraction error correction methods, whereas commonly used ones include the spherical stratification algorithm, the mapping function method, and three-dimensional ray tracing method. Commonly used approaches of error correction in engineering practice are as follows:

1. Only angle measurement data is available in troposphere:

According to the meteorological data from observation site, use simplified model of the control center to correct the angle data in atmospheric refraction correction processing.

Correction formula is:

$$E = E_C - \Delta E_N \quad (3.36)$$

$$\Delta E_N = N_S^0 \operatorname{ctg} E_c$$

$$N_S^0 = \frac{77.6}{T} \left(P + \frac{4810 \times P_e}{T} \right) \times 10^{-6}$$

$$T = T_0 + t$$

$$P_e = 6.1078 \times 10^{7.63t/(241.9+t)} \times U$$

where T is the absolute temperature, $T_0 = 273.15^\circ\text{C}$. t is the ground temperature $^\circ\text{C}$. U is the ground relative humidity (%). P is the ground atmospheric pressure (hPa, mbar). P_e is the ground water vapor pressure (hPa, mbar).

2. Both angle measurement data and ranging data are available at certain epoch in troposphere:

According to the meteorological data from observation site, use atmospheric refraction correction formula of the control center to correct the ranging and elevation data. The correction formula is as follows:

$$R'_n = R_n - \Delta R_n \quad (3.37)$$

$$\Delta R_n = N_S^0 \csc E_c (1 - e^{-20,000C})/C$$

$$E = E_C - \Delta E_N$$

$$\Delta E_N = N_S^0 \operatorname{ctg} E_c - \frac{N_S^0 (R + R_0 \sin E_c) \cos E_c}{CRR_0 \sin^3 E_c} (1 - e^{-20000C})$$

$$N_S^0 = \frac{77.6}{T} \left(P + \frac{4810 \times P_e}{T} \right) \times 10^{-6}$$

$$T = T_0 + t$$

$$P_e = 6.1078 \times 10^{7.63t/(241.9+t)} \times U$$

where refractivity C takes a statistical average $1.4142 \times 10^{-4} \text{ m}^{-1}$.

3.4.3 Ionospheric error correction

The ionosphere is a region of Earth's upper atmosphere from 60 to 1000 km altitude. Various radiations from the Sun and other celestial bodies upon the gas molecules in the ionosphere produced strong ionization, which generates a large number of free electrons and positive ions. Ionization in the ionosphere can be described in the total electron content, which is unstable and closely related with the outbreak of solar flares, the number of sunspots, magnetic storms, geomagnetic and their changes, and has impact on communications, navigation, radar, and aerospace. The ionospheric delay is proportional to the total electron content in the signal propagation path and is inversely proportional to the signal frequency. The higher the frequency is, the smaller the ionospheric impact is.

Domestic and foreign scholars have been committed to the study of modification of ionospheric propagation effects and proposed different ionospheric delay correction methods and models. In the early 1970s it was suggested to use dual frequency for ionospheric delay error correction. And more different ionospheric correction models have been proposed. At

present, the adopted ionospheric delay correction approaches differ in satellite navigation systems and differential augmentation systems. In general, differential correction method, dual-frequency/multifrequency correction method, ionospheric empirical model method, and IONEX global ionospheric model are most widely used.

At present, the dual-frequency correction method is the most widely used ionospheric delay correction method. Dual-frequency correction method can achieve good correction accuracy and can correct ionospheric effect up to about 90%. Tri-frequency correction method is theoretically the ionospheric delay correction method precision with highest accuracy but requires high observation precision.

In the dual-frequency observations, the combination of dual-frequency observations can be used for ionospheric error correction. The dual method use difference of dual observations to estimate ionospheric delay at L1 and L2 frequencies, respectively. Since code observables include:

$$\begin{aligned}\delta\rho_{l1} &= \frac{(\rho_2 - \rho_1)f_2^2}{f_1^2 - f_2^2} \\ \delta\rho_{l2} &= \frac{(\rho_2 - \rho_1)f_1^2}{f_1^2 - f_2^2}\end{aligned}\tag{3.38}$$

where f_1 and f_2 are dual carrier frequencies; ρ_1 and ρ_2 are dual-frequency code observables; and $\delta\rho_{l1}$ and $\delta\rho_{l2}$ are dual-frequency ionospheric delay.

For carrier observations, there is a similar formula:

$$\begin{aligned}\delta\rho_{c1} &= \frac{(\rho_2 - \rho_1)f_1^2}{f_1^2 - f_2^2} \\ \delta\rho_{c2} &= \frac{(\rho'_1 - \rho'_2)f_1^2}{f_1^2 - f_2^2}\end{aligned}\tag{3.39}$$

where ρ'_1 and ρ'_2 are dual-frequency carrier observations.

The multifrequency observations must correct ionospheric effect through the linear combination independent of ionosphere, which weakens the influence of the ionospheric delay and at the same time magnifies the influence of the observation noise, multipath residuals, and so on. The correction accuracy of multifrequency ionospheric delay depends on the frequency number of observations, frequency values and intervals, pseudo-range accuracy, the correction method, ionosphere higher order delay, and so on. Dual-frequency correction tries to select two groups of data with large-interval frequency and small pseudo-range errors. Dual-frequency correction method can correct more than 90% of the ionospheric delay error. In this method, observation noise is smaller, and calculation is simple with low hardware requirements. Furthermore, this method is easy to be implemented in engineering.

In engineering practice, GNSS observation network can be used to generate ionospheric delay correction model based on global ionospheric real observations, where the ionospheric model parameters $\alpha_i, \beta_i (i = 0, 1, 2, 3)$ in GPS navigation message are input parameter. Ionospheric refraction error is calculated as follows:

1. At any epoch t the ionospheric delay T_g in the zenith direction ($E = 90^\circ$)

$$T_g = DC + A \cos [2\pi(t' - T_p)/P] \quad (3.40)$$

$$\begin{cases} A = \sum_{i=0}^3 \alpha_i \varphi_m^i \\ P = \sum_{i=0}^3 \beta_i \varphi_m^i \end{cases} \quad (3.41)$$

where $DC = 5$ ns is the evening ionospheric delay, $T_p = 50,400$ s is the local time corresponding to the largest ionospheric delay, P is the ionospheric delay function period (s), A is the ionospheric delay function amplitude(s). φ_m is the geomagnetic latitude of ionosphere K' point (the intersection of the center ionosphere and the line connecting the spectrum spread device K and the space object), and t' is the hour angle of K' point at corresponding time t .

2. Geocentric angle E_A between the spread spectrum device K and K' point

$$E_A = \frac{445}{E + 20} - 4 \quad (3.42)$$

where E is the elevation of the spread spectrum device K in observing space objects.

3. Geocentric longitude and latitude of K' point

$$\begin{cases} \varphi_{K'} = \varphi_K + E_A \cos \alpha \\ \lambda_{K'} = \lambda_K + E_A \sin \alpha / \cos \varphi_{K'} \end{cases} \quad (3.43)$$

where φ_K, λ_K is the geocentric longitude and latitude of spread spectrum device K , and α is the azimuth of the spectrum spread device K in observing space objects.

4. The local time t' at K' Point.

$$t' = (\text{UT} + \lambda_{K'}/15) \times 3600(\text{s}) \quad (3.44)$$

where UT is the corresponding UTC for the observation time t .

5. The geomagnetic latitude φ_m at K' point.

$$\varphi_m = \varphi_{K'} + 11.6 \cos (\lambda_{K'} - 291^\circ) \quad (3.45)$$

6. The ionospheric delay T'_g in the direction of elevation E at any time t .

$$T'_g = \text{SF} \cdot T_g = \left\{ 1 + [2(96^\circ - E)/90^\circ]^3 \right\} \cdot T_g \cdot f_{\text{GPS}}^2 \cdot f_{\text{KP}}^{-2} \quad (3.46)$$

where SF is the obliquity factor, $f_{\text{GPS}} = 1575.42$ MHz is the operating frequency of the GPS signal, and f_{KP} is the operating frequency of the spread spectrum device, which takes the downlink frequency 2282.4 MHz.

For accurate correction of the postmission processed data, the global ionospheric delay model published by IGMAS can be used [103], which is not repeated here.

3.4.4 General relativistic effect error correction

According to Einstein's general relativity theory, light propagation will be distorted in a gravitational field, and the speed will be slower. It results in longer light propagation time from the space objects to stations than there is no gravitational field, which is called electromagnetic wave delay effect. The ranging correction caused by this effect is called general relativistic effect correction in ranging. Here we only consider the ranging general relativity effect correction caused by the Sun and Earth's gravitational fields.

Relativistic effect correction caused by the gravitational field of the sun is:

$$\begin{aligned} \Delta_1 &= (1 + \gamma)R_{\text{RL1}} \\ &= (1 + \gamma) \frac{GM_s}{c^2} 1_g \left(\frac{r_1 + r_2 + \rho}{r_1 + r_2 - \rho} \right) \end{aligned} \quad (3.47)$$

where M_s : the mass of the Sun, $GM_s = 1.327124 \times 10^{20}$; r_1 is the distance from the Sun to the space object; r_2 is the distance from the Sun to the observation site; and γ is the correction factor for the relativistic effect. It can be taken as estimated quantity, and its normal value is 1.

Relativistic effect correction caused by the gravitational field of the Earth is:

$$\begin{aligned} \Delta_2 &= (1 + \gamma)R_{\text{RL2}} \\ &= (1 + \gamma) \frac{GM_E}{c^2} 1_g \left(\frac{r'_1 + r'_2 + \rho}{r'_1 + r'_2 - \rho} \right) \end{aligned} \quad (3.48)$$

where M_E is Earth's mass, and $GM_E = 3.9860044 \times 10^{14} \text{ m}^3/\text{s}^2$. r'_1 is the distance from Earth's core to the space object; r'_2 is the distance from the geocenter to the observation site.

The relativistic effect correction of the range by the Sun and Earth's gravitational field is:

$$\begin{aligned} \Delta \rho_{\text{RL}} &= \Delta_1 + \Delta_2 \\ &= (1 + \gamma)(R_{\text{RL1}} + R_{\text{RL2}}) \end{aligned} \quad (3.49)$$

3.4.5 Vertical deflection correction

For shafting optical data the site coordinates are expressed in astronomical coordinates, while orbit determination uses geodetic coordinates. Thus vertical deflection correction for shafting data is required. Correction method is as follows:

$$\begin{aligned}
 A' &= A - (\lambda - L)\sin \varphi - (\xi \sin A' - \eta \cos A') \operatorname{ctg} Z_S \\
 Z_G &= Z_S + (\xi \cos A' + \eta \sin A') \\
 E' &= \frac{\pi}{2} - Z_G
 \end{aligned} \tag{3.50}$$

where A is the raw measurement data, A', E' is obtained data after the vertical deflection correction, λ, φ are the longitude and latitude in astronomical coordinates, L is the longitude in geodetic coordinate system, and ξ, η are the meridian and prime components of the vertical deflection. Z_S is astronomical zenith distance, that is, the angle between the vertical line of the site and the observation direction. Z_G is the zenith of the Earth.

In certain sites with large vertical deviation, dynamic correction of the error could reach the magnitude of one minute of arc.

3.5 Relationship between detection network and orbit accuracy

The near-Earth objects with a period of 90 minutes orbit the Earth about 16 passes a day. For a detection network with reasonable longitude distribution (e.g., eight radar stations are evenly laid on the equator), theoretically ascension of the object from south to north and descension from north to south can be observed at least eight times a day. Arc length of each observation should be a few minutes. Each country's specific detection network can actually observe a few liters lower, and the length of each observation arcs, according to the country, can be laid detection equipment span longitude, latitude span and space objects' orbital inclination and altitude may be. In general, the goal of space object cataloging is to use minimal equipment resources to catalog as many space objects as possible. Thus in catalog orbit determination requirements, usually one arc of observation is required, and the data types are mainly low precision phased array radar and optical data. For space object collision avoidance and warning missions, precision tracking and observation of space objects is required. For precision orbit determination, three and more arcs of observations are generally required in space object tracking. The data types shall include high-precision measurement radar data, in addition to the phased array radar data and optical data.

In order to better illustrate the relationship between the accuracy of orbit determination and the amount of observation data, it is assumed that radars, deployed in different longitude locations, track a Sun-synchronous object with an orbital altitude of 480 km. Measurement data are generated by simulation. The orbit determination and extrapolation

Table 3-1 Calculation results of orbit determination and prediction error.

Calculation error		Observations	One pass of ascension orbit	Two passes of ascension orbit	Three passes of ascension orbit	Four passes of ascension orbit	Five passes of ascension orbit	Six passes of ascension orbit	Seven passes of ascension orbit	Eight passes of ascension orbit
		One pass of descension orbit	Two passes of descension orbit	Three passes of descension orbit	Four passes of descension orbit	Five passes of descension orbit	Six passes of descension orbit	Seven passes of descension orbit	Eight passes of descension orbit	
Calculation items										
Orbit determination error	Rms of position (m)	113.7	12.8	4.2	1.9	1.4	1.3	1.2	1.1	
	Rms of velocity (m/s)	0.1151	0.0136	0.0044	0.0020	0.0013	0.0011	0.0010	0.0009	
One day	Direction <i>R</i> (m)	137.7	39.9	33.6	30.4	28.4	25.4	25.8	15.5	
	Direction <i>T</i> (m)	8363.1	383.9	210.4	197.5	132.6	121.6	114.6	13.7	
	Direction <i>N</i> (m)	2062.6	28.6	13.0	8.0	5.0	3.5	3.7	2.7	
	The position <i>P</i> (m)	8558.4	384.1	210.4	200.5	133.8	121.6	114.6	20.9	
Three days	Direction <i>R</i> (m)	137.7	49.3	38.5	35.7	35.1	29.3	28.5	28.1	
	Direction <i>T</i> (m)	26316.4	3660.3	2031.3	1637.2	1189.3	1039.4	745.1	708.8	
	Direction <i>N</i> (m)	2062.6	31.5	13.7	4.1	3.5	3.5	3.3	3.5	
	The position <i>P</i> (m)	26370.7	3660.3	2031.5	1637.2	1189.3	1039.4	745.1	709.3	
Seven days	Direction <i>R</i> (m)	272.9	64.2	54.2	62.1	47.5	41.2	39.9	15.0	
	Direction <i>T</i> (m)	62,211.1	18,620.0	10,297.8	10,981.4	8041.8	5771.7	3885.2	4001.2	
	Direction <i>N</i> (m)	2062.6	39.4	14.0	7.0	6.5	5.6	3.7	0.9	
	The position <i>P</i> (m)	62,223.9	18,620.0	10,297.9	10,981.5	8041.9	5771.7	3885.2	4001.3	

prediction are implemented according to different measurement data within 24 hours. Table 3–1 shows the orbit determination errors and prediction error of object location for 1, 3, and 7 days.

As is seen from Table 3–1, with increasing of the orbit measurement data arcs, the position RMS error for orbit determination is reduced from 100 m to a few meters; the velocity RMS error is reduced from decimeter/second to millimeter/second; and the position prediction error for seven days is reduced from over 60 to 4 km. According to the abovementioned simulation results and a lot of statistics, calculation of space objects' collision warning usually needs two passes of both ascension and descension orbital data, thus the orbit prediction accuracy can meet the demand that the position prediction error for 3 days is within a magnitude of kilometers. To achieve the prediction accuracy for 24 hours that the position error is within 100 m and error in radial or normal direction is within 10 m, measurements should be performed for at least three passes of both ascension and descension orbits. Based on the current level of dynamics, even if the detection equipment distributed around the world is used intensively for measurement and orbit determination of a certain space object, the prediction error of orbit position for 7 days is still within ten kilometers. Accordingly, broader geological deployment of sites and more space object observation by optical and radar equipment will bring higher orbit determination precision of space objects. This is conducive to space object collision warning calculation. Therefore a reasonable plan of detection resources scheduling, namely, the use of appropriate detection resources at the right time, is very important for efficient completion of collision warning.

Furthermore, it should be noted that the previous calculations are performed according to the simulation of radar equipment. If radar equipment is replaced by optical device, and under good weather conditions and daylight and shadow requirements, the number of observable arcs of the satellite per day is 0.6. That is, for an average of 3 days, there are two arcs available. As the optical device's data precision and density is less than radar devices, if unfavorable weather results in unavailable observation by optical devices, the number of trackable arcs will be less than normal. And this will reduce the accuracy of orbit determination. Thus to answer for the detection requirement in the colorful warning stage of collision warning, optical detectors cannot be used as a primary warning device, but only as auxiliary of the radar equipment.

Space environment and object orbit

The natural and artificial environments when on-orbit spacecraft encounter are known as space environments. From ground to the designed orbit, spacecraft have experienced a number of different environments. According to the current information, all changes of natural space environment are closely related to the change of the Sun. The Sun is not only the source of material and radiation but also controls the changes of atmosphere and ionosphere, cosmic rays of Earth's adjacent area, and the orbit evolution of space objects, and so on.

Space environment has a very significant effect on spacecraft. Thereinto, gravitational field, upper atmosphere, and solar radiation affect the orbit and life of spacecraft; radiation belts of the Earth, solar cosmic rays, galactic cosmic rays, and solar radiation bring radiation damage to the materials and coatings of spacecraft; a large amount of space debris and micrometeoroid damages optical lens and mechanical structural of spacecraft; atomic oxygen brings chemical damage to the materials and coatings of spacecraft; magnetospheric plasma and solar electromagnetic radiation affect the surface potential of spacecraft; solar electromagnetic radiation, cold dark environment, and the vacuum environment of upper atmosphere affect the thermal state of spacecraft. This chapter focuses on the impact of the upper atmosphere on the orbits of spacecraft.

4.1 Atmospheric effect on space object orbit

The on-orbit space objects will be influenced by various forces. Thereinto, atmospheric drag is a typical nonconservative force, and the effect on orbit prediction is directly proportional to time square. Because people have not completely mastered the physical mechanism of upper atmospheric density variation, until now the present mode error is about 15% for almost all of the atmospheric density patterns in the inactive period of solar activities (the error is bigger in the period of intense solar activities). This will cause the same uncertainty of atmospheric drag perturbation and bring huge impact on orbit prediction of low on-orbit space objects. And it is directly related to the confidence coefficient of the collision warning of spacecraft. This section will focus on the impact of atmospheric drag on orbit prediction.

The calculation method of objects influenced by atmospheric drag is shown as follows:

$$f_{DG} = \frac{1}{2} \frac{A}{m} c_d \rho v^2 \quad (4.1)$$

where $A_m = (A/m)$ is object area–mass ratio (the ratio of windward area and quality); c_d is atmospheric damping coefficient; ρ is atmospheric density of objects' location; and v is velocity that the centroid of the object is relative to the local atmosphere.

In the calculation of atmospheric drag, the general empirical atmospheric model is adopted to calculate the atmospheric density. However, due to the changes, the upper atmosphere becomes very complex and easily gets affected by the changes of space environment (such as solar activities), which causes great difficulties for empirical modeling. In the calculation of atmospheric drag, the uncertainty of atmospheric density is the main error source of the calculation. In recent years, part of satellites carries a high-precision accelerometer, which can be adopted to perform the inversion of atmospheric density to analyze the precision of density model with the use of satellites' acceleration data. According to the analysis results, the model error of atmospheric density is generally 15% in the conditions of inactive solar activities and geomagnetic quiet period, whereas it can reach 100% (even more) when intense solar activities and geomagnetic storms occur. This will cause the same uncertainty of atmospheric perturbation and bring huge impact on orbit prediction of low-orbit space objects.

In the calculation of atmospheric drag, another nonnegligible error source is the area–mass ratio of space objects. For domestic spacecraft the geometry sizes are precisely known. Although area–mass ratio will change with the changes of attitude during on-orbit flight of spacecraft, the range of variation is known. For space debris, their area–mass ratio cannot be obtained, and it is generally greater than that of spacecraft. So the impact of atmospheric drag calculation is greater. Meanwhile, atmospheric damping coefficient c_d is not a fixed value. And c_d is a description of parameter that free atmospheric molecules impact the surface of objects, which is connected with factors such as the variety of atmospheric molecules, the shape of objects' surface, the capacities of ejection and adsorption for material, and the impact angle. And these factors in space are often unpredictable. Therefore only the estimated value of c_d can be given. In the engineering practice, c_d is usually fixed as 2.2, and the deviation between the constant value 2.2 and the real value c_d will be introduced into the calculation of atmospheric drag. Taking into account the uncertainties of atmospheric drag coefficient and effective area–mass ratio, the ballistic coefficient $B_* = A_m c_d$ can be defined in some application of engineering. If the measured data meets a certain length, the drag error can be reduced by solving B_* during the process of orbit determination. Since the two parameters of ballistic coefficients are variable, A_m should be generally fixed to solve c_d . The set value A_m and calculated value c_d in orbit determination are adopted in orbit prediction.

Taking objects I, II, III, and IV in nearly circular orbit for example, the heights of which are, respectively, 200, 400, 500, and 600 km, the uncertain impact of atmospheric drag on orbit position prediction is introduced. The same area–mass $A_m = 0.002$ and space environmental parameters (inactive period) are given, and the error of 24-hour orbit prediction should be compared whether to consider the atmospheric perturbation when the simulation is performed. And MSIS00 empirical model is adopted for atmospheric density model. [Table 4–1](#) shows 24-hour orbit error of different orbital prediction in the components of R

Table 4–1 24-Hour orbit error for different orbital height prediction.

Object no.	Orbit altitude (km)	Error of R (km)	Error of T (km)	Error of N (km)
I	200	2.2	270	0.08
II	400	0.04	2.6	0.005
III	500	0.008	0.44	0.002
IV	600	0.002	0.09	0.001

(radial), T (lateral), and N (normal). Seen from Table 4–1, for objects I, II, III, and IV, the position errors of 1-day atmospheric prediction are, respectively, about 270, 2.6, 0.44, and 0.09 km. Thus it can be seen, the lower altitude the orbit has the greater impact on object orbit prediction the atmosphere has. And it will mainly influence the error along direction T . Atmospheric perturbation has great effect on LEO object orbit prediction, and the uncertainty of atmospheric density will make the whole atmospheric perturbation become the minimum degree of perturbation in the modeling of the entire LEO space objects.

4.2 Atmospheric density model

The real-time atmospheric density often cannot be measured, and the general experience (or semiempirical) models and physical models are adopted to calculate atmospheric density. Empirical models are based on atmospheric diffusion balance equation to establish a mathematic model of the neutral atmospheric composition density. And the distribution and change of atmospheric density can be analyzed from the perspectives of experience and statistics. The physical model is concerned with the mechanism of interaction between the neutral atmosphere and ionosphere. And the atmosphere caused by energy input, the changes of ionospheric composition, and a series of complex physical processes can be described as physical equations to be used in the afterward theoretical study. This section focuses on the common empirical atmospheric model in orbit calculation of space objects.

By using abroad databases such as balloon soundings, satellite drag, mass spectrometers, and incoherent scatter, a number of empirical atmospheric models are built, which are divided into one-dimensional model only changing with the height, and three-dimensional model, in which the height, longitude, latitude, season, Sunday, and other factors are considered, including the standard and reference atmosphere. Generally, the standard atmosphere shows the cross section of Earth's atmosphere idealized and steady-state average from Earth's surface to mid-latitude region (1000 km) under the medium conditions of solar activity. The typical models include US Standard Atmosphere in 1962, US Standard Atmosphere Supplement in 1966, and US Standard Atmosphere in 1976, which represent the average state of standard atmosphere that cannot fully meet the requirements. And in orbit determination prediction in near-Earth orbit satellite, the reference atmosphere is usually adopted. The typical models include CIRA (International Reference Atmosphere) series, Jacchia series, DTM series, and MSIS series. CIRA series are recommended by International Space

Committee (COSPAR), which include CIRA1961, CIRA1965, CIRA1972, and CIRA1986. Jacchia series are based on atmospheric density database of satellites' orbit decay and inversion, which includes J65, J70, J71, J77, MSFC/J70, and MET and MET V2.0. DTM series adopt J71 model that are based on independent static thermal diffusion equilibrium assumptions from different thermosphere composition, which include DTM78, DTM94, and DTM2000. In the series of MSIS the measurement data of satellites, rocket-borne mass spectrometer, and the incoherent scattering radar are fitted in the high thermosphere, which is close to the results of the global atmospheric circulation system in the lower thermosphere. Then a series of models are generated, including MSIS77, MSIS83, MSIS86, MSIS90 (MSIS90), and MSIS00 (NRLMSIS00). Currently, in the prediction of space objects, the frequently used atmospheric density models include the exponential model, HP (Harris–Priester) model, J71, J77, DTM78, DTM94, DTM2000, MSIS86, MSIS90, MSIS00, and MET-V2.

The upper atmosphere is very complex and easily influenced by space environment, which causes many difficulties for empirical (or semiempirical) modeling. In addition, the accuracy and the spatial and temporal resolution of modeling data are limited, which cannot perform more comprehensive measurement for a variety of global atmospheric environment. That will lead to lower accuracy for existing models. And it can be said that no single model of the upper atmosphere can completely and accurately describe the upper atmosphere. In recent years, compared the predicted atmospheric density with measured data by using various high-precision satellite accelerometers, the differences between the predicted and measured can be found. The error of such models is generally from 15% to 30%, while it can reach 100% or even higher during the period of space environmental disturbances.

4.2.1 Atmospheric density modeling principle

Atmospheric density model is established based on hydrostatic principle [72–74]. In order to obtain the first-hand data, the data fitting is performed by combining theoretical analysis with the introduction of the parameters to solve the atmospheric density model.

4.2.1.1 Hydrostatic principle

The statics equation related to the atmospheric density mainly includes the ideal gas density equation, which is shown as follows:

$$\rho = \frac{PM}{gRT} \quad (4.2)$$

where P is absolute pressure; M is average molecular mass composed of the entire atmosphere; g is gravitational acceleration; R is general gas constant; and T is absolute temperature.

The hydrostatic equation that pressure changes with heights is shown as follows:

$$\frac{dP}{dh} = -\rho g \quad (4.3)$$

where h denotes the height.

The widely accepted atmospheric drag equation is shown as follows:

$$a_D = -\frac{1}{2}\rho v^2 \frac{c_d A}{m} \quad (4.4)$$

where a_D is acceleration caused by atmospheric drag; m is objects' quality; v is the velocity that objects are relative to atmosphere; A is cross-sectional area that objects are forced by atmospheric drag; and c_D is drag coefficient.

4.2.1.2 Data acquisition technology

There are two main types of data acquisition methods: direct measurement method [75,76] and inversion method [77–80].

Direct measurement method is mainly used to obtain atmospheric density data directly through various devices. For example, the atmospheric density detector adopts a method of using inside gas pressure and temperature of direct detection sensor, which can obtain free atmospheric density through the basic molecular dynamics theory.

Inversion method is the mainstream and research focus currently. Through using this method, atmospheric density can be inverted by measuring the force of satellites. For example, the acceleration caused by all nonconservative forces can be measured with the use of on-board accelerometer. These forces include atmospheric drag and lift, solar radiation pressure, and Earth's albedo radiation pressure (including Earth's reflected light pressure and the infrared radiation pressure); and atmospheric drag is the maximum among them. The solar radiation pressure and Earth's albedo radiation pressure can be calculated by using a certain model, thus the atmospheric drag and lift can be separated. Satellites' resistance and lift are direct ratio with the atmospheric density around a satellite. According to the relationship between them, atmospheric density can be calculated.

In direct measurement method or inversion method, the data sources are from on-orbit spacecraft. The number of on-orbit spacecraft provided with such measurements is limited. Therefore the all-time and all-weather status of atmospheric changes cannot be overwritten when modeling. In contrast, two-line orbital elements (TLE) of space objects have a great advantage. According to the US space Situation Report statistics, the Surveillance Network of the United States Space has cataloged more than 40,000 space objects, of which more than 17,000 are currently in orbit. It is an effective way to inverse atmospheric density with the use of orbital decay TLE. In 2005 Picone et al. proposed a method of rapidly obtaining atmospheric density from TLE data [81]. And Lean et al. applied this method in the study of Starshine satellite [82].

4.2.1.3 Introduction of parameters and fitting technique

The main variables of various types of atmospheric density models include diurnal variation, seasonal variation, semiannual changes, solar activity and geomagnetic activity, latitude, local time, and day of year.

As the representative of solar radiation energy, $F_{10.7}$ is the main parameter of the calculation of atmospheric model. After decades of years of development, the error of parametric model has not been improved yet. Therefore researchers have proposed new solar radiation index such as $E_{10.7}$, $S_{10.7}$, $M_{10.7}$, and $Y_{10.7}$ to improve atmospheric models. The new radiation index is smaller than the conventional $F_{10.7}$, which can better characterize the impact of solar radiation on atmospheric density. It requires further evaluation of the correlation with the use of solar radiation index. In fact, without considering the physical meaning of each radiation index, any kind of radiation index reflects the same change in density if the impact on density can be characterized from a single statistical. That is one of the reasons why a large number of models can be adopted to characterize the size of the solar radiation with the use of accessible $F_{10.7}$.

In addition to solar radiation index, geomagnetic index is another important parameter that is used as the input of atmospheric models to characterize the impact of the status of geomagnetic activities on upper atmosphere. Before using JB2008 model, A_p or K_p indexes are adopted as model input parameters among various reference atmospheric models. In 2008 Bowman used Dst index in the new JB2008 model instead of A_p index [83]. From the relationship between linear and density, Dst is more consistent with density [84].

Elements such as diurnal variation, seasonal variation, semiannual variation, latitude, local time, and day of year have impact on atmospheric density. From the start of J64 model, they are gradually revised and added to improve the density model accuracy [72,74,80,83,85–90].

Cross correlation coefficient and root mean square error are usually used to evaluate the fitting results [73].

$$CC = \frac{\sum_{i=0}^{N-1} [(x_i - \bar{x})(y_i - \bar{y})]}{\sqrt{\sum_{i=0}^{N-1} (x_i - \bar{x})^2} \sqrt{\sum_{i=0}^{N-1} (y_i - \bar{y})^2}} \quad (4.5)$$

$$RMSE = \sqrt{\frac{\sum_{i=0}^{N-1} (x_i - y_i)^2}{N}} \quad (4.6)$$

where x_i is the first-hand measurement data, y_i and x_i correspond to the fitting results, and \bar{x} and \bar{y} are, respectively, measurement results and the mean results of the fitting sequence.

Or to adopt relative proportions evaluation method [83,86].

$$RMS = \sqrt{\frac{\sum_{i=0}^{N-1} ((x_i/y_i) - (\bar{x}/\bar{y}))^2}{N-1}} \quad (4.7)$$

4.2.2 Introduction of current atmospheric density models

After years of development, atmospheric models have developed a variety of series and types. According to the applicative height and region of American National Standard, atmospheric models can be divided into six categories, as shown in Table 4–2 [74].

Table 4–2 Atmospheric models according to application scope.

Types	Application scope	Typical model
Global model	Global area	CIRA86 model Suitable height: 0–2000 km
Regional model	Used by some nations or regions	Chinese national standard atmospheric model in 1980 Suitable height: 0–120 km
Middle atmospheric model	Suitable for middle atmosphere	AFGL atmospheric composition profile model in 1986 Suitable height: 0–120 km
Thermosphere atmospheric model	Suitable for thermosphere layer	DTM2000 model Suitable height: 120–1500 km
Distance model	Suitable height: local area	RRA-2006 model Suitable height: 0–70 km
Planetary model	Applicable to other planets	Mars-GRAM-2001 model Suitable height (Mars): 0–1000 km

Currently, the frequently used atmospheric models mainly are Jacchia series, MET series, DTM series, MSIS series, and CIRA series. Fig. 4–1 depicts several series of the development process and relationships. In 1978 the first DTM model was (DTM78) published. Until now, there are DTM94, DTM2000, DTM2009, and other models introduced, which mainly use the observational data of satellite resistance to do modeling. In recent years, ATMOP program of ESA launches the latest model DTM2013, which absorbs the data of high-precision on-board accelerometer. In 1977 MSIS model is first formed, then MSIS83, MSIS86, and MSIS90 are subsequently published, which first adopt atmospheric temperature and concentration measurements. In 2000 US Naval Research Laboratory added a new “oxygen ions” in the architecture of the model, which was improved to obtain MSIS00 model. DCA (dynamic atmospheric correction) is developed in Russia, which uses observational data to correct the value of calculation once every 3 hours to realize the continuous calibrating model technology. High-Accuracy Satellite Drag Model was developed in the United States on the basis of DCA. Both of them are based on J70 model. There are more and more scholars in the study of their correction performance on basic models [73]. Jacchia series are an atmospheric density model that was first established. And in the existing analysis assumptions, most of them are from Jacchia series. Table 4–3 illustrates a series of atmospheric density model properties [74,80,83,85–89] in detail.

Taken together, the accuracy of DTM and MSIS model is similar, and they use a similar model framework to, respectively, establish the atmospheric change expressions for different densities of atmospheric composition. The model parameters are obviously more than those in Jacchia, so the details of the density are better than Jacchia, with the average accuracy slightly better. In the orbit determination and prediction of space objects, the different orbital calculation of velocity and accuracy are obtained at different stages and for different purposes. In order to make different accuracy match different computation speed, different

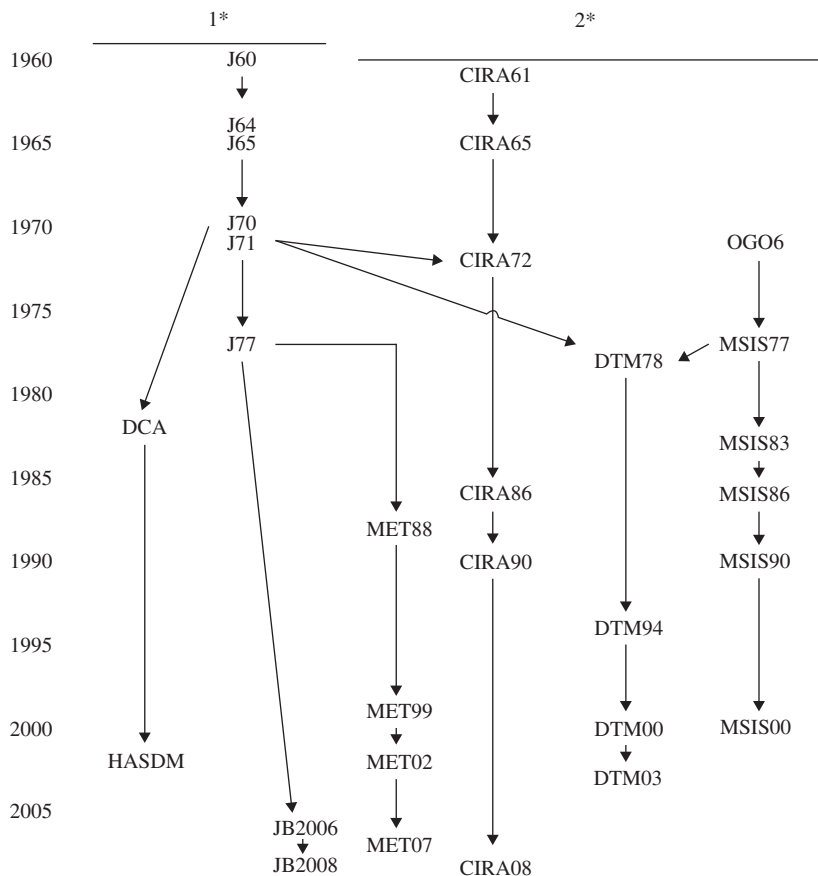


FIGURE 4-1 Development process of atmospheric model.
 Notes: (1) The intricate relationship of borrowing or citing between series of models is not shown. (2) Figure "1*" indicates that the calculation of atmospheric density model is from the data of satellites' drag. Figure "2*" indicates model temperature and atmosphere form a derivation based on ground observational data and field testing equipment [72].

atmospheric models are chosen under different requirements. The most typical and frequently used models include a simple exponential model, Jacchia77 model with moderate calculation and accuracy, MSISE00 model with higher computation and accuracy.

4.2.2.1 Index model

In order to compensate for the insufficiency of one-dimensional atmospheric models, the maximum and minimum values of atmospheric density are used in the improved HP model to perform diurnal variation correction. HP model can provide the maximum and minimum values of diurnal variation of atmospheric density at various heights with different forms,

Table 4-3 Characteristics of atmospheric models.

Series	Main models	Characteristics	Limitation	Development direction
Jacchia	J60 J64 J65 J70 J71 J77 JB2006 JB2008	<ol style="list-style-type: none"> 1. It is the first model of the series, which belongs to semiempirical model. And it is the basis of other series 2. Main applicable height is 90–2500 km 3. Models are classical and reliable, and the calculation is general. Therefore it is widely used, especially in J71 and J77 models 	<ol style="list-style-type: none"> 1. The accuracy of the model decreases due to lack of large amount of data when it is in high altitude ($h > 1100$ km, J71 model) 2. The smoothness of short-term dynamic results is poor 	<ol style="list-style-type: none"> 1. The relationship between the relevant parameters and atmospheric density should be revised based on the observational data. For example, the formula of outer atmospheric density and semiannual changes of density should be constantly revised 2. While continuing to introduce new parameters to describe the relevant parameters more accurately. For example, the new solar activity index and Dst parameters 3. To introduce more data, to optimize models, and to continuously improve the scope of application. For example, JB2008 has improved the applicability of intense geomagnetic storms, and the applicable height is enhanced to 90–4000km 4. To improve calculation methods and computational efficiency. For example, Jacchia-Roberts is the version to increase the calculation speed based on J70
MET	MET88 MET99 MET02 MET07	<ol style="list-style-type: none"> 1. Based on Jacchia model, therefore it is also listed in Jacchia series 2. Main applicable height is 90–2500 km 3. It can be applied in afterward and real-time prediction 	<ol style="list-style-type: none"> 1. The prediction accuracy is not high. Because as the solar EUV of model input, the assessment of heat amount is inaccurate 	Inherently, it belongs to Jacchia series, so the development direction is consistent with Jacchia series
DTM	DTM78 DTM94 DTM00	<ol style="list-style-type: none"> 1. The data foundation of model derivation is abundant, which includes the total mass density (Jacchia data), satellite accelerometer 	<ol style="list-style-type: none"> 1. The height is 250–900 km, and the estimation accuracy is poor 	<ol style="list-style-type: none"> 1. A rich source of data to improve the accuracy of the model. For example, compared with DTM78 model, satellite

(Continued)

Table 4–3 (Continued)

Series	Main models	Characteristics	Limitation	Development direction
	DTM03	<p>data, exosphere temperature measurement data, mass spectrometer data, the relative density change by measuring the wind, and orbit determination obtain relative density exosphere temperature measurement data, incoherent scattering radar data</p> <p>2. Main applicable height: 120–1500 km</p> <p>3. The treatment effect is better when the height range is 250–900 km</p>	<p>2. The model ignores the impact of longitude</p> <p>3. The model cannot reproduce wavy disturbances less than 3000 km, which seriously affect the uncertainty of the model</p>	<p>accelerometer data and the relative density change data by measuring the wind are added to the data source of DTM00</p> <p>2. To introduce new parameters as input, and to improve the model to enhance the applicability of the model</p>
MSIS	OGO-6 MSIS77 MSIS83 MSIS86 MSIS90 MSIS00	<p>1. The specified accuracy can be obtained by using fewer parameters. And in China’s manned space engineering, the atmospheric density model is MSIS90</p> <p>2. Main applicable scope is 90–2500 km</p> <p>3. The prediction accuracy is stable, and MSIS00 is the most influential upper atmosphere density model that is widely used</p>	<p>The applicability of the model is better, only in some cases with the resolution lower than other models</p>	<p>1. To optimize the data using, such as drag and accelerometer data</p> <p>2. To strengthen the role of the air component, for example, oxygen ion contribution</p> <p>3. To enhance the low-level model’s seamless connectivity</p>
Ion CIRA	CIRA61 CIRA65 CIRA72 CIRA86 CIRA90 CIRA08	<p>1. Directly absorb the advantages of other models</p> <p>2. The main scope is 0–2000 km. And it is the only model in several series where the height below 90 km is applicable</p>	<p>1. It is ineffective in the lower layers because of the data</p> <p>2. It is ineffective when a large air turbulence happens</p>	<p>1. Continue to absorb the strengths of other models For example, CIRA08model fully borrowed the advantage of density models such as JB2008, GRAM7, MSIS00, as well as the advantage of wind model GWEM</p> <p>2. Continue to improve the scope of application For example, the height scope of CIRA08 increased to 0–4000 km</p>

which is based on $F_{10.7 \text{ cm}}$ solar radiation flow. In the calculation process, first, the maximum and minimum values of space objects situated at a certain height are used to calculate the altitude of atmospheric density situated at a certain height. The model is applicable to calculate atmospheric density at the altitude of 100 km above. Calculation process is shown as follows:

1. Calculation of space objects' position

The height of reference ellipsoid for space objects is shown as follows:

$$h = r - \frac{R_E(1-f)}{\sqrt{1-e_E^2 \cos^2 \varphi'}} \quad (4.8)$$

$$\cos \varphi' = \frac{\sqrt{x_o^2 + y_o^2}}{r} \quad (4.9)$$

where φ' is geocentric latitude of space objects; x_o , y_o , z_o is position vector in the Earth-fixed coordinate system for space objects.

Latitude of space objects is shown as follows:

$$\varphi = \arctan \frac{z_b}{(1-e_E^2)\sqrt{x_o^2 + y_o^2}} \quad (4.10)$$

2. Calculation of solar position

The definition of solar hour angle α is shown in Fig. 4–2, where O is geocenter; S is the Sun; V is space object; and OA and OB are r_s and r projected in equatorial plane.

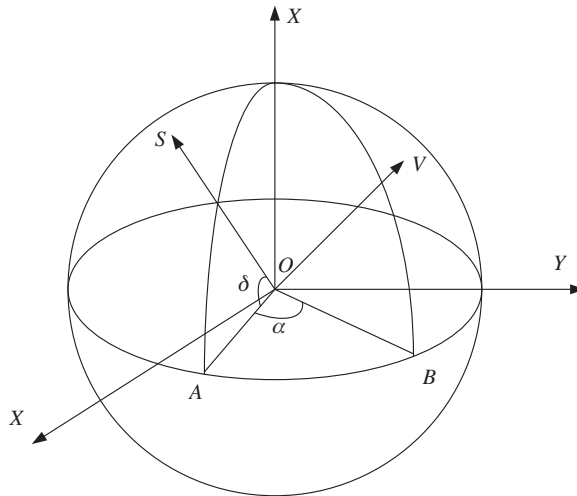


FIGURE 4–2 Positions of the Sun and space objects located on the Earth.

The unit vector of the Sun in the Earth-fixed coordinate system is

$$r_{sb} = \begin{pmatrix} \hat{x}_{sb} \\ \hat{y}_{sb} \\ \hat{z}_{sb} \end{pmatrix} = \begin{pmatrix} \cos \delta_S \cos \lambda_S \\ \cos \delta_S \sin \lambda_S \\ \sin \delta_S \end{pmatrix} \quad (4.11)$$

$$\delta_S = \arcsin \hat{z}_{sb} \quad (4.12)$$

$$\alpha = \frac{\hat{x}_{sb}\hat{y}_b - \hat{y}_{sb}\hat{x}_b}{|\hat{x}_{sb}\hat{y}_b - \hat{y}_{sb}\hat{x}_b|} \cos^{-1} \frac{\vec{OA} \cdot \vec{OB}}{|\vec{OA}| \cdot |\vec{OB}|} \quad (4.13)$$

$$\vec{OA} = \begin{pmatrix} \hat{x}_{sb} \\ \hat{y}_{sb} \end{pmatrix}, \quad \vec{OB} = \begin{pmatrix} \hat{x}_b \\ \hat{y}_b \end{pmatrix} \quad (4.14)$$

3. Calculation of atmospheric density for space objects

$$\rho_o = \rho_N \left(1 + \frac{\rho_D - \rho_N}{\rho_N} \cos^B \frac{\tau}{2} \right) \quad (4.15)$$

where B is input constant to adjust the change rate of diurnal variation for atmospheric density, and generally $B = 4$; τ , ρ_D , and ρ_N are, respectively,

$$\begin{aligned} \tau &= \alpha - 37.0^\circ + 6.0^\circ \sin(\alpha + 43.0^\circ) \quad \tau \in (-180^\circ, 180^\circ) \\ \rho_D &= \rho_{\min} \left(1 + \frac{\rho_{\max} - \rho_{\min}}{\rho_{\min}} \cos^{2.2} \eta \right) \\ \rho_N &= \rho_{\min} \left(1 + \frac{\rho_{\max} - \rho_{\min}}{\rho_{\min}} \sin^{2.2} \theta \right) \end{aligned} \quad (4.16)$$

where ρ_{\max} and ρ_{\min} are, respectively, the maximum and minimum atmospheric density for space objects at the height h .

$$\eta = \frac{1}{2} |\varphi - \delta_S|; \quad \theta = \frac{1}{2} |\varphi + \delta_S|$$

The height h is between h_i and h_{i+1} in the tabulated value.

$$\begin{aligned} \rho_{\min}(h) &= B_1 \rho_{\min}(h_i) e^{(h_i - h)/H_{\min}} \\ \rho_{\max}(h) &= B_2 \rho_{\max}(h_i) e^{(h_i - h)/H_{\max}} \end{aligned} \quad (4.17)$$

where B_1 and B_2 are two input constants, which can be used to adjust the amplitude of atmospheric density diurnal variation, and generally $B_1 = 1$ and $B_2 = 1$. H_{\min} and H_{\max} are shown as follows:

$$\begin{aligned} H_{\min} &= \frac{(h_i - h_{i+1})}{\lg((\rho_{\min}(h_{i+1}))/(\rho_{\min}(h_i)))} \\ H_{\max} &= \frac{(h_i - h_{i+1})}{\lg((\rho_{\max}(h_{i+1}))/(\rho_{\max}(h_i)))} \end{aligned} \quad (4.18)$$

4.2.2.2 Jacchia77 atmospheric model

Jacchia77 atmospheric model is applicable to the calculation of atmospheric density at the height of 90 km above, which can be divided into two parts. The first part is a static atmospheric model, and the second is a dynamic atmospheric model, with considering various atmospheric changes. Based on these changes, the static atmospheric correction is performed.

The calculation process of Jacchia77 atmospheric model is shown as follows:

1. Calculation of the related position values of the Sun and satellites

Formulas (4.8) and (4.9) are adopted to calculate height of satellites and latitude of subsatellite point. With the use of formulas (4.11)–(4.14), Sun's unit vector r_{sb} in Earth-fixed coordinate, solar declination δ_s and solar hour angle α are obtained.

2. Calculation of $T_{1/2}$ using 10.7 cm solar radiation flow

$$T_{1/2} = 5.48\bar{F}^{0.8} + 101.8F^{0.4} \quad (4.19)$$

where F is daily average value of 10.7 cm solar radiation flow. \bar{F} is weighted average of F during six solar rotation periods (164 days). And

$$\bar{F} = \frac{\sum WF}{\sum W} \quad (4.20)$$

where W is weight coefficient. And

$$W = e^{-((t-t_0)/\tau)^2} \quad (4.21)$$

where t_0 is the corresponding time to the desired \bar{F} . τ is taken as three solar rotation periods or 71 days. F and \bar{F} can be found in the database, and the desired value of time (namely value t in the previous day) is obtained with the use of linear interpolation.

3. Calculation of average molecular weight \bar{M} in upper atmosphere

If $T_\infty = T_{1/2}$, average molecular weight \bar{M} at height h is calculated. The computing process can be found in Step 6 for detail. The temperature of each atmospheric component is T .

4. Calculation of pseudo-temperature of each atmospheric component

$$T'_{\infty i} = T_{1/2} \left\{ 1 + 0.15 \frac{\delta_s}{\varepsilon} \sin \varphi + 0.24 \cos \varphi \left[f_i(\alpha) - \frac{1}{2} \right] \right\} \quad (4.22)$$

where $i = 1-6$, which is corresponding to such atmospheric components as N_2 , O_2 , O , Ar , He , and H . And $\varepsilon = 230.44^\circ$, $f_i(\alpha)$ can be shown as follows:

$$f_i(\alpha) = \cos^n \frac{1}{2} (\alpha + \beta_i) + 0.08 \cos [3(\alpha + \beta_i) - 75^\circ] \quad (4.23)$$

where

$$n = 2 + \cos^2 \frac{2\varphi^2}{\pi}$$

$$\beta_i = -35^\circ + 27^\circ \left(\frac{\bar{M}}{M_i} - 1 \right) \quad (i = 1 - 5)$$

$$\beta_6 = -60^\circ$$

5. Calculation of geoeffectiveness correction

The impact of geomagnetic thermal effects on the temperature of upper atmosphere is shown as follows:

$$\Delta T_E = 54.2 \times K'_p (1 + 0.027 e^{0.4K'_p}) \sin^3 \Phi \quad (4.24)$$

where K'_p means K_p at the time $t - \tau$; $\tau = 0^d.1 + 0^d.2 \cos^2 \Phi$, and Φ is magnetic latitude. And the approximated calculation can be performed with the following formula.

$$\sin \Phi = 0.9792 \sin \varphi + 0.2028 \cos \varphi \cos(\lambda - 291^\circ) \quad (4.25)$$

where λ is longitude of subsatellite point.

6. Calculation of particle concentration for each atmospheric component

Taken $T_{\infty i} = T'_{\infty i} + \Delta T_E$ as pseudo-temperature for atmospheric component i , the particle concentration of each atmospheric component is calculated by resolving Jacchia77 model. The calculation method is shown as follows:

1. Calculation of constant coefficients

$$\begin{cases} X_{500} = \frac{500.0 - 125.0}{6356.766 + 500.0} \\ K_x = \frac{2.0 \times (6356.766 + 125.0)}{125.0 - 90.0} \\ V_h = K_x \frac{100.0 - 90.0}{6356.766 + 100.0} - 1.0 \end{cases} \quad (4.26)$$

$$\begin{cases} W_0 = \frac{1 - V_h}{1 + V_h} \\ W_1 = W_0 + 1 \end{cases} \quad (4.27)$$

$$\begin{cases} C_0^* = \hat{C}_3 W_0^3 + \hat{C}_2 W_0^2 + \hat{C}_1 W_0 + \hat{C}_0 \\ C_1^* = (3\hat{C}_3 W_0^2 + 2\hat{C}_2 W_0 + \hat{C}_1) W_1 \\ C_2^* = (3\hat{C}_3 W_0 + \hat{C}_2) W_1^2 \\ C_3^* = \hat{C}_3 W_1^3 \end{cases} \quad (4.28)$$

$$\begin{cases} \hat{C}_0 = 28.573844 \\ \hat{C}_1 = -0.471730 \\ \hat{C}_2 = -0.106679 \\ \hat{C}_3 = 0.047675 \end{cases} \quad (4.29)$$

$$\begin{cases} \bar{M}'_0 = \frac{1}{C_0^* - C_1^* + C_2^* - C_3^*} \\ g_{av} = \frac{9.80655 \times 6356.766^2}{K_x(6356.766 + 90.0)} \\ g_{ax} = \frac{9.80655 \times 6356.766^2}{6356.766 + 125.0} \end{cases} \quad (4.30)$$

2. Calculation of coefficients correlated with $T_{\infty i}$

$$\begin{cases} D = 3110.743363T_{\infty i}^{-0.4197668} - 5.719352 \times 10^{-2}T_{\infty i}e^{-(T_{\infty i}/1187.417)} + 22.58421 \\ T_x = 188.0 + 110.5 \lg(Y_0 + \sqrt{1.0 + Y_0^2}) \\ Y_0 = 0.0045(T_{\infty i} - 188.0) \end{cases} \quad (4.31)$$

$$\begin{cases} \Gamma = \frac{T_{\infty i} - T_x}{G_x(6356.766 + 125.0)} \\ G_x = 1.9 \frac{T_x - 188.0}{125.0 - 90.0} \\ \alpha = \frac{\Gamma D}{\Gamma D - 1.0} \end{cases} \quad (4.32)$$

$$\begin{cases} \tau_0 = \frac{T_x + 188.0}{T_x - 188.0} \\ \tau_1 = \frac{-2.0 \times 188.0 T_x}{T_x - 188.0} \end{cases} \quad (4.33)$$

$$\begin{cases} a_t = \frac{D}{\alpha(T_x - T_{\infty i})} \\ b_t = -2a_t T_x - D \\ c_t = a_t T_{\infty i}^2 + D T_{\infty i} \end{cases} \quad (4.34)$$

$$\begin{cases} n_H(500) = 5.94 + 28.9T_{\infty i}^{-0.25} \\ T_{500} = T_{\infty} + \frac{\alpha(T_x - T_{\infty})e^{-DX_{500}}}{e^{-DX_{500}} - 1 + \alpha} \\ X_{\infty} = \lg \left\{ \left[\frac{\alpha(T_x - T_{\infty}) \times 10^{14} + 1}{1 - \alpha} \right]^{1/D} \right\} \end{cases} \quad (4.35)$$

$$h_{\infty} = \begin{cases} 2500.0 & T_{\infty i} \geq 1386.5 \\ \frac{6356.766X_{\infty} + 125.0}{1 - X_{\infty}} & T_{\infty i} < 1386.5 \end{cases} \quad (4.36)$$

a_n^* and b_n^* are calculated as follows:

$$\begin{cases} G_x^* = 0.475 \times \frac{6356.766 + 125.0}{6356.766 + 90.0} \times \frac{188.0}{T_x} \\ a_5^* = 0.06205282 \lg(T_{\infty} + 213.9884) - 0.6286968 \\ a_6^* = 0.06555111 \lg(T_{\infty} - 329.6454) - 0.1520990 \end{cases} \quad (4.37)$$

$$\begin{cases} a_1^* = -G_x^* + a_5^* - \frac{T_x + 188.0}{T_x - 188.0} \\ a_2^* = -G_x^* + a_6^* + 1.5 \\ a_3^* = G_x^* - 2.0a_5^* \\ a_4^* = G_x^* - 2.0a_6^* - 0.5 \end{cases} \quad (4.38)$$

$$\begin{bmatrix} b_1^* \\ b_2^* \\ b_3^* \\ b_4^* \\ b_5^* \\ b_6^* \\ b_7^* \\ b_8^* \\ b_9^* \end{bmatrix}^T = \begin{bmatrix} C_0^* \\ C_1^* \\ C_2^* \\ C_3^* \end{bmatrix}^T \times \begin{bmatrix} a_1^* & a_2^* & a_3^* & a_4^* & a_5^* & a_6^* & 0 & 0 & 0 \\ 0 & a_1^* & a_2^* & a_3^* & a_4^* & a_5^* & a_6^* & 0 & 0 \\ 0 & 0 & a_1^* & a_2^* & a_3^* & a_4^* & a_5^* & a_6^* & 0 \\ 0 & 0 & 0 & a_1^* & a_2^* & a_3^* & a_4^* & a_5^* & a_6^* \end{bmatrix} \quad (4.39)$$

3. Calculation of particle concentration of each atmospheric component when $h \leq 100$ km (homogeneous layer)

$$h_d = \min(h, 100 \text{ km})$$

Taken atmospheric particle concentration when $h \leq 100$ km (2) with the use of corresponding value of $T_{\infty 6}$ in (2).

$$V_H = K_x \frac{h_d - 90.0}{6356.766 + h_d} - 1.0 \quad (4.40)$$

$$\rho' = \frac{\rho'_0 T_0}{\bar{M}'_0} \left(\frac{\bar{M}'}{T} \right) e^{\{-g_{av}/R\tau_1\} \left[\sum_{n=1}^9 b_n^* (V_H^n + (-1)^{n-1}) \right]} \quad (4.41)$$

where $\rho'_0 = 3.43 \times 10^{-6}$ kg/m²; ρ'_0 is the unamend atmospheric density at a height of 90 km; $T_0 = 188$ K, which is atmospheric temperature at a height of 90 km; and \bar{M}'_0 is the average molecular weight at a height of 90 km, which is given in formula (4.30).

$$\left(\frac{\bar{M}'}{T}\right) = \frac{1}{\tau_1} \sum_{n=1}^9 b_n^* V_H^{n-1} \quad (4.42)$$

Thus the particle concentration n'_{Hi} of each atmospheric component in the homogeneous layer is

$$\left\{ \begin{array}{l} n'_{Hi} = A_v \times 10^3 \frac{q_{Si}}{\bar{M}_s} \rho' \quad (i = 1, 4, 5) \\ n'_{H2} = A_v \times 10^3 \frac{1 + q_{SE}}{\bar{M}_s - 1} \rho' \\ n'_{H3} = A_v \times 10^3 \frac{2}{\bar{M}'} \left(1 - \frac{\bar{M}'}{\bar{M}_s}\right) \rho' \\ n'_{H6} = 0.0 \end{array} \right. \quad (4.43)$$

where A_v is Avogadro's constant, $A_v = 6.02257 \times 10^{23} \text{ mol}^{-1}$; q_{Si} is gas component i at sea level, which is the proportion of atmosphere per unit volume. The values are shown in Table 4–4; $\bar{M}_s = 28.96$ is average atmospheric molecular weight at sea level, \bar{M}' is shown as follows:

$$\bar{M}' = C_0^* + C_1^* V_h + C_2^* V_h^2 + C_3^* V_h^3$$

The temperature of homogeneous layer is

$$T_H = \frac{\tau_1}{\sum_{n=1}^6 a_n^* V_H^{n-1}} \quad (4.44)$$

If $h \leq 100$ km, then turn to step (8) after the calculation of step (3). Otherwise, continue with the following calculation.

4. Calculation of particle concentration and temperature (at the height of $100 \leq h \leq 125$ km).

According to pseudo-temperature $T_{\infty i}$ of atmospheric component I , each corresponding value $T_{\infty i}$ is calculated with the formulas in step (2). Taken

Table 4–4 Atmospheric component coefficients of Jacchia77.

i	Gas	q_s	M_i	α	C_t	C_s
1	N ₂	0.78110	28.0134	0.0	0.0	0.0
2	O ₂	0.20955	31.9988	0.0	1.03×10^{-5}	0.0
3	O	0.0	15.9994	0.0	-5.75×10^{-5}	-0.16
4	Ar	0.009343	39.948	0.0	3.07×10^{-5}	0.0
5	He	0.000005242	4.0026	-0.38	-6.30×10^{-5}	-0.79
6	H	0.0	1.00797	-0.25	0.0	0.0

$$\begin{cases} h_d = \min(h, 125.0 \text{ km}) \\ V_T = K_x \frac{h_d - 90.0}{6356.766 + h_d} - 1.0 \\ T_T = \frac{\tau_1}{\sum_{n=1}^6 a_n^* V_T^{n-1}} \end{cases} \quad (4.45)$$

The particle concentration of atmospheric component i is shown as follows:

$$n'_{T_i} = n'_{H_i} \left(\frac{T_H}{T_T} \right)^{1+a_i} e \left\{ -\frac{M_i g_{av}}{R T_1} \left[\sum_{n=1}^6 \frac{a_n^*}{n} (V_T^n - V_H^n) \right] \right\} \quad (4.46)$$

where n'_{H_i} is given by formula (4.43); T_H and V_H are, respectively, given by formulas (4.44) and (4.40); M_i is molecular weight of atmospheric component i , which is given in Table 4–4; and a_i is thermal conductivity of atmospheric component i , which is given in Table 4–4.

In the abovementioned calculation, $i = 1 - 5$. If $i = 6$, ion concentration of hydrogen atom H should be calculated separately, and the calculation method is in step (7).

If satellites' height h is within the range of $100 \text{ km} \leq h \leq 125 \text{ km}$, then the concentration of hydrogen atoms can be calculated in step (7). If $h > 125 \text{ km}$, continue the following calculation.

5. If $h > 125 \text{ km}$, the particle concentration of atmospheric component is calculated as follows:

$h_d = \min(h, h_\infty)$ (The value of h_∞ is given in step (2)).

$$X_E = \frac{h_d - 125.0}{6356.766 + h_d} \quad (4.47)$$

$$T_{Ei} = T_{\infty i} + \frac{\alpha(T_x - T_{\infty i})e^{-DX_E}}{e^{-DX_E} - 1.0 + \alpha} \quad (4.48)$$

$$n'_{Ei} = n'_{Ti} \left(\frac{T_x}{T_{Ei}} \right)^{1+\alpha_i+\gamma_i} \left(\frac{a_t T_{Ei}^2 + b_t T_{Ei} + c_t}{a_t T_x^2 + b_t T_x + c_t} \right) \left[\frac{1}{1-\alpha} + \frac{\alpha}{1-\alpha} \left(\frac{T_{\infty i} - T_x}{T_{Ei} - T_{\infty i}} \right) \right]^{r b_t / 2D} \quad (4.49)$$

where n'_{Ti} is given in formula (4.46). a_t , b_t , c_t , α , and T_x are calculated in step (2) as follows:

$$\gamma_i = \frac{M_i g_a (6356.766)^2}{R(6356.766 + 125.0)c_t} \quad (4.50)$$

where M_i is the molecular weight of each gas (see Table 4–4). And $g_a = 9.80655 \text{ m/s}^2$; $R = 8.31432 \text{ J/(k mol)}$.

Because the computer word length is limited, T_E in formula (4.48) turns to be T_∞ after the height of a satellite reaches a certain limit. And in formula (4.49)

$$a_t T_\infty^2 + b_t T_E + c_t = 0 \quad (4.51)$$

Thus in formula (4.49), the concentration of atmospheric particles has already been close to zero before the height of a satellite tends to infinity (2500 km). This is mainly caused by the restriction of computer word. Thus in formula (4.48), there is an effective height h_∞ . When $h < h_\infty$, the concentration of atmospheric particles can be calculated with formula (5.49). Provided,

$$T_\infty - T(h_\infty) = \varepsilon$$

when $\varepsilon = 10^{-14}$, the variation range of h_∞ can be obtained with formulas (4.47) and (4.48).

$$\begin{aligned} \text{When } T_\infty = 500\text{K}, \quad h_\infty = 1366.75 \text{ km;} \\ \text{When } T_\infty = 1386.5\text{K} \quad h_\infty = 2500 \text{ km.} \end{aligned}$$

Therefore if

$$h_\infty = \begin{cases} 2500.0 & (T_\infty \geq 1386.5) \\ \frac{6356.766X_\infty + 125.0}{1 - X_\infty} & (T_\infty < 1386.5) \end{cases} \quad (4.52)$$

$$X_\infty = \lg \left[\frac{\alpha(T_x - T_\infty) \times 10^{14} + 1}{1 - \alpha} \right]^{1/D} \quad (4.53)$$

when $h \leq h_\infty$, the particle concentration of atmospheric component at the height of h is calculated in step (5). When $h > h_\infty$, the calculated particle concentration of atmospheric component n'_{Ei} from step (5) is actually at the height of h_∞ . And the particle concentration of atmospheric component at the height of h should be calculated in step (6).

6. Calculation of atmospheric particle concentration n'_{hi} when $h > h_\infty$

$$\begin{aligned} X_h &= \frac{h - 125.0}{6256.766 + h} \\ n'_{hi} &= n'_{Ei} e^{[-(M_i R_{ax} / RT_{\infty i})(x_h - x_\infty)]} \end{aligned} \quad (4.54)$$

The value i of the above calculation is 1–5.

7. Calculation of particle concentration of hydrogen atom

Each corresponding value is calculated by using $T_{\infty 6}$ in step (2). Select $h_d = \min(h, h_\infty)$

$$X_E = \frac{h_d - 125.0}{6356.766 + h_d} \quad (4.55)$$

$$T_{E6} = T_{\infty 6} + \frac{\alpha(T_x - T_{\infty 6})e^{-DX_E}}{e^{-DX_E} - 1.0 + \alpha} \quad (4.56)$$

$$n'_{E6} = n_H(500) \left(\frac{T_{500}}{T_{E6}} \right)^{1+\alpha_6+\gamma_6} \left[\frac{a_t T_{E6}^2 + b_t T_{E6} + c_t}{a_t T_{500}^2 + b_t T_{500} + c_t} \right]^{\gamma_6/2} e^{(\gamma_6 b_t/2)(X_E - X_{500})} \quad (4.57)$$

where $n_H(500)$ and T_{500} are given from step (2); X_{500} is given from step (1).

$$\gamma_6 = \frac{M_6 g_a 6356.766^2}{R(6356.766 + 125.0)c_t} \quad (4.58)$$

If $h \leq h_{\infty}$, the result of formula (4.41) is the particle density of hydrogen atoms at the height of h , turning to step (8). If $h > h_{\infty}$, the calculation should be continued.

$$X_h = \frac{h - 125.0}{6356.766 + h} \quad (4.59)$$

$$n_{E6} = n'_{E6} e^{-(M_6 g_a / RT_{\infty 6})(X_h - X_{500})} \quad (4.60)$$

8. The empirical correction of particle concentration of atmospheric particles and calculation of atmospheric density

In the previous calculations, the decomposition degree of O_2 is determined with the use of the average molecular weight of the homogeneous layer. In the homogeneous layer above, the decomposition of the particle concentration for oxygen molecules and oxygen atoms is revised by using empirical correction formula. The correction coefficients are

$$F_2 = \begin{cases} 0.7244359601 & (h > 200 \text{ km}) \\ 10^{-0.07[1.0 + \tanh(0.18(h-111.0))]} & (h \leq 200 \text{ km}) \end{cases} \quad (4.61)$$

$$F_3 = \begin{cases} 1.0 & (h > 200 \text{ km}) \\ 10^{-0.24e^{[0.009(h-97.7)^2]}} & (h \leq 200 \text{ km}) \end{cases} \quad (4.62)$$

The concentration of particles for oxygen molecules and oxygen atoms are shown as follows:

$$\begin{aligned} n_{h2} &= n'_{h2} \cdot F_2 \\ n_{h3} &= n'_{h3} \cdot F_3 \end{aligned} \quad (4.63)$$

At the height h , the average molecular weight is shown as follows:

$$\bar{M} = \frac{\sum_{n=1}^6 n_{hi} M_i}{\sum_{i=1}^6 n_{hi}} \quad (4.64)$$

The static atmospheric density at the height is shown as follows:

$$\rho = 1.660421 \times 10^{-27} \times \bar{M} \times \sum_{i=1}^6 n_{hi} \quad (4.65)$$

9. The effect of equatorial waves and top height variations in homogeneous layer.

The variations of homogeneous layer at the top level are accompanied by geomagnetic thermal effects. The change is shown as follows:

$$\Delta H = 5.0 \times 10^3 \lg \left(0.01 \Delta T_E + \sqrt{1.0 + 0.0001 \Delta T_E^2} \right) \text{ (m)} \quad (4.66)$$

The effect of particle concentration on the atmospheric component i is shown as follows:

$$Dn_{i(1)} = C_{ii} \Delta H \quad (4.67)$$

where the value C_{ii} of each coefficient is given in [Table 4–4](#).

Geomagnetic thermal effects can also cause atmospheric density wave, the impact of which is shown as follows:

$$Dn_{i(2)} = 5.2 \times 10^{-4} \times 54.2 K_p (1.0 + 0.027 e^{0.4 K_p}) \cos^2 \Phi \quad (4.68)$$

where $\cos \Phi = \sqrt{1 - \sin^2 \Phi}$, and $\sin \Phi$ is given in formula [\(4.24\)](#).

10. Seasonal variation of latitude.

Here, the seasonal variation of latitude does not include the related latitude items to the height in the diurnal variation. The seasonal latitude is irrelevant to the height. A typical particle is called “winter helium outstanding.” The seasonal variation of latitude in atmospheric component is shown as follows:

$$Dn_{i(3)} = C_{Si} \frac{\delta_S}{\varepsilon} \sin \varphi \quad (4.69)$$

where δ_S is solar declination; ε is the angle between the equator and the ecliptic, and $\varepsilon = 23.44^\circ$; The value of C_{Si} is in [Table 4–4](#).

11. Semiannual variation.

The expression of semiannual variations for atmospheric density is basically the same as Jacchia71, which only has the change of coefficients in the expression.

$$Dn_{i(4)} = f(h)g(t) \quad (4.70)$$

where

$$\begin{cases} f(h) = (0.4 \times 10^{-5} h^2 + 0.05) e^{-0.0025h} \\ g(t) = 0.0284 + 0.382[1.0 + 0.467 \sin(2\pi\tau + 4.14)] \sin(4\pi\tau + 4.26) \end{cases} \quad (4.71)$$

where

$$\tau = \Phi + 0.0954 \left\{ \left[\frac{1}{2} + \frac{1}{2} \sin(2\pi\Phi + 6.04) \right]^{1.65} - \frac{1}{2} \right\} \quad (4.72)$$

And $\Phi = JD_{1978}/365.2422$.

where JD_{1978} is the Julian day number starting from 1978-01-00. And

$JD_{1978} = t_{MJD} - 43509.0$.

12. Correction of geomagnetic effect in the heat temperature atmosphere

$$Dn_{i(5)} = \beta_i \times \left(\frac{800}{T_\infty} \right)^m \times f'(h) \times (\sin\alpha)^{-1} \times (0.003 \times \Delta T_E) \quad (4.73)$$

$$f'(h) = -0.86 + 0.6 \left(\frac{h}{100} \right) - 0.00636 \left(\frac{h}{100} \right)^2 + 0.29 \times \left[1 + 1.7 \times \left(\frac{h}{100} - 1.27 \right)^2 + 0.3322 \times \left(\frac{h}{100} \right)^{13} \right]^{-1} \quad (4.74)$$

$$m = 1.7 \times \tan\alpha \times [0.005 \times (h - 100)]$$

β_i in each component is shown in Table 4–5.

13. Calculation of the revised atmospheric density ρ at the height of h .

$$\rho = A_{Vr} \times 10^{-3} \sum_{i=1}^6 M_i 10^{Dn_i} \quad (4.75)$$

where $A_{Vr} = 1.660421 \times 10^{-24}$, which is the reciprocal of the Avogadro constant. M_i is the molecular weight of atmospheric composition i , which is shown in Table 4–4.

$$Dn_i = \log n_{hi} + \Delta n_{Hi} + \Delta n_{Ei} + \Delta n_{SLi} + \Delta \rho_S + \Delta \log n_{ei}$$

n_{hi} is static particle concentration of atmospheric composition i , obtained from step (6). $Dn_{i(1)}$, $Dn_{i(2)}$, $Dn_{i(3)}$, $Dn_{i(4)}$, and $Dn_{i(5)}$ are, respectively, given by formulas (4.66), (4.67), (4.68), (4.60), and (4.70).

4.2.2.3 MSIS00 model

MSIS00 (US Naval Research Laboratory Mass Spectrometer and Incoherent Scatter Radar Extended, referred MSIS00) atmospheric model is developed by Naval Research Laboratory generated on the basis of MSIS90 model. With respect to MSIS90 model, MSIS00 model not only adds new satellite data but also absorbs the database of Jacchia model.

Table 4–5 β_i in each component of Jacchia77.

	He	Ar	O ₂	N ₂	O	H
β_i	0.1	1.5	1.16	1.0	0.52	0.46

Along with seven kinds of He, O, N₂, O₂, Ar, H, and N components in MSIS90 model, a new component that is introduced to MSIS00 model is anomalous oxygen. It comes from the analysis of Jacchia70 model. And in the region of high latitude and high elevation (higher than 600 km) in summer, the atmospheric density of Jacchia70 is obviously much higher than MSIS86 model. Hedin believes that active oxygen ions in the upper atmosphere brought these effects [89]. In a subsequent analysis of the satellite data, this deduction also can be corroborated.

The atmospheric density that calculated by MSIS00 model is the combined effect under the conditions of diffusion and mixture, taking into account space environment and chemical effects. The calculation steps of MSIS00 model are shown as follows:

1. Temperature calculation

a. The temperature calculation when $Z > Z_a$ (123.435 km) is shown as follows:

$$T_{(Z)} = T_{\omega} - (T_{\omega} - T_L)e^{-\delta \times \varepsilon(Z, Z_L)} \quad (4.76)$$

where

$$\delta = \frac{T'_L}{T_{\omega} - T_L} \quad (4.77)$$

$$\varepsilon(Z, Z_L) = \frac{(Z - Z_L)(R_p + Z_L)}{R_p + Z} \quad (4.78)$$

$$R_p = \frac{2 \times 980.616 \times 10^{-5} \times [1 - 0.0026373 \times \cos(2B)]}{3.085462 \times 10^{-6} + 2.27 \times 10^{-9} \times \cos(2B)} \quad (4.79)$$

$$T'_L = \bar{T}'_L(1 + G_8(L)) \quad (4.80)$$

$$T_{\omega} = \bar{T}_{\omega}(1 + G_9(L)) \quad (4.81)$$

$$T_L = \bar{T}_L(1 + G_{10}(L)) \quad (4.82)$$

$$\bar{T}_L = 386K \quad (4.83)$$

$$\bar{T}_{\omega} = 1037.14K \quad (4.84)$$

$$\bar{T}'_L = 16.19916K/km \quad (4.85)$$

where $Z_L = 120$ km; and Z , L , and B are, respectively, the height of calculated point, latitude, and longitude. $G_i(L)$ is the physics parameter of location, time, and space.

b. The temperature calculation that height Z is less than Z_a (123.435 km) is an interpolation process. The interpolating calculation is performed at five node heights ($Z_1 = Z_a$, $Z_2 = 110$, $Z_3 = 100$ km, $Z_4 = 90$ km, and $Z_5 = 72.5$ km). The node function can be obtained via the fitting of the rocket flight data and the US Standard Atmosphere.

$$T_{(Z)} = \left(A \times TT_l + B \times TT_h + \frac{(\beta_h - \beta_l)^2 \times \{ (A^3 - A) \times YZ_l + (B^3 - B) \times YZ_h \}}{6} \right)^{-1} \quad (4.86)$$

$$A = \frac{\beta_h - \beta}{\beta_h - \beta_l} \quad (4.87)$$

$$B = \frac{\beta - \beta_l}{\beta_h - \beta_l}$$

h and l are, respectively, the adjacent nodes, and height Z is in the position of five node heights.

where

$$\beta = \frac{\varepsilon(Z, Z_1)}{\varepsilon(Z_5, Z_1)} \quad (4.88)$$

$$\beta_l = \frac{\varepsilon(Z_l, Z_1)}{\varepsilon(Z_5, Z_1)} \quad (4.89)$$

$$TT_i = \frac{1}{T_{(Z_i)}} \quad (4.90)$$

$T_{(Z_i)}$ is calculated from (4.91)–(4.94).

$$T_{(Z_2)} = \left(\frac{(1 - G_S(P_{11}))}{244.999} \right)^{-1} \quad (4.91)$$

$$T_{(Z_3)} = \left(\frac{(1 - G_S(P_{12}))}{180.35} \right)^{-1} \quad (4.92)$$

$$T_{(Z_4)} = \left(\frac{(1 - G_S(P_{13}))}{181.889} \right)^{-1} \quad (4.93)$$

$$T_{(Z_5)} = \left(\frac{(1 - G_S(P_{14}))}{212.865} \right)^{-1} \quad (4.94)$$

The calculation process of YZ_i is shown as follows:

$$YZ_5 = \frac{UN - 0.5 \times U_4}{0.5 \times YY_4 + 1} \quad (4.95)$$

$$YZ_i = YY_i \times YZ_{i+1} + U_i \quad (4.96)$$

$$YY_i = \frac{(s_i - 1)}{P_i} \quad (4.97)$$

$$UN = \frac{3}{\beta_5 - \beta_4} \times \left(YD_2 - \frac{TT_5 - TT_4}{\beta_5 - \beta_4} \right) \quad (4.98)$$

$$U_i = P_i^{-1} \times \left(6 \times (\beta_{i+1} - \beta_{i-1})^{-1} \times \left(\frac{TT_{i+1} - TT_i}{\beta_{i+1} - \beta_i} - \frac{TT_i - TT_{i-1}}{\beta_i - \beta_{i-1}} \right) - S_i \times U_{i-1} \right) \quad (4.99)$$

$$S_i = \frac{\beta_i - \beta_{i-1}}{\beta_{i+1} - \beta_{i-1}} \quad (4.100)$$

$$P_i = S_i \times YY_{i-1} + 2 \quad (4.101)$$

$$YY_1 = -0.5 \quad (4.102)$$

$$U_1 = \frac{3}{\beta_2 - \beta_1} \times \left(\frac{TT_2 - TT_1}{\beta_2 - \beta_1} - YD_1 \right) \quad (4.103)$$

$$YD_1 = - \frac{T'(z_1) \times \varepsilon(z_5, z_1)}{T^2(z_1)} \quad (4.104)$$

$$YD_2 = - \frac{T'(z_5) \times \varepsilon(z_5, z_1)}{T^2(z_5)} \times \left(\frac{R_p + Z_5}{R_p + Z_1} \right)^2 \quad (4.105)$$

$T'(Z_1)$ is the temperature gradient of Z_1 .

$$T'(Z_1) = (T_\omega - T(Z_1)) \times \delta \times \left(\frac{R_p + Z_1}{R_p + Z_1} \right)^2 \quad (4.106)$$

$T'(Z_5)$ is the temperature gradient of Z_5 .

$$T'(Z_5) = 3.8245 \times 10^{-5} \times T_{(Z_5)}^2 \times (1 + G_S(P_{15})) \quad (4.107)$$

P_{11} , P_{12} , P_{13} , P_{14} , and P_{15} are five group fitting constants that can be seen in P coefficient table. $G_S(P^i)$ is the function related to time, location, and spatial parameters. And the calculation is shown as follows:

$$G_S(P^i) = \sum_{j=1}^{11} T_j \quad (4.108)$$

The calculation of T_j is shown as follows:

T_1 is the impact term of solar $F_{10.7 \text{ cm}}$ radiation parameters. And

$$T_1 = P_{(22)}^i \times (\bar{F}_{10.7} - 150) \quad (4.109)$$

T_2 is time-independent item. And

$$T_2 = P_{(2)}^i \times P_{(2,0)} + P_{(3)}^i \times P_{(4,0)} + P_{(23)}^i \times P_{(6,0)} + P_{(27)}^i \times P_{(1,0)} \\ + P_{(28)}^i \times P_{(3,0)} + P_{(29)}^i \times P_{(5,0)} \quad (4.110)$$

T_3 is anniversary even term. And

$$T_3 = \left(P_{(19)}^i + P_{(48)}^i \times P_{(2,0)} + P_{(30)}^i \times P_{(4,0)} \right) \times C_{32} \\ + P_{(28)}^i \times P_{(3,0)} + P_{(29)}^i \times P_{(5,0)} \quad (4.111)$$

T_4 is semiannual even item. And

$$T_4 = \left(P_{(16)}^i + P_{(17)}^i \times P_{(2,0)} + P_{(31)}^i \times P_{(4,0)} \right) \times C_{18} \quad (4.112)$$

T_5 is anniversary odd item. And

$$T_5 = \left(P_{(10)}^i \times P_{(1,0)} + P_{(11)}^i \times P_{(3,0)} + P_{(36)}^i \times P_{(5,0)} \right) \times C_{14} \quad (4.113)$$

T_6 is semiannual odd item. And

$$T_6 = \left(P_{(38)}^i \times P_{(1,0)} \right) \times C_{39} \quad (4.114)$$

T_7 is diurnal item shown as follows:

$$T_{71} = P_{(12)}^i \times P_{(2,1)} \times C_{14} \quad (4.115)$$

$$T_{72} = P_{(13)}^i \times P_{(2,1)} \times C_{14} \quad (4.116)$$

$$T_7 = \left(P_{(4)}^i \times P_{(1,1)} \times P_{(5)}^i \times P_{(3,1)} + T_{71} \right) \times C_T \quad + \left(P_{(7)}^i \times P_{(1,1)} \times P_{(8)}^i \times P_{(3,1)} + T_{72} \right) \times S_T \quad (4.117)$$

T_8 is half diurnal item.

$$T_{81} = \left(P_{(24)}^i \times P_{(3,2)} \times P_{(47)}^i \times P_{(5,2)} \right) \times C_{14} \quad (4.118)$$

$$T_{82} = \left(P_{(34)}^i \times P_{(3,2)} \times P_{(49)}^i \times P_{(6,3)} \right) \times C_{14} \quad (4.119)$$

$$T_8 = \left(P_{(6)}^i \times P_{(2,2)} \times P_{(42)}^i \times P_{(4,2)} + T_{81} \right) \times C_{2T} \\ + \left(P_{(9)}^i \times P_{(2,2)} \times P_{(43)}^i \times P_{(4,2)} + T_{82} \right) \times S_{2T} \quad (4.120)$$

T_9 is diurnal item of the thirds.

$$T_9 = P_{(40)}^i \times P_{(3,3)} \times S_{3T} \times P_{(41)}^i \times P_{(3,3)} \times C_{3T} \quad (4.121)$$

T_{10} is geomagnetic impact item.

$$T_{10} = APDF \times \left(P_{(33)}^i \times P_{(46)}^i \times P_{(2,0)} \right) \quad (4.122)$$

T_{11} is longitude item.

$$\begin{aligned} T_{11} = & \left(1 + P_{(1,0)} \times \left(P_{(81)}^i \times \cos(d - P_{(82)}^i) + P_{(86)}^i \times \cos(2 \times d - P_{(87)}^i) \right) \right) + P_{(84)}^i \times \cos(d - P_{(85)}^i) \\ & + P_{(88)}^i \times \cos(2 \times (d - P_{(89)}^i)) \times \left(\left(P_{(65)}^i \times P_{(2,1)} + P_{(66)}^i \times P_{(4,1)} + P_{(67)}^i \times P_{(6,1)} + P_{(75)}^i \times P_{(1,1)} \right) \right. \\ & + P_{(76)}^i \times P_{(3,1)} + P_{(77)}^i \times P_{(5,1)} \left. \right) \times CL + \left(P_{(91)}^i \times P_{(2,1)} + P_{(92)}^i \times P_{(4,1)} + P_{(93)}^i \times P_{(6,1)} + P_{(78)}^i \times P_{(1,1)} \right) \\ & + P_{(79)}^i \times P_{(3,1)} + P_{(80)}^i \times P_{(5,1)} P_{(77)}^i \left. \right) \times SL \end{aligned} \quad (4.123)$$

In the abovementioned calculations the calculation formula of each parameter is shown as follows:

$$A_{PDF} = (AP_1 - 4) + \left(\left(P_{(45)}^i - 1 \right) \times \left((AP_1 - 4) + \left(e^{-P_{(44)}^i \times (AP_1 - 4)} - 1 \right) / P_{(44)}^i \right) \right) \quad (4.124)$$

$$F_1 = 1 + P_{(48)}^i \times (\bar{F}_{10.7} - 150) + P_{(20)}^i \times (F_{10.7} - \bar{F}_{10.7}) + P_{(21)}^i \times (F_{10.7} - \bar{F}_{10.7})^2 \quad (4.125)$$

$$F_2 = 1 + P_{(50)}^i \times (\bar{F}_{10.7} - 150) + P_{(20)}^i \times (F_{10.7} - \bar{F}_{10.7}) + P_{(21)}^i \times (F_{10.7} - \bar{F}_{10.7})^2 \quad (4.126)$$

$$EXP_1 = e^{-\left(10,800 \times |P_{(52)}^i| / (1 + P_{(139)}^i \times (45 - |B|)) \right)} \quad (4.127)$$

$$EXP_2 = e^{-10,800 \times |P_{(54)}^i|} \quad (4.128)$$

$$G_O(A) = \left(A - 4 + \left(P_{(26)}^i - 1 \right) \times \left(A - 4 + \left(e^{-|P_{(25)}^i| \times (A-4)} - 1 \right) / |P_{(25)}^i| \right) \right) \quad (4.129)$$

$$\begin{aligned} S_{G_o}(x) = & \left(G_O(AP_2) + \left(G_O(AP_3) \times x + G_O(AP_4) \times x^2 + G_O(AP_5) \times x^3 \right) \right. \\ & \left. + \left(G_O(AP_6) \times x^4 + G_O(AP_7) \times x^{12} \right) \times (1 - x^8) / (1 - x) \right) / (1 + x^5(1 - x^{19}) / (1 - x)) \end{aligned} \quad (4.130)$$

$$A_{PT}(1) = S_{G_o}(EXP_1) \quad (4.131)$$

$$A_{PT}(3) = S_{G_o}(EXP_2) \quad (4.132)$$

$$C_L = \cos\left(\frac{\pi}{180} L\right) \quad (4.133)$$

$$S_L = \sin\left(\frac{\pi}{180} L\right) \quad (4.134)$$

$$S_T = \sin\left(\frac{\pi}{180}(L + UTC \times 15)\right) \quad (4.135)$$

$$C_T = \cos\left(\frac{\pi}{180}(L + UTC \times 15)\right) \quad (4.136)$$

$$S_{2T} = \sin\left(2 \times \frac{\pi}{180}(L + UTC \times 15)\right) \quad (4.137)$$

$$C_{2T} = \cos\left(2 \times \frac{\pi}{180}(L + UTC \times 15)\right) \quad (4.138)$$

$$S_{3T} = \sin\left(3 \times \frac{\pi}{180}(L + UTC \times 15)\right) \quad (4.139)$$

$$C_{3T} = \cos\left(3 \times \frac{\pi}{180}(L + UTC \times 15)\right) \quad (4.140)$$

$$C_{32} = \cos\left(\frac{2\pi}{365}(d - P_{(32)}^i)\right) \quad (4.141)$$

$$C_{18} = \cos\left(\frac{4\pi}{365}(d - P_{(18)}^i)\right) \quad (4.142)$$

$$C_{14} = \cos\left(\frac{2\pi}{365}(d - P_{(14)}^i)\right) \quad (4.143)$$

$$C_{39} = \cos\left(\frac{4\pi}{365}(d - P_{(39)}^i)\right) \quad (4.144)$$

where $P_{(n,m)}$ is Legendre function; d is the calculating time corresponding to the number of the year; $F_{10.7}$ is the pridian value of solar radiation of 10.7 cm; $\bar{F}_{10.7}$ is the average value of 81-day solar radiation of 10.7 cm; AP_1 is the geomagnetic index value a_p of the day; AP_2 is the geomagnetic index value a_p of current 3 hours; AP_3 is the geomagnetic index value a_p 3 hours before; AP_4 is the geomagnetic index value a_p 6 hours before; AP_5 is the geomagnetic index value a_p 9 hours before; AP_6 is the average value of the geomagnetic index value 12–33 hours before; and AP_7 is the average value of the geomagnetic index value 36–59 hours before.

2. Calculation of atmospheric density

MSIS00 model provides two calculating results of atmospheric density. And the first result represents the measurable atmospheric density, while the second result represents the effective atmospheric density.

The calculation of the measurable atmospheric density is the integration for the distribution of the diffusion and mixing, and the unit of atmospheric density ρ is shown as follows:

$$\rho = 1.66 \times 10^{-24} \sum_{i=1}^7 (m_i \times N_i(Z, m_i)) \quad (\text{g/cm}^3) \quad (4.145)$$

where $i = 1, \dots, 7$, the sequence of the corresponding atmospheric component is He, O, N₂, O₂, Ar, H, N, and m_i , which are, respectively, 4, 16, 28, 32, 40, 1, and 14. And the nominal value of the molecular weight for each component is $N_i(Z, m_i)$. And

$$N_i(Z, m_i) = N_{di} \left(1 + e^{A \times \ln(N_{mi}/N_{di})} \right)^{1/A} C_1^i(Z) C_2^i(Z) \quad (4.146)$$

$$A = \frac{M_h}{(\bar{M}_m - M_i)} \quad (4.147)$$

where N_{di} is diffused distribution density; N_{mi} is mixed distribution density; and $C_1^i(Z)$, $C_2^i(Z)$ are, respectively, the space environment and chemical correction factor of the i th component.

where $M_h = 28$; $\bar{M}_m = 28.95$; M_i is the nominal values of the molecular weight for each component.

The effective atmospheric density is the sum of the measurable atmospheric density and the density of active oxygen atoms.

$$\rho_e = \rho + 1.66 \times 10^{-24} N_8(Z) \quad (\text{g/cm}^3) \quad (4.148)$$

where $N_8(Z)$ is the density of the active oxygen atom at the height Z . In MSIS00 model the density of the active oxygen atom is not isolated as the diffused and mixed distribution density.

3. Diffusion distribution

$$N_{di} = N_{Li} D_i(Z, m_i) \left(\frac{T_{(2L)}}{T_{(Z)}} \right)^{1+\alpha} \quad (4.149)$$

$$D_i(Z, m_i) = D_{Bi}(Z, m_i) \quad (Z \geq Z_\alpha) \quad (4.150)$$

$$D_i(Z, m_i) = D_{Bi}(Z, m_i) \times \left(\frac{T_{(Z_L)}}{T_{(Z)}} \right)^{1+\alpha} \times e^{-r_3 \times r_1} \quad (Z < Z_\alpha) \quad (4.151)$$

$$D_{Bi}(Z, m_i) = \left(\frac{T_{(Z_L)}}{T_{(Z)}} \right)^{\gamma^2} e^{-\delta \times r_2 \times \varepsilon(Z, Z_L)} \quad (4.152)$$

$$r_2 = \frac{m_i g_L}{(\delta R_g T_\omega)} \quad (4.153)$$

$$g_L = \frac{g_s}{(1 + (Z_L/R_p))^2} \quad (4.154)$$

$$g_a = \frac{g_s}{(1 + (Z_a/R_p))^2} \quad (4.155)$$

$$N_{Li} = \bar{N}_{Li} e^{G_i(L)} \quad (4.156)$$

$$g_s = 980.616[1 - 0.0026373\cos(2L)] \quad (4.157)$$

where $R_g = 831.4$ and \bar{N}_{Li} are the average density of each component at Z_L . According to the sequence, the following values are shown. They are in the sequence of 2.577179×10^7 , 8.001985×10^{10} , 3.00389×10^{11} , 3.0736266×10^{10} , 1.15451049×10^9 , $224, 553.9$, and 57.3587×10^7 .

$$r_3 = m_i \times \frac{g_s}{(1 + (Z_L/R_p))^2} \times \frac{\varepsilon_{(Z_2, Z_L)}}{R_g} \quad (4.158)$$

$$r_1 = \sum_{n=1}^4 \left(H_n \times \left((1 - A_n^2) \times \frac{TT_n}{2} + B_n^2 \times \frac{TT_{n+1}}{2} + \left(\left(\frac{A_n^2}{2} - \frac{1 + A_n^4}{4} \right) \times YZ_n + \left(\frac{B_n^4}{4} - \frac{B_n^2}{2} \right) \times YZ_{n+1} \right) \times \frac{H_n^2}{6} \right) \right) \quad (4.159)$$

$$H_n = \beta_{n+1} - \beta_n \quad (4.160)$$

$$A_n = \frac{(\beta_{n+1} - XX_n)}{H_n} \quad (4.161)$$

$$B_n = \frac{(XX_n - \beta_n)}{H_n} \quad (4.162)$$

$$XX_n = \begin{cases} \beta_{n+1} & \left(\beta_{n+1} \leq \frac{\varepsilon_{(Z, Z_1)}}{\varepsilon_{(Z_5, Z_1)}} \right) \\ \frac{\varepsilon_{(Z, Z_1)}}{\varepsilon_{(Z_5, Z_1)}} & \left(\beta_{n+1} > \frac{\varepsilon_{(Z, Z_1)}}{\varepsilon_{(Z_5, Z_1)}} \right) \end{cases} \quad (n < 4) \quad (4.163)$$

$$XX_4 = \frac{\varepsilon_{(Z, Z_1)}}{\varepsilon_{(Z_5, Z_1)}} \quad (4.164)$$

$G_i(L)$ is a function fitted by of the measured atmospheric data, which is a low-order spherical harmonic function related to the location, time, and spatial physics parameters.

$$G_i(L) = P_{(31)}^i + \sum_{j=1}^{13} T_j \quad (4.165)$$

The calculation of T_j is shown as follows:

T_1 is impact item of solar $F_{10.7}$ cm radiation parameters.

$$T_1 = P_{(20)}^i \times (F_{10.7} - \bar{F}_{10.7}) \left(1 + P_{(60)}^i \times (\bar{F}_{10.7} - 150) \right) + P_{(21)}^i \times (F_{10.7} - \bar{F}_{10.7})^2 + P_{(22)}^i \times (\bar{F}_{10.7} - 150) + P_{(30)}^i \times (\bar{F}_{10.7} - 150)^2 \quad (4.166)$$

T_2 is time-independent item.

$$T_2 = P_{(2)}^i \times P_{(2,0)} + P_{(3)}^i \times P_{(4,0)} + P_{(23)}^i \times P_{(6,0)} + P_{(15)}^i \times P_{(2,0)} \times (\bar{F}_{10.7} - 150) + P_{(27)}^i \times P_{(1,0)} \quad (4.167)$$

T_3 is anniversary even order item.

$$T_3 = P_{(19)}^i \times \cos\left(\frac{2\pi}{365} (d - P_{(32)}^i)\right) \quad (4.168)$$

T_4 is semiannual even item.

$$T_4 = \left(P_{(16)}^i + P_{(17)}^i \times P_{(2,0)}\right) \times \cos\left(\frac{4\pi}{365} \times (d - P_{(18)}^i)\right) \quad (4.169)$$

T_5 is anniversary odd item.

$$T_5 = F1 \times \left(P_{(10)}^i \times P_{(1,0)} + P_{(11)}^i \times P_{(3,0)}\right) \cos\left(\frac{2\pi}{365} \times (d - P_{(14)}^i)\right) \quad (4.170)$$

T_6 is semiannual odd item.

$$T_6 = P_{(38)}^i \times P_{(1,0)} \times \cos\left(\frac{4\pi}{365} \times (d - P_{(39)}^i)\right) \quad (4.171)$$

T_7 is diurnal term.

$$T_7 = F_2 \times C_T \times \left(P_{(4)}^i \times P_{(1,1)} + P_{(5)}^i \times P_{(3,1)} + P_{(28)}^i \times P_{(5,1)} + P_{(12)}^i \times P_{(2,1)} \times \cos\left(\frac{2\pi}{365} \times (d - P_{(14)}^i)\right) \right) + F_2 \times S_T \times \left(P_{(7)}^i \times P_{(1,1)} + P_{(8)}^i \times P_{(3,1)} + P_{(29)}^i \times P_{(5,1)} + P_{(13)}^i \times P_{(2,1)} \times \cos\left(\frac{2\pi}{365} \times (d - P_{(14)}^i)\right) \right) \quad (4.172)$$

T_8 is semi diurnal items.

$$T_8 = F_2 \times C_{2T} \times \left(P_{(6)}^i \times P_{(2,2)} + P_{(42)}^i \times P_{(4,2)} + P_{(24)}^i \times P_{(3,2)} + P_{(36)}^i \times P_{(5,2)} \right) \times \cos\left(\frac{2\pi}{365} \times (d - P_{(14)}^i)\right) + F_2 \times S_{2T} \times \left(P_{(9)}^i \times P_{(2,2)} + P_{(43)}^i \times P_{(4,2)} + \left(P_{(34)}^i \times P_{(3,2)} + P_{(37)}^i \times P_{(5,2)} \right) \times \cos\left(\frac{2\pi}{365} \times (d - P_{(14)}^i)\right) \right) \quad (4.173)$$

T_{10} is three diurnal variation.

$$\begin{aligned}
T_{10} &= F_2 \times S_{3T} \times \left(P_{(40)}^i \times P_{(3,3)} + P_{(94)}^i \times P_{(4,3)} + P_{(47)}^i \times P_{(6,3)} \right) \\
&\quad \times \cos \left(\frac{2\pi}{365} \times \left(d - P_{(14)}^i \right) \right) + F_2 \times C_{3T} \times \left(P_{(41)}^i \times P_{(3,3)} + \left(P_{(95)}^i \times P_{(4,3)} + P_{(49)}^i \times P_{(6,3)} \right) \right) \\
&\quad \times \cos \left(\frac{2\pi}{365} \times \left(d - P_{(14)}^i \right) \right)
\end{aligned} \tag{4.174}$$

T_9 is the impact items of geomagnetic index Ap .

If $P_{(52)}^i$ is equal to 0, then

$$\begin{aligned}
T_9 &= A_{PDF} \times \left(P_{(33)}^i + P_{(46)}^i \times P_{(2,0)} + P_{(35)}^i \times P_{(4,0)} + \left(P_{(101)}^i \times P_{(1,0)} + P_{(102)}^i \times P_{(3,0)} + P_{(103)}^i \times P_{(5,0)} \right) \right) \\
&\quad \times \cos \left(\frac{2\pi}{365} \times \left(d - P_{(14)}^i \right) \right) + \left(P_{(122)}^i \times P_{(1,1)} + P_{(123)}^i \times P_{(3,1)} + P_{(124)}^i \times P_{(5,1)} \right) \\
&\quad \times \cos \left(0.2618 \times \left(\frac{L}{15} + UTC - P_{(125)}^i \right) \right)
\end{aligned} \tag{4.175}$$

If $P_{(52)}^i$ is not equal to 0, then

$$\begin{aligned}
T_9 &= A_{PT}(1) \times \left(P_{(51)}^i + P_{(97)}^i \times P_{(2,0)} + P_{(55)}^i \times P_{(4,0)} + \left(P_{(126)}^i \times P_{(1,0)} + P_{(127)}^i \times P_{(3,0)} + P_{(128)}^i \times P_{(5,0)} \right) \right) \\
&\quad \times \cos \left(\frac{2\pi}{365} \times \left(d - P_{(14)}^i \right) \right) + \left(P_{(129)}^i \times P_{(1,1)} + P_{(130)}^i \times P_{(3,1)} + P_{(131)}^i \times P_{(5,1)} \right) \\
&\quad \times \cos \left(0.2618 \times \left(\frac{L}{15} + UTC - P_{(132)}^i \right) \right)
\end{aligned} \tag{4.176}$$

T_{11} is the item related to longitude.

$$\begin{aligned}
T_{11} &= \left(1 + P_{(81)}^i \times (\bar{F}_{10.7} - 150) \right) \times \left(\left(P_{(65)}^i \times P_{(2,1)} + P_{(66)}^i \times P_{(4,1)} + P_{(67)}^i \times P_{(6,1)} + P_{(104)}^i \times P_{(1,1)} \right) \right. \\
&\quad \left. + P_{(105)}^i \times P_{(3,1)} + P_{(106)}^i \times P_{(5,1)} + \left(P_{(110)}^i \times P_{(1,1)} + P_{(111)}^i \times P_{(3,1)} + P_{(112)}^i \times P_{(5,1)} \right) \right) \\
&\quad \times \cos \left(\frac{2\pi}{365} \times \left(d - P_{(14)}^i \right) \right) \times \cos \left(\frac{\pi}{180} \times L \right) + \left(P_{(91)}^i \times P_{(2,1)} + P_{(92)}^i \times P_{(4,1)} + P_{(93)}^i \times P_{(6,1)} \right) \\
&\quad + P_{(107)}^i \times P_{(1,1)} + P_{(108)}^i \times P_{(3,1)} + P_{(109)}^i \times P_{(5,1)} + \left(P_{(113)}^i \times P_{(1,1)} + P_{(114)}^i \times P_{(3,1)} + P_{(115)}^i \times P_{(5,1)} \right) \\
&\quad \times \cos \left(\frac{2\pi}{365} \times \left(d - P_{(14)}^i \right) \right) \times \sin \left(\frac{\pi}{180} \times L \right)
\end{aligned} \tag{4.177}$$

T_{12} is item mixing time and longitude.

$$\begin{aligned}
 T_{12} = & \left(1 + P_{(96)}^i \times P_{(1,0)}\right) \left(1 + P_{(82)}^i \times (\bar{F}_{10.7} - 150)\right) \times \left(1 + P_{(120)}^i \times P_{(1,0)} \times \cos\left(\frac{2\pi}{365} \times (d - P_{(14)}^i)\right)\right) \\
 & \times \left(P_{(69)}^i \times P_{(1,0)} + P_{(70)}^i \times P_{(3,0)} + P_{(71)}^i \times P_{(5,0)}\right) \times \cos\left(0.000072722 \times (UTC \times 3600 - P_{(72)}^i)\right) \\
 & + \left(P_{(77)}^i \times P_{(3,2)} + P_{(78)}^i \times P_{(5,2)} + P_{(79)}^i \times P_{(7,2)}\right) \times \left(1 + P_{(138)}^i \times (\bar{F}_{10.7} - 150)\right) \\
 & \times \cos\left(0.000072722 \times (UTC \times 3600 - P_{(80)}^i)\right) + 2 \times \frac{\pi}{180} L
 \end{aligned} \tag{4.178}$$

T_{13} is the mixed item of time, latitude, and geomagnetic index.

If $P_{(52)}^i$ is equal to 0, then

$$\begin{aligned}
 T_{13} = & A_{PDF} \times \left(1 + P_{(121)}^i \times P_{(1,0)}\right) \times \left(P_{(61)}^i \times P_{(2,1)} + P_{(62)}^i \times P_{(4,1)} + P_{(63)}^i \times P_{(6,1)}\right) \\
 & \times \cos\left(\frac{\pi}{180} \times (L - P_{(64)}^i)\right) + A_{PDF} \times \left(P_{(116)}^i \times P_{(1,1)} + P_{(117)}^i \times P_{(3,1)} + P_{(118)}^i \times P_{(5,1)}\right) \\
 & \times \cos\left(\frac{2\pi}{365} \times (d - P_{(14)}^i)\right) \times \cos\left(\frac{\pi}{180} \times (L - P_{(119)}^i)\right) + A_{PDF} \\
 & \times \left(P_{(84)}^i \times P_{(1,0)} + P_{(85)}^i \times P_{(3,0)} + P_{(86)}^i \times P_{(5,0)}\right) \times \cos\left(0.000072722 \times (UTC \times 3600 - P_{(76)}^i)\right)
 \end{aligned} \tag{4.179}$$

If $P_{(52)}^i$ is not equal to 0, then

$$\begin{aligned}
 T_{13} = & APT(1) \times \left(1 + P_{(133)}^i \times P_{(1,0)}\right) \times \left(P_{(53)}^i \times P_{(2,1)} + P_{(99)}^i \times P_{(4,1)} + P_{(68)}^i \times P_{(6,1)}\right) \\
 & \times \cos\left(\frac{\pi}{180} \times (L - P_{(98)}^i)\right) + APT(1) \times \left(P_{(134)}^i \times P_{(1,1)} + P_{(135)}^i \times P_{(3,1)} + P_{(136)}^i \times P_{(5,1)}\right) \\
 & \times \cos\left(\frac{2\pi}{365} \times (d - P_{(14)}^i)\right) \times \cos\left(\frac{\pi}{180} \times (L - P_{(137)}^i)\right) + APT(1) \\
 & \times \cos\left(0.000072722 \times (UTU \times 3600 - P_{(59)}^i)\right) \times \left(P_{(56)}^i \times P_{(1,0)} + P_{(57)}^i \times P_{(3,0)} + P_{(58)}^i \times P_{(5,0)}\right)
 \end{aligned} \tag{4.180}$$

4. Mixed distribution

$$N_{mi} = N_{hi}(h_i, m_i) \times D_i(Z, \bar{M}_0) \times \left(\frac{T_{(ZL)}}{T_{(Z)}}\right) \tag{4.181}$$

$$N_{hi}(h_i, m_i) = N_{Li} \times D_i(h_i, m_{di}) \tag{4.182}$$

where $m_{di} = m_i - \bar{M}_0$, and h_i is the height of isothermal layer of each atmospheric component.

$$h_1 = 100, h_2 = 105, h_4 = 105, h_5 = 105, h_6 = 95, h_7 = 105$$

$$h_3 = 105 \times 0.962736 \times \left(1 + 0.140925 \times \sin B \times \cos \left(\frac{2\pi}{365} (d + 8.45398) \right) \right)$$

And d is the number of day in the year.

5. Space environment and chemical correction factor are shown as follows:

$$\ln(C_1^i(Z)) = \ln \left(\frac{R1^i \times N_{h3}(h_3, m_3)}{N_{hi}(h_i, m_i)} \right) \times \left(1 + e^{(Z-Zh1^i)/h1^i} \right)^{-1} \quad (4.183)$$

$$\ln(C_2^i(Z)) = R2^i \times \left(1 + e^{(Z-Zh2^i)/h2^i} \right)^{-1} \quad (4.184)$$

where $R1^i$, $H1^i$, $ZH1^i$, $R2^i$, $H2^i$, and $ZH2^i$ are fitting coefficients. The functional calculation of $G_i(L)$ and $GS(P^i)$ are obtained by using the fitting constant P^i .

4.3 Systematic error and random error of atmospheric density models

The calculation error of atmospheric density is not only connected with the precision of atmospheric density model itself but also closely related to the space environment parameter that can characterize the conditions of space environments. And the main space environment parameters that affect the atmospheric density are solar 10.7 cm wavelength (2800 MHz) radio radiation flux $F_{10.7}$ and geomagnetic index Ap . In the orbital calculation of space objects, if it is the postmission processing that delays more than 2 months, the measured value of $F_{10.7}$ and Ap can be directly invoked. However, in the prediction analysis of future events such as collision warning, space object decay forecast, and TT&C station guiding and tracking forecast, the predicted orbit needs to be used, to calculate the atmospheric density; the forecast value for 2 months of solar radiation flux and geomagnetic index need to be input. The longer the parameter prediction time span is, the larger the forecast error is. Thus the prediction error of solar activity parameters will be introduced to the calculation of atmospheric density error, which will cause the error of orbit calculation.

In this section, atmospheric density obtained from CHAMP on-board accelerometer data inversion is taken as the standard to analyze the atmospheric density precision calculated by MSIS00 model in January and April of the year 2010. Furthermore, the factors causing the systematic error and accidental error of atmospheric density are analyzed. Fig. 4–3 shows the variation of $F_{10.7}$ of January and April in 2010. As shown here, the amplitude of variation for $F_{10.7}$ is more than 20 (changes from 70 to 90). And the radio radiation flux is in the middle level. In April 2010 $F_{10.7}$ is almost less than 80. And the radio radiation flux is at a low level. The variation every 3 hours in January and April of the year 2010 is given in Fig. 4–4. It can be seen that a majority of Ap is less than 10 in January, 2010, and solar activities are calmer. In April 2010 a majority of Ap is less than 20. And since a sudden huge magnetic

storm occurred on April 5, the maximum value of A_p reached 180. Affected by this huge storm, small storms continued the following 2 days. On April 12 a medium storm occurred. Small storms happened on April 14 and 15. And on 23 April the magnetic field perturbation happened. Atmospheric density systematic error and the daily average value of A_p (accidental error) calculated with the MSIS00 model are shown in Tables 4–6 and 4–7, which are based on the inversion with CHAMP on-board accelerometer data in January and April 2010. It can be seen from the two tables that the atmospheric density systematic error calculated by MSIS00 model is more than 20% in January, and lower than 10% in April in most cases; thus the systematic error of MSIS00 model is larger in January than in April. Fig. 4–3 shows that the $F_{10.7}$ is generally larger in January than in April. Fig. 4–4 shows that the average value of A_p is generally lower in January than in April. It can be concluded that of all the space environment parameters input to calculate the atmospheric density with the MSIS00 model, the radio radiation flux $F_{10.7}$ is the main factor that brings about the systematic error. Fig. 4–5 shows the maximum absolute value of the atmospheric density error calculated with the MSIS00 model in January and April 2010. It can be seen that the value is at the

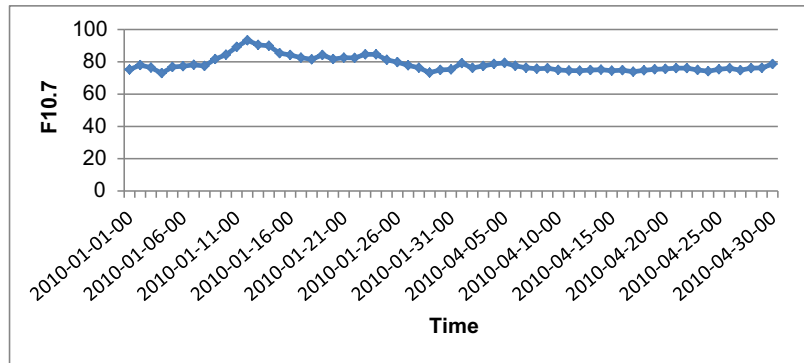


FIGURE 4–3 Variation of $F_{10.7}$ of 2010-01 and 2010-04.

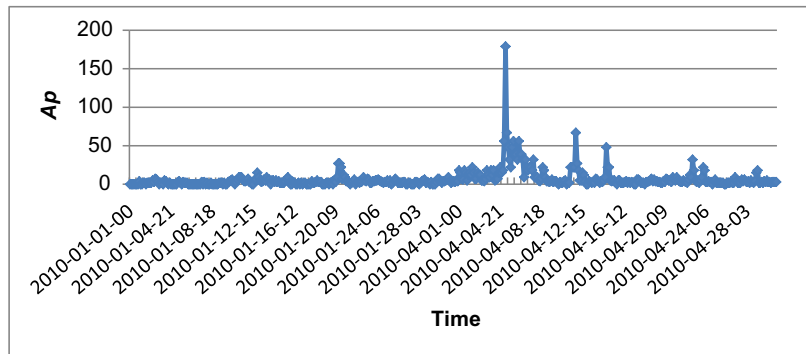


FIGURE 4–4 Variation of A_p every 3 hours of 2010-01 and 2010-04.

magnitude of 10^{-12} in January and mostly the same in April. In April 5–7, 12, 14, 15, and 23, where magnetic storms and perturbations happened, the maximum value reached the magnitude of 10^{-11} , while in April 5, where the huge magnetic storm took place, the accidental error had an obvious jump. It can be seen that A_p is the main factor that affects the atmospheric density calculated with MSIS00 model.

Table 4–6 MSIS00 atmospheric density model precision in January 2010.

Time	Average A_p	Systematic error (%)	Time	Average A_p	Systematic error (%)
2010-01-01	0	51	2010-01-16	1	30
2010-01-02	1	47	2010-01-17	1	28
2010-01-03	4	42	2010-01-18	3	29
2010-01-04	2	29	2010-01-19	1	23
2010-01-05	1	25	2010-01-20	12	25
2010-01-06	1	25	2010-01-21	5	12
2010-01-07	0	25	2010-01-22	3	15
2010-01-08	1	25	2010-01-23	5	18
2010-01-09	1	26	2010-01-24	4	13
2010-01-10	3	29	2010-01-25	3	16
2010-01-11	6	27	2010-01-26	3	34
2010-01-12	4	24	2010-01-27	1	37
2010-01-13	7	32	2010-01-28	3	38
2010-01-14	4	28	2010-01-29	1	42
2010-01-15	4	37	2010-01-30	5	43

Table 4–7 MSIS00 atmospheric density model precision in April 2010.

Time	Average A_p	Systematic error (%)	Time	Average A_p	Systematic error (%)
2010-04-01	12	9	2010-04-16	3	9
2010-04-02	13	9	2010-04-17	3	11
2010-04-03	9	9	2010-04-18	3	12
2010-04-04	13	10	2010-04-19	4	14
2010-04-05	55	20	2010-04-20	4	9
2010-04-06	44	17	2010-04-21	6	8
2010-04-07	22	12	2010-04-22	6	8
2010-04-08	12	9	2010-04-23	10	10
2010-04-09	6	9	2010-04-24	7	9
2010-04-10	3	8	2010-04-25	3	8
2010-04-11	12	11	2010-04-26	2	9
2010-04-12	19	14	2010-04-27	4	10
2010-04-13	3	10	2010-04-28	3	10
2010-04-14	10	10	2010-04-29	6	9
2010-04-15	8	10	2010-04-30	3	9

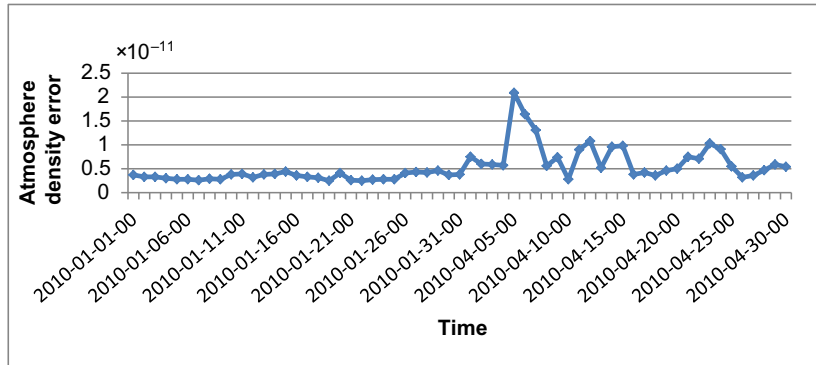


FIGURE 4-5 Maximum absolute value of the atmospheric density error calculated with the MSIS00 model of 2010-01 and 2010-04.

The previous analysis shows that in the period of time in days, the atmospheric density model calculates the average deviation of the difference between the basic presentation system characteristics, the size of the average deviation of the day with the characterization of the Sun 10.7 cm wavelength radio emission parameters 27 days a traffic $F_{10.7}$ small cycles and 13 years is a big cycle, as well as the validity of the model using the data changes. Regarding month as the unit of time, a certain regular changes are presented. Regarding year as the unit of time, the inconspicuous regular changes are presented. Thus regarding day as the unit of time, it is still considered that the major factor causing systematic errors is $F_{10.7}$ in the short term. While the transition of the geomagnetic index A_p is short-term and occasional changes. Regarding hour as the unit of time, many times or even dozens of times of jump may occur. This transition causes multiple errors of the calculated values for the atmospheric density model occur within a few hours. Therefore regarding day as the unit of time, it is considered that the transition of geomagnetic index A_p will cause accidental errors of the atmospheric density.

4.4 Prediction confidence level of space environment parameters influenced atmospheric density

According to the timeliness requirement of space object surveillance capacity and collision warning, the prediction confidence of environmental forecast parameters is analyzed from three different time nodes with respect to 24, 72, and 168 hours.

4.4.1 Analysis of $F_{10.7}$ prediction confidence level

$F_{10.7}$ prediction confidence level is defined as follows. Assume the total number of samples is M , the given error is ε , if the sum of samples which satisfy

$$\left| \frac{F_{10.7p} - F_{10.7r}}{F_{10.7r}} \right| \leq \varepsilon \quad (4.185)$$

is M , then the confidence level is

$$P_F = \frac{M}{N} \quad (4.186)$$

where $F_{10.7p}$ and $F_{10.7r}$ are, respectively, the predicted values of $F_{10.7}$ and the exact values published afterward.

In this section, taking $F_{10.7}$ published on the website (US Celestrak) for the next 3 months as standard, large sample statistical sampling was conducted in three periods of solar activity in nearly 10 years from 2003 to 2013, including low solar activity ($F_{10.7} < 80$), normal solar activity ($80 < F_{10.7} < 120$), and high solar activity ($F_{10.7} > 120$); and the given error ε of $F_{10.7}$ forecast of different time span in different solar activity periods when P_F is greater than 90% is analyzed. According to the statistical analysis, $F_{10.7}$ change in a short term is relatively slow, there is no strong correlation between the prediction error and the value of $F_{10.7}$ itself. That is, in low solar activity, normal solar activity, and high solar activity years, $F_{10.7}$ forecast with the same time span gives similar error, the results are shown in [Table 4–8](#).

4.4.2 Analysis of Ap prediction confidence level

Assume the total number of samples is N , and given error ε , if

$$\left| \frac{Ap_p - Ap_r}{Ap_r} \right| \leq \varepsilon \quad (4.187)$$

The sum of its samples is M , then the confidence level is

$$P_A = \frac{M}{N} \quad (4.188)$$

where Ap_p and Ap_r are, respectively, the predicted values of Ap and the exact values published afterward.

In this section, taking Ap published every day on US Celestrak website for the next 3 months as standard, the statistical sampling of large sample is performed with three periods, which are recent geomagnetic activity quiet period ($Ap < 25$), small geomagnetic disturbance period ($25 < Ap < 50$), and geomagnetic storm period ($Ap > 50$) from 2003 to 2013. When the prediction confidence level Ap is more than 90%, the given errors ε of different days are predicted during the period of different activities. The results are shown in [Table 4–9](#). As is seen from [Table 4–9](#), during the period of quiet geomagnetic activity, Ap prediction error is about 20%; during the period of small geomagnetic disturbance, Ap prediction error is about 60%; and during the period of geomagnetic storm, Ap prediction error is about 85%. The predicting time scale has smaller influence on Ap prediction error.

Table 4–8 $F_{10.7}$ prediction precision.

Prediction time span	1 day	3 days	7 days
ε (%)	2	5	10

Table 4–9 A_p prediction precision.

Geomagnetic activity	Prediction time span			
	Error (%)	1 days	3 days	7 days
Geomagnetic quiet	ε	18.6	19.5	21.9
Magnetic disturbance	ε	58.7	60.1	62.8
Magnetic storm	ε	83.4	85.9	87.1

4.4.3 Impact of environmental parameters on orbit prediction error

According to the analysis in Section 4.4.2, under different solar activities and geomagnetic environment, the impact of the prediction error with input parameters for $F_{10.7}$ and A_p atmospheric density model on space object orbit prediction (using MSIS00 atmospheric density model) at different heights can be simulated and analyzed with the addition of corresponding prediction error to the device.

Table 4–10 gives the impact of a different solar radiation flux $F_{10.7}$ at the height of 400–1000 km on orbit prediction error of space objects of different heights. In order to minimize its impact of geomagnetic index, assume magnetic is in the magnetic quiet period and take $A_p = 7$. In addition, take surface-to-mass ratio as 0.02, which is the approximation of surface-to-mass ratio for most satellites. It can be seen from Table 4–10, for the space of different orbital heights, 1-day orbit prediction error caused by $F_{10.7}$ is less than 1 m, mainly because the $F_{10.7}$ value input in the MSIS00 atmospheric density model is the value of the day before and the 81-day average value. The $F_{10.7}$ of the previous day has a measured value and is not affected by the forecast error. 81 days is three solar rotation period, and the prediction error of $F_{10.7}$ value of some days has little influence on the 81-day average value; therefore $F_{10.7}$ error has little effect on the orbit forecast for 1 day, as the forecast time span increases, $F_{10.7}$ error cumulative effects gradually increase; for objects with an orbital altitude of 500 km and above, the 3-day track forecast errors caused by the error of $F_{10.7}$ is less than 300 m in low solar activity years and normal solar activity years, and less than 600 m in high solar activity years; for objects with an orbital altitude of 600 km and above, the 7-day track forecast errors caused by the error of $F_{10.7}$ is less than 800 m in low solar activity years and normal solar activity years, and less than 2 km in high solar activity years, therefore, for dangerous objects within 7 days of the screening phase, when the solar activity is not high, $F_{10.7}$ errors are less likely to cause missed alarm; for 1000 km high spatial goals, no matter in low,

Table 4–10 Impact of $F_{10.7}$ prediction error on orbit prediction error.

Orbit attitude (km)	$F_{10.7}$	Orbit prediction error (m)											
		1 day				3 days				7 days			
		Position error	<i>R</i> direction error	<i>T</i> direction error	<i>N</i> direction error	Position error	<i>R</i> direction error	<i>T</i> direction error	<i>N</i> direction error	Position error	<i>R</i> direction error	<i>T</i> direction error	<i>N</i> direction error
400	Solar minimum	0.388	0.007	0.388	0.001	490.8	3.10	490.8	0.123	5368.2	24.37	5368.1	1.308
	Normal	1.017	0.016	1.017	0.001	1178.0	7.79	1178.0	0.297	12,822.6	66.40	12,822.5	3.133
	Solar maximum	1.936	0.029	1.936	0.002	2055.6	13.97	2055.6	0.519	22,208.1	131.29	22,207.8	5.436
500	Solar minimum	0.068	0.002	0.068	0.001	89.0	0.53	89.0	0.022	982.9	4.01	982.9	0.230
	Normal	0.221	0.004	0.221	0.001	279.4	1.72	279.4	0.069	3066.9	13.24	3066.9	0.719
	Solar maximum	0.482	0.008	0.482	0.001	582.8	3.66	582.7	0.143	6331.8	29.15	6331.8	1.484
600	Solar minimum	0.015	0.001	0.015	0.001	18.7	0.11	18.7	0.005	206.9	0.82	206.9	0.048
	Normal	0.054	0.002	0.054	0.001	71.9	0.43	71.9	0.018	794.5	3.23	794.5	0.182
	Solar maximum	0.134	0.003	0.134	0.001	176.1	1.07	176.1	0.043	1924.1	8.03	1924.1	0.439
700	Solar minimum	0.005	0.001	0.005	0.001	5.0	0.03	5.0	0.002	54.9	0.22	54.9	0.013
	Normal	0.016	0.001	0.016	0.001	20.5	0.12	20.5	0.006	226.4	0.89	226.4	0.051
	Solar maximum	0.042	0.002	0.042	0.001	56.7	0.34	56.7	0.014	622.0	2.47	622.0	0.138
1000	Solar minimum	0.002	0.001	0.002	0.001	0.6	0.01	0.6	0.001	6.3	0.03	6.3	0.002
	Normal	0.002	0.001	0.002	0.001	1.4	0.01	1.4	0.001	14.9	0.06	14.9	0.004
	Solar maximum	0.003	0.001	0.003	0.001	3.3	0.02	3.3	0.002	36.1	0.14	36.1	0.008

normal, or high solar activity years, the track error $F_{10.7}$ prediction error caused is no more than 50 m, that is, for objects with an orbit height of more than 1000 km, $F_{10.7}$ prediction error has little effect on its track.

Further analysis, when the forecast time span is longer than 24 hours, when the average value of 81-day $F_{10.7}$ has the same error as that of the day before, the average value of 81-day $F_{10.7}$ has more impact than that of the previous day. According to analysis results in Section 4.3, $F_{10.7}$ will lead to systematic errors in atmospheric density, thereby causing system errors in orbit determination and prediction; system error can be solved in the orbit determination process. By prediction correction with the system error solved, the impact on the track forecast accuracy can be greatly weakened.

Table 4–11 gives the impact of A_p under different geomagnetic conditions on different space prediction error of space target orbits at different altitudes from 400 to 1000 km. In order to minimize the $F_{10.7}$ impact, assume that solar activity at a low level and take $F_{10.7} = 80$. Meanwhile, take 0.02 as object surface-to-mass ratio. Table 4–11 shows that, for space objects with the orbital altitude more than 700 km, the impact of A_p prediction error on orbit prediction error is small, even in 7-day prediction in the period of magnetic storms, the position error is about 1.5 km, which is the equal of cataloging and orbit determination. There is little impact on the screening of dangerous objects. Table 4–11 shows that, for the space objects with the orbital altitude less than 700 km, the impact of A_p prediction error on orbit prediction position error increases sharply with the lower orbit altitude. At the same time, when the position error increases rapidly with the prediction time-length increasing, the position error in the period of geomagnetic storm is much larger than it is in the periods of magnetic disturbance and magnetic quiet. Take 7-day prediction for example, in the geomagnetic quiet period, the position prediction errors of space objects are, respectively, about 3, 0.6, and 0.1 km at the orbital altitudes of 400, 500, and 600 km. In the period of magnetic disturbance, the position prediction errors of space objects are, respectively, about 19, 4.3, and 1.1 km at the orbital altitudes of 400, 500, and 600 km. In the period of magnetic disturbance, the position prediction errors of space objects are, respectively, about 63, 15, and 4 km at the orbital altitudes of 400, 500, and 600 km. For the objects at the orbital altitude less than 700 km, whether for the stage of 7-day screening of dangerous objects, the phase of 3-day yellow alert or the phase of 1-day red alert, the impact of A_p error on its orbit cannot be ignored.

From the above analysis, we can find that the impact of space environment parameter error on low-orbit space object prediction is great. The statistical result in Table 4–11 shows that when the confidence level of A_p prediction is greater than 90%, its impact on orbit prediction is great. And under special circumstances, it is greater. Ref. [91] analyzed the impact of different atmospheric density at different geomagnetic conditions on the 24-hour orbit prediction. According to the results of the analysis, when the magnetic disturbance happens, the 24-hour prediction error of YG1A-93 satellite reaches 10 km. When the magnetic activities are more intense or object surface-to-mass ratio increases, there is greater impact of space environmental parameters on orbit prediction.

Table 4-11 Impact of A_p prediction error on orbit prediction error.

Orbit attitude (km)	Geomagnetic conditions	Orbit prediction error (m)											
		1 day				3 days				7 days			
		Position error	<i>R</i> direction error	<i>T</i> direction error	<i>N</i> direction error	Position error	<i>R</i> direction error	<i>T</i> direction error	<i>N</i> direction error	Position error	<i>R</i> direction error	<i>T</i> direction error	<i>N</i> direction error
400	Geomagnetic quiet	63	1.09	63	0.02	571	3.99	571	0.14	3109	14.3	3109	0.77
	Magnetic disturbance	381	6.33	381	0.12	3440	25.2	3440	0.87	18,725	109	18,725	4.63
	Magnetic storm	1277	21.0	1277	0.40	11,553	92.5	11,552	2.92	62,966	570	62,964	15.6
500	Geomagnetic quiet	12	0.19	12	0.00	113	0.74	113	0.03	615	2.66	615	0.15
	Magnetic disturbance	87	1.43	87	0.03	790	5.46	790	0.19	4309	20.2	4309	1.03
	Magnetic storm	301	4.98	301	0.09	2733	19.7	2733	0.67	14,912	82.3	14,912	3.55
600	Geomagnetic quiet	2.6	0.04	2.6	0.00	24	0.15	24	0.01	130	0.55	130	0.03
	Magnetic disturbance	23	0.37	23	0.01	205	1.38	205	0.05	1120	4.93	1120	0.26
	Magnetic storm	84	1.41	84	0.02	755	5.24	755	0.18	4131	19.4	4131	0.96
700	Geomagnetic quiet	0.6	0.01	0.6	0.00	5.6	0.04	5.6	0.00	31	0.13	31	0.01
	Magnetic disturbance	6.3	0.10	6.3	0.00	57	0.38	57	0.01	314	1.35	314	0.07
	Magnetic storm	26	0.45	26	0.01	233	1.59	233	0.05	1275	5.68	1275	0.29
1000	Geomagnetic quiet	0.05	0.00	0.05	0.00	0.5	0.004	0.5	0.00	2.5	0.01	2.5	0.002
	Magnetic disturbance	0.3	0.01	0.3	0.00	2.7	0.02	2.7	0.00	15	0.06	15	0.004
	Magnetic storm	1.3	0.02	1.3	0.00	12	0.08	12	0.00	65	0.28	65	0.01

4.5 Calculation strategy of atmospheric perturbation for spacecraft collision avoidance warning calculation

In order to minimize the impact of space environment on space object orbit, the credibility of spacecraft collision warning results should be enhanced. And the strategy of orbit determination in the calculation of spacecraft collision warning is particularly critical. Orbit determination strategies include the selection of orbit measurement data and dynamic models and solution of orbital parameters; and orbit determination strategy is the key factor affecting orbit prediction accuracy.

4.5.1 Resolving atmospheric damping coefficient and absorbing systematic error

The accuracy of the calculation of atmospheric drag model is the largest source of the error for low-orbit space object determination and prediction. And according to the existing level of awareness, the error of atmospheric drag model is mainly composed by the following four types of error. For space object windward atmospheric drag, the uncertainty of the area causes area–mass ratio error, atmospheric density model error, $F_{10.7}$ prediction error of solar $F_{10.7}$ radiation flux characterization parameter, and A_p prediction error of geomagnetic index characterization parameter. These four errors are not the same in the phases of afterward orbit determination and real-time orbit prediction.

The uncertainty of atmospheric drag area depends on the attitude of space objects. In the measurement of cooperative objects, the object attitude can be obtained precisely through internal telemetry parameters of cooperation objects. In the noncooperative object measurements, the area of object windward atmospheric drag, attitude, and quality are unknown parameters. When the attitude of the space object is stable or it changes with the law of short cycle, the surface–mass ratio error can be regarded as systematic error of day order of magnitude. In [Section 4.3](#) the atmospheric density model error and $F_{10.7}$ characterization parameters' prediction error can be regarded as systematic errors of day order of magnitude. In most times of a year, geomagnetism is calm. In the magnetic quiet period the impact of prediction error for geomagnetic index characterization parameters on atmospheric model is small, and the atmospheric density error is basically systematic errors of day order of magnitude. It can be seen that in the geomagnetic quiet period, the four main sources of error are the dominant terms with systematic errors of day order of magnitude. While in a year of 365 days, the geomagnetic quiet days account for about 90%. In formula (4.1), in the calculation of atmospheric drag f_{DG} , four major atmospheric drag error terms such as c_d are in parallel. When the systematic biases of four major error terms is dominated, they will have strong correlation of c_d . When the orbit is determined, c_d and orbital elements can be regarded as unknown quantity and calculated using the measured data rail arc length of day order of magnitude. And the systematic biases of atmospheric drag model can be absorbed by the calculated c_d . In the orbit prediction, when the orbit extrapolating can be performed with the

Table 4–12 Position error statistics of 24-hour prediction (whether resolving c_d for space object of different types).

Object sequence	Orbital altitude (km)	Position error (resolving c_d)				Position error (fixing c_d)			
		P (m)	R (m)	T (m)	N (m)	P (m)	R (m)	T (m)	N (m)
1	276	1518	24	1518	11	3882	46	3882	11
2	452	278	4	278	1.	465	7	465	1.
3	514	262	2	257	47	317	2	314	47

use of the calculated orbit and c_d , the systematic biases of four major atmospheric drag error terms are effectively weakened.

In order to more directly reflect the absorption of systematic error by calculating atmospheric damping c_d , Table 4–12 gives whether the orbit objects of different orbit types can resolve c_d to predict the statistical results of 24-hour orbit position error (P denotes total position error; R , T , and N are, respectively, its distribution at radial direction, lateral direction, and normal direction). Among them, the three object orbits are nearly circular orbits with an orbital altitude of average height, and the fixed c_d is nonresolving c_d of the orbit determination process. The orbit prediction is performed by using the previous calculated value c_d . It can be seen from Table 4–12, for objects 1, 2, 3, and 4, the 24-hour prediction can be performed by using the fixed c_d .

With respect to using the calculated value c_d to predict orbits, the position error increase approximately 2.5, 1.7, and 1.2 times, mainly in T direction. Moreover, with the increase of prediction length, the error grows intensely. Therefore the accuracy of LEO orbit prediction can be significantly improved with the use of the calculated c_d .

4.5.2 Application of atmospheric damping coefficient and analysis of orbit determination and prediction under normal geomagnetism conditions

How to calculate atmospheric damping coefficient intensively is an engineering practice problem. And the calculation accuracy is related to such factors as orbit measurement accuracy, data arc length, space environment parameters, and atmospheric density model. And different attitudes of the object orbit are given through comparative analysis in Ref. [92].

In this section, first, a certain target is selected at the attitude of 340 km, then we use all-time orbit measurement data of 0.5, 1, 1.5, and 2 days to analyze its orbit position error and the component of the position error for 36-hour prediction in the radial (R), track (T), normal (N) directions. The results are shown in Table 4–13, where, during the process of orbit determination, the object position and speed only can be calculated with the use of 0.5-day data, while the object position, speed, and atmospheric damping c_d can be calculated at the same time by using the data of 1, 1.5, and 2 days. Table 4–13 shows that the shorter the data arc is, the smaller the orbit determination error is. However, the orbit prediction error is the largest using 0.5-day data and the smallest using 1.5-day data. The main reason is

Table 4–13 Prediction precision with different length data for orbit determination.

Length of arc (day)	Position error (m)			36-Hour position error (m)		
	<i>R</i>	<i>T</i>	<i>N</i>	<i>R</i>	<i>T</i>	<i>N</i>
0.5	52.1	21.2	19.6	85.2	– 6345.5	22.7
1	81.0	62.0	51.4	78.3	– 5440.7	16.4
1.5	96.1	189.2	52.6	– 17.6	1323.0	– 3.6
2	– 34.8	– 361.9	– 5.5	– 32.4	4919.6	– 7.4

because the process of orbit determination is the process of approaching measurement data. And the shorter the arc is, the fewer the constraints are. Of course, if orbit determining precision is high, the arc cannot be too short. The concrete value is correlated with object orbit altitude. Precise orbit prediction is not only associated with the orbit determination but also affected by dynamic model precision. For the object at the attitude of 340 km, the atmospheric model error of dynamic models plays a leading role in orbit prediction error determination. Though the precision of orbit determination is high with the use of 0.5-day data, it cannot correctly solve the atmospheric damping coefficient c_d , and the deviation of orbit measurement data is large when using c_d and c_d to predict orbit. Therefore the orbit prediction error spreads quickly. Compared with orbit prediction by using 1.5-day data, the data orbit prediction error increases with the use of the data of 1 and 1.5 days. The main reason is the resolving of c_d is incorrect. And the data arc of the measured orbit data is too short, as well as the redundant information is not enough with the use of the least square method to perform orbit determination, which leads to the inaccurate c_d . Conversely, if the arc of the measured data is too long, given rail track use arc length is, in this process due to the space environment, such as changes in attitude objectives, based on the order of days difference between the system of assumptions no longer exists, c_d big variations, and orbit solving a c_d value, which is considered within the entire length of the arc segment c_d to a fixed value, thus resulting prediction error increases. To solve this problem, it is suggested that a segmentation solution is used to calculate c_d . This method can only improve the orbit accuracy but does not contribute to the improving of orbit prediction error.

In addition to the effect of the arc for orbit determination on the calculated accuracy of c_d , it is closely related to the atmospheric density model itself [93]. In this section, take a satellite with the orbit altitude of 600 km for example, the orbit determination is performed by using the measurement data of 1, 2, 3, 4, 5, 6, and 7 days to predict the orbit accuracy of 1, 7, and 30 days. The statistical results are given in Table 4–14. It can be seen from Table 4–14 that the orbit accuracy prediction is related to factors such as initial orbit accuracy (orbit determination with the use of the data and atmospheric density model) and the accuracy of dynamic models (the atmospheric density model when forecasting). After calculating c_d and using it to predict orbit, the effects of different atmospheric density model for short-term orbit prediction (1-day prediction) on the accuracy is not obvious. And the short-time prediction accuracy is affected by the use of the orbital arc. When adopting different

atmospheric models, the prediction accuracy is almost the same by using the measurement data less than 6 days, while the prediction error increases significantly by using the measurement data of 6 or 7 days. During the process of medium- and long-term orbit prediction (the prediction of 7 or 30 days), MSIS and DTM78 have obvious advantages in comparison with Jacchia77. Moreover, the prediction accuracy with the use of 6- or 7-day orbit measurement data is better than that using short arc data. It is difficult to find a best model under any circumstances that is why various models can be used in the world at present. Under the condition of quasi-real-time orbit prediction, the minimum orbit prediction error is difficult to achieve due to the unstable accuracy of space environment parameters used.

In summary, the calculated precision of atmospheric damping coefficient c_d for low-orbit objects is related to a variety of factors. When the prediction time scale is longer than 3 days,

Table 4–14 The maximum position error with different atmospheric models unit: m.

Model	Prediction time span			
	Orbit determination span (day)	1 day	7 day	30 day
JACCHIA77	1	20.22	2390.56	62,104.38
	2	58.83	1372.30	46,472.36
	3	40.23	1701.86	51,118.44
	4	37.96	1746.11	51,728.31
	5	49.66	1618.22	50,160.31
	6	96.77	1148.28	44,694.76
	7	151.94	662.95	39,339.49
DTM78	1	46.55	1185.94	38,336.89
	2	76.91	412.62	24,665.76
	3	38.85	1038.38	35,010.41
	4	32.81	1151.55	36,623.92
	5	57.52	843.05	32,603.23
	6	118.49	497.68	24,907.58
	7	166.37	685.87	19,876.20
MSIS00	1	30.76	1671.20	42,608.08
	2	69.53	599.36	25,349.68
	3	40.92	1127.30	33,161.04
	4	37.03	1202.36	34,250.88
	5	58.53	937.92	30,769.91
	6	116.75	444.30	23,352.17
	7	172.75	657.77	17,428.52
MSIS90	1	20.20	1735.35	42,372.15
	2	51.94	835.46	27,765.95
	3	39.05	1074.53	31,349.93
	4	40.72	1059.30	31,159.03
	5	68.75	701.50	26,356.44
	6	114.39	456.54	20,478.69
	7	152.49	604.09	16,430.39

Table 4–15 Suitable length of orbit determination arc at different orbit attitudes.

Orbit attitude (km)	Suitable orbit span (day)
300–400	1.5–2
400–500	2–2.5
500–600	2.5–3
600–800	3–4
> 800	> 4

DTM or MSIS atmospheric density models are generally adopted according to the statistical results of the experiences or orbit prediction accuracy. Table 4–15 gives the suggested length of the arc for nearly circular orbit objects at different attitudes (as to the ellipse object, especially noncooperative object, it is difficult to perform orbit measurement and determination). In addition, the effect of space environment on the orbit determination and prediction is large. In Table 4–15 the suggested arc is under the normal conditions for solar activity. When the variation of space environment parameters Ap is large, c_d can be calculated by shortening the time span of orbit determination in order to improve orbit prediction accuracy.

4.5.3 Application of atmospheric damping coefficient and analysis of orbit determination and prediction under abnormal geomagnetism conditions

When the quasi-real-time orbit calculation and prediction of early warning are performed, there is no measurement value Ap . When storms occur, the value c_d is abnormal by detecting and calculating. But when storms occur at the first time, the suitable strategy should be chosen to improve the track forecast accuracy. In the forecast of orbits, the determination and predictive accuracy of orbital period change rate is directly related to the predictive accuracy of orbits. In LEO space object orbits the semimajor axis error is 800 m, corresponding to the error that the variable ratio is 1 second. Because the flight speed of space objects is 8 km/s, the orbit prediction error in the orbital flight direction for N-pass orbit prediction is $8 \times N$ km. In Ref. [91], more details about the impact of geomagnetic index on the variability of low-orbit satellite orbital period and orbital precision are studied. In this section, take the magnetic storm on March 17, 2015, for example, the calculated c_d of different objects is consistent with the change of Ap .

At 00:11 p.m. March 22, 2015, Beijing time, the outbreak of large X-ray flares (X2.2 class) in the solar active region AR2297 reached the orange alert level. Since the approach to the solar disk for AR2297 on March 5, the frequent outbreaks produced a X2.2 class and 10 M-level X-ray flares. On March 15 a full halo coronal mass ejection (CME) took place, which reached the Earth at around 11:00 on March 17. And the solar wind speed increased to about 670 km/s. Meanwhile, southward interplanetary magnetic field component fell to the lowest

around -28 nT. Affected by Earth's magnetic field, the geomagnetic index A_p reached 117. The reproducible coronal hole high-speed stream (CIR) reached the Earth at 21:00 on March 18. Affected by the combined effect of the high-speed fluid in the polar corona Hole and CNE, the solar wind speed went up to 760 km/s. And the sustained geomagnetic disturbance between March 17 and 19 occurred. Thus a total of 12 hours of disturbance means the level of big storms. The level of moderate geomagnetic storms reached after 12 hours of disturbance; the level of small storms reached after 40 hours of disturbance; and the active level reached after 15 hours of disturbance. The geomagnetic storm is the strongest storms since entering the 24th solar cycle (starting from the year of 2008).

Fig. 4–6 gives A_p changes from March 15 to 20, 2015. And Table 4–16 shows the orbital altitude, quality, area, attenuation amount of semimajor axis, and value of c_d of four different objects. Fig. 4–7 shows the changes of c_d for four different objects from March 15 to 20, 2015. In contrast to Figs. 4–6 and 4–7, the values of c_d and A_p have a very good consistency. Namely, the error of A_p can be absorbed through calculating the atmospheric damping coefficient c_d . Table 4–16 shows that the atmospheric damping will cause the attenuation of object orbits. And the magnetic storm will increase the attenuation of object orbits. But the four goals are the maximum for the calculated c_d on March 17. The attenuation is maximized on March 18. The analysis of the reasons shows that A_p is maximized on March 17, while the orbital decay has certain continuity.

Upon the completion of orbit determination, the calculated value of c_d is detected and found to be abnormal. So it needs to modify the orbit determination and prediction strategy to stabilize the orbit forecast accuracy under the condition of geomagnetic anomaly. From a large number of statistics, it can be found that, the severe transition of A_p index generally occurs within a few hours when the geomagnetic happens. Then it quickly returns to the

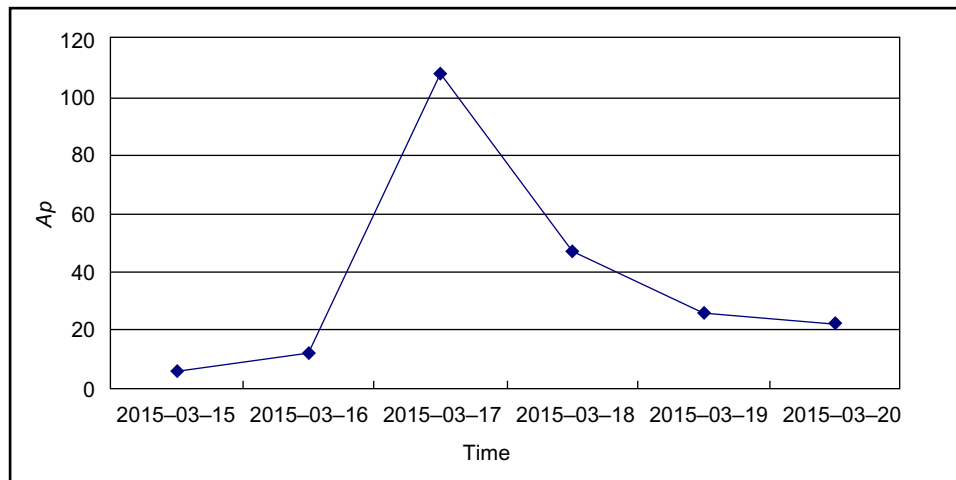
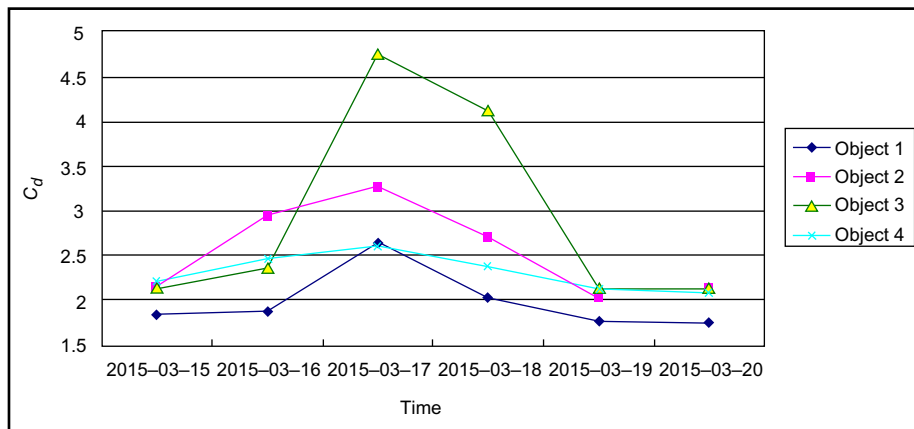


FIGURE 4–6 Variety of A_p from 2015-03-15 to 2015-03-30.

Table 4–16 Statistics of the calculation for orbital decay and atmospheric damping.

Object sequence	H_p (km)	H_a (km)	Quality (kg)	Windward area (m ²)	Date (UTC)	Flat semimajor axis attenuation (m)	Resolving C_d
1	305	334	450.0	3.6	2015-03-15	709.87	1.85
					2015-03-16	690.77	1.87
					2015-03-17	910.63	2.65
					2015-03-18	1044.85	2.04
					2015-03-19	746.43	1.77
					2015-03-20	723.47	1.75
2	276	303	460.0	3.6	2015-03-15	1230.45	2.14
					2015-03-16	1259.79	2.95
					2015-03-17	1601.78	3.26
					2015-03-18	2098.48	2.71
					2015-03-19	1493.38	2.02
					2015-03-20	1528.99	2.14
3	467	482	67.0	0.273	2015-03-15	75.11	2.15
					2015-03-16	68.06	2.36
					2015-03-17	59.69	4.75
					2015-03-18	136.40	4.12
					2015-03-19	73.49	2.13
					2015-03-20	54.70	2.12
4	463	479	3100.0	22.1	2015-03-15	26.38	2.21
					2015-03-16	31.85	2.47
					2015-03-17	32.98	2.60
					2015-03-18	75.82	2.38
					2015-03-19	22.59	2.12
					2015-03-20	45.96	2.08

**FIGURE 4–7** Variety of C_d for four different objects from 2015-03-15 to 2015-03-30.

normal value or associated with several small magnetic disturbance. And its duration is no more than 1–2 days. When geomagnetic storms occurs, the calculation of c_d is abnormal. At the moment, there is only predicted value and no measured value in the input document of geomagnetic index used for orbit determination. The predicted value does not reflect the true state of geomagnetic storms according to the normal level. Therefore the value c_d under this condition will inevitably bring about huge errors for subsequent orbit prediction. In [Table 4–16](#), take object 2 for example, the geomagnetic index reached the extreme values on March 17. The daily calculated value c_d changed from 2.14 to 3.26 on March 15. After the 1-day change, it returned to 2.02 on March 19. The attenuation of semimajor axis for object 2 was from 1.2 to 2 km then lowered to the level of 1.5 km. It caused a 0.7-second error of orbital period change rate. And the impact on orbit prediction is as follows. The prediction of one pass was 5.6 km (0.7×8); the maximum error of the prediction of 1 day (16 passes) was 90 ($16 \times 0.7 \times 8$) km. Therefore when the calculated value c_d is abnormal through orbit determination, the abnormal c_d cannot be used directly to perform the orbit prediction of postcollision warning. At this point the best way to reduce the influence of magnetic storms on the orbit prediction accuracy is to readjust a reasonable Ap value of the artificial construct that day and the next few days to meet the normal variation for the calculated c_d based on the latest published statistical data or Ap statistics experience. With the use of c_d , the orbit prediction of collision warning is performed to reduce the impact of storms on collision warning credibility to some extent.

Through continuous efforts of the International Space Environment scholars, people have a certain understanding of the cause of geomagnetic storms. According to the current level of understanding, geomagnetic storms are associated with the intensity of solar CMEs. The occurrence of solar CMEs after 24–48 hours produces a “shock,” which reaches the Earth and causes geomagnetic storms. Thus through the real-time monitoring of CMEs, the occurrence of geomagnetic storms can be predicted 24 hours in advance. The recognition provides the possibilities to predict geomagnetic storms, especially a direct basis of judging the credibility of 24-hour collision warning. In the calculation and prediction of low-orbit space objects, the error of atmospheric drag perturbation model is the primary item of orbit determination and prediction. Among the four factors causing error in this model, the surface-mass ratio, the atmospheric density model and the $F_{10.7}$ parameter prediction model are all systematic errors measured in days, which can be eliminated by solving c_d . Only Ap prediction error cannot be controlled when a geomagnetic storm occurs. Through monitoring the changes of sunspots, the four error items that affect atmospheric drag perturbation models can be controlled when there are no geomagnetic storms for the next 24 hours. The days of sunspots’ outbreaks in a year are less than 10%, even in solar maximum. This means that, in most cases, no magnetic storms would happen for the next 24 hours. This fully shows that the orbit forecast accuracy is controllable for low-orbit space objects within 24 hours. Based on this, the high confidence level of collision warning can be achieved.

Spacecraft collision warning orbit calculation method

Space debris and spacecraft flight safety first need to get large quantities of space debris orbit information, so the space debris orbit calculation and prediction is an important part of the space debris monitoring. Space object orbit calculation refers primarily to the process that first to obtain orbital measurement data through space surveillance network (SSN); second to solve the value of the orbital parameters using measurement data and orbit determination algorithm; then to store the updated orbit parameters; and finally, to quickly make short-term, medium-term or long-term orbit prediction using the latest orbital parameters and designated prediction model as needed.

Orbital calculations consist of precise orbit calculation and cataloged orbital calculations, wherein the precise orbit calculation principle is to use all resources for measurement and calculation to track, measure, and obtain the most accurate space object orbit as possible. Principles of cataloging orbital calculation are to allocate resources rationally to maintain the maximum amount of space on the destination catalog as possible in the case that system resources are limited. Thus in the pursuit of the ultimate goal accuracy, precision orbital calculation method of the model around the world is basically the same, which uses numerical integration approach with the minimum truncation error, the most sophisticated dynamic model, and the best method of valuation. As a simplified method with low accuracy, cataloged orbital calculations include many ways according to different simplifying ways and objectives.

Commonly used cataloging methods include numerical, analytical, and semianalytical methods. The space object orbital elements currently released by the US SSN mainly use the analytical method based on SGP4/SDP4 orbit prediction model. Meanwhile, the data used for space safety analysis and collision warning are input into JSpOC orbit extrapolation calculation model to perform the “special perturbation” calculation, here “special perturbation” is the numerical cataloging algorithm. Every day the United States performs space object orbit determination for several times and orbit determination information for each space object is updated in JSpOC database (high-accuracy catalog). Russia adopts a semianalytical method, which includes the main effect of $J_{mn}(m, n \leq 5)$. As for the high-orbit object, the solar radiation is considered, and a more complex model of the sun and moon perturbation is also used. Purple Mountain Observatory also set up a semianalytical method based on the quasi-mean element method, which contains a more complete mechanical model that transforms the satellite movement calculation into mean element equations of motion and expression of the short-period perturbations.

5.1 Precise orbital calculation method

5.1.1 Orbital parameters optimal estimation method

Orbital parameter estimation is in fact to obtain the best estimation of the orbital parameters under the premise of obtaining a series of observations. The best estimation can minimize the difference between the theoretical value calculated from the observed data and measured values. The most commonly used orbital parameter estimation method is based on the method of least squares orbit improvements, which are applicable to any dynamic models. Kalman filtering, batch least squares, least squares estimation with a priori and other common orbit determination methods are evolved on the basis of the traditional method of least squares according to different requirements such as timeliness and accuracy.

The dynamic model corresponding to artificial space object motion:

$$\begin{cases} \dot{\mathbf{X}} = F(\mathbf{X}, t) \\ \mathbf{X}(t_0) = \mathbf{X}_0 \end{cases} \quad (5.1)$$

where \mathbf{X} is the state quantity to be improved. As for different orbit determination, it has a different meaning. It can be Kepler element of the object σ . It also can be position and velocity vectors and other dynamic parameter vectors \mathbf{P}^* . Take near-earth-orbit object, for example, \mathbf{P}^* is generally ballistic coefficient b^* . When the state quantities are considered as position and velocity vectors:

$$\mathbf{X} = [\mathbf{r}, \dot{\mathbf{r}}, b^*]^T \quad (5.2)$$

Eq. (5.1) is an n -dimensional first-order nonlinear equation. The form of the general solution can be written as:

$$\mathbf{X}(t) = \mathbf{X}(\mathbf{X}_0, t) \quad (5.3)$$

The observation quantity of space object monitoring equipment is a nonlinear function of the state quantity of the object, represented by the following formula:

$$\begin{aligned} Y_i &= G(\mathbf{X}_i, t_i) + \varepsilon_i \\ &= \tilde{G}(\mathbf{X}_0, t_0, t_i) + \varepsilon_i, \quad i = 1, \dots, m \end{aligned} \quad (5.4)$$

where Y_i are the actual observation quantities (observations for short, referred to as O), when t_i . $\tilde{G}(\mathbf{X}_0, t_0, t_i)$ is the calculation observation quantities (calculations for short, referred to as C), when the dynamic model is used to calculate t_i based on the initial state \mathbf{X}_0 . ε_i is random noise.

In fact due to the inaccuracy of the initial state \mathbf{X}_0 the calculations and observations do not match. The difference between the observations and calculations is called "O-C", or observation residuals. Orbit improvement is to estimate the optimal value $\hat{\mathbf{X}}_0$ of the initial

state quantity \mathbf{X}_0 through a series of observations, so that the weighted mean square sum of observation residuals is minimum.

Define the vectors:

$$\mathbf{Y} = \begin{bmatrix} Y_1 \\ \vdots \\ Y_m \end{bmatrix}, \quad \tilde{\mathbf{G}}(\mathbf{X}_0, t_0, t) = \begin{bmatrix} \tilde{G}_1(\mathbf{X}_0, t_0, t_1) \\ \vdots \\ \tilde{G}_m(\mathbf{X}_0, t_0, t_m) \end{bmatrix},$$

$$\boldsymbol{\varepsilon} = \begin{bmatrix} \varepsilon_1 \\ \vdots \\ \varepsilon_m \end{bmatrix}, \quad \mathbf{W} = \begin{bmatrix} W_1 & & 0 \\ & \ddots & \\ 0 & & W_m \end{bmatrix} \quad (5.5)$$

where \mathbf{W} is the weight matrix of $m \times m$ order, W_i is the weight coefficient of observations every time. It is supposed that the accuracy of observations is unequal every time, so

$$\mathbf{Y} = \tilde{\mathbf{G}}(\mathbf{X}_0, t_0, t) + \boldsymbol{\varepsilon} \quad (5.6)$$

As mentioned earlier, orbit improvement is to minimize the weighted mean square sum of observation residuals, so

$$Q = \boldsymbol{\varepsilon}^T \boldsymbol{\varepsilon} = [\mathbf{Y} - \tilde{\mathbf{G}}(\mathbf{X}_0, t_0, t)]^T \mathbf{W} [\mathbf{Y} - \tilde{\mathbf{G}}(\mathbf{X}_0, t_0, t)] \quad (5.7)$$

is minimum.

To minimize Q , supposed $\hat{\mathbf{X}}_0$ is the optimal estimation value of \mathbf{X}_0 , so

$$\left. \frac{\partial Q}{\partial \mathbf{X}_0} \right|_{\mathbf{x}_0 = \hat{\mathbf{x}}_0} = -2[\mathbf{Y} - \tilde{\mathbf{G}}(\hat{\mathbf{X}}_0, t_0, t)]^T \mathbf{W} \left. \frac{\partial \tilde{\mathbf{G}}}{\partial \mathbf{X}_0} \right|_{\mathbf{x}_0 = \hat{\mathbf{x}}_0} = 0 \quad (5.8)$$

The previous formula includes n nonlinear functions with n unknown variants. Only an iterative method can be used, so the process of orbit determination needs to be linearized.

It is assumed that the initial value of the state vector \mathbf{X}_0^* is relatively close to the optimal estimation $\hat{\mathbf{X}}_0$, $\tilde{\mathbf{G}}(\mathbf{X}_0, t_0, t)$ in formula (5.4) is expanded near \mathbf{X}_0^* , then

$$Y = \tilde{\mathbf{G}}(\hat{\mathbf{X}}_0^*, t_0, t) + \left. \frac{\partial \tilde{\mathbf{G}}}{\partial \mathbf{X}_0} \right|_{\mathbf{x}_0 = \mathbf{x}_0^*} (\hat{\mathbf{X}}_0 - \mathbf{X}_0^*) + \boldsymbol{\varepsilon} \quad (5.9)$$

to make

$$\mathbf{y} = \mathbf{Y} - \tilde{\mathbf{G}}(\mathbf{X}_0^*, t_0, t) \quad (5.10)$$

$$\mathbf{x} = \hat{\mathbf{X}}_0 - \mathbf{X}_0^* \quad (5.11)$$

$$\mathbf{B} = \left. \frac{\partial \tilde{\mathbf{G}}}{\partial \mathbf{X}_0} \right|_{\mathbf{x}_0 = \mathbf{x}_0^*} \quad (5.12)$$

Then formula (5.10) can form a linear system:

$$\mathbf{y} = \mathbf{B}_x + \epsilon \quad (5.13)$$

Formula (5.13) is the observation error equation of orbit improvement, also known as conditional equation.

Based on formula (5.13), conditions to satisfy the optimal estimation are:

$$-2(\mathbf{y} - \mathbf{B}_x)^T \mathbf{W} \mathbf{B} = 0 \quad (5.14)$$

This solution is:

$$\mathbf{x} = (\mathbf{B}^T \mathbf{W} \mathbf{B})^{-1} \mathbf{B}^T \mathbf{W} \mathbf{y} \quad (5.15)$$

The formula above is called the normal equation, where, $\mathbf{B}^T \mathbf{W} \mathbf{B}$ is called method matrix. This is the weighted least squares estimation. The whole process is actually carried out iteratively. Inverse $(\mathbf{B}^T \mathbf{W} \mathbf{B})^{-1}$ of the method matrix output after convergence is the covariance matrix of the estimated parameter. Its diagonal element is the variance of the estimated parameter error.

5.1.2 Numerical integration

There are a lot of methods to solve problems of numerical integration, which consist of the single-step and multistep methods according to calculation relativity. The single-step method needs only the value of one dependent variable function to obtain the value of the independent variables corresponding to other dependent variables. The multistep process will need function values of multiple independent variables to obtain the solution. In terms of acceleration calculating times to obtain the same accuracy the multistep method is more effective than the single-step method. Usually, the single-step method is used in the initial stage of numerical integration and provides function values of the beginning self-variants for the multistep method.

The multistep method consist of I and II types according to orders. The I type method is a first-order integral; the II type method indicates direct resolution to second-order differential equation. The two methods also consist of the fixed order and step integration and the variable order and step integration. Different from the method of the fixed order and step integration, the method of variable order and step integration estimates the local truncation error on each node and meets the error limits by changing the order and step size to control the integration error. This means a lot more computation.

This section gives a widely used Runge–Kutta single-step integration method, RK7(8), which uses nested technique to estimate local truncation error in order to control integration step. This method can be directly used to solve a motion equation, or as a starter for other multistep methods. This is a Runge–Kutta method presented by Fehlberg to solve the first-

order equation $y^{(1)} = f(t, y)$. This method gives two groups of formula of 7 and 8 orders simultaneously. The resulting difference between the two groups of formula is used to estimate the local truncation error in order to achieve the purpose of control step. So, this is a method to nest the 7th and 8th order formula.

The 7th-order formula is:

$$\hat{y}_{n+1} = y_n + h \sum_{k=0}^{10} \hat{c}_k f_k \quad (5.16)$$

The 8th-order formula is:

$$y_{n+1} = y_n + h \sum_{k=0}^{12} c_k f_k \quad (5.17)$$

where $f_0 = f(t_n, y_n)$

$$f_k = f\left(t_n + \alpha_k h, y_n + h \sum_{j=0}^{k-1} \beta_{k,j} f_j\right) \quad (k = 1, 2, \dots, 12) \quad (5.18)$$

The constant $\hat{c}_k, c_k, \alpha_k, \beta_{k,j}$ is available in the relevant bibliography; the book will not repeat them.

y_{n+1} is the obtained resolution of the next step. The estimation formula of local truncation error is:

$$T_{n+1} = \hat{y}_{n+1} - y_{n+1} \quad (5.19)$$

Gain by calculation:

$$T_{n+1} = \frac{41}{840}(f_0 + f_{10} - f_{11} - f_{12}) \quad (5.20)$$

If the required absolute error limit is ε_a the relative error limit is ε_r , so that:

$$T_r = \max_j \frac{|T_{n+1}(j)|}{|y_{n+1}(j)| + |y_n(j)| + (\varepsilon_a/\varepsilon_r)} \quad (5.21)$$

Then there is the measurement value that decides whether integration of this step is to be rejected or be accepted:

$$\eta_r = \frac{T_r}{(7.5\varepsilon_r)} \quad (5.22)$$

If $\eta_r > 1$, integration is rejected, otherwise integration is successful.

The step stretching factor is calculated as follows:

$$\text{When } \eta_r > 1; \quad d = \begin{cases} 0.025, & \eta_r \geq \frac{0.9}{0.025} \\ \frac{0.9}{(10\eta_r)^{1/8}}, & \eta_r < \frac{0.9}{0.025} \end{cases}$$

$$\text{When } \eta_r \leq 1; \quad d = \begin{cases} 20, & \eta_r \leq \left(\frac{0.9}{20}\right)^8 \\ \frac{0.9}{\eta_r^{1/8}}, & \eta_r > \left(\frac{0.9}{20}\right)^8 \end{cases}$$

If the next step is h^* , then

$$h^* = dh.$$

5.1.3 Numerical calculation of precise orbit

5.1.3.1 The elements system

The numerical calculation of precise orbit method applies mechanical model for numerical integration during orbit extrapolation. Since the input parameters of the mechanical model are instantaneous orbital parameters, the used radical system is close radical. According to the parameters, elements can be further divided into the position and velocity of the satellite, the elements of Kepler, the first-category elements without singularities, and the second-category elements without singularities [5]. Currently the position and velocity are commonly used. During orbit extrapolation in Section 5.1.1 with position and velocity vector required to be solved: $\mathbf{X} = [\mathbf{r}, \dot{\mathbf{r}}, \mathbf{P}^*]^T$, the appropriate mechanical model is used for numerical integration. In the case that initial orbital parameters are identical to the perturbation parameters, the more sophisticated the used mechanical model is, the higher the extrapolation accuracy. In accordance with the degree of precision of the selected mechanical model the numerical orbit determination can be divided into precise orbit determination and simple orbit determination.

5.1.3.2 Method matrix

According to Section 5.1.1, the method matrix $\mathbf{B}^T \mathbf{W} \mathbf{B}$ needs to be calculated during the orbital parameters optimization. Matrix \mathbf{B} can be calculated by multiplication of a number of matrices. Then $\mathbf{B} = (\partial Y / \partial(\mathbf{r}, \dot{\mathbf{r}})) (\partial(\mathbf{r}, \dot{\mathbf{r}}) / \partial \mathbf{X})$. Specific calculation includes the following two steps:

1. Calculating the partial derivative $\partial Y / \partial(\mathbf{r}, \dot{\mathbf{r}})$ related to the position and velocity of observations:

The partial derivative of velocity and position relative to the range:

$$\frac{\partial \rho}{\partial \mathbf{r}} = \frac{1}{\rho} (\mathbf{r} - \mathbf{R})^T \quad \frac{\partial \rho}{\partial \dot{\mathbf{r}}} = 0 \quad (5.23)$$

where \mathbf{R} is radial direction vector of the station.

The partial derivative of velocity and position relative to the range rate:

$$\frac{\partial \dot{\rho}}{\partial \dot{\mathbf{r}}} = \frac{1}{\rho} \left[(\dot{\mathbf{r}} - \dot{\mathbf{R}}) - \frac{\dot{\rho}}{\rho} (\mathbf{r} - \mathbf{R}) \right]^T \quad \frac{\partial \rho}{\partial \mathbf{r}} = \frac{1}{\rho} (\mathbf{r} - \mathbf{R})^T \quad (5.24)$$

The partial derivative of velocity and position relative to the azimuth:

$$\rho \cos E \frac{\partial A}{\partial \mathbf{r}} = (a_1, a_2, a_3)^T \quad \frac{\partial A}{\partial \dot{\mathbf{r}}} = 0 \quad (5.25)$$

where

$$\begin{aligned} a_1 &= -\sin S \cos A + \cos S \sin B \sin A \\ a_2 &= \cos S \cos A + \sin S \sin B \sin A \\ a_3 &= -\cos B \sin A \end{aligned}$$

The partial derivative of velocity and position relative to the angle of pitch:

$$\rho \frac{\partial E}{\partial \mathbf{r}} = (e_1, e_2, e_3)^T \quad \frac{\partial E}{\partial \dot{\mathbf{r}}} = 0 \quad (5.26)$$

where

$$\begin{aligned} e_1 &= \cos S \cos B \cos E + \sin S \sin E \sin A + \cos S \sin B \sin E \cos A \\ e_2 &= \sin S \cos B \cos E - \cos S \sin E \sin A + \sin S \sin B \sin E \cos A \\ e_3 &= \sin B \cos E - \cos B \sin E \cos A \end{aligned}$$

B and S appearing in the above formulas are the latitude of stations and local sidereal time, respectively.

2. The variational equation is used to calculate the state transition matrix $\Phi(t)$.

In orbit improvement process the partial derivative of the current state relative to the initial state vector needs to be used. As for numerical methods, while equations of motion are integrated, the variational equation is integrated to obtain the partial derivative that constitutes the state transition matrix. On both sides of Eq. (5.1), the partial derivative of the argument vector is sought to obtain the second-order linear ordinary differential equations:

$$\dot{\mathbf{Y}} = A(t)\mathbf{Y} + B(t)\dot{\mathbf{Y}} + C(t) \quad (5.27)$$

This equation is called variational equation, where $A(t)$, $B(t)$, and $C(t)$ are the function of t , \mathbf{r} , $\dot{\mathbf{r}}$ and \mathbf{P}^* , obtained simultaneously while calculating perturbation acceleration. Solutions of variational equations became the state transition matrix.

$$\Phi(t) = \begin{bmatrix} \frac{\partial \vec{r}}{\partial P} \\ \frac{\partial \dot{\vec{r}}}{\partial P} \end{bmatrix}_{6 \times l}$$

Integration of equations of motion and variation can be performed simultaneously, for example, Y_1 , Y_2 , and Y_3 are used to express three row vectors of \mathbf{Y} , respectively, namely

$$\mathbf{Y} = (\vec{r}^T, Y_1, Y_2, Y_3, \dot{\vec{r}}^T, \dot{Y}_1, \dot{Y}_2, \dot{Y}_3)^T$$

So the two equations are combined into the following initial value problem of second-order ordinary differential equations

$$y^{(2)} = f(t, y, y^{(1)}) \quad (5.28)$$

$$t = t_0, \quad y_0 = y(t_0), \quad y_0^{(1)} = y^{(1)}(t_0) \quad (5.29)$$

To solve the problem is to obtain $y(t)$, $y^{(1)}(t)$ corresponding to t based on t_0 , $y(t_0)$, $y^{(1)}(t_0)$ according to Eq. (5.28).

5.1.3.3 Dynamical modeling strategy

A key factor affecting orbit determination precision is the theoretical observations precision. The accuracy of the theoretical observation depends on the precision of the mechanical model. Mechanical models used for precise orbit determination include 70×70 order Earth gravity model, a three-dimensional model of the atmosphere, sunlight pressure model (cone model of earth shadow), the gravitational model of the third body such as the Sun and Moon, the model of sea and solid tide and general relativity effects model. Table 5–1 describes the magnitude of each perturbation of the LEO spacecraft:

Table 5–1 Magnitude comparison of each main perturbation.

Perturbation	Magnitude	Remarks
Earth gravity field J_2 items	10^{-3}	—
Earth gravity field J_3, J_4 items	10^{-6}	—
Atmospheric drag	$10^{-6}10^{-4}$	Area-to-mass ratio 0.002 m ² /kg Area-to-mass ratio 0.2 m ² /kg (the height is about 200 km)
Solar gravity	0.6×10^{-7}	—
Moon's gravity	1.2×10^{-7}	—
Sunlight pressure	0.6×10^{-8}	Equivalent area-to-mass ratio 0.05 Solar radiation pressure reflection coefficient 0.5
Perturbation of Earth and ocean tide	10^{-8}	—
Deformation perturbation owing to Earth rotation	$10^{-11} - 10^{-10}$	—
Effects of general relativity	$10^{-11} - 10^{-9}$	—

5.2 Cataloged orbit calculation method

5.2.1 Simple numerical method (simplified dynamic model)

Orbital parameters optimal estimation method used by simple numerical orbit determination is the same as the method used by precise orbit determination. The dynamic model used by the two is different. Based on the current level of research and engineering, the orbit perturbation model calculations can be very easily considered as the magnitude 10^{-9} by general numerical integration method. It is difficult for the analytical calculation to consider the perturbation magnitude of 10^{-6} . The simple numerical method simplifies the dynamic models at the expense of the orbit accuracy in order to improve computational efficiency. Mechanical models used for LEO spacecraft include 16×16 order Earth gravity field model; two-dimensional atmospheric model (such as Harris–Priester), and Sun/moon gravity model (for high-orbit object, there are also sunlight pressure models). Comparison of the models used by the simple numerical method and the precision orbital calculation method respectively is shown in Table 5–2. The parameter estimation and orbit extrapolation used by the simple numerical method and the precise orbital calculation method are basically the same.

5.2.2 Cataloging orbit calculation with two-line element

5.2.2.1 The US cataloging system

Since 1957, North American Air Defense Command (NORAD) has developed an analytical model of orbit prediction, which is combined with observations of the US Global Observation Network (SSN) to generate the world’s largest space object catalog database and published it in the form of TLE (two-line element). Since 1980, the US Department of Defense (DOD) announced a mathematical model of SGP4/SDP4 model and the

Table 5–2 Comparison of perturbation models used by the simple numerical method and the precise orbital calculation method.

Perturbation	Simple numerical method	Precise orbital calculation method
Earth’s gravitational field	16×16 order	70×70 order
Atmospheric drag	Two-dimensional atmospheric model	Three-dimensional atmospheric model
	Harris–Priester; index model	(MSISE-90, etc.)
Solar gravity	Considered	Considered
Moon’s gravity	Considered	Considered
Sunlight pressure	Considered	Considered
Perturbation of Earth and ocean tide	Not considered	Considered
Deformation perturbation owing to Earth rotation	Not considered	Considered
Effects of general relativity	Not considered	Considered

corresponding FORTRAN code, the program code is constantly amended in actual use, and there have been many versions. In 2006 Vallado et al. summarized all versions and offers the latest program code which is fully compatible with the US DOD.

The SGP model, established by Hilton and Kuhlman in 1966, is mainly used for near Earth objects. The gravitational field model mainly used the research work of Kozai Yoshihide (1959), which considers the effect of atmosphere on flat orbit as effect of relative time linear varieties.

Developed in 1970, SGP4 is mainly used for near Earth objects. It is the simplified model of the analytical theory presented by Ryan and Cranford in 1969. SGP4 uses gravitational field model proposed by Brouwer in 1959. The atmospheric model used the power density function. The difference between the SGP and SGP4 is the different presentation of the average velocity and resistance.

SDP4 is an extension of SGP4, which is used for deep-space orbit calculation. Due to great gravitational effects of the moon and sun on half-day and 1-day period orbits, SDP4 considers the influence of the moon and sun gravitation as well as Earth on certain sectoral and tesseral harmonics. It mainly includes gravity potential J_2-J_4 and recovers the short-period portion of the first-order J_2 of $O(e_0)$. Added to half-day and 1-day numerical integration resonance term, it can approximately indicate the effects of the sun and moon particle (P2).

The SGP8 model is used for near-Earth satellites and is obtained by the simplification of an extensive analytical theory of Hoots that uses the same gravitational and atmospheric models as Lane and Cranford did but integrates the differential equations in a much different manner.

Finally, the SDP8 model is an extension of SGP8 to be used for deep-space satellites. The deep-space effects are modeled in SDP8 with the same equations used in SDP4.

5.2.2.2 *The US two-line elements*

The US space object surveillance network generates TLEs based on SGP4/SDP4 model and issues them to the public. [Table 5–3](#) gives definition of US TLEs.

In the following take Dongfanghong-1, for example, one set of TLEs are listed:

```
0 DFH-1
1 04382U 70034A 15330.85908916 -.00000006 00000-0 12806-4 0 9997
204 382 68.4228 300.9240 185.4409 173.4391 13.06972537141074 1055939
```

As can be seen from the above two lines of elements, TLEs usually include three lines of elements. The serial number of the first line is zero, indicating that the object is Dongfanghong-1, named DFH-1 in the US cataloging database. The serial number of the second line is one, which shows that the epoch corresponding to the TLEs is the 330th day of 2015. Unit of .85908916 is day. It is the time from the current epoch to zero of the 330th day in 2015. The serial number of the third line is two, which shows the orbital inclination, RAAN, eccentricity, perigee anomaly, and mean anomaly. It should be noted the directly readout orbital element is the mean element under the TEME coordinate system. The SGP4/

Table 5–3 Definition of the US TLEs.

No.	Column	Meaning	Instructions and notes
0.1	01	Object name	Character string containing up to 24 characters
1.1	01	Line number	The value is 1
1.2	03–07	Satellite catalog number	Expressed with five decimal numbers, up to 99,999 objects can be cataloged
1.3	08	Satellite security category identification	U represents a nonsecret object, S represents the secret one (TLEs of the secret object are private)
1.4	10–11	International designator of satellite	Year of launch is expressed with two decimal numbers, for example, 03 represents 2003
1.5	12–14		Serial number of the launch is expressed with three decimal numbers, for example, 111 represents the 111th launch of the same year
1.6	15–17		The sequence of object generated in the launch of this time is expressed with characters, for example, C represents the third object generated in this launch
1.7	19–20	Epoch date	Year is expressed with two decimal numbers, for example, 03 represents 2003
1.8	21–32		The number of days (day of the year), eight significant digits are saved after the decimal point (accurate to 1 ms)
1.9	34–43	The first-order variation rate of mean motion(1/2)	The unit is pass/day ²
1.10	45–52	The second-order variation rate of mean motion(1/6)	The unit is pass/day ³ , the first 6 bits are the fractional part, and last 2 bits are exponential parts. For instance, $-12,345 - 6$ represents -0.12345×10^{-6}
1.11	54–61	The ballistic coefficient denoting atmospheric drag is $B^*(=0.5c_d S/M\rho_0)$	The unit is the reciprocal of the Earth's equatorial radius, with the same representation as 1.10
1.12	63	Orbit determination model type	Internal use, now set to 0, with SGP4 and SDP4
1.13	65–68	Element groups	
1.14	69	Check digit	
2.1	01	Line number	The value is 2
2.2	03–07	Satellite catalog number	The same as 1.2
2.3	09–16	Orbital inclination	Unit: degrees, four digits after the decimal point
2.4	18–25	Orbit RAAN	Unit: degrees, four digits after the decimal point
2.5	27–33	Orbital eccentricity	Decimal (1234567 represents 0.1234567), seven significant digits
2.6	35–42	Perigee argument	Unit: degrees, four digits after the decimal point
2.7	44–51	Mean anomaly	Unit: degrees, four digits after the decimal point
2.8	53–63	Mean velocity	Unit: pass/day
2.9	64–68	Passes relative to the epoch	Unit: pass, the first pass indicates that the satellite passes through RAAN for the first time
2.10	69	Check digit	

RAAN, Right ascension of the ascending node; TLE, two-line elements.

SDP4 models need to be used for converting it into the instantaneous position and speed under TEME coordinate system. The United States also issued various algorithms of SGP4/SDP4 model via the Internet. If the position and speed of other coordinate systems (such as J2000.0) need to be obtained, refer to Chapter 2, Basics of orbital calculation for spacecraft collision avoidance.

5.2.2.3 Orbital principle of SGP4 model

The orbit element input by SGP4 is TLE. Orbital eccentricity, orbital inclination, RAAN, perigee anomaly, and mean anomaly given in TLE are the initial average elements, but the initial average element of the semimajor axis is not given directly in TLE. Before the SGP4 model is used for orbit prediction, we first need to perform a series of calculation of TLE element characterizing angular movement of mean motion in order to obtain the initial average elements of orbit semimajor axis [94]:

$$a_1 = n_0^{-2/3} \quad (5.30)$$

$$\delta_1 = \frac{3 J_2 (3\theta^2 - 1)}{4 a_1^2 \beta^3} \quad (5.31)$$

$$a_0 = a_1 \left(1 - \frac{1}{3} \delta_1 - \delta_1^2 - \frac{134}{81} \delta_1^3 \right) \quad (5.32)$$

$$\delta_0 = \frac{3 J_2 (3\theta^2 - 1)}{4 a_0^2 \beta^3} \quad (5.33)$$

$$n_0'' = \frac{n_0}{1 + \delta_0} \quad (5.34)$$

$$a_0'' = \frac{a_0}{1 - \delta_0} \quad (5.35)$$

where $\theta = \cos i_0''$, $\beta = (1 - e_0''^2)^{1/2}$. Variables of the above formulas have been normalized. In other words the unit of length is the Earth's equatorial reference ellipsoid average radius a_E , the mass unit is the mass of Earth M_E , time unit is $(a_E^3/GM_E)^{1/2}$, and G is Newtonian gravitational constant.

After obtaining the value of a_0'' the next step is to calculate parameters involved in the solution of the atmospheric perturbation. First we need to determine the s value of the atmospheric density model expressions based on perigee altitude. When the orbit altitude at perigee h_p is more than 156 km, $s = 1.01222928$; when $98 \text{ km} < h_p < 156 \text{ km}$, $s^* = a_0''(1 - e_0'') - s + 1$ is used to replace s ; when $h_p \leq 98 \text{ km}$, $s^* = 20/6378.135 + 1$ is used to replace s . Once the value of s is obtained, other factors in the solution of the atmospheric perturbation need to be calculated, such as the value of $C_1, C_3, C_4, C_5, D_2, D_3, D_4, \xi, \eta$.

Next the satellite position and velocity vector at the time of t , which is obtained from propagation of the initial mean element at the time of t_0 , is to be calculated.

1. Based on the major zonal harmonic terms, the perturbation in long term is calculated from the initial mean element, the mean element $l''_{DF}, g''_{DF}, h''_{DF}$ of angle variable at the time of t is obtained (atmosphere drag effects is not considered). Angle variables are defined as follows:

$$\begin{cases} l = M \\ g = \omega \\ h = \Omega \end{cases} \quad (5.36)$$

$$l'' = l''_0 + \left[1 + \frac{3J_2(-1 + 3\cos i'')}{4L''G''^3} + \frac{3J_2^2(13 - 78\cos^2 i'' + 137\cos^4 i'')}{64L''G''^7} \right] \times n''_0(t - t_0) \quad (5.37)$$

$$g'' = g''_0 + \left[\frac{3J_2(1 - 5\cos^2 i'')}{4G''^4} + \frac{3J_2^2(7 - 114\cos^2 i'' + 395\cos^4 i'')}{64G''^8} - \frac{15J_4(3 - 36\cos^2 i'' + 49\cos^4 i'')}{32G''^8} \right] \times n''_0(t - t_0) \quad (5.38)$$

$$h'' = h''_0 + \left[\frac{3J_2\cos i''}{2G''^4} + \frac{3J_2^2(4 - 19\cos^2 i'')}{8G''^8} - \frac{15J_4\cos i''(3 - 7\cos^2 i'')}{16G''^8} \right] \times n''_0(t - t_0) \quad (5.39)$$

2. The analysis solution of atmosphere drag perturbation is calculated to obtain the mean element of orbital variables at the time of t with the atmospheric drag perturbation considered:

$$a'' = a''_0[1 - C_1(t - t_0) - D_2(t - t_0)^2 - D_3(t - t_0)^3 - D_4(t - t_0)^4]^2 \quad (5.40)$$

$$\begin{cases} l'' = l''_{DF} + n''_0 \left[\frac{3}{2}C_1(t - t_0)^2 + (D_2 + 2C_1^2)(t - t_0)^3 \right. \\ \quad \left. + \frac{1}{4}(3D_3 + 12C_1D_2 + 10C_1^2)(t - t_0)^4 \right. \\ \quad \left. + \frac{1}{5}(3D_4 + 12C_1D_3 + 6D_2^2 + 30C_1^2D_2 + 15C_1^4)(t - t_0)^5 \right] \\ \quad + \delta l_D \\ \delta l_D = -\frac{2}{3}(q_0 - s)^T B * \xi^4 \frac{a}{e''_0 \eta} [(1 + \eta \cos l''_{DF})^3 - (1 - \eta \cos l''_0)^3] \\ \quad + B * C_3 \cos g''_0(t - t_0) \end{cases} \quad (5.41)$$

$$g'' = g''_{DF} - \delta l_D \quad (5.42)$$

$$h'' = h''_{DF} - \frac{21 n''_0 J_2 \cos i''}{4 a''_0{}^2 \beta_0^2} C_1(t - t_0)^2 \quad (5.43)$$

$$e'' = e''_0 - B * C_4(t - t_0) - B * C_5[\sin(l''_{DF} + \delta l_D) - \sin l''_0] \quad (5.44)$$

$$i'' = i''_0 \quad (5.45)$$

where

$$\theta = \cos i''_0$$

$$\xi = \frac{1}{a''_0 - s}$$

$$\eta = a''_0 e''_0 \xi$$

$$\beta = (1 - e''_0)^{1/2}$$

$$C_2 = (q_0 - s)' \xi^4 n''_0 (1 - \eta^2)^{7/2} \left[a''_0 \left(1 + \frac{3}{2} \eta^2 + 4e_0 \eta + e_0 \eta^3 \right) \right] \\ + \frac{3}{4} \frac{J_2 \xi}{(1 - \eta^2)} \left(-\frac{1}{2} + \frac{3}{2} \theta^2 \right) (8 + 24\eta^2 + 3\eta^4)$$

$$C_1 = B * C_2$$

$$C_3 = -\frac{2(q_0 - s)^\tau J_3 n''_0 \sin i''_0}{J_2 e''_0}$$

$$C_4 = 2n''_0 (q_0 - s)^\tau \xi^5 a''_0 \beta^2 (1 - \eta^2)^{7/2} \left\{ \left[2\eta(1 + e''_0 \eta) + \frac{1}{2} e''_0 + \frac{1}{2} \eta^3 \right] \right. \\ \left. - \frac{J_2 \xi}{a''_0 (1 - \eta^2)} \left[3(1 - 3\theta^2) \left(1 + \frac{3}{2} \eta^2 - 2e''_0 \eta - \frac{1}{2} e''_0 \eta^3 \right) \right] \right. \\ \left. + \frac{3}{4} (1 - \theta^2) (2\eta^2 - e''_0 \eta - e''_0 \eta^3) \cos 2g''_0 \right\}$$

$$C_5 = 2(q_0 - s)^\tau \xi^4 a''_0 \beta^2 (1 - \eta^2)^{-7/2} \left[1 + \frac{11}{4} \eta(\eta + e''_0) + e''_0 \eta^3 \right]$$

$$D_2 = 4a''_0 \xi C_1^2$$

$$D_3 = \frac{4}{3} a''_0 \xi^2 (17a''_0 + S) C_1^3$$

$$D_4 = \frac{2}{3} a''_0 \xi^3 (221a''_0 + 31s) C_1^4$$

When the perigee altitude is less than 220 km, the above equation is simplified as:

$$a'' = a''_0 [1 - C_1(t - t_0)]^2 \quad (5.46)$$

$$l'' = l''_{DF} + \frac{3}{2} n''_0 C_1 (t - t_0)^2 \quad (5.47)$$

$$g'' = g''_{DF} \quad (5.48)$$

$$h'' = h''_{\text{DF}} - \frac{21 n_0'' J_2 \cos i''}{4 a_0''^2 \beta_0^2} C_1 (t - t_0)^2 \quad (5.49)$$

$$e'' = e''_0 - B * C_4 (t - t_0) \quad (5.50)$$

$$i'' = i''_0 \quad (5.51)$$

3. Orbit variables σ' are calculated which take into account the long-period items.

$$\begin{aligned} e_l &= -\frac{G \times G_l}{L''^2 e''} \\ a' &= a'' \\ i' &= i'' \\ l' + g' + h' &= l'' + g'' + h'' + (l_l + g_l + h_l) \\ &= -\frac{J_3 \sin i''}{4 J_2 a'' (1 - e''^2)} (e'' \cos g'') \left(\frac{3 + 5\theta}{1 + \theta} \right) \\ h' &= h'' \end{aligned} \quad (5.52)$$

$$\begin{aligned} e' \cos g' &= (e'' + e_l) \cos g'' - e'' g_l \sin g'' = e'' \cos g'' \\ e' \sin g' &= (e'' + e_l) \sin g'' - e'' g_l \cos g'' = e'' \sin g'' - \frac{J_3 \sin i''}{2 J_2 a'' (1 - e''^2)} \end{aligned} \quad (5.53)$$

The generalized Kepler equation is solved

$$(E' + g') - [(l' + g' + h') - h''] = e' \cos g' \sin (E' + g') - e' \sin g' \cos (E' + g') \quad (5.54)$$

Newton iteration method can be used to solve $(E' + g')$.

4. The instantaneous orbital parameters are calculated which takes into account the short-period items.

The instantaneous value of the orbit element is obtained, and then the satellite position and velocity at time t are obtained based on the instantaneous value of the orbit elements. In this process the true anomaly needs to be obtained through solving the Kepler equation. The SGP4 model eliminates solving the Kepler equation through variable conversion in order to reduce computation (Hoots, 1981). The following is the conversion process from the old variables to the new variables:

Old variables: $a', i', e' \cos g', e' \sin g', l' + g' + h', h'$

New variables: $r', \dot{r}' + r' \dot{f}', i', h', u'$

$$\begin{aligned} r' &= a' (1 - e' \cos E') \\ \dot{r}' &= \frac{L'}{r'} e' \sin E' \\ r' \dot{f}' &= \frac{L' \sqrt{1 - e'^2}}{r'} \end{aligned} \quad (5.55)$$

$$\begin{cases} i' = i' \\ h' = h' \\ u' = \arctan\left(\frac{\sin u'}{\cos u'}\right), u' = f' + g' \end{cases} \quad (5.56)$$

The variables used in above conversion are calculated as follows:

$$\begin{aligned} e' \cos E' &= (e' \cos g') \cos (E' + g') + (e' \sin g') \sin (E' + g') \\ e' \sin E' &= (e' \cos g') \sin (E' + g') + (e' \sin g') \cos (E' + g') \end{aligned} \quad (5.57)$$

$$e' = \sqrt{(e' \cos E')^2 + (e' \sin E')^2} \quad (5.58)$$

$$\begin{aligned} \cos u' &= \frac{a'}{r'} \left[\cos (E' + g') - e' \cos g' + \frac{(e' \sin g')(e' \sin E')}{1 + \sqrt{1 - e'^2}} \right] \\ \sin u' &= \frac{a'}{r'} \left[\sin (E' + g') - e' \sin g' + \frac{(e' \cos g')(e' \sin E')}{1 + \sqrt{1 - e'^2}} \right] \end{aligned} \quad (5.59)$$

The short-period main harmonic items are calculated as follows:

$$\begin{aligned} \delta r &= \frac{a'e'}{\sqrt{1-e'^2}} \sin f' l_s + \frac{r'}{a'} a_s - a' \cos f' e_s \\ &= \frac{J_2}{4p'} (1 - \cos^2 i') \cos 2u - \frac{3J_2}{4p'^2} (3\cos^2 i' - 1)r \end{aligned} \quad (5.60)$$

$$\delta i' = -\frac{1}{2} \frac{n'e'}{\sqrt{1-e'^2}} \sin f' a_s + n' a' e' \cos f' \left(\frac{a'}{r'}\right)^2 l_s = 0$$

$$\begin{aligned} \delta r \dot{f} &= -\frac{1}{2} n' \sqrt{1-e'^2} \left(\frac{a'}{r'}\right) a_s + \frac{n'a'}{\sqrt{1-e'^2}} \left(\frac{a'}{r'}\right) (\cos f' - e' + e' \cos^2 f') e_s \\ &\quad - n' a' e' \sin f' \left(\frac{a'}{r'}\right)^2 l_s \\ &= \frac{J_2 n'}{2p'} \left[(1 - \cos^2 i') \cos 2u - \frac{3}{2} (1 - 3\cos^2 i') \right] \end{aligned} \quad (5.61)$$

$$\delta i = i_s = \frac{3J_2}{4p'^2} \cos i' \sin 2u'$$

$$\delta h = h_s = \frac{3J_2}{4G^4} \cos i' \sin 2(f' + g')$$

$$\delta u = \frac{1}{1-e'^2} (2 + e' \cos f') \sin f' e_s + \frac{1}{(1-e'^2)^{3/2}} (1 + e' \cos f')^2 l_s + g_s$$

$$= -\frac{1}{8} \frac{J_2}{p'^2} (7\cos^2 i' - 1) \sin 2u'$$

Up to now, the instantaneous value of the following six elements at time t can be obtained:

$$\begin{aligned}
 r &= r' + \delta r \\
 \dot{r} &= \dot{r}' \\
 r\dot{f} &= r'\dot{f}' + \delta(r\dot{f}) \\
 i &= i' + \delta i \\
 h &= h' + \delta h \\
 u &= u' + \delta u
 \end{aligned} \tag{5.62}$$

Therefore the position and velocity vector of space objects at time t can be calculated:

$$\begin{aligned}
 \mathbf{r} &= r\mathbf{U} \\
 \dot{\mathbf{r}} &= \dot{r}\mathbf{U} + (r\dot{f})\mathbf{V}
 \end{aligned} \tag{5.63}$$

where

$$\begin{aligned}
 \mathbf{U} &= \mathbf{M} \sin u + \mathbf{N} \cos u \\
 \mathbf{V} &= \mathbf{M} \cos u - \mathbf{N} \sin u
 \end{aligned} \tag{5.64}$$

$$\mathbf{M} = \begin{pmatrix} -\sin h \cos i \\ \sin h \cos i \\ \sin i \end{pmatrix}, \quad \mathbf{N} = \begin{pmatrix} \cos h \\ \sin h \\ 0 \end{pmatrix} \tag{5.65}$$

5.2.2.4 Orbit determination based on SGP4 model

TLEs are a set of radicals generated by NORAD based on the general perturbation theory to forecast the position and velocity of space objects. TLEs issued now are generated with SGP4 or SDP4. The US SSN regularly updates the TLEs of space objects but does not issue the algorithm to determine TLEs. A set of orbit determination methods based on SGP4 model is provided here. In this section the SDP4/SGP4 model of TLE is analyzed; orbit determination method based on the SDP4/SGP4 Models is proposed combining with least squares orbit determination method.

Orbit determination methods based on SGP4 model, and the mean elements cataloging method to be introduced in the next section, are similar to the precise orbit calculation method in parameter estimation. The main difference between the models includes calculation of the partial derivative matrix in addition to the different extrapolated orbit model. The state vector \mathbf{X} based on SGP4 model include the six orbit element $\boldsymbol{\sigma}$ and the trajectory coefficient B^* , so $\mathbf{B} = (\partial Y / \partial(\mathbf{r}, \dot{\mathbf{r}}))(\partial(\mathbf{r}, \dot{\mathbf{r}}) / \partial \boldsymbol{\sigma})(\partial \boldsymbol{\sigma} / \partial \mathbf{X})$. How to calculate $\partial(\mathbf{r}, \dot{\mathbf{r}}) / \partial \boldsymbol{\sigma}$ and $\partial \boldsymbol{\sigma} / \partial \mathbf{X} = \partial \boldsymbol{\sigma} / \partial(\boldsymbol{\sigma}_0, B^*)$ will be expatiated in the following:

1. To calculate the partial derivative $\partial(\mathbf{r}, \dot{\mathbf{r}})/\partial\sigma_j$ of the position and velocity relative to the six Kepler elements,

$$\begin{aligned}\frac{\partial \mathbf{r}}{\partial a} &= \frac{1}{a} \mathbf{r}, & \frac{\partial \mathbf{r}}{\partial e} &= H \mathbf{r} + K \dot{\mathbf{r}}, & \frac{\partial \mathbf{r}}{\partial i} &= \frac{z}{\sin i} \hat{\mathbf{R}} \\ \frac{\partial \mathbf{r}}{\partial \Omega} &= (-y \mathbf{x} 0), & \frac{\partial \mathbf{r}}{\partial \omega} &= \hat{\mathbf{R}} \times \mathbf{r}, & \frac{\partial \mathbf{r}}{\partial M} &= \frac{1}{n} \dot{\mathbf{r}}\end{aligned}\quad (5.66)$$

$$\begin{aligned}\frac{\partial \dot{\mathbf{r}}}{\partial a} &= -\frac{1}{2a} \dot{\mathbf{r}}, & \frac{\partial \dot{\mathbf{r}}}{\partial e} &= H' \mathbf{r} + K' \dot{\mathbf{r}}, & \frac{\partial \dot{\mathbf{r}}}{\partial i} &= \frac{\dot{z}}{\sin i} \hat{\mathbf{R}} \\ \frac{\partial \dot{\mathbf{r}}}{\partial \Omega} &= (-\dot{y} \mathbf{x} 0), & \frac{\partial \dot{\mathbf{r}}}{\partial \omega} &= \hat{\mathbf{R}} \times \dot{\mathbf{r}}, & \frac{\partial \dot{\mathbf{r}}}{\partial M} &= -n \left(\frac{a}{r}\right)^3 \mathbf{r}\end{aligned}\quad (5.67)$$

where

$$H = -\frac{a}{p} (\cos E + e), \quad K = \frac{\sin E}{n} \left(1 + \frac{r}{p}\right) \quad (5.68)$$

$$H' = \frac{\sqrt{a} \sin E}{p} \left[1 - \frac{a}{r} \left(1 + \frac{p}{r}\right)\right], \quad K' = \frac{a}{p} \cos E \quad (5.69)$$

$$\hat{\mathbf{R}} = \frac{1}{\sqrt{p}} (\mathbf{r} \times \dot{\mathbf{r}}) \quad (5.70)$$

where $p = a(1 - e^2)$.

2. To calculate the State transition matrix $\partial\sigma/\partial\sigma_0$,

Take the SGP4 model, for example, long-term or long-period changes of the orbit elements are (parameters of the equations refer to related documentation):

$$M_{\text{DF}} = M_0 + \left[1 + \frac{3k_2(-1 + 3\theta^2)}{2a_0''^2 \beta_0^3} + \frac{3k_2^2(13 - 78\theta^2 + 137\theta^4)}{16a_0''^4 \beta_0^7}\right] n_0''(t - t_0) \quad (5.71)$$

$$\omega_{\text{DF}} = \omega_0 + \left[-\frac{3k_2(1 - 5\theta^2)}{2a_0''^2 \beta_0^4} + \frac{3k_2^2(7 - 114\theta^2 + 395\theta^4)}{16a_0''^4 \beta_0^8} + \frac{5k_4(3 - 36\theta^2 + 49\theta^4)}{4a_0''^4 \beta_0^8}\right] n_0''(t - t_0) \quad (5.72)$$

$$\Omega_{\text{DF}} = \Omega_0 + \left[-\frac{3k_2\theta}{a_0''^2 \beta_0^4} + \frac{3k_2^2(4\theta - 19\theta^3)}{2a_0''^4 \beta_0^8} + \frac{5k_4\theta(3 - 7\theta^2)}{2a_0''^4 \beta_0^8}\right] n_0''(t - t_0) \quad (5.73)$$

$$e = e_0 - B * C_4(t - t_0) - B * C_5(\sin M_p - \sin M_0) \quad (5.74)$$

$$a = a_0'' [1 - C_1(t - t_0) - D_2(t - t_0)^2 - D_3(t - t_0)^3 - D_4(t - t_0)^4]^2 \quad (5.75)$$

For the model SDP4, formulas (5.74) and (5.75) are simplified as:

$$e = e_0 - B * C_4(t - t_0) \quad (5.76)$$

$$a = a_0''[1 - C_1(t - t_0)]^2 \quad (5.77)$$

Thus it can be obtained that:

$$\begin{aligned} \frac{\partial \sigma}{\partial \sigma_0} &= \begin{pmatrix} \frac{\partial a}{\partial a} & \frac{\partial a}{\partial e} & \frac{\partial a}{\partial i} & \frac{\partial a}{\partial \Omega} & \frac{\partial a}{\partial \omega} & \frac{\partial a}{\partial M} & \frac{\partial a}{\partial B^*} \\ \frac{\partial e}{\partial a} & \frac{\partial e}{\partial e} & \frac{\partial e}{\partial i} & \frac{\partial e}{\partial \Omega} & \frac{\partial e}{\partial \omega} & \frac{\partial e}{\partial M} & \frac{\partial e}{\partial B^*} \\ \frac{\partial i}{\partial a} & \frac{\partial i}{\partial e} & \frac{\partial i}{\partial i} & \frac{\partial i}{\partial \Omega} & \frac{\partial i}{\partial \omega} & \frac{\partial i}{\partial M} & \frac{\partial i}{\partial B^*} \\ \frac{\partial \Omega}{\partial a} & \frac{\partial \Omega}{\partial e} & \frac{\partial \Omega}{\partial i} & \frac{\partial \Omega}{\partial \Omega} & \frac{\partial \Omega}{\partial \omega} & \frac{\partial \Omega}{\partial M} & \frac{\partial \Omega}{\partial B^*} \\ \frac{\partial \omega}{\partial a} & \frac{\partial \omega}{\partial e} & \frac{\partial \omega}{\partial i} & \frac{\partial \omega}{\partial \Omega} & \frac{\partial \omega}{\partial \omega} & \frac{\partial \omega}{\partial M} & \frac{\partial \omega}{\partial B^*} \\ \frac{\partial M}{\partial a} & \frac{\partial M}{\partial e} & \frac{\partial M}{\partial i} & \frac{\partial M}{\partial \Omega} & \frac{\partial M}{\partial \omega} & \frac{\partial M}{\partial M} & \frac{\partial M}{\partial B^*} \\ \frac{\partial B^*}{\partial a} & \frac{\partial B^*}{\partial e} & \frac{\partial B^*}{\partial i} & \frac{\partial B^*}{\partial \Omega} & \frac{\partial B^*}{\partial \omega} & \frac{\partial B^*}{\partial M} & \frac{\partial B^*}{\partial B^*} \end{pmatrix} \\ &= \begin{pmatrix} 1 & 0 & 0 & 0 & 0 & 0 & \frac{\partial a}{\partial B^*} \\ 0 & 1 & 0 & 0 & 0 & 0 & \frac{\partial e}{\partial B^*} \\ 0 & 0 & 1 & 0 & 0 & 0 & 0 \\ \frac{\partial \Omega}{\partial a} & 0 & 0 & 1 & 0 & 0 & 0 \\ \frac{\partial \omega}{\partial a} & 0 & 0 & 0 & 1 & 0 & 0 \\ \frac{\partial M}{\partial a} & 0 & 0 & 0 & 0 & 1 & 0 \\ 0 & 0 & 0 & 0 & 0 & 0 & 1 \end{pmatrix} \end{aligned} \quad (5.78)$$

where

$$\begin{aligned} \frac{\partial a}{\partial B^*} &= 2a_0''[1 - C_1(t - t_0) - D_2(t - t_0)^2 - D_3(t - t_0)^3 - D_4(t - t_0)^4] [-C_2(t - t_0) \\ &\quad - 2D_2C_2/C_1(t - t_0)^2 - 3D_3C_2/C_1(t - t_0)^3 - 4D_4C_2/C_1(t - t_0)^4] \end{aligned}$$

$$\frac{\partial e}{\partial B^*} = -C_4(t - t_0) - C_5(\sin M_p - \sin M_0)$$

$$\frac{\partial \Omega}{\partial a} = -\frac{3n_0}{2a_1}(t - t_0)\Omega_1$$

$$\frac{\partial \omega}{\partial a} = -\frac{3n_0}{2a_1}(t - t_0)\omega_1$$

$$\frac{\partial M}{\partial a} = -\frac{3n_0}{2a_1}(t - t_0)M_1$$

5.2.3 The mean elements cataloging orbit calculation method

According to Chapter 2, Basics of orbital calculation for spacecraft collision avoidance, if the equation of orbit motion only considers the two-body problem, it can be solved directly to get six orbital elements. However, as described in Chapter 4, Space environment and object orbit, space objects are affected by various perturbations in real circumstances, the equation of motion performs as the perturbed two-body problem. As for the solution of perturbed two-body problem, the classical perturbation method was used to find solution of a small parameter power series. Since the orbit period around the Earth is shorter, the convergence range of power series of the solution is large. As for perturbation equation of artificial celestial body, an improved perturbation method was proposed by Kozai. The so-called mean element method is a series expansion method that is deployed near the mean element σ^* or average element $\bar{\sigma}$. This method uses the orbit elements as the basic variables to more clearly reflect the geometry state of the orbit. Different from the classical perturbation method, it divides perturbation terms into long-term, long-period, and short-period items. Since the generated small parameter power series solution is the expansion of power series based on consideration of the long-term mean elements, forecast accuracy and stability of long arc is higher relatively to the classical perturbation method [4]. A small law denominator phenomenon will appear in perturbation items of the mean elements method. As for the problem that singularities will happen to small e or i orbit, Liu Lin proposed the quasimean elements method, making long-period items with slow changes being saved in the mean elements, avoiding that problems happen to the long-period item of elements. It is proved that the quasimean elements method will not bring loss of accuracy [94].

5.2.3.1 Orbit extrapolation

5.2.3.1.1 The mean element method

The perturbation motion equation in the form of element can be expressed as:

$$\frac{d\sigma}{dt} = f_0(a) + \sum_i f_i(\sigma, t, \varepsilon^i) \quad (5.79)$$

$$\boldsymbol{\sigma} = (aei\Omega\omega M)^T \mathbf{f}_0 = \delta n, \delta = (000001)^T \quad (5.80)$$

where \mathbf{f}_0 is part of the equation of motion with no perturbation. \mathbf{f}_i is part of the equation of motion with perturbation and the magnitude is $O(\varepsilon^i)$. As for the Earth satellite, the magnitude of ε and the nonspherical second-order harmonics is the same.

The mean element at any time is defined as:

$$\bar{\boldsymbol{\sigma}}(t) = \bar{\boldsymbol{\sigma}}(t_0) + \delta \bar{n}(t - t_0) + \sum_i \boldsymbol{\sigma}_i(t - t_0) \quad (5.81)$$

$$\bar{\boldsymbol{\sigma}}(t_0) = \boldsymbol{\sigma}(t_0) - [\boldsymbol{\sigma}_1^1(t_0) + \cdots + \boldsymbol{\sigma}_s^1(t_0)] \quad (5.82)$$

where $\bar{\boldsymbol{\sigma}}(t_0)$ is the original mean element.

Taylor expansion is performed on the right function of perturbation motion equation at the mean element of the time t .

$$\begin{aligned} & \frac{d}{dt} \left[\bar{\boldsymbol{\sigma}}(t) + \boldsymbol{\sigma}_s^{(1)} + \boldsymbol{\sigma}_s^{(2)} + \cdots + \boldsymbol{\sigma}_l^{(1)} + \boldsymbol{\sigma}_l^{(2)} + \cdots \right] \\ &= f_0(\bar{\boldsymbol{\sigma}}) + \frac{\delta f_0}{\delta \mathbf{a}} \left[\mathbf{a}_s^{(1)} + \mathbf{a}_s^{(2)} + \cdots + \mathbf{a}_l^{(1)} + \mathbf{a}_l^{(2)} + \cdots \right] + \frac{1}{2} \frac{\delta^2 f_0}{\delta \mathbf{a}^2} \left[\mathbf{a}_s^{(1)} + \cdots + \mathbf{a}_l^{(1)} + \cdots \right]^2 \\ &+ \cdots + f_1(\bar{\boldsymbol{\sigma}}, t, \varepsilon) + \sum_{j=1}^6 \frac{\delta f_1}{\delta \sigma_j} [\boldsymbol{\sigma}_s^{(1)} + \cdots + \boldsymbol{\sigma}_l^{(1)} + \cdots]_j + \cdots + f_2(\bar{\boldsymbol{\sigma}}, t, \varepsilon) + \cdots \end{aligned} \quad (5.83)$$

The right functions of equations of perturbation motion can be divided into three different types: secular item $\mathbf{f}_{ic}(\boldsymbol{\sigma}, t, \varepsilon^i)$, long-period item $\mathbf{f}_{il}(\boldsymbol{\sigma}, t, \varepsilon^i)$, and short-period item $\mathbf{f}_{is}(\boldsymbol{\sigma}, t, \varepsilon^i)$, wherein c , l , and s , represent, respectively, secular-term item, long-period item, and short-period item.

The power and nature of each item on both sides of the equation are compared to get:

$$\bar{\boldsymbol{\sigma}}_0(t) = \bar{\boldsymbol{\sigma}}_0 + \delta \bar{n}(t - t_0) \quad (5.84)$$

$$\boldsymbol{\sigma}_1(t - t_0) = \int_{t_0}^t (\mathbf{f}_{1c})_{\bar{\boldsymbol{\sigma}}} dt \quad (5.85)$$

$$\boldsymbol{\sigma}_s^{(1)}(t) = \int_t \left[\delta \frac{\partial n}{\partial \mathbf{a}} \mathbf{a}_s^{(1)} + \mathbf{f}_{1s} \right]_{\bar{\boldsymbol{\sigma}}} dt \quad (5.86)$$

$$\boldsymbol{\sigma}_2(t - t_0) = \int_{t_0}^t \left[\frac{1}{2} \delta \frac{\partial^2 n}{\partial \mathbf{a}^2} (\mathbf{a}_s^{(1)})_c^2 + \left(\sum_{j=1}^6 \frac{\partial \mathbf{f}_1}{\partial \sigma_j} (\boldsymbol{\sigma}_s^{(1)})_j \right)_c + \mathbf{f}_{2c} \right]_{\bar{\boldsymbol{\sigma}}} dt \quad (5.87)$$

$$\boldsymbol{\sigma}_l^{(1)}(t) = \int_t \left[\delta \frac{\partial n}{\partial \mathbf{a}} \mathbf{a}_l^{(2)} + \delta \frac{1}{2} \frac{\partial^2 n}{\partial \mathbf{a}^2} (\mathbf{a}_s^{(1)})_l^2 + \left(\sum_{j=1}^6 \frac{\partial \mathbf{f}_1}{\partial \sigma_j} (\boldsymbol{\sigma}_s^{(1)} + \boldsymbol{\sigma}_l^{(1)})_j \right)_l + \mathbf{f}_{2l} \right]_{\bar{\boldsymbol{\sigma}}} dt \quad (5.88)$$

$$\sigma_s^{(2)}(t) = \int_t \left[\delta \frac{\partial n}{\partial a} a_s^{(2)} + \delta \frac{1}{2} \frac{\partial^2 n}{\partial a^2} (a_s^{(1)})^2 + \left(\sum_{j=1}^6 \frac{\partial f_1}{\partial \sigma_j} (\sigma_s^{(1)} + \sigma_l^{(1)})_j \right)_s + f_{2s} \right]_{\bar{\sigma}} dt \quad (5.89)$$

The mean elements method, which considers main zonal harmonic terms of the Earth nonspherical gravitational perturbations, can be used to get variation or the right ascension Ω and the argument of perigee ω . The formula of the first-order secular term is:

$$\Omega_1 = -\frac{A_2}{p^2} n \cos i \quad (5.90)$$

$$\omega_1 = \frac{A_2}{p^2} n \cos i \left(2 - \frac{5}{2} \sin^2 i \right) \quad (5.91)$$

where $A_2 = (3/2)J_2$, $J_2 = 1.082636 \times 10^{-3}$, the orbit elements involved in the formula are the mean elements.

5.2.3.1.2 The quasimean element method

Since the integral function contains the factor $\cos \omega$, during the process of obtaining long-period item by integration, the long-term variability of the argument of perigee in the results of integration will appear in the denominator $\sin \omega/\omega_1$. When $\omega_1 \rightarrow 0$, the singularity problem (normally agreed singularity) will be caused, and now $i \rightarrow 63^\circ 26'$ or $i \rightarrow 116^\circ 34'$, which is also called critical inclination. The mean element method needs to be adjusted in some degree in order to solve the critical inclination problem, and the quasimean element method is used to construct the perturbation analysis solution to eliminate the agreed singularity caused by small denominators. The mean element method, as described above, selects the mean element at the time t as a reference solution for the Taylor expansion of right function of the perturbing motion equations, while the quasimean element method selects the quasimean element at the time t as a reference solution for the Taylor expansion of right function of the perturbing motion equations. Here the quasimean element is defined as:

$$\bar{\sigma}(t) = \bar{\sigma}^{(0)}(t) + \sigma_c(t) + \Delta\sigma_l^{(1)}(t) + \dots \quad (5.92)$$

where

$$\sigma_c(t) = \sigma_1(t - t_0) + \sigma_2(t - t_0) + \dots \quad (5.93)$$

$$\Delta\sigma_l^{(1)}(t) = \sigma_l^{(1)}(t) - \sigma_l^{(1)}(t_0) \quad (5.94)$$

$$\bar{\sigma}^{(0)}(t) = \bar{\sigma}_0 + \delta\bar{n}_0(t - t_0) \quad (5.95)$$

$$\bar{\sigma}_0 = \sigma_0 - [\sigma_s^{(1)}(t_0) + \sigma_s^{(2)}(t_0) + \dots] \quad (5.96)$$

It can be seen from definition of the quasimean element that the long-period items of the mean element method will appear in the form of long-period changing items, namely, $\Delta\sigma_l^{(1)}(t) = \sigma_l^{(1)}(t) - \sigma_l^{(1)}(t_0)$. When normally agreed singularities appear in the orbital motion, even if $\sigma_l^{(1)}(t)$ and $\sigma_l^{(1)}(t_0)$ fail at the same time, the impact on the long-period changing items is only limited. And because only the short-period items of the right function of the perturbing equations of motion are expanded, the normally agreed singularities will not result in ineffectiveness of the quasimean element method.

The perturbation equations of motion (5.79) are expanded at the quasimean element of time t to get:

$$\begin{aligned} \frac{d}{dt} [\bar{\sigma}(t) + \sigma_s^{(1)}(t) + \sigma_s^{(2)}(t) + \dots] = \\ f_0(\bar{a}) + \frac{\partial f_0}{\partial a} [a_s^{(1)} + a_s^{(2)} + \dots] + \frac{1}{2} \frac{\partial^2 f_0}{\partial a^2} [a_s^{(1)} + \dots]^2 + \dots + \\ f_1(\bar{\sigma}, t, \varepsilon) + \sum_{j=1}^6 \frac{\partial f_1}{\partial \sigma_j} [\sigma_s^{(1)}(t) + \dots]_j + \dots + f_2(\bar{\sigma}, t, \varepsilon^2) + \dots \end{aligned} \quad (5.97)$$

The items with the same power and nature on both sides of the equation are compared:

$$\bar{\sigma}^{(0)}(t) = \bar{\sigma}_0 + \int_{t_0}^t \delta \bar{n} dt = \bar{\sigma}_0 + \delta \bar{n}(t - t_0) \quad (5.98)$$

$$\sigma_1(t - t_0) = \int_{t_0}^t (f_{1c})_{\bar{\sigma}} dt \quad (5.99)$$

$$\sigma_s^{(1)}(t) = \int_t \left[\delta \frac{\partial n}{\partial a} a_s^{(1)} + f_{1s} \right]_{\bar{\sigma}} dt \quad (5.100)$$

$$\sigma_2(t - t_0) = \int_{t_0}^t \left[\frac{1}{2} \delta \frac{\partial^2 n}{\partial a^2} (a_s^{(1)})_c^2 + \left(\sum_{j=1}^6 \frac{\partial f_1}{\partial \sigma_j} (\sigma_s^{(1)})_j \right)_c + f_{2c} \right]_{\bar{\sigma}} dt \quad (5.101)$$

$$\Delta\sigma_l^{(1)}(t) = \int_{t_0}^t \left[\delta \frac{1}{2} \frac{\partial^2 n}{\partial a^2} (a_s^{(1)})_l^2 + \left(\sum_{j=1}^6 \frac{\partial f_1}{\partial \sigma_j} (\sigma_s^{(1)})_j \right)_l + f_{2l} \right]_{\bar{\sigma}} dt \quad (5.102)$$

$$\sigma_s^{(2)}(t) = \int_t \left[\delta \frac{\partial n}{\partial a} a_s^{(2)} + \delta \frac{1}{2} \frac{\partial^2 n}{\partial a^2} (a_s^{(1)})_s^2 + \left(\sum_{j=1}^6 \frac{\partial f_1}{\partial \sigma_j} (\sigma_s^{(1)})_j \right)_s + f_{2s} \right]_{\bar{\sigma}} dt \quad (5.103)$$

The related orbit elements are all quasimean elements.

Compared with the formula given by the mean element method, only the integral expression of the long-period changing items disaccords with the mean element method. In fact, although the first-order secular integral formula of the mean element method is similar in the form to the one of the quasimean element method, the first and 0-order secular terms

constructed by the two methods are also different. Thus the difference of the long-period items between the two methods is compensated by the secular items. The remaining difference exists in the third order, which can be accepted in the case that integration time is not long.

5.2.3.2 State transition matrix

Generally speaking, the calculation of state transition matrix is realized by directly obtaining partial derivative of the state differential equations, which is $\Phi(t_0, t) = (\partial X / \partial X_0)$. Since its role in determining the orbit is to provide the coefficients of the correction quantity X_0 obtained during iterative process, the coefficients will only affect the speed of convergence of the iteration but generally will not affect the accuracy of the results of convergence. Thus the state transition matrix of two-body problem is generally adopted when the mean element method is used for orbit determination, namely,

$$\frac{\partial \sigma}{\partial \sigma_0} = \begin{bmatrix} 1 & 0 & 0 & 0 & 0 & 0 \\ 0 & 1 & 0 & 0 & 0 & 0 \\ 0 & 0 & 1 & 0 & 0 & 0 \\ 0 & 0 & 0 & 1 & 0 & 0 \\ 0 & 0 & 0 & 0 & 1 & 0 \\ -\frac{3}{2} \sqrt{\frac{GM}{a^5}} & 0 & 0 & 0 & 0 & 1 \end{bmatrix}$$

where σ is the mean or quasimean element.

5.2.4 Precision analysis

Orbit precision of space objects directly affects the success rate of spacecraft surveillance and confidence of spacecraft collision warning risk analysis. Factors affecting orbit precision mainly include orbit measurement data quality and orbital calculation method. The orbit measurement data and orbital calculation method together determine the initial orbit accuracy. This section focuses on influence of the orbital calculation method on orbit accuracy in the case that orbit measurement data are error-free. Second, the error characteristics of the space objects cataloging orbit have been elaborated, the relationship between the orbit error in different forms, and the propagation with time are described in detail.

5.2.4.1 Simple numerical method accuracy analysis

According to [Section 5.2.1](#), the simple numerical method and the precise orbit calculation method differ mainly in the perturbation model. As for nearly circular orbit with different altitude, the two methods are used for orbit prediction, respectively, and compared in the case that initial orbit is the same. [Table 5–4](#) lists statistics of the orbit prediction accuracy based on two kinds of model strategy of orbit determination.

Table 5-4 Relatively precise orbit prediction accuracy with the simple numerical method.

Orbit altitude	300 km			500 km			800 km		
	Differences of accuracy (m)	Time		Differences of accuracy (m)	Time		Differences of accuracy (m)	Time	
		Simple numerical method (s)	Precise orbit determination (s)		Simple numerical method (s)	Precise orbit determination (s)		Simple numerical method (s)	Precise orbit determination (s)
Days for prediction	Differences of accuracy (m)	Simple numerical method (s)	Precise orbit determination (s)	Differences of accuracy (m)	Simple numerical method (s)	Precise orbit determination (s)	Differences of accuracy (m)	Simple numerical method (s)	Precise orbit determination (s)
1 day	300	0.7	1.4	200	0.7	1.3	100	0.7	1.4
3 days	800	2	4	500	2	4	300	2	4
7 days	1700	4	8	1200	–	8	1000	4	8

According to [Table 5–4](#), prediction error between the simple numerical method and precise orbit determination method is within 500 m for 1 day, 1 km for 3 days, and 2 km for 7 days. Prediction accuracy with the simple numerical methods can meet with the object guide requirements of subsequent week and object catalog needs, greatly reducing the computing complexity and machine-hour. But as for the collision warning, precise orbit determination strategy is needed to meet the requirements of a low false alarm rate, which will be reflected in Chapter 6, Spacecraft collision warning and avoidance strategy.

5.2.4.2 The US cataloging precision analysis

SGP4/SDP4 model can be adapted to objects with various types of orbits, which can be divided into LEO (orbital altitude is less than 5000 km, $e < 0.1$), semisynchronous orbit (about 20,000 km), geostationary orbit (36,000 km around), and elliptical orbit ($e > 0.1$) according to orbital altitude and eccentricity [96]. Precision analytical approach is as follows: the precision orbit prediction model is used for orbit prediction; the predicted position and velocity are used as analog observations; and precise orbit is used to calibrate precision after SGP4/SDP4 model is used for orbit calculation. Analog data take a point every 2 minutes, which are the whole-arc observations. The orbit of an object, whose altitude at perigee is less than 1500 km, is predicted for 3 + 7 days. Data for the first 3 days are used for orbit determination; data for the last 7 days are compared to the orbit predicted by the model. The orbit of an object, whose altitude at perigee is more than 1500 km, is predicted for 10 + 30 days.

Orbit determination method described in [Section 5.2.2](#) is used for orbit determination; and SGP4/SDP4 models are used for prediction. The orbit predicted by precise orbit prediction software is taken as normal orbit, and the predicted and normal orbits are compared. Suppose the number of observation data is k , positional deviation between the predicted and normal orbits is y_j , then

$$\sigma^* = \sqrt{\frac{U}{k}}, \quad (5.104)$$

$$U = \sum_{j=1}^k (y_j^T W_j y_j) \quad (5.105)$$

Prediction accuracy is the maximum deviation of the position between the predicted and normal orbits within the prediction period. According to the statistics of various orbits, the formula of orbit determination accuracy range for different space objects is given, as well as prediction error of different space objects for n days.

1. Nearly circular LEO object

When the orbit altitude is less than or equal to 1600 km, orbit determination accuracy is 0.3–1 km; when orbital altitude is more than 1600 km, orbit determination accuracy is 0.25–0.4 km.

Table 5–5 LEO object classification.

Types of orbits	A	B	C	D
Orbit altitude (km)	$h_p < 400$	$400 \leq h_p < 600$	$600 \leq h_p < 1200$	$h_p \geq 1200$

Table 5–6 LEO objects prediction accuracy ($F_{10.7} = 100$).

Types of orbits	Orbit error (km)		
	Prediction for 1 day	Prediction for 3 days	Prediction for 7 days
A	10	40	300
B	7	30	200
C	6	15	70
D	2	10	10

Orbit prediction accuracy of LEO objects is highly relevant to the orbit altitude. LEO objects are divided into four categories based on the experience, as shown in Table 5–5. Table 5–6 lists the prediction accuracy of LEO objects.

It can be concluded from the earlier.

- a. If the SGP4/SDP4 models are used for processing LEO objects, orbit determination accuracy is within 100 m. Orbit prediction accuracy is highly relevant to the orbit altitude; the lower the altitude, the worse the orbit determination accuracy.
 - b. The position error of LEO objects predicted for 3 days is less than 40 km.
2. Nearly circular high-altitude objects
- Nearly circular high-altitude objects are mainly in semisynchronous and geostationary orbits. The orbit with altitude between 18,500 and 21,500 km is classified as semigeosynchronous orbit, and the orbit with altitude between 33,000 and 38,000 km is classified as geosynchronous orbit.

According to the statistics, orbit determination precision for semisynchronous objects is between 0.4 and 1.5 km, and orbit determination precision for synchronous objects is between 1.5 and 3.2 km. With the increasing of the orbit altitude, orbit determination error is increasing. Orbit determination error of synchronous objects is more than the one of semisynchronous objects. Prediction error of geosynchronous objects for 15 days does not exceed 40 km nor does semisynchronous objects for 30 days.

3. The elliptical objects

Orbit determination precision of the elliptical objects is not associated with the altitude at perigee, but is highly relevant to the eccentricity. The greater the eccentricity, the greater is the orbit determination error. Given the eccentricity is e , orbit determination precision of the elliptical objects decreases with increasing eccentricity, in particular.

Table 5–7 Elliptical objects classification.

Types of orbits	A	B	C	D
Orbit altitude at perigee (km)	$h_p < 400$	$400 \leq h_p < 600$	$600 \leq h_p < 1200$	$h_p \geq 1200$

Table 5–8 Elliptical objects prediction accuracy.

Types of orbits	Orbit error (km)		
	Prediction for 1 day	Prediction for 3 day	Prediction for 7 day
A	20	100	500
B	20	100	200
C	20	100	150
D	20	40	50

When $0.1 < e \leq 0.6$, the orbit determination error is less than 5 km; when $0.6 < e \leq 0.8$, the error is less than 10 km; and when $e > 0.8$, the error is greater than 10 km. Orbit determination accuracy is within 10 km.

Orbit prediction precision of the elliptical objects is not associated with the eccentricity but is highly relevant to the altitude at perigee. The elliptical objects are divided into four categories according to orbit altitude at perigee based on experience, as shown in [Table 5–7](#).

[Table 5–8](#) shows the maximum position prediction error of various orbit objects for n days.

It can be concluded that position prediction error of elliptical objects is less than 20 km for 1 day and less than 100 km for 3 days. Orbit prediction precision of the elliptical objects is highly relevant to the altitude at perigee. The lower the altitude at perigee, the greater is the prediction error.

5.2.4.3 Precision analysis with the mean element method

This section mainly describes the orbit determination and prediction accuracy with the quasi-mean element method. Same as [Section 5.2.2](#), precise orbit data are used as observations in order to eliminate error caused by the observation data. Mechanical model and orbit altitude classification used for precise orbit calculation is also the same as [Section 5.2.4](#). Owing to the low orbit of objects whose altitude is less than 400 km, precise orbit for 1 day is used for orbit determination. As for GEO objects, precise orbit for 7 days is used for orbit determination. As for other objects in various orbits, precise orbit for 3 days is used for orbit determination.

1. Nearly circular LEO object

Orbit determination accuracy of nearly circular LEO objects is relevant to the altitude. When the altitude is less than 400 km, the orbit determination error is relatively unstable;

Table 5–9 LEO objects prediction accuracy ($F_{10.7} = 100$).

Types of orbits	Orbit error (km)		
	Prediction for 1 day	Prediction for 3 days	Prediction for 7 days
A	3	8	100
B	2	7	30
C	0.5–0.6	1–2.6	7–9
D	0.3–1.5	1.2–2.0	3.0–12

the position error is between 800 m and 3 km, and the mean position error is about 1.5 km. When the altitude is between 400 m and 600 km, the position error is about 500 m. When the altitude is between 600 and 1200 m, the position error is about 300 m. When the altitude is more than 1200 km, the position error is about 100 m.

The mean elements method is used for the prediction of the improved initial orbit; the precise orbit is use for calibration of the orbit. The results are shown in Table 5–9.

It can be concluded from the earlier:

1. If the mean element method is used for processing LEO objects, orbit determination accuracy is within 100 m. Orbit prediction accuracy is highly relevant to the orbit altitude; the lower the altitude, the worse is the orbit determination accuracy.
2. The position error of LEO objects predicted for 3 days is less than 10 km.
2. Nearly circular high-altitude objects

According to the statistics, orbit determination precision for semisynchronous objects is within 2 km, and orbit determination precision for synchronous objects is within 5 km. With the increase of the orbit altitude, orbit determination error is increasing. Orbit determination error of synchronous objects is more than the one of semisynchronous objects. Prediction error of geosynchronous objects for 15 days does not exceed 40 km nor does semisynchronous objects for 30 days.

3. The highly elliptical objects

According to the statistics, orbit determination precision for the elliptical objects is within 3 km. Prediction error of highly elliptical objects for 15 days does not exceed 40 km.

5.2.4.4 Space object catalog error characteristic orbital analysis

Orbit error can be expressed in the form of Kepler orbital elements, position, and velocity. Long-term calculations and theoretical analysis shows that the expression of the position and velocity error in RTN coordinate system is more conducive to the breakdown of the error, thus relationship between the position and rate error and Kepler orbit element error in RTN directions is described in detail and the variation of the orbit error with time in the three directions is also described [97,98].

In the inertial coordinate the instantaneous element of initial orbit is set as $\sigma(a, e, i, \Omega, \omega, M)$, the position is set as $\mathbf{r}, \dot{\mathbf{r}}$, the orbit element error is set as

$\Delta\sigma(\Delta a, \Delta e, \Delta i, \Delta\Omega, \Delta\omega, \Delta M)$, the position and velocity error is set as $\Delta\mathbf{r}, \Delta\dot{\mathbf{r}}$. Relationship between the position and velocity error and the orbit element error can be derived as follows:

$$\begin{aligned}\Delta\mathbf{r} &= \frac{\mathbf{r}}{a}\Delta a + (H\mathbf{r} + K\dot{\mathbf{r}})\Delta e + (-\boldsymbol{\Omega} \times \mathbf{r})\Delta i + (-\mathbf{Z} \times \mathbf{r})\Delta\Omega \\ &\quad + (-\mathbf{N} \times \mathbf{r})\Delta\omega + \frac{\dot{\mathbf{r}}}{n}\Delta M \\ \Delta\dot{\mathbf{r}} &= \frac{\dot{\mathbf{r}}}{2a}\Delta\mu pa + (H'\mathbf{r} + K'\dot{\mathbf{r}})\Delta e + (-\boldsymbol{\Omega} \times \dot{\mathbf{r}})\Delta i + (-\mathbf{Z} \times \dot{\mathbf{r}})\Delta\Omega \\ &\quad + (-\mathbf{N} \times \dot{\mathbf{r}})\Delta\omega + \frac{\mu}{nr^3}\Delta M\end{aligned}\quad (5.106)$$

where $\hat{\boldsymbol{\Omega}} = (\cos\Omega\sin\Omega)$ is unit vector in the direction of orbit right ascension; $\hat{\mathbf{Z}} = \begin{pmatrix} 0 \\ 0 \\ 1 \end{pmatrix}$ is unit vector in the Z direction of inertial coordinate system; $\hat{\mathbf{N}} = 1/\sqrt{\mu p}(\mathbf{r} \times \dot{\mathbf{r}})$ is unit vector in the normal direction of the orbit surface. The formulas of symbols H, K, H', K', μ, n are:

$$H = -\frac{a}{p}(\cos E + e),$$

$$K = \left(1 + \frac{e}{p}\right) \frac{\sin E}{n},$$

$$H' = \frac{\sqrt{\mu a}}{p} \frac{\sin E}{r} \left[1 - \frac{a}{r} \left(1 + \frac{e}{r}\right)\right],$$

$$K' = \frac{a}{p} \cos E,$$

$\mu = GM \oplus$ is the Earth's gravitational constant;

$n = \sqrt{\mu/a^3} = 2\pi/T$ is the mean angular velocity of the satellite.

where T is the period of satellite motion; $p = a(1 - e^2)$; $r = |\mathbf{r}|$; and E is the eccentric anomaly.

The position and velocity error vector in the inertial coordinate system is projected onto RTN coordinate system to obtain:

$$\begin{cases} P_R = \frac{r}{a}\Delta a - a \cos f \Delta e + \frac{ae}{\sqrt{1-e^2}} \sin f \Delta M \\ P_T = r \cos i \Delta\Omega + a \left(1 + \frac{r}{p}\right) \sin f \Delta e + r \Delta\omega + \frac{a^2 \sqrt{1-e^2}}{r} \Delta M \\ P_N = r \sin u \Delta i - r \sin i \cos u \Delta\Omega + \frac{r}{\sqrt{(r\Delta i)^2 - (r \sin i \Delta\Omega)^2}} \sin(u + \varphi_0) \end{cases}\quad (5.107)$$

where $\sin \varphi_0 = \sin i \Delta\Omega / \sqrt{\Delta i^2 + \sin^2 i \Delta\Omega^2}$, $\cos \varphi_0 = \Delta i / \sqrt{\Delta i^2 + \sin^2 i \Delta\Omega^2}$.

$$\left\{ \begin{array}{l} V_R = \frac{r}{2a} \Delta a - \sqrt{\frac{\mu}{p}} \frac{a}{r} \sin f \Delta e + \frac{\sqrt{\mu p}}{r} \cos i \Delta \Omega - \frac{\sqrt{\mu p}}{r} \Delta \omega - \frac{\mu}{n} \left(\frac{1}{r^2} \right) \Delta M \\ V_T = \sqrt{\frac{\mu}{p}} \frac{a}{p} (\cos f + e) \Delta e + \frac{\sqrt{\mu}}{p} e \sin f \cos i \Delta \Omega + \sqrt{\frac{\mu}{p}} e \sin f \Delta \omega \\ V_N = \sqrt{\frac{\mu}{p}} [(1 + e \cos f) \cos u + e \sin f \sin u] \Delta i + \\ \sqrt{\frac{\mu}{p}} [(1 + e \cos f) \sin i \sin u - e \sin f \sin i \cos u] \Delta \Omega \end{array} \right. \quad (5.108)$$

For nearly circular orbits the formula can be further simplified as:

$$\left\{ \begin{array}{l} P_R \approx \Delta a - a \cos f \Delta e \\ P_T \approx a \cos i \Delta \Omega + 2a \sin f \Delta e + a(\Delta \omega + \Delta M) \\ P_N \approx a(\sin u \Delta i - \sin i \cos u \Delta \Omega) \end{array} \right. \quad (5.109)$$

$$\left\{ \begin{array}{l} V_R \approx -\frac{1}{2} \Delta a - n a \sin f \Delta e - n a \cos i \Delta \Omega - n a (\Delta \omega + \Delta M) \\ V_T \approx n a \cos f \Delta e \\ V_N \approx n a (\cos u \Delta i + \sin i \cos u \Delta \Omega) = n a \left[\sin \left(u + \frac{\pi}{2} \right) \Delta i - \sin i \cos \left(u + \frac{\pi}{2} \right) \Delta \Omega \right] \end{array} \right. \quad (5.110)$$

The position and velocity error are compared to have the following relationship:

$$\left\{ \begin{array}{l} V_R \approx -\frac{2\pi}{T} P_T \\ V_T \approx -\frac{2\pi}{T} P_R \\ V_N \approx \frac{2\pi}{T} P_N \left(u + \frac{\pi}{2} \right) \end{array} \right. \quad (5.111)$$

Error relationship of orbit elements between t and t_0 can be deduced approximately as follows:

$$\Delta a_t \approx \Delta a_0 + \Delta \dot{a} (t - t_0); \Delta e_t \approx \Delta e_0 + \Delta \dot{e} (t - t_0); \Delta i_t \approx \Delta i_0 + \Delta \dot{i} (t - t_0); \Delta \Omega_t \approx \Delta \Omega_0 + \Delta \dot{\Omega} (t - t_0); \Delta \omega_t \approx \Delta \omega_0 + \Delta \dot{\omega} (t - t_0); \Delta M_t \approx \Delta M_0 + \Delta \dot{M} (t - t_0)$$

According to orbit perturbation basics, e, i, Ω, ω errors are small in the six orbit elements and change slowly with time; owing to effects of atmospheric drag, error variation of the semimajor axis a changes faster than other elements. M error changes fast with time and is associated with the semimajor axis errors.

$$\Delta M_t \approx \Delta M_0 + \Delta \dot{M} (t - t_0) = \Delta M_0 - \frac{3n}{2a} (\Delta a_0 (t - t_0) + \Delta \dot{a} (t - t_0)^2) \quad (5.112)$$

As can be seen, T -direction position error has ΔM_t items, which contain a squared term and the first power term of time, and diverge rapidly with time delay. R -direction position error only contain the first power term of time, initial semimajor axis error, and the eccentricity error. Variation rate of the semimajor axis error $\Delta \dot{a}$ is relatively smaller than variation rate of ΔM_t , so the long-term divergence of Δa_t is not obvious. N -direction position error is determined by Δi_t and $\Delta \Omega_t$ and vibrate according to a sinusoid based on the orbital period. The above theoretical analysis is highly consistent with Table 3–1 simulation in Chapter 3, Space object detection technology. When tracking data of more than two passes of ascension and descension orbits are used and after orbit determination accuracy is stable, the position prediction error in both radial R and normal N directions is small and is stable based on prediction duration and T -direction error is maximum and diffuses greatly based on prediction duration.

Spacecraft collision warning and avoidance strategy

Spacecraft collision warning and avoidance strategy is closely related to the detection capability and tracking efficiency of early warning systems. Theoretically, spacecraft collision warning and avoidance strategy can be very simple: what is needed is only a minimum approaching distance threshold. If the distance between the spacecraft and the space object is within the threshold, then avoidance maneuver is needed, otherwise, the spacecraft will be safe. However, to satisfy the abovementioned situation, detection system should meet the following three conditions: (1) a reasonable distributed detection system network able to track all passes and orbits of all space objects could be calculated without any error; (2) orbit dynamics model is accurate enough that the orbit prediction precision over 1 week would be 10 m or better, with no error divergence; and (3) there is no need to consider fuel consumption cost, orbit control time, and spacecraft effective working time and life span. Obviously, to meet the abovementioned three conditions is unrealistic.

Facing with tens of thousands of space objects, based on current technology, the above conditions could not be satisfied even using up global detection resources. Therefore in engineering, in order to carry out high accurate spacecraft collision warning analytical work, a kind of reasonable and feasible collision warning and avoidance strategy must be drawn up.

In fact, collision warning and avoidance strategy is the unification of the coordination between the capacity and accuracy of the entire detection resources as well as the spacecraft capacity of emergency response and feasible countermeasures. In spacecraft engineering, a successful and implementable collision warning strategy should meet the following three principles: (1) no missing alarm and fewer false alarms, (2) no interference to spacecraft routine work, and (3) sufficient time for avoidance maneuver with the lowest consumption.

In order to maintain the catalog integrity of tens of thousands space objects, the detection resources should be distributed averagely so that at least one pass of tracking data of each object (especial LEO object) can be obtained within 24 hours. As illustrated in Section 3.5, based on 2–3 minutes of moderate-precision radar measurement data per day, the orbit precision of cataloged space objects could be at the kilometer level, the 24-hour propagated orbit precision could be at 10-km level, and the 7-day propagated orbit precision could be at 100-km level. This is the common capacity of detection resources in the world. Using the abovementioned orbit determination and orbit prediction for collision warning, there must be a large number of false alarms. If the latter is applied in engineering for spacecraft avoidance, a great quantity of useless maneuvers of spacecraft and lots of unnecessary fuel consumption will be inevitable. Ultimately, the collision warning work loses its engineering

value. Accordingly, the accuracy of orbit determination and orbit prediction becomes the key factor of the engineering feasibility of collision warning.

By using the measuring data of 1 day (or more) collected by global detection resources, the orbit precision of a space object can be more accurate than 10 m (see Section 3.5). However, considering the error of atmospheric model (particularly in Section 4.5), the orbit prediction precision in 24 hours could be several hundred meters, and that in 7 days could be 10 km. Therefore the collision warning based on orbit prediction of 100 m is the best means that current technology can achieve. To complete the orbit determination and prediction with the accuracy of 100 m of a space object, 1–2 days are needed in engineering. Considering the preparation for orbit control, a complete and feasible cycle of orbit measurement, prediction, early warning, and avoidance control will take 2–3 days, generally. Though it is not feasible for detection resources to make precision orbit determination and collision warning of all space objects in 3 days, it can be done if only for a few potential objects that really might be risky for collision. This chapter will discuss the following issues: how to select reasonable objects for precision orbit determination and collision warning with no missing alarm in 3 days ahead, as well as how to exclude false alarms and improve the reliability of early warning after precise orbit determination.

6.1 Collision warning calculation

There are two methods for space object collision warning: the minimum distance method (Box method) and the method based on probability of collision (Pc method). The minimum distance method is a kind of average method. NASA is the first one who adopted the method. If a space object enters the box area of $5 \text{ km} \times 25 \text{ km} \times 5 \text{ km}$ in RTN direction (radial, tangential, normal to the orbital plane), the object will be monitored with special attention. If the object enters the box area of $2 \text{ km} \times 5 \text{ km} \times 2 \text{ km}$ in RTN direction according to the calculation based on the latest orbit parameters, the decision on whether to perform avoidance maneuvers in action should be made combined with actual situations. However, the method does not consider the uncertainties of object position and geometry, resulting in high false alarm rate. Therefore scholars later proposed the probability of collision method for early warning. In fact, both methods have limitations. Nevertheless, according to the different features of objects and prediction duration, to carry out a comprehensive work of risk object screening, early warning and avoidance maneuvers based on the combination of the two methods may achieve success both theoretically and in engineering.

6.1.1 Risky object screening

The total number of measurable on-orbit space objects currently is around 16,000. The present available detection resources cannot afford to track and calculate orbits of all objects, and the calculation is unimaginable too. In order to reduce workload and improve computation efficiency, approaching analysis and risky object screening need to be done. In other words, before orbit prediction, the large amount of objects that will never collide with a

spacecraft needs to be removed first. The objects that might collide with the spacecraft and are within a certain distance to the spacecraft should be picked out for further orbit calculation and error analysis.

6.1.1.1 Screening by perigee and apogee

In order to find objects that might collide with the spacecraft in a short time, the initial screening of large quantities of space objects is needed. The first criterion is perigee and apogee. The objects whose perigee is greater than the spacecraft apogee and the objects whose apogee is smaller than the spacecraft perigee are removed. Further analysis will be made to the remaining objects.

Changes in perigee and apogee are mainly manifested in two aspects: one is the change in short term and the other is long term.

6.1.1.1.1 Short-term change of perigee

According to the basic theoretical knowledge of space object orbit, it is found that perigee can be expressed as:

$$H_p = a(1 - e) = (\bar{a} + a_s^{(1)})(1 - \bar{e} + e_s^{(1)}) = \bar{a}(1 - \bar{e}) + \bar{a}e_s^{(1)} + a_s^{(1)}(1 - \bar{e}) + a_s^{(1)}e_s^{(1)}. \quad (6.1)$$

where H_p , a , and e are, respectively, the instantaneous perigee, semimajor axis, and eccentricity of the space object; \bar{a} and \bar{e} are, respectively, the mean semimajor axis and mean eccentricity; while $a_s^{(1)}$ and $e_s^{(1)}$ are, respectively, the first-order, short-term items of the mean semimajor axis and mean eccentricity. For space objects the perigee change is mainly decided by two items in the middle of formula Eq. (6.1). Based on the orbit characteristic, the change of $\bar{a}e_s^{(1)}$ is within 10 km, and the change of $a_s^{(1)}(1 - \bar{e})$ is relevant with J_2 by 10^{-3} , which is usually within 10 km too. Therefore according to the characteristics of space object, it can be estimated that the change of perigee is generally about 10 km.

The change of apogee is similar to the change of perigee in short term.

6.1.1.1.2 Long-term change of perigee

As for LEO space object, the long-term change of its perigee is mainly influenced by atmospheric effects, resulting in decrease of perigee. The relationship between semimajor axis attenuation (m/ring) and atmospheric density, surface-to-mass ratio, and the semimajor axis is [3]:

$$da = -2\pi C_D \frac{S}{M} \rho a^2 \quad (6.2)$$

where C_D is the coefficient of atmospheric drag, S/M is the surface-to-mass ratio, and ρ is the atmospheric density.

According to the abovementioned formula and historical experience, the perigee change in 24 hours is within a few 100 m.

The change of apogee is similar to the change of perigee in long term.

Based on the abovementioned short-term and long-term changes, the estimation of space orbit is generally about a dozen kilometers, or up to 20 km.

6.1.1.1.3 Calculation and analysis of space object orbit change

To support the abovementioned theoretical analysis and estimation results, some actual satellite data are calculated. The change of perigee is shown from Figs. 6–1 to 6–4.

6.1.1.2 Screening by the geocentric distance of intersection

The second criterion is the geocentric distance of intersection. For two objects on two orbital planes, as long as the inclination or right ascension of the two objects is not equal, there will be two intersection points theoretically. The two objects might collide with each other only at the intersection points, so the geocentric distance of intersection becomes an important reference for the screening for risk objects, too. Space targets are screened according to the intersection geocentric distance, leaving targets that may pose a threat to spacecraft on-orbit for further analysis.

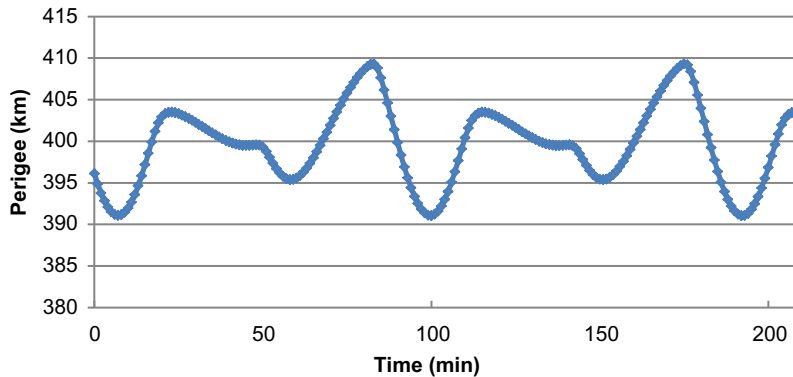


FIGURE 6–1 The perigee variation of object 25544 ($H_a = 410$ km, $H_p = 401$ km).

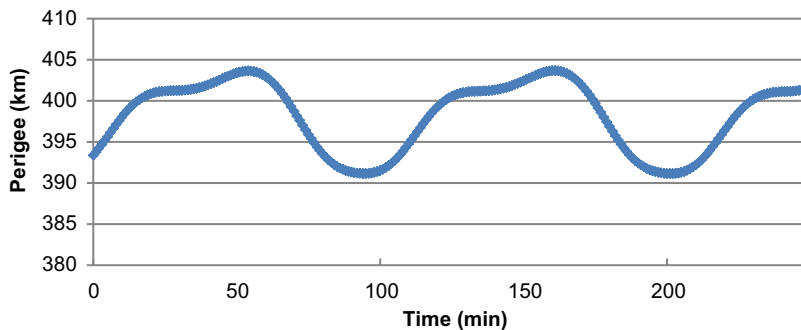


FIGURE 6–2 The perigee variation of object 21393 ($H_a = 1765$ km, $H_p = 398$ km).

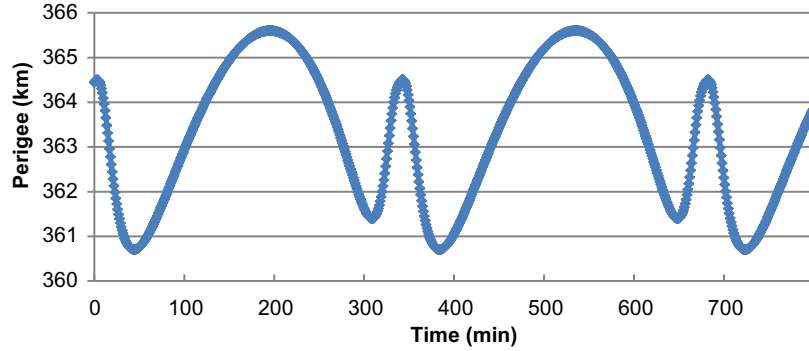


FIGURE 6-3 The perigee variation of object 28920 ($H_a = 19,126$ km, $H_p = 361$ km).

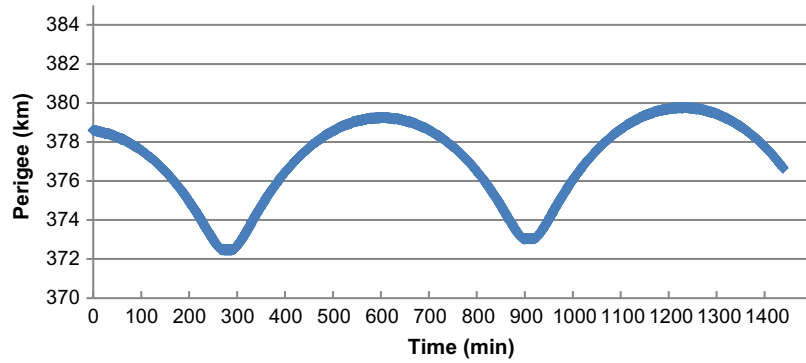


FIGURE 6-4 The perigee variation of object 39774 ($H_a = 35,513$ km, $H_p = 372$ km).

As shown in Fig. 6-5, i_0 and i_1 refer to the inclination of the spacecraft and orbit debris; A and B refer to orbit ascending node; C refers to the intersection of orbital planes; Θ refers to the intersection angle; \widehat{AB} refers to the difference of ascending node $\Delta\Omega$; \widehat{AC} refers to the arc u_0 from the spacecraft to the ascending node; and \widehat{BC} refers to the arc u_1 from the ascending node to the intersection. It can be obtained the following:

$$\cos\theta = \cos i_1 \cos i_0 + \sin i_1 \sin i_0 \cos\Delta\Omega \quad (6.3)$$

$$\sin u_1 = \frac{\sin\Delta\Omega}{\sin\theta} \sin i_1 \quad (6.4)$$

$$\sin u_0 = \frac{\sin\Delta\Omega}{\sin\theta} \sin i_0 \quad (6.5)$$

By using the abovementioned formula, u_0 u_1 can be calculated and then the geocentric distance of intersection r_0 r_1 can be obtained. According to the geocentric distance of intersection, the space objects whose $|r_0 - r_1| > \Delta d$ can be removed.

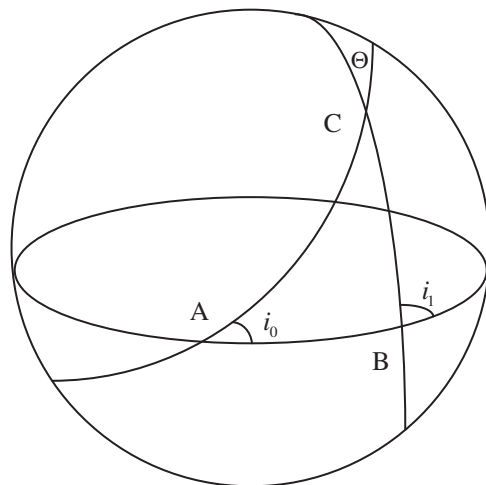


FIGURE 6-5 The celestial sphere diagram of satellites and debris.

When calculating the geocentric distance between two objects, the time difference between the two objects crossing the intersection point can be calculated simultaneously. However, as the two-body model is adopted in the calculation, using the time difference as a screening criteria will lead to a high false dismissal rate in practical engineering, thus it is often discarded.

6.1.1.3 Screening by the minimum distance between orbital planes

The third criterion is the minimum distance between two orbital planes. According to the criterion, the objects that may pose a threat to the spacecraft are picked out for further analysis.

The screening by the minimum distance between two orbital planes considers the geometry relationship of the two orbital planes. The intersection of two orbital planes is shown in Fig. 6-6.

For two elliptical orbits, there must be two closest distance d_1 and d_2 , which are near the intersection line. d_1 and d_2 are called the minimum distance between two orbital planes. If the minimum distance between two orbital planes is greater than the threshold D , then there would be no possibility of collision for the two objects. Since the calculation of d_1 and d_2 is narrated in Ref. [107], herein it is omitted.

The three methods introduced here do not need detailed orbital calculation, but only qualitative judgment using four slow-varying parameters a, e, i , and Ω in the six elements of orbit. As long as one of the methods is used, the target whose orbit satisfies any one of the conditions will not collide with the primary target. Thus the calculation workload can be reduced by an order of magnitude with the minimum amount of computation and the fastest speed.

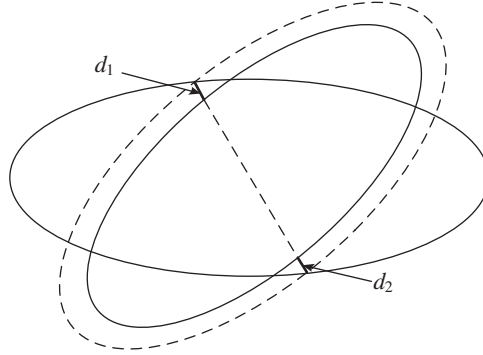


FIGURE 6–6 Screening by the minimum distance between two orbital planes.

6.1.2 The minimum distance calculation

The minimum distance and related parameters of two approaching objects is one of the important factors to determine whether there is a risk of collision. Neglecting the orbit prediction error, the factor becomes crucial for collision possibility calculation. Parameters involved in the minimum distance method includes the minimum distance between two objects, the distance component in UNW (or RTN) direction, the approaching velocity, the approaching angle, etc.

6.1.2.1 The minimum distance

For the relative minimum distance between two space objects, the main factor affecting the accuracy of the result is orbit propagation precision. Therefore for relevant objects, high-precision dynamic model should be adopted to make orbit extrapolation calculation. The method mainly consists of three parts that are discussed in the following subsections.

6.1.2.1.1 Space object orbit propagation

The dynamic model of space object orbit propagation is

$$\ddot{\mathbf{r}} = \mathbf{a}_0 + \mathbf{a}_\varepsilon \quad (6.6)$$

$$\mathbf{a}_0 = -\frac{GM_e}{r^3} \mathbf{r} \quad (6.7)$$

$$\mathbf{a}_\varepsilon = \sum_{i=1}^6 \mathbf{a}_i \quad (6.8)$$

where G refers to Earth gravitational constant, \mathbf{a}_0 refers to the gravity acceleration of the center of the particle earth, and \mathbf{a}_ε refers to the total perturbation acceleration. The involving perturbation models are as follows: Earth nonspherical perturbation, the third-body

perturbation, atmospheric damping perturbation, solar radiation pressure, earth tide, tidal perturbation, and relativistic effects.

6.1.2.1.2 The minimum distance calculation

Suppose the spacecraft position vector is $\mathbf{r}_1 = (x_1 \ y_1 \ z_1)^T$, the space object position vector is $\mathbf{r}_2 = (x_2 \ y_2 \ z_2)^T$, then the relative distance of the two objects is

$$D = \sqrt{(x_1 - x_2)^2 + (y_1 - y_2)^2 + (z_1 - z_2)^2} \quad (6.9)$$

The relative distance at all epoch between the spacecraft and the space object can be obtained, and then find the minimum one among them.

6.1.2.1.3 The relationship between relative velocity and relative distance at minimum distance

In J2000 geocentric inertial coordinate system, suppose the position vectors of the spacecraft and the space object are, respectively, \mathbf{r}_1 and \mathbf{r}_2 ; the velocity vectors of the spacecraft and the space object are, respectively, \mathbf{v}_1 and \mathbf{v}_2 ; and then the relative distance vector between the two will be

$$\Delta \mathbf{r} = \mathbf{r}_1 - \mathbf{r}_2 \quad (6.10)$$

Then the approaching velocity between the two will be

$$\Delta \mathbf{v} = \mathbf{v}_1 - \mathbf{v}_2 \quad (6.11)$$

The square of the relative distance vector will be

$$|\Delta \mathbf{r}|^2 = (\mathbf{r}_1 - \mathbf{r}_2) \cdot (\mathbf{r}_1 - \mathbf{r}_2) \quad (6.12)$$

Since now the minimum distance is achieved, then

$$\frac{d|\Delta \mathbf{r}|^2}{dt} = 2(\mathbf{r}_1 - \mathbf{r}_2) \cdot \frac{d(\mathbf{r}_1 - \mathbf{r}_2)}{dt} = 2(\mathbf{r}_1 - \mathbf{r}_2) \cdot (\mathbf{v}_1 - \mathbf{v}_2) = 0 \quad (6.13)$$

It can be obtained that

$$\Delta \mathbf{r} \cdot \Delta \mathbf{v} = 0 \quad (6.14)$$

This indicates that when the distance is the minimum, the relative position vector is perpendicular to the relative velocity vector. This feature can be used as a modified formula for iterative calculation of the nearest distance and greatly improves the calculation efficiency and accuracy.

6.1.2.2 The distance calculation in three directions

In order to describe the approaching of two space objects, besides the minimum distance, the distance components in three directions in UNW (or RTN) coordinate are also used.

In J2000 geocentric inertial coordinate system, suppose the position vectors of the spacecraft and space object at the minimum distance are \mathbf{r}_1 and \mathbf{r}_2 , the relative distance between two objects will be

$$\Delta \mathbf{r} = \mathbf{r}_1 - \mathbf{r}_2 \quad (6.15)$$

Then in UNW coordinate system with the center of mass of the spacecraft as the origin, the distance components of the minimum distance in three directions are

$$\Delta \mathbf{r}_{\text{UNW}} = \mathbf{M}_{\text{UNW}} \cdot \Delta \mathbf{r} \quad (6.16)$$

where \mathbf{M}_{UNW} represents the transformation matrix from J2000 inertial coordinate system to UNW coordinate system.

Then in RTN coordinate system with the center of mass of the spacecraft as the origin, the distance components of the minimum distance in three directions are

$$\Delta \mathbf{r}_{\text{RTN}} = \mathbf{M}_{\text{RTN}} \cdot \Delta \mathbf{r} \quad (6.17)$$

where \mathbf{M}_{RTN} represents the transformation matrix from J2000 inertial coordinate system to RTN coordinate system.

6.1.2.3 The precision evaluation of three distance components

Among all thresholds in collision warning, the distance threshold is mainly relevant to the error of orbit prediction, which is determined by orbit determination error and prediction models. The orbit determination error is decided by the quality and number of data acquired by detection resources. Orbit prediction errors of different space objects are shown from Figs. 6–7 to 6–9.

According to Figs. 6–7 to 6–9 and the analysis in Section 5.2.4, the following conclusions for near-circular orbit objects are listed as follows:

1. The prediction error in radical and normal direction is relatively stable and is much smaller than that in tracking direction.
2. The prediction error is mainly in tracking direction, which is of rapid divergence over time. The lower the orbit altitude is, the more serious the divergence is. The prediction error in tracking direction is not of zero mean distribution. Instead, there is some systematical deviation; the prediction error is near the side of real trajectory.
3. The prediction error in radical direction is of divergence over time (but relative slowly) and systematical deviation. The lower the orbit altitude is, the more serious the divergence is.

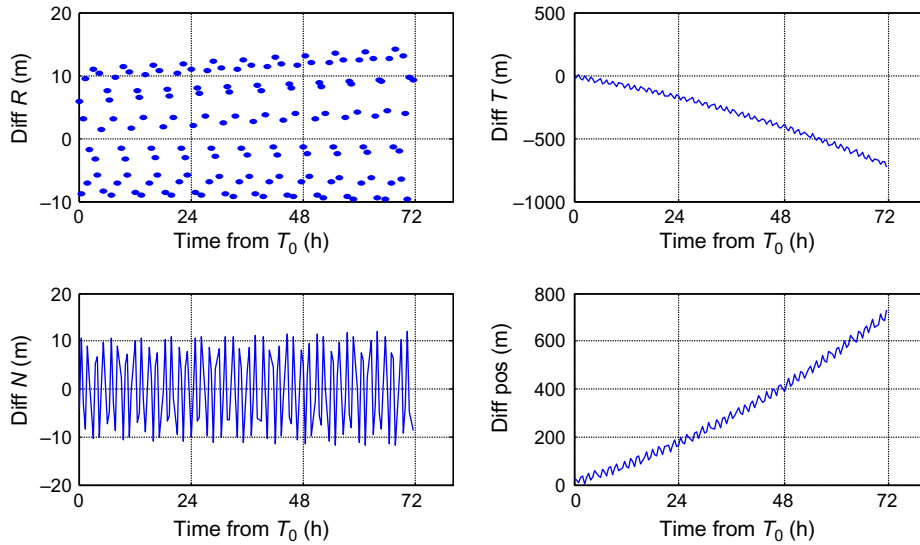


FIGURE 6-7 Orbit prediction error of object 1.

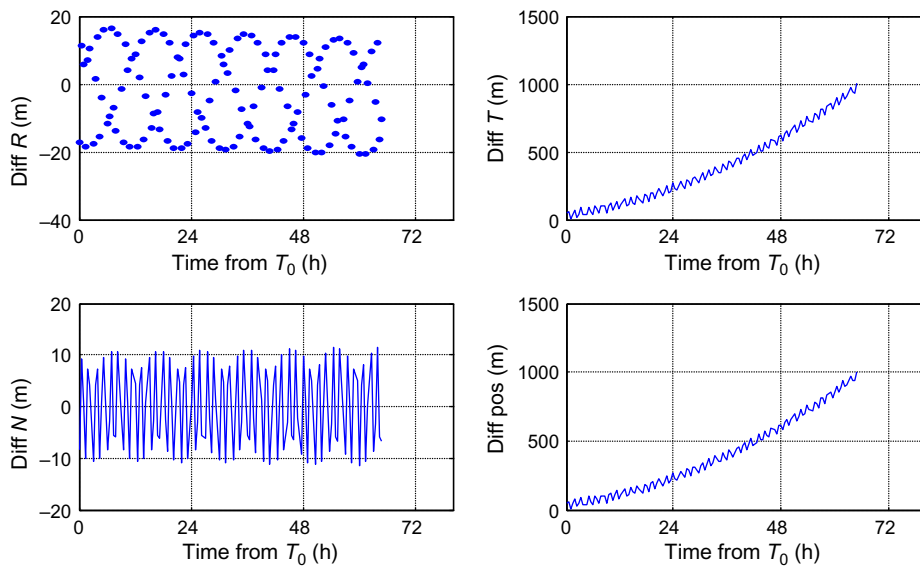


FIGURE 6-8 Orbit prediction error of object 2.

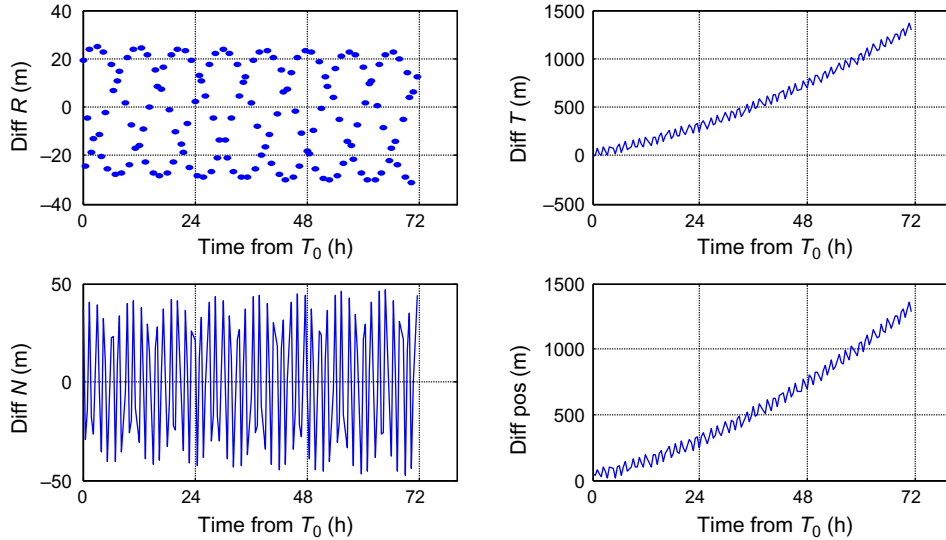


FIGURE 6–9 Orbit prediction error of object 3.

4. The prediction error in normal direction is smaller, most of which is under 100 m. Usually, it is of zero mean distribution, given nice measurement data constraint.

Therefore besides the minimum distance, radical distance is also considered to be an importance reference for collision warning threshold. Because the accuracy in radical and normal direction is much higher than that in tracking direction, by radical error, a great quantity of false alarms can be removed. If the velocity vectors of two objects at the approaching epoch are parallel or near parallel, normal error can also be used for removing false alarms.

6.1.2.4 Approaching angle and velocity calculation

In J2000 geocentric inertial coordinate system, suppose the position vectors of the spacecraft and space object are, respectively, \mathbf{r}_1 and \mathbf{r}_2 ; the velocity vectors of the spacecraft and space object are, respectively, \mathbf{v}_1 and \mathbf{v}_2 ; and then the approaching angle between the two objects will be

$$\theta = \arccos \frac{\mathbf{v}_1 \cdot \mathbf{v}_2}{|\mathbf{v}_1| \cdot |\mathbf{v}_2|} \quad (6.18)$$

Then the approaching velocity between the two objects will be

$$\Delta \mathbf{v} = |\mathbf{v}_1 - \mathbf{v}_2| \quad (6.19)$$

6.1.3 The probability of collision method

In space object collision risk analysis, the calculation of the probability of collision is one of the foundations. The probability of collision method adopts probability of collision as the index to describe collision risk degree. Probability of collision is defined as the probability of collision of two space objects, the position prediction of which is of errors. The calculation of probability of collision relies on the position, velocity, and the position covariance matrix information of spacecraft and space debris when they come across.

6.1.3.1 Probability of collision

Probability of collision is the probability when the distance between the center of objects is smaller than the combination of equivalent radius, which can be illustrated as $P_c = P(\rho < R)$ [107–109]. The distance between two objects is $\rho = |\rho| = |\mathbf{r}_1 - \mathbf{r}_2|$. The actual position of two objects are \mathbf{r}_1 and \mathbf{r}_2 , which can be expressed as the combination of the distribution center of two objects and a random error vector, that is, $\mathbf{r}_1 = \mathbf{r}_{1o} + \mathbf{e}_1$ and $\mathbf{r}_2 = \mathbf{r}_{2o} + \mathbf{e}_2$.

It is demonstrated in Section 6.1.2 that when the minimum distance between the two objects is achieved, the two objects are on a plane that is perpendicular to the relative velocity vector, and the plane is defined as the encounter plane. In this way the uncertainty of the position of two objects is allowed to be projected to the encounter plane so that the three-dimensional problem is simplified into a two-dimensional (2D) problem.

For the encounter plane, the function of probability of collision $f(x, z)$ and probability of collision P_c is calculated as the 2D Gaussian probability density function (PDF) is

$$f(x, z) = \frac{1}{2\pi\sigma'_x\sigma'_z} \exp \left[-\frac{1}{2} \left(\frac{(x-\mu_x)^2}{\sigma'_x{}^2} + \frac{(z-\mu_z)^2}{\sigma'_z{}^2} \right) \right] \quad (6.20)$$

where σ'_x and σ'_z are components of the error, while μ_x and μ_z are the distance components of the relative distance in the coordinate system of encounter plane. The probability of collision can be expressed as the integral of PDF in the circular domain:

$$P_c = \iint_{x^2+z^2 \leq R^2} f(x, z) dx dz \quad (6.21)$$

The probability of collision results mainly contains the following items: object size, relative position, relative velocity, and position errors.

6.1.3.2 The maximum probability of collision

Theoretical and practical analysis show that, for a given intersection location, speed, geometry, and size of two objects, the probability of collision will increase with the increase of the position error uncertainty. Under certain conditions of the positional error, the probability of collision reaches the maximum, then the probability of collision decreases when the position error increases. In practical engineering applications the maximum probability of collision calculation is very important. Because the actual position error and the covariance matrix of

spacecraft and space object are generally unknown or only the shape without the specific size of the error ellipsoid is known, it is necessary to determine the probability of collision in the worst case. The maximum probability of collision can be also used for prescreening of space objects. When the maximum probability of collision is less than a threshold, it is supposed that the object will not pose a threat to spacecraft [101].

2D normal distribution PDF is as follows:

$$f(x, z) = \frac{1}{2\pi\sigma'_x\sigma'_z} \exp\left[-\frac{1}{2}\left(\frac{(x-\mu_x)^2}{\sigma'^2_x} + \frac{(z-\mu_z)^2}{\sigma'^2_z}\right)\right] \quad (6.22)$$

The probability of collision can be expressed as the integral of PDF in the circular domain:

$$P_c = \iint_{x^2+z^2 \leq R^2} f(x, z) dx dz \quad (6.23)$$

Because of the token independence of integral, the variable z is replaced by variable y in the following to be convenient. The unequal variance PDF is expressed as:

$$f(x, y) = \frac{1}{2\pi\sigma_x\sigma_y} \exp\left[-\frac{1}{2}\left(\frac{(x-\mu_x)^2}{\sigma^2_x} + \frac{(y-\mu_y)^2}{\sigma^2_y}\right)\right] \quad (6.24)$$

The probability of collision P_c is expressed as

$$P_c = \frac{1}{2\pi\sigma^2} \iint_{x^2+y^2 \leq R^2} \exp\left[-\frac{(x-\mu_x)^2 + (y-\mu_y)^2}{2\sigma^2}\right] dx dy \quad (6.25)$$

Suppose

$$\mu_r = \sqrt{\mu_x^2 + \mu_y^2} \quad (6.26)$$

Define dimensionless variable

$$v = \frac{\mu_r^2}{2\sigma^2}, \quad u = \frac{R^2}{2\sigma^2} \quad (6.27)$$

Probability of collision P_c can be reduced to the form of infinite series. The first item is adopted as the approximation of P_c :

$$P_c = e^{-v}(1 - e^{-u}) \quad (6.28)$$

In order to find the maximum of P_c , differentiate P_c of σ , and suppose the partial derivative is 0, then

$$\begin{aligned}\frac{\partial P_c}{\partial \sigma} &= \frac{\partial P_c}{\partial v} \frac{\partial v}{\partial \sigma} + \frac{\partial P_c}{\partial u} \frac{\partial u}{\partial \sigma} \\ &= e^{-v}(1 - e^{-u}) \frac{\mu_r^2}{\sigma^3} - e^{-v} e^{-u} \frac{R^2}{\sigma^3} = 0\end{aligned}\quad (6.29)$$

Rearranging the equation, we obtain

$$u = \ln \left(1 + \frac{R^2}{\mu_r^2} \right) \quad (6.30)$$

When P_c is the maximum, σ is

$$\sigma_D = \frac{R}{\sqrt{2 \ln \left(1 + (R^2 / \mu_r^2) \right)}} \quad (6.31)$$

The formula is substituted into the probability of collision of a first-order approximation expression, the maximum probability of collision $P_{c\max}$ is

$$P_{c\max} = \frac{R^2}{R^2 + \mu_r^2} \left(\frac{\mu_r^2}{R^2 + \mu_r^2} \right)^{\mu_r^2 / R^2} \quad (6.32)$$

Define dimensionless variable

$$\lambda = \frac{\mu_r^2}{R^2} = \frac{v}{u} \quad (6.33)$$

Then the maximum probability of collision $P_{c\max}$ is

$$P_{c\max} = \frac{\lambda^\lambda}{(1 + \lambda)^{1 + \lambda}} \quad (6.34)$$

6.1.3.3 Influence of related parameters on probability of collision

Because there are errors in measurement and much uncertainty in orbit trajectory, in collision warning analysis, the influence of space motion (approaching distance, approaching angle), space orbit minimum distance, probability of collision, and other parameters must be considered. In space rendezvous determination, the influence factors and scales on collision warning need to be analyzed deeply.

The calculation of probability of collision comprehensively considers the geometry of rendezvous, the orbit prediction error, the size of object, and other factors, which is a comprehensive risk assessment index. However, in collision warning engineering, approaching

distance (and its UNW components), relative velocity, and rendezvous angle are important risk assessment indexes too. Under some situations, Box method based on UNW distance is more reliable, but more reliable indicates more conservative.

In such cases, it is necessary to understand the probability of collision, the UNW components of approaching distance, and their relationship in rendezvous geometry for further understanding of two indexes and their significance in reasonable application.

6.1.3.3.1 The Influence of distance and position error in N direction on probability of collision

According to the explicit formulation of probability of collision, probability of collision decreases with the distance increase in N direction. Fig. 6–10 shows the variation curve of probability of collision P_c with the distance change in N direction.

Fig. 6–11 shows P_c variation with the distance change in N direction too. However, its vertical coordinate axis is in logarithmic form. Fig. 6–11 shows that when $N > 2 \text{ km} \approx 4\sigma_N$, $P_c < 10^{-8}$.

The influence of the overall position prediction error is the same with the influence in each direction in the following: the probability of collision P_c increases first and then decreases after reaching its maximum value. Suppose the distance in N direction changes and other conditions remain unchanged. Fig. 6–12 shows P_c variation with the distance error standard deviation variation in N direction. When $\sigma_N = 0.0315 \text{ km} \approx N$, P_c reaches its maximum 2.966×10^{-4} .

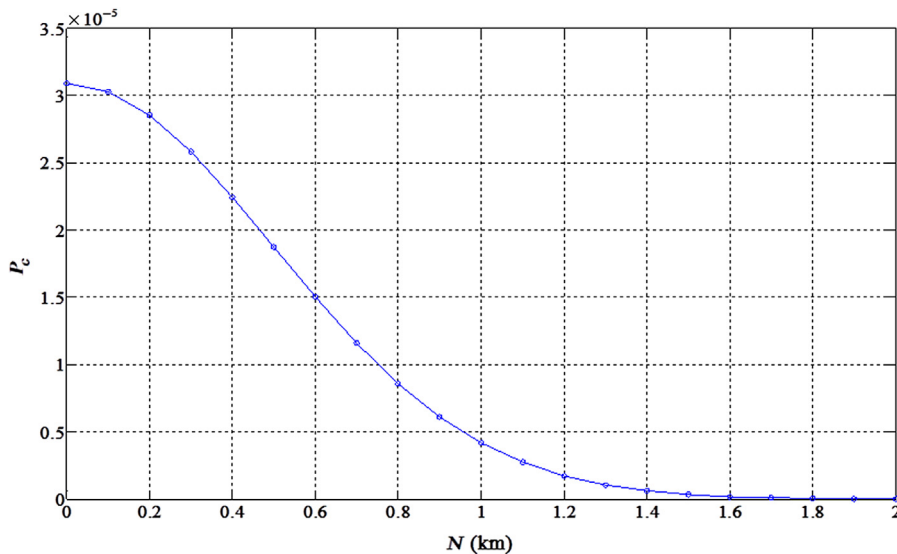


FIGURE 6–10 P_c variation with the distance change in N direction.

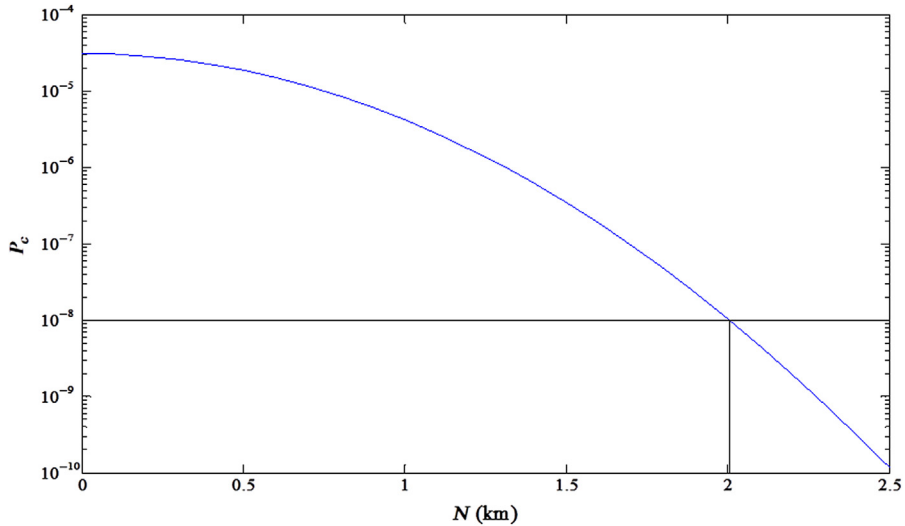


FIGURE 6-11 P_c variation with the distance change in N direction (vertical coordinate axis in logarithmic form).

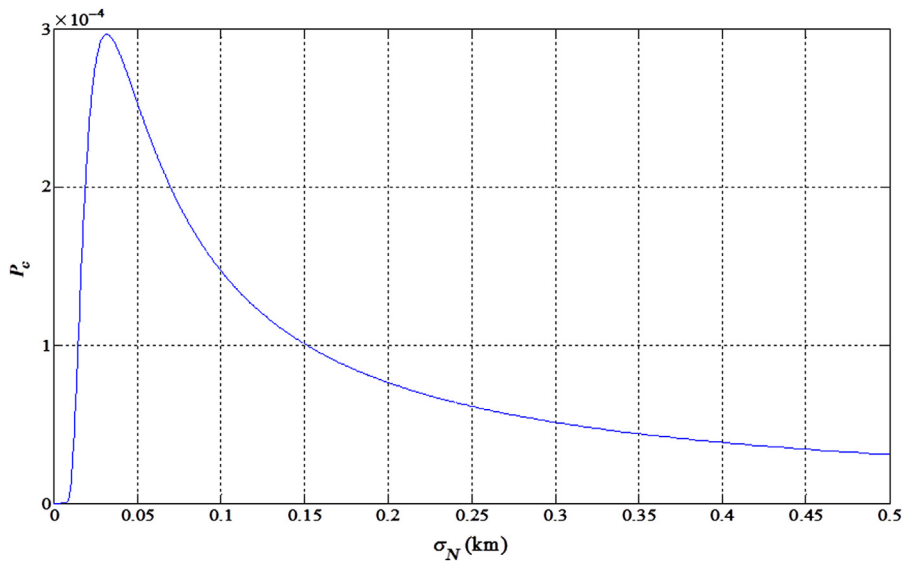


FIGURE 6-12 P_c variation with the distance error standard deviation variation in N direction.

6.1.3.3.2 The Influence of distance and position error in U and W direction on probability of collision

According to the explicit formulation of probability of collision, probability of collision decreases with the increase of the joint distance in U and W direction $\sqrt{U^2 + W^2}$. In the case where other conditions remain unchanged, Fig. 6-13 shows the variation of probability

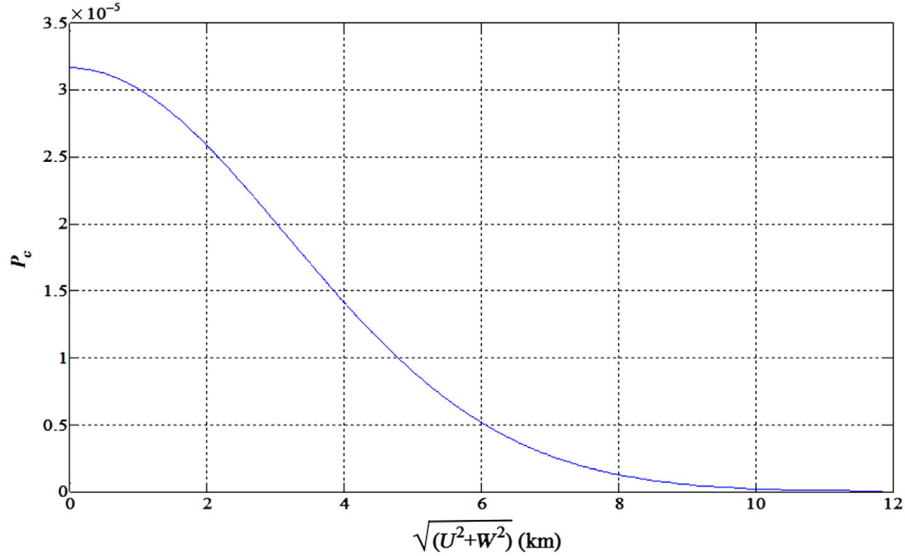


FIGURE 6–13 P_c variation with the change of $\sqrt{U^2 + W^2}$.

of collision P_c with the change of $\sqrt{U^2 + W^2}$. When $\sqrt{U^2 + W^2} > 10 \text{ km} \approx 3\sigma_{UW}$, P_c is already very small.

Suppose the error in U and W direction changes with the scale factor k , and other conditions remain unchanged. Fig. 6–14 shows the variation of probability of collision P_c with the change of k . When $k = 0.221$, that is, $\sigma_{UW} = 0.221 \times 3.1554 = 0.6973 \text{ km}$, P_c reaches its maximum 8.678×10^{-5} .

6.1.3.3.3 The influence of approaching angle on probability of collision

The influence of orbital plane angle φ on probability of collision depends on the shape and the size of the joint error ellipsoid. In general, the prediction error in U direction is larger than that in W direction. At this time, with the orbital plane angle φ increasing from 0 to π , the joint error in U and W direction decreases. If the prediction error in U direction is greater than that in W direction, with the orbital plane angle φ increasing from 0 to π , the joint error in U and W direction increases. This result is derived by the following equation. The joint error variance on horizontal plane is

$$\sigma_{UW}^2 = \sigma_U^2 \cos^2 \frac{\varphi}{2} + \sigma_W^2 \sin^2 \frac{\varphi}{2} = \sigma_U^2 + (\sigma_W^2 - \sigma_U^2) \sin^2 \frac{\varphi}{2} \quad (6.35)$$

When $\sigma_W^2 < \sigma_U^2$, σ_{UW}^2 decreases with the increase of φ in $[0, \pi]$; when $\sigma_W^2 > \sigma_U^2$, σ_{UW}^2 increases with the increase of φ in $[0, \pi]$.

In most cases where the orbital error is large, probability of collision decreases with the increase of error. When $\sigma_W^2 < \sigma_U^2$, probability of collision increases with the increase of φ in $[0, \pi]$; when $\sigma_W^2 > \sigma_U^2$, the probability of collision decreases with the increase of φ in $[0, \pi]$.

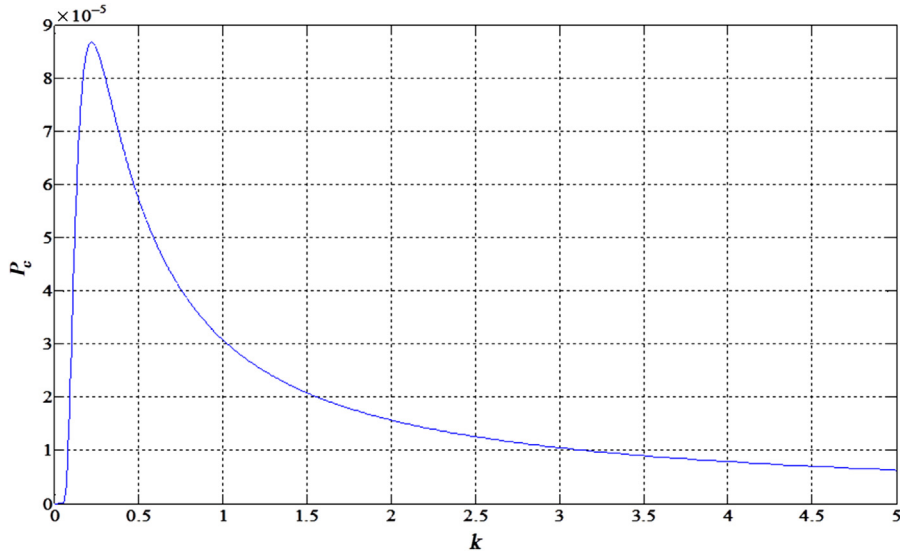


FIGURE 6-14 P_c variation with the change of k .

Fig. 6-15 shows P_c variation with the change of approaching angle. Because $\sigma_W^2 < \sigma_U^2$, σ_{UW}^2 decreases with the increase of φ , and the probability of collision increases first, and then decreases after reaching its maximum.

By analyzing the factors that affect probability of collision, we can get the following conclusions:

1. Because of the difference of the joint error ellipsoid shape, the impact of the angle between orbital planes on probability of collision is different. When the error in T direction is greater than that in N direction, the probability of collision increases with the increase of the angle between orbital planes; when the error in T direction is smaller than that in N direction, the probability of collision decreases with the increase of the angle between orbital planes. Generally, in position prediction, the error in T direction is always greater than that in R and N direction, so the probability of collision usually increases with the increase of the angle between orbital planes.
2. The influence of the overall position prediction error is the same with the influence in each direction in the following: the probability of collision increases first, and then decreases after reaching its maximum.

6.2 The method of spacecraft avoidance

On-orbit avoidance is an important measure for the safety of space mission. Collision avoidance maneuver is defined as to make sure that spacecraft do not collide with other space objects by orbit maneuvers based on comprehensive consideration of mission constraints

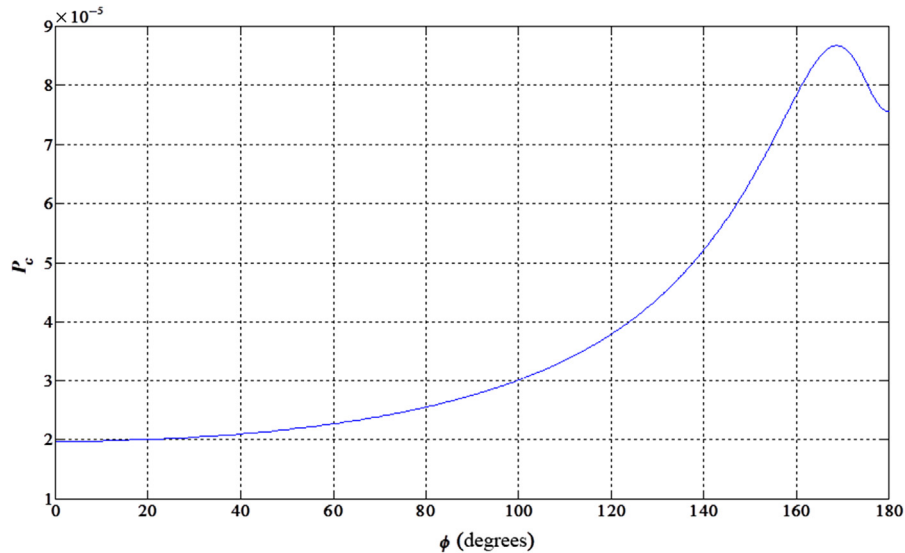


FIGURE 6-15 P_c variation with the change of approaching angle.

and orbit maintenance, according to the analysis of collision warning and information such as collision risk and geometric relation. Based on collision risk analysis, collision avoidance maneuver is able to give the guidelines and criteria of whether avoidance maneuver is needed, and the calculation methods and implementation strategies of optimal collision avoidance maneuvers, including the selection of direction and duration of thrust. Therefore avoidance maneuver is essentially a problem of orbit maneuvers, the essence of which is optimal transfer and mission constraints. In the choice for avoidance maneuver opportunity, spacecraft should be under the monitoring of tracking stations, and after orbit transfer, real-time measurement data could be obtained immediately so that the avoidance result can be evaluated. In calculation of speed increment the performance of spacecraft engine such as fuel and thrust needs to be considered too.

At present, many studies cast a light on impulse maneuvers for collision avoidance. According to the duration between rendezvous collision and orbit maneuvers, two collision avoidance strategies are offered: short-term and middle-term strategies. Short-term strategy is realized by altitude avoidance method. Since orbit prediction is made when collision is coming, a tangential velocity increment added by onetime pulse is adopted by this strategy so that the distance (radial distance) between the altitudes of two objects at the time when they approach each other is enlarged. Obviously, the required speed increment is greater. For middle-term strategy the method of separation in tracking direction is adopted. If there is still a long time before the rendezvous occurs, several small increments of velocity in tracking direction is then adopted so that the tangential distance between two objects at the approaching point will be increased. In other words, both the objects will encounter the intersection site, but they will be there in different time instead of simultaneously.

6.2.1 Altitude avoidance method

Altitude avoidance method is to pose a velocity increment along tracking direction during $n + 1/2$ ($n = 0, 1, 2, \dots$) orbit pass before potential collision, raising or lowering the altitude of spacecraft, and therefore when the spacecraft goes through the expected intersection site, there will be a radial distance from the risky object so as to avoid collision.

It is certain that at t_1 , the spacecraft may collide with an object. It is required that within t_0 , orbit maneuvers should be implemented, and because the potential collision is close to the maneuver time, altitude avoidance strategy is adopted. It can be seen that the key points of altitude avoidance are that the position and velocity of spacecraft at the time of maneuver and the object position are known, and orbit elements and velocity increment need to be calculated.

Suppose when no avoidance maneuver is taken, the spacecraft orbit is σ_0 and σ_1 at t_0 and t_1 . If orbit maneuver is taken at t_0 , then the spacecraft orbit is σ'_0 and σ'_1 at t_0 and t_1 .

According to the theory of orbit motion and avoidance constraints, there are

$$\begin{aligned}\sigma_1 &= \sigma_0 + \overline{\sigma}_1(t_1 - t_0) + \overline{\sigma}_s(t_1) - \overline{\sigma}_s(t_0) \\ \sigma'_1 &= \sigma'_0 + \overline{\sigma}'_1(t_1 - t_0) + \overline{\sigma}'_s(t_1) - \overline{\sigma}'_s(t_0) \\ \sigma'_0 &= \sigma_0 + \Delta\sigma_0(\Delta v) \\ r(\sigma'_1) &= r(\sigma_1) + \Delta r\end{aligned}\quad (6.36)$$

where σ_0 and σ_1 are the instantaneous orbit elements at t_0 and t_1 , $\overline{\sigma}_1$ and $\overline{\sigma}_s$ are the long-periodic and short-periodic coefficients of the orbit elements before the orbit changes; σ'_0 and σ'_1 are the instantaneous orbit element at t_0 after the orbit changes at t_0 and t_1 ; $\overline{\sigma}'_1$ and $\overline{\sigma}'_s$ are the long-periodic and short-periodic coefficients of the orbit elements after the orbit changes; $\Delta\sigma_0(\Delta v)$ represents the change of orbit elements caused by the speed variation after the orbit changes at t_0 ; and r is the position vector and Δr is the change of the position.

Because the energy consumption of orbit maneuver is small, the increment is small, too. Therefore $\Delta\sigma(\Delta a/a, \Delta e, \Delta i, \Delta\Omega, \Delta\omega, \Delta M)$ is generally of the amount of $O(10^{-3})$, and the difference between $\overline{\sigma}_1(\overline{\sigma}_0)$ and $\overline{\sigma}'_1(\overline{\sigma}'_0)$ is of $O(J_2 \cdot \Delta\sigma_{a,e,i}) = O(10^{-6})$. Similarly, the difference between $\overline{\sigma}_s$ and $\overline{\sigma}'_s$ is of $O(10^{-6})$. Since the altitude avoidance method is often taken in emergency when the maneuver time and collision time is relatively close (no more than one cycle), there is $\Delta\sigma = (\overline{\sigma}'_1 + \overline{\sigma}_1)(t_1 - t_0) + (\overline{\sigma}'_s(t_1) - \overline{\sigma}_s(t_1)) - (\overline{\sigma}'_s(t_0) - \overline{\sigma}_s(t_0))$, which is about the magnitude of $O(10^{-5})$.

Based on the abovementioned analysis, in calculation of avoidance maneuver, two-body computation can be adopted. Lambert Flight Time Theory is adopted by this book for calculation. The calculation steps are as follows:

1. The iterative equation of semimajor axis a is obtained by the Lambert equation:

$$F(a) = n(t_2 - t_1) - ((\alpha - \sin\alpha) - (\beta - \sin\beta)) = 0 \quad (6.37)$$

The Newton iterative method is used for solving Eq. (6.37). Through Taylor expansion, it is estimated an initial value a_0 , and only get to Δa ,

$$F(a) = F(a_0) + \left(\frac{dF}{da}\right)\Delta a = 0 \quad (6.38)$$

$$\frac{dF}{da} = -\frac{3n}{2a}(t_2 - t_1) + \frac{r_1 + r_2 + c}{2a^2} \tan \frac{\alpha}{2} - \frac{r_1 + r_2 - c}{2a^2} \tan \frac{\beta}{2} \quad (6.39)$$

where $n = \sqrt{\mu/a^3}$

$$\begin{cases} \sin \frac{\alpha}{2} = \sqrt{\frac{r_1 + r_2 + c}{4a}} \\ \sin \frac{\beta}{2} = \sqrt{\frac{r_1 + r_2 - c}{4a}} \end{cases} \quad (0 \text{ degrees} < \beta < \alpha \leq 180 \text{ degrees}) \quad (6.40)$$

$$c = |\vec{r}_1 - \vec{r}_2|$$

Δt_m is the time when the minimum energy ellipse flies from t_0 to t_1 :

$$\Delta t_m = \sqrt{\frac{S^3}{2\mu}} \frac{[\alpha_m - \sin \alpha_m + (\beta_m - \sin \beta_m)]}{2} \quad (6.41)$$

In formula Eq. (6.41),

$$S = \frac{r_1 + r_2 + c}{2} \quad (6.42)$$

For the control problem where the geocentric distance r_1, r_2 and its angle Δf are known, the semimajor axis can be obtained based on the relationship between Δt and Δt_m , and the value of Δf :

$$\Delta t = t_2 - t_1 \quad (6.43)$$

$$\tan \Delta f = \frac{\mathbf{r}_2 \times \mathbf{r}_1}{\mathbf{r}_2 \cdot \mathbf{r}_1} \quad (6.44)$$

When $\Delta f \leq 180$ degrees, $\Delta t \leq \Delta t_m$

$$\begin{aligned} F(a) &= n(t_2 - t_1) - [(\alpha - \sin \alpha) - (\beta - \sin \beta)] \\ \frac{dF}{da} &= -\frac{3n}{2a}(t_2 - t_1) + \left(\frac{r_1 + r_2 + c}{2a^2} \tan \frac{\alpha}{2} - \frac{r_1 + r_2 - c}{2a^2} \tan \frac{\beta}{2} \right) \end{aligned} \quad (6.45)$$

When $\Delta f \geq 180$ degrees, $\Delta t \geq \Delta t_m$

$$\begin{aligned} F(a) &= n(t_2 - t_1) - [2\pi - (\alpha - \sin \alpha) - (\beta - \sin \beta)] \\ \frac{dF}{da} &= -\frac{3n}{2a}(t_2 - t_1) - \left(\frac{r_1 + r_2 + c}{2a^2} \tan \frac{\alpha}{2} + \frac{r_1 + r_2 - c}{2a^2} \tan \frac{\beta}{2} \right) \end{aligned} \quad (6.46)$$

When $\Delta f \geq 180$ degrees, $\Delta t \leq \Delta t_m$

$$F(a) = n(t_2 - t_1) - [(\alpha - \sin\alpha) + (\beta - \sin\beta)]$$

$$\frac{dF}{da} = -\frac{3n}{2a}(t_2 - t_1) + \left(\frac{r_1 + r_2 + c}{2a^2} \tan \frac{\alpha}{2} + \frac{r_1 + r_2 - c}{2a^2} \tan \frac{\beta}{2} \right) \quad (6.47)$$

When $\Delta f \geq 180$ degrees, $\Delta t \geq \Delta t_m$

$$F(a) = n(t_2 - t_1) - [2\pi - (\alpha - \sin\alpha) + (\beta - \sin\beta)]$$

$$\frac{dF}{da} = -\frac{3n}{2a}(t_2 - t_1) - \left(\frac{r_1 + r_2 + c}{2a^2} \tan \frac{\alpha}{2} - \frac{r_1 + r_2 - c}{2a^2} \tan \frac{\beta}{2} \right) \quad (6.48)$$

Also because

$$\Delta a = -\frac{F(a_0)}{(dF/da)_0} \quad (6.49)$$

Therefore the semimajor axis after avoidance is

$$a_1 = a_0 + \Delta a \quad (6.50)$$

2. Judge whether a_1 meets the accuracy requirement, namely, $|a_1 - a_0| \leq \varepsilon$. If not, Taylor expansion of $F(a)$ needs to be done at a_1 . Do it repeatedly until the required accuracy of a is obtained.
3. For normal spacecraft, since the flight path is usually a circular orbit, the velocity increment of orbit maneuver can be expressed as:

$$\Delta v = v_2 - v_1 = \sqrt{\mu \left(\left(\frac{2}{r_1} - \frac{1}{a_2} \right) - \left(\frac{2}{r_1} - \frac{1}{a_1} \right) \right)} \quad (6.51)$$

This method uses Lambert Flight Principles, replacing the precision orbit prediction method by a simplified model of two-body Kepler. By the given constraints, the avoidance maneuver velocity increment is solved.

On this basis, combined with the 2D probability of collision integration method, using fixed-step searching method, the optimal solution of avoidance maneuver velocity increment can be obtained.

6.2.2 Time avoidance method

Time avoidance method is to pose several velocity increments along tracking direction during $n(n \geq 2)$ orbit passes before the potential collision, raising or lowering the altitude of spacecraft, and therefore the spacecraft will not go through the intersection site at the original time so as to avoid collision with risky object.

It can be seen that the key point of time avoidance is the calculation of the velocity increment at the maneuver point given the position and velocity of spacecraft at the time of maneuver and the object position. The steps of computation are as follows:

1. The orbital period before maneuver is

$$T_1 = \frac{2\pi}{\sqrt{\mu/a_1^3}} \quad (6.52)$$

2. According to the avoidance constraints, it is assumed that Δt_a needs to be staggered to the expected collision time, the orbital period after maneuver is

$$T_2 = T_1 + (-1)^j \Delta t_a / \frac{t_1 - t_2}{T_1} \quad (j = 1, 2) \quad (6.53)$$

3. Thus the semimajor axis of the object orbit is

$$a_2 = \sqrt[3]{\frac{\mu}{(2\pi/T_2)^2}} \quad (6.54)$$

4. Therefore the orbit maneuver velocity increment can be expressed as

$$\Delta v = v_2 - v_1 = \sqrt{\mu \left[\left(\frac{2}{r_1} - \frac{1}{a_2} \right) - \left(\frac{2}{r_1} - \frac{1}{a_1} \right) \right]} \quad (6.55)$$

Directly by the relationship between orbit period and semimajor axis, and the given constraints, the desired velocity increment can be obtained.

On this basis, combined with the 2D probability of collision integration method, using fixed-step searching method, the optimal solution of velocity increment of the avoidance maneuver can be obtained.

6.3 Collision warning strategy for spacecraft safety operation and case studies

Due to the increasing utilization rate of space resources and increasing number of space objects, the orbit environment of spacecraft is deteriorating, and the probability of collision of space objects is growing. The destruction of any satellite will bring immeasurable loss to the national economy and national security. In order to protect the safety of space missions and reduce the costs by false alarms, it is necessary to formulate and improve organizational procedures and construct an integrated system of collision warning and avoidance.

According to the accuracy of orbit prediction and the desired time for avoidance measures, the procedures of spacecraft collision warning and avoidance are divided into four stages: risky objects screening, daily warning analysis, precision collision warning, and avoidance control.

6.3.1 Risky objects screening

Collision warning calculations of all on-orbit spacecraft in 7 days are carried out by normal cataloging orbit data every day. If there is any approaching event entering the risky threshold of collision warning, supplementary tracking plans will be added for those risky objects so as to accumulate measurement data for future judgment of risky degrees.

In order to verify the feasibility of the risky objects screening algorithm, a case study of nine on-orbit spacecraft with more than 15,000 space objects in space on August 21, 2014, is made. The first screening is made by the altitude of perigee and apogee. The second screening is made by the geocentric distance of intersection. The third screening is made by the minimum distance between orbital planes. The following is the results of eight different screening conditions.

Screening condition 1:

1. Perigee is lower than 20 km, and apogee is higher than 20 km.
2. The geocentric distance of intersection is 50 km.

Screening condition 2:

1. Perigee is lower than 20 km, and apogee is higher than 20 km.
2. The minimum distance between orbital planes is 50 km.

Screening condition 3:

1. Perigee is lower than 20 km, and apogee is higher than 20 km.
2. The geocentric distance of intersection is 20 km.

Screening condition 4:

1. Perigee is lower than 20 km, and apogee is higher than 20 km.
2. The minimum distance between orbital planes is 20 km.

Screening condition 5:

1. Perigee is lower than 40 km, and apogee is higher than 40 km.
2. The geocentric distance of intersection is 50 km.

Screening condition 6:

1. Perigee is lower than 40 km, and apogee is higher than 40 km.
2. The minimum distance between orbital planes is 50 km.

Screening condition 7:

1. Perigee is lower than 40 km, and apogee is higher than 40 km.
2. The geocentric distance of intersection is 20 km.

Screening condition 8:

1. Perigee is lower than 40 km, and apogee is higher than 40 km.
2. The minimum distance between orbital planes is 20 km.

The results show that:

1. Due to different distribution of the number of objects in different altitudes, the percentage of risky objects for under screening conditions increases first and then decreases with the increase of orbit altitude. According to the analysis in [Tables 6–1 to 6–5](#), the results are influenced by the volume ratio of objects in different altitudes.
2. For the objects below 500 km the percentage of risky objects is about 10% by the screening of perigee and apogee; for the objects from 500 to 900 km, the percentage of risky objects is about 40% by the screening of perigee and apogee; for the objects above 900 km the percentage of risky objects is about 30% by the screening of perigee and apogee. To some extent the influence of the threshold in the screening by perigee and apogee is limited on the results. It is indicated that for the method of perigee and apogee screening, the precision requirements for rendezvous time and orbit prediction are not

Table 6–1 Approaching events screening (Screening condition 1).

Object	Altitude (km)	Perigee (km)	Apogee (km)	After first screening		After second screening	
				Number	Percentage	Number	Percentage
Satellite1	500 or less	367	377	620	4.1	144	1.0
Satellite2		473	492	1336	8.8	468	3.1
Satellite3	500–900	581	586	2256	14.8	1003	6.6
Satellite4		620	662	3561	23.4	1832	12.0
Satellite5		684	697	3849	25.3	2102	13.8
Satellite6		786	794	5346	35.2	3139	20.7
Satellite7		816	831	5967	39.3	3418	22.5
Satellite8	900 or more	981	1196	5025	33.1	1220	8.0
Satellite9		1190	1211	2628	17.3	466	3.1

Table 6–2 Approaching events screening (Screening condition 2).

Object	Altitude (km)	Perigee (km)	Apogee (km)	After first screening		After second screening	
				Number	Percentage	Number	Percentage
Satellite1	500 or less	367	377	620	4.1	146	1.0
Satellite2		473	492	1336	8.8	468	3.1
Satellite3	500–900	581	586	2256	14.8	1004	6.6
Satellite4		620	662	3561	23.4	1836	12.1
Satellite5		684	697	3849	25.3	2103	13.8
Satellite6		786	794	5346	35.2	3147	20.7
Satellite7		816	831	5967	39.3	3425	22.5
Satellite8	900 or more	981	1196	5025	33.1	1227	8.1
Satellite9		1190	1211	2628	17.3	472	3.1

Table 6-3 Approaching events screening (Screening condition 3).

Object	Altitude (km)	Perigee (km)	Apogee (km)	After first screening		After second screening	
				Number	Percentage	Number	Percentage
Satellite1	500 or less	367	377	620	4.1	79	0.5
Satellite2		473	492	1336	8.8	248	1.6
Satellite3	500–900	581	586	2256	14.8	542	3.6
Satellite4		620	662	3561	23.4	966	6.4
Satellite5		684	697	3849	25.3	1127	7.4
Satellite6		786	794	5346	35.2	1801	11.8
Satellite7		816	831	5967	39.3	1722	11.3
Satellite8	900 or more	981	1196	5025	33.1	503	3.3
Satellite9		1190	1211	2628	17.3	234	1.5

Table 6-4 Approaching events screening (Screening condition 4).

Object	Altitude (km)	Perigee (km)	Apogee (km)	After first screening		After second screening	
				Number	Percentage	Number	Percentage
Satellite1	500 or less	367	377	620	4.1	80	0.5
Satellite2		473	492	1336	8.8	248	1.6
Satellite3	500–900	581	586	2256	14.8	542	3.6
Satellite4		620	662	3561	23.4	966	6.4
Satellite5		684	697	3849	25.3	1129	7.4
Satellite6		786	794	5346	35.2	1807	11.9
Satellite7		816	831	5967	39.3	1726	11.3
Satellite8	900 or more	981	1196	5025	33.1	504	3.3
Satellite9		1190	1211	2628	17.3	235	1.6

Table 6-5 Approaching events screening (Screening condition 5).

Object	Altitude (km)	Perigee (km)	Apogee (km)	After first screening		After second screening	
				Number	Percentage	Number	Percentage
Satellite1	500 or less	367	377	721	4.8	180	1.2
Satellite2		473	492	1595	10.5	547	3.6
Satellite3	500–900	581	586	2713	17.8	1311	8.6
Satellite4		620	662	4078	26.9	2050	13.5
Satellite5		684	697	4512	29.7	2505	16.5
Satellite6		786	794	6340	41.8	3785	24.9
Satellite7		816	831	6859	45.2	4034	26.6
Satellite8	900 or more	981	1196	5462	36.0	1248	8.2
Satellite9		1190	1211	2784	18.3	518	3.4

high, and therefore the method is suitable for initial screening for long-term collision warning based on cataloging orbit data.

3. For the objects below 500 km the percentage of risky objects is about 5% by the screening of perigee and apogee combined with the geocentric distance of intersection or the minimum distance between orbital planes; for the objects from 500 to 900 km the percentage of risky objects is about 30% by the screening of perigee and apogee combined with the geocentric distance of intersection or the minimum distance between orbital planes; for the objects above 900 km the percentage of risky objects is about 15% by the screening of perigee and apogee combined with the geocentric distance of intersection or the minimum distance between orbital planes. The smaller the geocentric distance of intersections or the minimum distance between orbital planes is, the smaller the percentage is.
4. With the same screening conditions of perigee and apogee, the number of risky objects screened by the geocentric distance of intersection is smaller than that screened by the minimum distance between orbital planes. The screening by the geocentric distance of intersection may cause missing alarms. Therefore the minimum distance between orbital planes is better than the geocentric distance of intersection as a screening algorithm.
5. In actual warning calculation the screening condition of perigee and apogee is required to be larger than 20 km, the minimum distance between orbital planes is required to be larger than the warning threshold. It can be reasonably adjusted according to actual situation so as to ensure screening efficiency without missing alarms.
6. By using the perigee and apogee as well as the minimum distance between orbital planes as screening conditions, the object number that needs to be further calculated is lessened, shortening warning calculation duration and improving warning efficiency (Tables 6–6 and 6–7).

In the stage of risky objects screening, the screening thresholds are mainly related to the orbit shape of space object, including perigee, apogee, the geocentric distance of

Table 6–6 Approaching events screening (Screening condition 6).

Object	Altitude (km)	Perigee (km)	Apogee (km)	After first screening		After second screening	
				Number	Percentage	Number	Percentage
Satellite1	500 or less	367	377	721	4.8	182	1.2
Satellite2		473	492	1595	10.5	547	3.6
Satellite3	500–900	581	586	2713	17.8	1312	8.7
Satellite4		620	662	4078	26.9	2054	13.5
Satellite5		684	697	4512	29.7	2506	16.5
Satellite6		786	794	6340	41.8	3794	25.0
Satellite7		816	831	6859	45.2	4041	26.6
Satellite8	900 or more	981	1196	5462	36.0	1255	8.3
Satellite9		1190	1211	2784	18.3	524	3.5

Table 6–7 Approaching events screening (Screening condition 7).

Object	Altitude (km)	Perigee (km)	Apogee (km)	After first screening		After second screening	
				Number	Percentage	Number	Percentage
Satellite1	500 or less	367	377	721	4.8	79	0.5
Satellite2		473	492	1595	10.5	248	1.6
Satellite3	500–900	581	586	2713	17.8	542	3.6
Satellite4		620	662	4078	26.9	966	6.4
Satellite5		684	697	4512	29.7	1127	7.4
Satellite6		786	794	6340	41.8	1801	11.8
Satellite7		816	831	6859	45.2	1722	11.3
Satellite8	900 or more	981	1196	5462	36.0	503	3.3
Satellite9		1190	1211	2784	18.3	234	1.5

Table 6–8 Approaching events screening (Screening condition 8).

Object	Altitude (km)	Perigee (km)	Apogee (km)	After first screening		After second screening	
				Number	Percentage	Number	Percentage
Satellite1	500 or less	367	377	721	4.8	80	0.5
Satellite2		473	492	1595	10.5	248	1.6
Satellite3	500–900	581	586	2713	17.8	542	3.6
Satellite4		620	662	4078	26.9	966	6.4
Satellite5		684	697	4512	29.7	1129	7.4
Satellite6		786	794	6340	41.8	1807	11.9
Satellite7		816	831	6859	45.2	1726	11.4
Satellite8	900 or more	981	1196	5462	36.0	504	3.3
Satellite9		1190	1211	2784	18.3	235	1.6

intersection, and the minimum distance between orbital planes. These parameters are related to the semimajor axis a , the eccentricity e , right ascension of ascending node Ω , and the argument of perigee ω but have no relations to mean anomaly M , which is hard to predict. According to Section 5.2.4, in normal cataloging orbit prediction, the element M in tracking direction is hard to predict, the forecast error of which in 7 days reaches hundreds of kilometers, whereas the error of perigee and apogee in 7 days is less than 40 km, and the error of the minimum distance between orbital planes is less than 20 km. Therefore based on cataloging orbit prediction and the threshold in Table 6–8, using perigee, apogee, and the minimum distance between two orbital planes to screen the potential risky rendezvous in the next 7 days, the number of objects that need attention can be lessened by 90% without missing alarms, leaving good conditions for further observation on remaining 10% risky objects and removing false alarms.

Two principles are obeyed in the risky object screening stage: (1) based on the current orbit cataloging, without adding detection resources, to screen risky objects that might collide with spacecraft in 7 days and (2) on the basis of no missing alarm, to reducing the number of risky objects so that detection resources can satisfy further observation needs.

6.3.2 Daily warning analysis

In the stage of daily warning analysis, the analysis on the risky objects in the future 7 days will be made every day, on the basis of maintaining orbit cataloging and current workload of detection network. Though the risky objects are reduced by 90% in the first stage, most of the remaining objects are still false alarms. According to the results, for a satellite in the orbit of 500–1000 km, there would be two-to-three potential collision warnings, most of which will not actually occur. False alarm rate is too high that if it is used as the guidance for spacecraft avoidance, normal work of spacecraft would be impossible, and high fuel consumption would shorten the life span of spacecraft sharply. However, objects that might cause real collision with very low probability are among those objects. We should identify them.

In order to find reliable information among the collision data with high false alarm rate, the remaining 10% risky objects should be further monitored by detection resources. However, the observation work of all remaining objects is still huge and impossible to complete. According to Table 3–1, for a space object lower than 500 km, by using tracking data of two passes of orbit ascension or descension, the 3-day orbit prediction accuracy will reach the order of kilometer, and the accuracy of orbit position in radical and normal directions will be 20–30 m. In this way the accuracy is improved by one-to-two magnitudes. From the day of risky objects screening that is 7 days ahead of potential collision to the day that is 3 days ahead of potential collision, there are still 3 days for detection network to adjust observation plans. At the moment, what need to do is only to add more observation of an ascension or descension orbit pass to the current tracking plans, which is the lowest adjustment for the plan. Using the additional 2–3 days tracking data, the orbit prediction could be of the order of kilometer, and the accuracy of orbit position in radical and normal direction could be 10 m, based on which high reliable collision analysis could be done by using reasonable distance thresholds.

The choice of thresholds for minimum distance method is related to the precision of detection resources, the size of space objects, the inclination and altitude of object orbit, the computation software accuracy and calculation time. In the process of risky object screening, due to the requirement of calculation accuracy and efficiency, the method of simple numerical orbit cataloging calculation proposed in this chapter is recommended for calculation. However, simple numerical orbit cataloging calculation, American two-line element calculation method, average elements orbit cataloging calculation and half-numerical and half-analysis orbit cataloging calculation all can be used for orbit calculation and collision warning in the stage of risky object screening. However, in the following stages, numerical method with high-precision models is recommended. Generally, the collision warning of risky objects in 3 days calculated by precision orbit method after screening by risky objects

screening stage and additional observation of two passes of orbit ascension or descension is defined as yellow warning.

On the basis of no false dismissals, yellow warning is of high credibility, lessening the probability of false alarms. The formulation of a proper threshold for yellow warning should ensure that the probability of false alarm is low enough that it has no influence on the life span and normal operation of spacecraft, and there will not be any false dismissals. According to the current number of space objects, the capability of detection network, and the comprehensive performance of spacecraft, there should be no more than three-to-five false alarms of yellow warning for each spacecraft every year.

6.3.3 Precision collision warning

When yellow warning is issued and risky objects are identified, in the next 48 hours, the countable risky objects will be observed and tracked by detection resources with concentration to acquire high-precision orbit data 24 hours before the potential collision. In the next 48 hours after yellow warning is released, five passes of orbit ascension and descension or at least two passes of orbit ascension and descension of precision observation data should be acquired by detection network. According to Table 3–1, based on two passes of tracking data, orbit prediction accuracy in 24 hours will reach the order of a 100 m, satisfying very basic collision warning analysis. Based on five passes of tracking data, orbit prediction accuracy in 24 hours will be within a 100 m, whose credibility is highly improved. The collision warning of objects that cannot be removed in this stage is called red warning.

The premise and foundation of accuracy improvement of orbit prediction is to acquire orbit measurement data as much as possible. Even for red warning, the accuracy of dynamic models, especially atmospheric drag models is a major factor that affects the precision of orbit prediction and the bottleneck of confidence level. In Section 4.5 the major four factors that affect the precision of atmospheric drag model are discussed in detail. The error of area–mass ratio of object, atmospheric density model, and average $F_{10.7}$ value in 81 days can be determined as parameter c_d in the stage of daily collision analysis together with other orbit parameters, 2–3 days after risk object is proposed. In the stage of precision collision warning, based on more measurement orbit data, the error can be further corrected dynamically. Meanwhile, the influence of solar $F_{10.7}$ flows and its changes in 24 hours on atmospheric density is mainly reflected in the process in atmospheric heating. Studies show that its influence on atmospheric density will be delayed in 24 hours. In the prediction of orbit determination, as long as the quasi-real-time measured data of $F_{10.7}$ are acquired, its effect on orbit position prediction in 24 hours can be ignored. Therefore the impact of the first three factors on orbit prediction in 24 hours can be reduced to the minimum. However, for the fourth factor geomagnetic index, its impact on orbit prediction in 24 hours cannot be corrected by c_d . Especially, if there is significant geomagnetic storm in 24 hours, the accuracy of orbit prediction in 24 hours will decrease by an order of magnitude.

Through researches scientists found that before geomagnetic storms, there must be an intense solar storm erupting from sunspot 24–48 hours ahead. Therefore by observing the sun, it can be predicted whether there will be an anomaly jump of geomagnetic index. The

probability of the occurrence of this kind of anomaly jump in a year is no greater than 10%. That is to say, for red warning released 24 hours before intersection, in 90% cases, orbit prediction error caused by the uncertainty of atmospheric drag perturbation model can be controlled within a certain range. Therefore collision warning threshold can be set according to different orbital altitudes of space objects. In the process, special attention should be paid to the pattern that orbit precision in radial and normal direction is higher than that in tracking direction.

With appropriate threshold in radial direction, most of the false alarms in yellow warnings can be removed effectively. Red warning released in this case is highly credible. For space objects of normal size, the probability of collision is generally higher than 10^{-4} in red warning, meaning that there would be a real collision event among 10,000 times of red warning. However, given the very serious damage of collision, to guarantee complete safety, we recommend that the work of avoidance control can be carried out for space objects with the ability of on-orbit maneuvers, especially for manned spacecraft or spacecraft with high values. Indicated by sunspots observation and the calculation of c_d , if a geomagnetic storm may occur in the next 24–48 hours or the red warning is in the period of a geomagnetic storm, proving that the confidence level of the red warning is lower, then avoidance control can be decided whether to be carried out based on the calculated probability of collision warning and the maximum probability comprehensively.

The accuracy of orbit prediction is higher if red warning is released near the collision point, giving a higher credibility. However, the preparation procedure of space object orbit control requires relatively longer time. In addition, theoretically, fuel consumption will be less if orbit control is carried out earlier, whereas the result of avoidance control is better. Therefore from this point of view, it is better to carry out the avoidance control earlier. Considering the controllable 24-hours atmospheric drag model errors and the feasibility of intensive observations of detection network, red warning is suggested to be released 24 hours in advance of a potential collision.

6.3.4 Avoidance control

The procedure of avoidance control starts 24 hours before the collision. Generally, avoidance control should be carried out 6 hours before collision. First, based on the theoretical post-control orbit, collision warning analysis of spacecraft orbit in the next 3 days after the avoidance control will be made so that safety assessment of postcontrol could be carried out. If a yellow warning event exists, recalculate the theoretical postcontrol orbit. Repeat the process, until there will be no yellow warning event.

The selection of orbit avoidance strategy is related to the capacities and status of spacecraft control components in each direction, as well as the orbit control decision-making capability of spacecraft management department. In most cases the follow-up tasks of spacecraft should also be considered in the process of the above choice. Accordingly, the selection of orbit avoidance strategy is often a complex process. Altitude avoidance method and time avoidance method given in [Section 6.2](#) are two typical algorithms. For both algorithms, the theoretical postcontrol orbit must be analyzed to ensure that there would not be any new risks.



References

- [1] L. Jisheng, Satellite Precise Orbit Determination, The People's Liberation Army Press, Beijing, 1995.
- [2] L. Jisheng, Satellite Orbit Determination, National Defense Industry Press, Beijing, 2003.
- [3] L. Lin, An Introduction of Astrodynamics, Nanjing University Press, Nanjing, 2006.
- [4] L. Lin, Orbit Theory of Spacecraft, National Defense Industry Press, Beijing, 2000.
- [5] L. Lin, Orbit Theory of Space Target, National Defense Industry Press, Beijing, 2000.
- [6] X. Qifeng, GPS Satellite Navigation and Precise Position, The People's Liberation Army Press, Beijing, 2000.
- [7] X. Qifeng, Space Geodesy, The People's Liberation Army Press, Beijing, 2014.
- [8] W. Ziqing, Mathematic Model of GPS Relative Positioning, China Surveying and Mapping Publishing House, Beijing, 1998.
- [9] W. Lianda, Orbit Probe of Satellite and Space Debris, China Science and Technology Press, Beijing, 2012.
- [10] Z. Huatong, Common Earth Coordination and Transformation, The People's Liberation Army Press, Beijing, 1990.
- [11] H. Cheng, L. Lin, Reference Coordinate System and Space Applications, Publishing House of Electronics Industry, Beijing, 2015.
- [12] Y. Jianping, Principles and Applications of Satellite Navigation System, China Astronautic Publishing House, Beijing, 2003.
- [13] Z. Rongzhi, et al., MSIS-90 atmosphere model and application in low earth orbit calculation, in: Chinese Astronomical Society Orbit Mechanics Conference, 1996.
- [14] Z. Rongzhi, et al., GPS and application in space TT&C, in: Chinese Astronomical Society Orbit Mechanics Conference, 1996.
- [15] Z. Rongzhi, et al., Progress on orbit determination precise of Xian satellite control center, in: Beijing Space TT&C Conference, 2000.
- [16] Z. Rongzhi, et al., The orbit characteristics of two DSP satellites, in: Rome International Conference of Space Operation, 2006.
- [17] Z. Rongzhi, et al., Determination of single GPS-Antenna-Attitude of Champ, in: ION GPS of the USA, 2002.
- [18] Z. Rongzhi, et al., Single GPS position, in: ION GPS of Canada, 1990.
- [19] D. Heng, et al., Space Debris, China Astronautic Publishing House, Beijing, 2007.
- [20] Z. Shuqiang, et al., Rocket-Born GNSS Data Processing, National Defense Industry Press, Beijing, 2015.
- [21] L. Zhenghang, et al., GPS Measurement and Data Processing, Wuhan University Press, Wuhan, 2010.
- [22] L. Zhenghang, et al., Space Geodesy, Wuhan University Press, Wuhan, 2009.

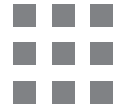
- [23] X. Fuwen, Precise determination of the new SLR station of Shanghai observatory, *Prog. Astron.* 25 (2) (2007).
- [24] Y. Fumin, The third generation satellite laser ranging system of Shanghai observatory, *China Sci. (A)* 20 (8) (1990) 844–850.
- [25] F. Jianxing, Center-of-mass model of satellites used for laser ranging, *Acta Astron. Sin.* 29 (11) (2000).
- [26] L. Lisheng, et al., *External Trajectory Measurement Data Processing*, National Defense Industry Press, Beijing, 2002.
- [27] Q. Xianping, J. Wenhai, Evaluation of CHAMP satellite orbit with SLR measurements, *Geomat. Inf. Sci. Wuhan. Univ.* 30 (1) (2005).
- [28] L.P. Mark, Autonomous orbit determination for two spacecrafts from relative position measurements, *J. Guidance Control. Dyn.* 22 (2) (1999) 305–312.
- [29] L.E. Schutz, B.D. Tapley, P.A.M. Abusali, et al., Dynamic orbit determination using GPS measurements from TOPEX/POSEIDON, *Geophys. Res. Lett.* 21 (19) (1994) 2179–2182.
- [30] D. Svehla, M. Rothacher, Kinematic and reduced-dynamic precise orbit determination of low earth orbiters, *Adv. Geosci.* (2002).
- [31] H. Bock, Efficient Methods for Determining Precise Orbits of Low Earth Orbiters Using the Global Positioning System, (Ph.D. thesis), Astronomical Institute University of Berne, Switzerland, 2003.
- [32] J.H. Kwon, D.G. Brzezinska, C.K. Hong, Kinematic orbit determination of Low Earth Orbiters using triple differences, in: *Proceedings of The Institute of Navigation National Technical Meeting*, 28–30 January, San Diego, CA, 2002, pp. 762–770.
- [33] V. Szebehely, *Theory of Orbits (Chapter 5)*, Academic Press, New York and London, 1967.
- [34] J. Degnan, *Satellite Laser Ranging: Current Status and Future Prospects*, 1985, GE-23(4).
- [35] M. Rutkowska, The accuracy of orbit estimation for the low-orbit satellites LARETS and WESTPAC, *Adv. Space Res.* 36 (2005) 498–503.
- [36] C. Urschl, W. Gurtner, Validation of GNSS orbits using SLR observations, *Adv. Space Res.* 36 (2005) 412–417.
- [37] R. Kolenkiewicz, D.E. Smith, Advances in SLR orbit determination, *Adv. Space Res.* 19 (11) (1997) 1661–1665.
- [38] P. Lejba, S. Schillak, Determination of orbits and SLR stations' coordinates on the basis of laser observations of the satellites Starlette and Stella, *Adv. Space Res.* 40 (2007) 143–149.
- [39] U. Schreiber, M. Schneider, Is there a next generation SLR-technology? *Adv. Space Res.* 30 (2) (2002) 157–161.
- [40] P.H. Andersen, K. Aksnes, Precise ERS-2 orbit determination using SLR, PRARE, and RA observations, *J. Geodesy* 72 (1998) 421–429.
- [41] E. Wnuk, S. Schillak, Stability of coordinates of the Borowiec SLR station (7811) on the basis of satellite laser ranging, *Adv. Space Res.* 30 (2) (2002) 413–418.
- [42] ILRS, SLR/LLR Data Anomalies. <http://ilrs.gsfc.nasa.gov/slr_problems_text.html>, 2000.
- [43] IERS, Bulletin B IERS. <<http://ilrs.obspm.fr/iers/bul/bulb/>>, 2000.
- [44] NASA, Eccentricity Information for SLR Occupations.
- [45] <<ftp://cddisa.gsfc.nasa.gov/pub/slrocc/slrecc.txt>>, 2000.
- [46] J.J. Degnan, M.R. Pearlman, The International Laser Ranging Service. <<http://ilrs.gsfc.nasa.gov>>.
- [47] L. Shaomin, N. Wei, Maxin, et al., Research on space target detection technology, *Natl. Def. Sci. Technol.* 30 (3) (2009) 6–13.

- [48] L. Zhenwei, Research in optoelectronic observation technologies for space objects, Graduate Univ. Chin. Acad. Sci. (2014).
- [49] L. Meiyang, Research on method of star identification and celestial positioning of CCD astronomical images, Graduate Univ. Chin. Acad. Sci. (2010).
- [50] C. Zhao, L. Cheng, H. Weihong, Methods accurately locating optical positions of space object based on CCD stellar images, *Astron. Res. Technol.* 7 (3) (2010) 231–237.
- [51] Z. Jinyu, Error analysis and compensation technology of optoelectronic telescope, Graduate Univ. Chin. Acad. Sci. (2005).
- [52] Z. Xiaoyao, Research on error analysis and modification of target positioning in optoelectronic observation system, Graduate Sch. Natl. Univ. Def. Technol. (2011).
- [53] G. Yanluo, W. Helong, Study on accuracy analysis of airborne electro-optical detecting and tracking system, *Electron. Opt. Control.* 11 (2) (2004) 18–20.
- [54] Zijinshan Observatory of Chinese Academy of Sciences, Method of Real-Time Celestial Positioning Space Targets, CN1710377.2005-12-21.
- [55] Z. Xiaoxiang, W. Lianda, The basic parameters of telescope static point model, *Acta Astron. Sin.* 42 (2) (2001) 198–205.
- [56] H. Xue, Z. Jingxu, Z. Jinyu, et al., Forecast for orientation errors of alt-alt photoelectric telescope, *Opt. Precis. Eng.* 7 (2010) 1595–1604.
- [57] P. Yiding, Z. Xiaoxiang, L. Chunlin, 65cm alt-alt photoelectric telescope static orientation model, *Acta Astron. Sin.* 47 (2) (2006) 224–230.
- [58] Z. Xiangming, Research on alt-alt photoelectric telescope precise orientation model, Graduate Univ. Chin. Acad. Sci. (2010).
- [59] M.I. Skolnik, *Introduction to Radar System*, McGraw-Hill Book CO, New York, 1980.
- [60] M.I. Skolnik, *Radar Handbook*, McGraw-Hill Co., Inc., New York, 1990.
- [61] D.K. Barton, S.A. Leonov, *Radar Technology Encyclopedia*, Artech House, Inc, Boston, MA and London, 1997.
- [62] D.K. Barton, *Modern Radar System Analysis*, Artech House, Norwood, MA, 1988.
- [63] D.K. Barton, *Radar System Analysis*, Artech House, Norwood, MA, 1977.
- [64] W. Xiaomo, Zhangguangyi, et al., *Radar and Detection*, National Defense Industry Press, Beijing, 2001.
- [65] Z. Guangyi, W. Dechun, et al., *Space Detection Phased Array Radar*, Science Press, Beijing, 2002.
- [66] A.W. Rihaczek, S.J. Hershkowitz, *Theory and Practice of Radar Target Identification*, Artech House, 2000.
- [67] W. Dechun, Optimization of radar search method, *Mod. Radar* 1 (3) (1979).
- [68] P.Z. Peebles, *Radar Principles*, John Wiley & Sons, New York, 1998.
- [69] W. Dechun, Analysis of monopulse angle tracking of Airborne pulse Doppler radar, *Mod. Radar* 6 (4,5) (1984).
- [70] L. Yuxi, *Analysis of Radar Accuracy*, National Defense Industry Press, Beijing, 1979.
- [71] R.J. Sullivan, *Radar Foundation for Imaging and Advanced Concepts*, Electronic Industry Press, Beijing, 2009.
- [72] W. Dechun, D. Jiahui, C. Wangdong, *Precision Tracking Radar Technology*, Electronic Industry Press, Beijing, 2006.
- [73] D.A. Vallado, D. Finkleman, *A Critical Assessment of Satellite Drag and Atmospheric Density Modeling*, American Institute of Aeronautics and Astronautics, 2008.
- [74] A.K. Arudra, *Atmospheric Density Estimation Using Satellite Precision Orbit Ephemerides*, University of Kansas, 2011, pp. 1–93.

- [75] American Institute of Aeronautics and Astronautics, American national standard: guide to reference and standard atmosphere models, in: ANSI/AIAA G-003C-2009, 2009.
- [76] Q. Guotai, Q. Shiyao, et al., Changes of the atmospheric density at SZ-3 orbit altitude, *Chin. J. Space Sci.* 24 (4) (2004) 269–274.
- [77] Q. Guotai, Q. Shiyao, et al., “SZ-2” atmospheric density detector measurement result II. Change of the thermosphere density during solar and geomagnetic activity, *Chin. J. Space Sci.* 23 (2) (2003) 135–141.
- [78] M. Juan, L. Siqing, L. Zhitao, et al., Atmospheric density calibration using the real-time satellite observation, *Chin. J. Space Sci.* 31 (4) (2011) 459–466.
- [79] W. Libin, F. Hanxian, J. Chunhua, et al., Comparison between the CHAMP/STAR derived thermospheric density and the NRLMSISE-00 model, *Chin. J. Space Sci.* 32 (5) (2012) 713–719.
- [80] C. Guangming, F. Yang, X. Zhengang, et al., Method of upper atmosphere density retrieving from accelerometer data, *J. PLA Univ. Sci. Technol.* 11 (3) (2010) 371–376.
- [81] B.R. Bowman, et al., A method for computing accurate daily atmospheric density values from satellite drag data, in: AAS 2004-179, AAS/AIAA Spaceflight Mechanics Meeting, Maui, HI, 2004.
- [82] J.M. Picone, J.T. Emmert, J.L. Lean, Thermospheric densities derived from spacecraft orbits: accurate processing of two-line element sets, *J. Geophys. Res.* 110 (2005) A03301. Available from: <https://doi.org/10.1029/2004JA010585>.
- [83] J.L. Lean, J.M. Picone, J.T. Emmert, et al., Thermospheric densities derived from spacecraft orbits: application to the Starshine satellites, *J. Geophys. Res.* 111 (2006) A04301. Available from: <https://doi.org/10.1029/2005JA011399>.
- [84] T. Bowman, et al., A new empirical thermospheric density model JB2008 using new solar and geomagnetic indices, in: AIAA 2008-6438, AIAA/AAS Astrodynamics Specialist Conference, Honolulu, HA, 2008.
- [85] L. Shushi, G. Jiancun, et al., Parameters input of MSIS90 thermosphere density model in orbit determination and forecasting, *Manned Spacefl.* 18 (6) (2012) 1–6.
- [86] B.R. Bowman, W.K. Tobiska, M.J. Kendra, The thermospheric semiannual density response to solar EUV heating, *J. Atmos. Solar-Terr. Phys.* (2008).
- [87] B.R. Bowman, W.K. Tobiska, et al., A new empirical thermospheric density model JB2006 using new solar indices, in: AIAA 2006-6166, AIAA/AAS Astrodynamics Specialist Conference, Keystone, CO, 2006.
- [88] A.E. Hedin, MSIS-86 thermospheric model, *J. Geophys. Res.* 92 (1987) 4649.
- [89] F.A. Marcos, J.O. Wise, et al., Accuracy of Earth’s thermospheric neutral density models, in: AIAA 2006-6167, AIAA/AAS Astrodynamics Specialist Conference, Keystone, CO, 2006.
- [90] J.M. Picone, A.E. Hedin, et al., NRLMSISE-00 empirical model of the atmosphere: statistical comparisons and scientific issues, *J. Geophys. Res.* 107 (A12) (2002) 1468.
- [91] S. Bruinsma, et al., The DTM-2000 empirical thermosphere model with new data assimilation and constraints at lower boundary: accuracy and properties, *J. Atmos. Solar-Terr. Phys.* 65 (2003) 1053.
- [92] Z. Rongzhi, L. Jisheng, Q. Penggao, et al., Influence of geomagnetic activity index on orbital period rate and determination precision of low earth orbit, in: The Orbital Dynamics Joint Conference of China Astronomical Society, 1996.
- [93] Q. Hongxing, W. Lianda, Z. Wei, et al., Comparison of atmospheric density models for LEO satellite orbit determination and orbit forecast, *J. Spacecr. TT&C Technol.* 25 (4) (2006) 12–25.
- [94] Q. Guotai, S. Lilin, L. Hong, Changes of thermospheric components and density in strong geomagnetic activities, *J. Space Sci.* 19 (2) (1999) 141–147.
- [95] C. Haowen, Application of Spacecraft Orbit Theory in Space Target Catalog, Nanjing University, 2012.
- [96] L. Lin, Theory and Application of Spacecraft Orbit Determination, Publishing House of Electronics Industry, Beijing, 2015.

- [97] W. Dong, Analysis on the accuracy of the SGP4/SDP4 model, *Acta Astron. Sin.* 50 (3) (2009) 332–339.
- [98] L. Zhonggui, Relative of satellite orbit error, *J. Spacecr. TT&C Technol.* 5 (2011) 45–49.
- [99] B. Xianzong, Research on Space Target Orbit Forecast Error and Collision Probability, Graduate School of National University of Defense Technology, 2013.
- [100] C. Lei, H. Lei, B. Xianzong, et al., *Space Target Orbit Dynamics and Error Analysis*, National Defense Industry Press, Beijing, 2010.
- [101] B. Xianzong, C. Lei, Research on calculation method of collision probability between space objects, *J. Astronautics* 29 (4) (2008).
- [102] F.K. Chan, *Spacecraft Collision Probability*, The Aerospace Press, 2008.
- [103] The State Council Information Office, P.R.C. Chinese Beidou Satellite Navigation System, People's Publishing House, Beijing, 2016.
- [104] J. Wenhai, et al., New progress of IGMAS, in: The Second CCGG Conference, 2016.
- [105] J.N. Pelton, *Space Debris and Other Threats From Outer Space* (Y. Kaizhong, Trans.), National Defense Industry Press, Beijing, 2016.
- [106] L. Ming, et al., Progress of new technology of space debris detecting and removing system, in: The 573th Discuss, Xiang Mountain Conference, 2016.
- [107] K.T. Event Jet Propulsion Lab. <<http://www2.jpl.nasa.gov/sl9/back3.html>>.
- [108] Launch of Sputnik on October 4, 1987. <www.history.nasa.gov/sputnik/>.
- [109] J. Logsdon, *John F. Kennedy and the Race to the Moon*, Palgrave-MacMillan, New York, 2010.
- [110] G. Robert, The Moon Man. <<http://www.legacy.com/ns/news-story.aspx?t=robertgoddard-the-moon-man&id=279>>.
- [111] Space.com Staff Report, New Debris-Tracking 'Space Fence' Passes Key Test, 2012.
- [112] Space.com, <<http://www.space.com/14867-space-fence-orbital-debris.html>> (accessed 12.03.12).
- [113] C. Moskowitz, Space junk problem is more threatening than ever, in: Report Warns, 2011.
- [114] Space News, <<http://www.space.com/12801-space-junk-threat-orbital-debris-report.html>> (Accessed 01.09.11).
- [115] The Looming Space Junk Crisis: It's Time to Take Out the Trash *Wired Magazine*. <www.wired.com/magazine/2010/05/ff_space_junk/all/1> (accessed 24.05.10).
- [116] Op cit, Clara Moskowitz, "Space junk. . ."
- [117] J.-C. Liou, N.L. Johnson, Risk in space from orbital debris, *Science* 311 (2006) 340–341.
- [118] NASA site on near earth objects. <<http://neo.jpl.nasa.gov/>>.
- [119] NOAA, Solar cycle progression and prediction, NOAA. <<http://www.swpc.noaa.gov/SolarCycle/>>.
- [120] New Debris-Tracing 'Space-Fence' Passes Key Test. <<http://www.space.com/14867-spacefence-orbital-debris.html>> (accessed 12.03.12).
- [121] Space Fence Mark II: Prototype S-Band Radar Track Space Debris. <<http://www.gizmag.com/space-fence-radar-detects-debris/21779/>>.
- [122] J.N. Pelton, A fund for global debris removal, in: As Presented at the International Association for the Advancement of Space Safety (IAASS) Conference in Versailles, France, November 2011 and International Space University Symposium on Space Debris, March 2012, 2012.
- [123] T. Sgobba, IAASS Study on Space Debris Remediation: An Operational and Regulatory Framework for Assured Debris Removal, November 2011.
- [124] The Inter-Agency Space Debris Coordinating Committee. <<http://www.iadc-online.org/index.cgi>>.
- [125] IADC Space Debris Mitigation Guidelines.

- [126] <http://www.iadc-online.org/index.cgi?item = docs_pub>.
- [127] Space Data Association. <<http://www.space-data.org/sda/about/members/>>.
- [128] J. Pearson, L. Eugene, J. Carroll, Commercial space debris removal, *Space Saf. Mag.* 1 (2011) 21–22.
- [129] Proceedings of the International Interdisciplinary Congress on Space Debris, May 7–9, 2009. <http://www.mcgill.ca/channels/events/item/?item_id = 104375> also see David Kushner.
- [130] The future of space: orbital cleanup of cluttered space, in: *Popular Science*, August 2010, pp. 60–64 and see: J.N. Pelton, The problem of space debris, in: *The Fundamentals of Satellite Communications*, Springer Press, New York, 2012, pp. 29–33.
- [131] Russia to Spend \$2 Billion For Space Clean Up. *Space Daily*, 2010. <<http://www.spacedaily.com/reports/Russia>> (accessed 10.11.10).
- [132] C. Bombardelli, et al., Dynamics of ion-beam propelled space debris. <<http://web.fmetsia.upm.es/ep2/docs/publicaciones/ahed11a.pdf>>.
- [133] A Super Solar Flare, NASA science news. <http://science.nasa.gov/science-news/science-at-nasa/2008/06may_carringtonflare/>.
- [134] A. Hadhazy, A Scary 13th: 20 Years Ago Earth Was Blasted With a Massive Plume of Solar Plasma, *Scientific American*, 2009. Available from: <http://www.scientificamerican.com/>.
- [135] <article.cfm?id = geomagnetic-storm-march-13-1989-extreme-space-weather> (accessed 13.03.09).
- [136] N. Fox, Coronal Mass Ejection, Goddard Space Flight Center, NASA, 2011. <http://www.istp.gsfc.nasa.gov/istp/nicky/cme-chase.html>. (accessed 6.04.11).
- [137] NASA-SOHO. <www.nasa.gov/mission_pages/soho/>.
- [138] NASA Stereo Satellite to Study Solar CMEs in Three Dimensions. <http://www.nasa.gov/mission_pages/stereo/>.
- [139] The Solar Backscatter Ultra-Violet Sensor on NOAA Satellites (SBUV/2). <<http://www.ballaerospace.com/page.jsp?page = 93>>.
- [140] The Earth's Magnetosphere Shield. <http://science.nasa.gov/science-news/science-at-nasa/2003/03dec_magneticcracks/>.
- [141] M. Adams, Earth's magnetic pole shift unleashing poisonous space clouds lined to mysterious bird deaths, *Natural News*. <http://www.naturalnews.com/030996_bird_deaths_pole_shift.html>, 2011 (accessed 13.01.11).
- [142] I. Stewart, L. John, *Earth: The Biography*, National Geographic Society, Washington, DC, 2007, pp. 57–63.
- [143] D. Morrison, C.R. Chapman, D. Steel, R.P. Binzel, Impacts and the public: communicating the nature of the impact hazard, in: M.J.S. Belton, T.H. Morgan, N.H. Samarasinha, D.K. Yeomans (Eds.), *Mitigation of Hazardous Comets and Asteroids*, Cambridge University Press, Cambridge, 2004. 2004. This version reflects a revision of the Torino Scale. Also see. http://neo.jpl.nasa.gov/images/torino_scale.jpg for more details..
- [144] J.N. Pelton, Taking potentially hazardous asteroids (PHAs) seriously—making the public aware, *Space Safety Magazine*, Fall 2012, 2012.
- [145] N. Firth, Massive asteroid could hit earth in 2182, Warn Scientists. <<http://www.dailymail.co.uk/sciencetech/article-1298285/Massive-asteroid-hit-Earth-2182-warn-scientists.html>>, 2010 (accessed 28.07.10).
- [146] U.N. Committee on the Peaceful Uses of Outer Space, Draft Report of the Working Group on the Long Term Sustainability of Space. <<http://www.oosa.unvienna.org/oosa/COPUOS/ac105l.html>>.



Index

Note: Page numbers followed by “*f*” and “*t*” refer to figures and tables, respectively.

A

Altitude avoidance method, 174–176, 185

Altitude–altitude mount, 50

Altitude–azimuth mount, 49–50

AN/FPQ-18 monopulse precision tracking radar, 46

ANFPS85 phased array radar, 37–38

Angle measurement

error, 41–44

error model, 59–61

of radar object, 38

Angle random error, 42

Angle variables, 135

Antenna gravity sag error, 43

Apogee, 157–158

Area integration, 22

Area-mass ratio of space objects, 74

Ariane rocket, 3–4

Astronomy, 11–14

Atmosphere

drag, 31–32

perturbation, 135–137

refraction, 57

Atmospheric damping coefficient, 115–116, 119–122

Atmospheric density calculation, 100–101
for space objects, 84

Atmospheric density models, 75–106, 79*t*
characteristics, 81*t*

development process, 80*f*

index model, 80–84

Jacchia77 atmospheric model, 85–94, 89*t*

MSIS00 model, 94–106, 108*t*

principle, 76–78

data acquisition technology, 77

hydrostatic, 76–77

parameters and fitting technique, 77–78

systematic and random error of, 106–109

Atmospheric diffusion balance equation, 75

Atmospheric drag, 73

equation, 77

models, 184

Atmospheric effect on space object orbit, 73–75

Atmospheric jitter, errors caused by, 58

Atmospheric perturbation calculation strategy

analysis of orbit determination, 116–122

atmospheric damping coefficient, 115–116, 119–122

prediction under

abnormal geomagnetism conditions,

119–122

normal geomagnetism conditions, 116–119

for spacecraft collision avoidance warning

calculation, 115–122

systematic error, 115–116

Atomic time, 16

Avoidance control, 185

B

Ballistic coefficient, 74

Balloon soundings, 75–76

BeiDou Navigation Satellite System, 17

BeiDou time, 17

Bistatic structure of radar, 36

Boresight swing error of optical systems, 58

Box method. *See* Minimum distance—method

C

Catadioptric telescope, 49

Cataloged orbit calculation method, 131–154.

See also Precise orbital calculation method

comparison of perturbation models, 131*t*

mean elements cataloging orbit calculation
method, 142–146

precision analysis, 146–154

simple numerical method, 131

- Cataloged orbit calculation method (*Continued*)
 with two-line element, 131–142
 orbit determination based on SGP4 model, 139–142
 orbital principle of SGP4 model, 134–139
 US cataloging system, 131–132
 US two-line elements, 132–134, 133*t*
- Cataloging methods, 123
- CCD image processing model, 54–55
- Celestial positioning, 50–51
 measurement model of, 53–56
 working mechanism and features of, 52
- CERIES (French ELINT satellite), 3–4
- CGCS2000. *See* China Geodesic Coordinate System 2000 (CGCS2000)
- Chemical correction factor, 106
- China Geodesic Coordinate System 2000 (CGCS2000), 19
- CIO. *See* Conventional international origin (CIO)
- CME. *See* Coronal mass ejection (CME)
- Code disk error, 42
- Collision prediction, 5–6
- Colorful warning, 8
- Colorless warning, 8
- Compensation techniques of telescopes, 56–64
- Conditional equation. *See* Observation error equation of orbit improvement
- Conventional international origin (CIO), 13, 19
- Conversion errors, 40–41
- Coordinate systems and major transformation formula, 18–21
 coordinate transformation, 21
 Earth-fixed coordinate system, 19
 geodetic system, 20
 instantaneous mean equatorial coordinate system, 18
 instantaneous true equatorial coordinates system, 18
 ITRS, 19
 quasi Earth-fixed coordinate system, 18–19
 RTN coordinate system, 21
 satellite coordinate system, 20
 topocentric coordinate system, 20
 2000.0 inertial coordinate system, 18
 UNW coordinate system, 20–21
- Coordinate transformation, 21
- Coordinated universal time (UTC), 16
- Coronal mass ejection (CME), 119–120, 122
- Correction coefficients, 92–93
- Cosmos (Russia defunct navigation satellite), 3–4
- Cross correlation coefficient, 78
- Curved surface array antenna, 46
- D**
- Daily warning analysis, 183–184
- Data acquisition technology, 77
- DCA. *See* Dynamic atmospheric correction (DCA)
- Declination axis, 49
- Delay error, 41
- Detection network and orbit accuracy relationship, 70–72
- Diffusion distribution, 101–105
- Direct detection sensor, 77
- Direct measurement method, 77
- DOD. *See* US Department of Defense (DOD)
- Doppler frequency shift, 39
- Doppler velocity measurement of pulse radars, 43
- DTM series, 75–76, 79
- Dual-frequency correction method, 67
- Dynamic atmospheric correction (DCA), 79
- Dynamic errors, 57–59
 lag error, 41, 43–44
- Dynamic measurement errors, 56
- Dynamical modeling strategy, 130
- E**
- Earth-fixed coordinate system, 19
- Earth's gravitational force, 22, 29–30
- Eccentricity, 132–134
- Ecliptic, 11, 15
- Effective atmospheric density, 100–101
- Electro-optical detection technology, 36–37, 48–64, 50*f*
 measurement errors and compensation techniques, 56–64
 measurement models of electro-optical telescope, 52–56
 principles, 48–50
 optical structure of electro-optical telescopes, 48–49

- optical telescope's mount structure, 49–50
 - telescopes measurement data types and positioning
 - measurement data, 50–51
 - working mechanism and features of positioning, 52
 - Electro-optical measurement, ground-based, 36
 - Electromagnetic fence, 36
 - Electronic scanning antenna, 46
 - Electronically scanned array antenna, 46
 - Elements system, 128
 - Elliptical objects, 149, 151
 - Empirical atmospheric models, 75–76
 - Empirical correction of particle concentration, 92–93
 - Empirical models, 75
 - Encoder error, 56–57
 - Energy integration, 22
 - Ephemeris calculation, 21
 - Ephemeris time, 15–16
 - Equator plane, 11
 - Equatorial mount, 49
 - Error compensation technology, 61–64
- F**
- Fast matching algorithm of star patterns, 54
 - Fitting technique, 77–78
 - Flight perturbation forces, 31–32
 - Four-constant model, 55
 - Frame-end sampling, 58
 - Frame-terminal sampling. *See* Frame-end sampling
- G**
- General relativistic effect error correction, 69
 - GEO satellites, 1–2
 - Geocentric angle, 68
 - Geodetic system, 20
 - Geoeffectiveness correction, 86
 - Geomagnetic
 - latitude, 68
 - thermal effects, 93
 - Geomagnetic index, 78
 - transition of, 109
 - GLOBUS 11, 37–38
 - GNSS observation network, 68–69
 - GNSS satellite, 1–2
 - GPS time (GPST), 16–17
 - GRAVES radar, 37–38
 - Ground-based detection, 35–37. *See also*
 - Electro-optical detection technology
 - electro-optical detection technology, 36–37
 - radio detection technology, 35–36
 - space-based detection, 37
 - Gust disturbance error, 42
- H**
- Hazards of space debris, 3–6
 - High-accuracy satellite drag model, 79
 - Horizontal plane, 11
 - Hour angle, 12
 - HP model, 80–85
 - Hydrostatic principle, 76–77
- I**
- ICG-10. *See* International Conference on Genomics (ICG-10)
 - Ideal gas density equation, 76
 - IERS. *See* International Earth Rotation and Reference Systems Service (IERS)
 - IGMAS. *See* International GNSS Monitoring and Assessment System (IGMAS)
 - Incoherent scatter, 75–76
 - Index model, 80–84
 - Instantaneous mean equatorial coordinate system, 18
 - Instantaneous orbital parameters, 137
 - Instantaneous true equatorial coordinates system, 18
 - Instrument tracking motion error, 57–58
 - Intensive observations, 8
 - International Atomic Time system (TAI system), 16
 - International Conference on Genomics (ICG-10), 14
 - International Earth Rotation and Reference Systems Service (IERS), 14
 - International GNSS Monitoring and Assessment System (IGMAS), 14

- International Reference Atmosphere series (CIRA series), 75–76, 79
 - International Space Station (ISS), 6–7
 - International Terrestrial Reference Frame (ITRF), 19
 - International Terrestrial Reference System (ITRS), 19
 - Inversion method, 77
 - Ionospheric delay, 68–69
 - Ionospheric error correction, 66–69
 - ISS. *See* International Space Station (ISS)
 - ITRF. *See* International Terrestrial Reference Frame (ITRF)
 - ITRS. *See* International Terrestrial Reference System (ITRS)
- J**
- J64 model, 78
 - Jacchia series, 75–76, 79
 - Jacchia77 atmospheric model, 85–94, 89*t*
 - JB2008 model, 78
 - Jitter error, 40
- K**
- Kalman filtering, 124
 - Kepler element, 124, 140
 - Kepler equation, 24, 137
 - Kepler theorem, 21
- L**
- Laplace integration, 22
 - Latitude of space objects, 83
 - Leap second, 16
 - Least squares orbit improvements, 124
 - “Longitude nutation”, 13
 - Lunisolar precession, 12
- M**
- Mass spectrometers, 75–76
 - Mean anomaly, 132–134, 181–182
 - Mean element
 - at any time, 143
 - cataloging orbit calculation method, 142–146
 - orbit extrapolation, 142–146
 - state transition matrix, 146
 - method, 142–144
 - Mean equator, 13
 - Mean square error of angle measurement error, 60
 - Mean sun, 15
 - Mean vernal equinox, 13
 - Measurement errors of telescopes, 56–64
 - angle measurement error model, 59–61
 - dynamic errors, 57–59
 - error compensation technology, 61–64
 - static errors, 56–57
 - Measurement models of electro-optical telescope, 52–56
 - celestial positioning, 53–56
 - shafting positioning, 53
 - Mechanical models, 130
 - Mechanical scanning tracking radar, 46
 - Mechanical tracking radar, 35
 - Meridian plane, 11
 - MET series, 79
 - Method matrix, 126, 128–130
 - Minimum distance, 156, 161–165
 - approaching angle and velocity calculation, 165
 - distance calculation in three directions, 163
 - method, 156
 - precision evaluation of three distance components, 163–165
 - relationship between relative velocity and relative distance, 162
 - risky objects screening by, 160
 - space object orbit propagation, 161–162
 - Mixed distribution, 105–106
 - Monopulse angle measurement, 38
 - Monostatic structure of radar, 36
 - Motion equation, 22
 - MSIS series, 75–76, 79
 - MSIS00 empirical model, 74–75
 - MSIS00 model, 79, 94–106, 108*t*
 - MSIS83 model, 79
 - MSIS86 model, 79
 - MSIS90 model, 79
 - Multipath error, 41–42
 - Multistep method, numerical integration, 126
- N**
- n*-dimensional first-order nonlinear equation, 124
 - NASA, 156

- Navy Space Surveillance System (NAVSPASUR), 47
 - Near-Earth objects, 70
 - Nearly circular high-altitude objects, 149, 151
 - Nearly circular LEO object, 148–151
 - Newton iterative method, 174–176
 - NOAA 7 satellite, 5
 - Nonlinear equations, 63
 - Nonsynchronized time sampling error, 58
 - NORAD. *See* North American Air Defense Command (NORAD)
 - Normal equation, 126
 - North American Air Defense Command (NORAD), 131–132
 - Numerical method, 123
 - Nutation, 12–14
- O**
- Object velocity measurement and tracking, 39
 - “Obliquity nutation”, 13
 - Observation error equation of orbit improvement, 126
 - On-orbit
 - avoidance, 172–173
 - space objects, 73
 - spacecraft, 5–6, 73, 77
 - Optical structure of electro-optical telescopes, 48–49
 - Optical telescope, 36
 - mount structure, 49–50
 - Optimal estimation value, 125
 - Orbit
 - determination, 71*t*
 - analysis, 116–122
 - based on SGP4 model, 139–142
 - method, 148
 - error, 151
 - extrapolation, 142–146
 - mean element method, 142–144
 - quasimean element method, 144–146
 - maneuver velocity increment, 177
 - prediction, 74–75, 163, 164*f*, 165*f*
 - variables, 137
 - Orbital calculations, 123
 - for spacecraft collision avoidance
 - astronomy, 11–14
 - coordinate systems and major transformation
 - formula, 18–21
 - space frames and basic planes, 12*f*
 - space object orbit, 21–33
 - time systems and major transformation
 - formula, 14–18
 - Orbital dynamics prediction models, 7
 - Orbital eccentricity, 134
 - Orbital equation, 23
 - Orbital inclination, 132–134
 - Orbital perturbations of space object, 29–33
 - on geostationary satellite orbit, 32*t*
 - on LEO satellite orbit, 31*t*
 - on resource satellite orbit, 32*t*
 - Orbital planes, 158–159
 - risky objects screening by, 160
 - Orbital principle of SGP4 model, 134–139
 - Oxygen ions, 79
- P**
- PAA. *See* Phased array antenna (PAA)
 - Parameters, 77–78
 - Partial derivative of argument vector, 129
 - Particle concentration
 - of atmospheric component, 88–90
 - of hydrogen atom, 91–92
 - Pc. *See* Probability of collision (Pc)
 - PDF. *See* Probability density function (PDF)
 - Perigee
 - anomaly, 134
 - long-term change of, 157–158
 - short-term change of, 157
 - variation, 158*f*, 159*f*
 - Perigee anomaly, 132–134
 - Perturbation
 - equations of motion, 145
 - motion equation, 142–143
 - Phased array antenna (PAA), 46–47
 - planar, 46
 - Phased array radar, 35, 46–47
 - Planetary precession, 12
 - Pole shift, 13–14
 - effect, 18–19
 - Precession, 12

- Precise orbital calculation method, 124–130.
See also Cataloged orbit calculation method
- numerical calculation, 128–130
 dynamical modeling strategy, 130
 elements system, 128
 magnitude comparison of perturbation, 130*t*
 method matrix, 128–130
 numerical integration, 126–128
 orbital parameters optimal estimation method, 124–126
- Precision analysis, 146–154
 with mean element method, 150–151
 simple numerical method accuracy analysis, 146–148
 space object catalog error characteristic orbital analysis, 151–154
 US cataloging precision analysis, 148–150
- Precision collision warning, 184–185
- Prediction accuracy, 148–149
- Prediction confidence level of space environment parameters, 109–114
 analysis of A_p prediction confidence level, 110, 111*t*
 analysis of $F_{10.7}$ prediction confidence level, 109–110, 111*t*
 impact of environmental parameters on orbit prediction error, 111–114, 112*t*, 114*t*
- Prediction error, 71*t*
 of solar activity parameters, 106
- Probability density function (PDF), 166
- Probability of collision (Pc), 156, 166
 influence of related parameters, 168–172
 maximum, 166–168
- Process errors, 44–45
- Propagation errors, 40–41
- Public correction models for measurement data, 64–70
 general relativistic effect error correction, 69
 ionospheric error correction, 66–69
 partial derivatives of each measurement element, 64–65
 tropospheric refraction error correction, 65–66
 vertical deflection correction, 70
- Purple Mountain Observatory, 123
- Q**
- Quantization error, 40, 44
- Quasi Earth-fixed coordinate system, 18–19
- Quasi-mean element method, 123, 144–146
- R**
- RAAN, 132–134
- Radar measurement technology, 37–48. *See also* Electro-optical detection technology
 data modeling, 39–45
 angle measurement error, 41–44
 mathematical model of systematic errors, 44–45
 ranging error, 40–41
 velocity measurement error, 44
- elements, 38–39
 object velocity measurement and tracking, 39
 radar object angle measurement and tracking methods, 38
 radar object range measurement and tracking methods, 38–39
 typical space surveillance radar, 45–48
- Radial distance, 173
- Radio detection technology, 35–36
- Radio radiation flux, 106–108
- Random error, 39–40
 of atmospheric density models, 106–109
- Range measurement of radar object, 38–39
- Ranging error, 40–41
- Ranging random error, 40–41
- Ranging system error, 41
- Real-time atmospheric density, 75
- Real-time celestial positioning, 55–56
- Receiving system thermal noise error, 42
- Red warning, 8, 184–185
- Reference ellipsoid, 11
 height for space objects, 83
- Reflecting telescope, 49
- Refracting telescope, 48–49
- Refractive error, 41, 43
- Relative distance, 162
- Relative error limit, 127
- Relative velocity, 162
- Relativistic effect correction, 69–70
- Risky object screening, 156–160, 178–183

- by geocentric distance of intersection, 158–160
 - celestial sphere diagram of satellites and debris, 160*f*
 - by minimum distance between orbital planes, 160
 - by perigee and apogee, 157–158
 - calculation and analysis of space object orbit change, 158
 - long-term change of perigee, 157–158
 - short-term change of perigee, 157
 - Root mean square error, 78
 - RTN coordinate system, 21
 - Runge–Kutta single-step integration method, 126–127
- S**
- S/N ratio. *See* Signal-to-noise ratio (S/N ratio)
 - Satellite
 - acceleration, 29
 - coordinate system, 20
 - drag, 75–76
 - SDP4 model, 132
 - SDP8 model, 132
 - “Seamless” electronic fences, 37–38
 - Seasonal variation of latitude, 93
 - Semianalytical method, 123
 - Semiannual variation, 93–94
 - Servo noise error, 40, 42
 - SGP model, 132
 - SGP4 model, 132
 - orbit determination based on, 139–142
 - orbital principle, 134–139
 - SGP4/SDP4 orbit prediction model, 123, 148
 - SGP8 model, 132
 - Shafting error, 43, 56
 - Shafting positioning, 50–51
 - measurement model of, 53
 - working mechanism and features of, 52
 - Sidereal time, 14–15
 - Signal-to-noise ratio (S/N ratio), 40
 - Simple numerical method accuracy analysis, 146–148
 - Single pulse precision tracking radars, 46
 - Single-step method, numerical integration, 126
 - Six orbital elements, 21
 - of space object motion, 23*f*
 - Six-constant model, 55
 - Solar hour angle, 83–84
 - Solar position calculation, 83–84
 - Solar radiation energy, 78
 - Solar time, 15
 - Space debris, 123
 - characteristics and hazards of, 3–6
 - Space environments, 73, 76, 106
 - atmospheric perturbation calculation strategy, 115–122
 - and chemical correction factor, 106
 - prediction confidence level of space environment parameters, 109–114
 - systematic and random error of atmospheric density models, 106–109
 - Space fence radar system, 47–48
 - Space object
 - catalog error characteristic orbital analysis, 151–154
 - detection technology, 35
 - detection network and orbit accuracy relationship, 70–72
 - electro-optical detection technology, 48–64
 - ground-based detection, 35–37
 - orbit determination and prediction error, 71*t*
 - public correction models for measurement data, 64–70
 - radar measurement technology, 37–48
 - distribution and characteristics, 1–3
 - monitoring equipment, observation quantity of, 124
 - position calculation, 83
 - two-body motion in space, 22
 - Space object orbit, 21–33, 73
 - atmospheric density model, 75–106
 - atmospheric effect on, 73–75
 - calculation, 9, 123
 - change calculation and analysis, 158
 - conversion of orbital elements
 - interchange between orbital elements and position/velocity, 25
 - partial derivative of acceleration with respect to position/velocity, 28–29

- Space object orbit (*Continued*)
 - partial derivative of coordinates and velocity, 27–28
 - partial derivative of elements with respect to coordinates and velocity, 25–27
 - integration of two-body problem, 22–25
 - orbital perturbations of space object, 29–33
 - propagation, 161–162
 - Space surveillance network (SSN), 123
 - Space surveillance radar, 45–48
 - mechanical scanning tracking radar, 46
 - phased array radar, 46–47
 - space fence, 47–48
 - Space targets, 158
 - Space-based detection, 37
 - Spacecraft collision warning, 6–9, 155–172
 - characteristics and hazards of space debris, 3–6, 4*t*
 - collision events in history, 5*t*
 - distribution and characteristics of space objects, 1–3, 2*f*
 - active spacecraft distribution in different orbits, 3*t*
 - increment of trackable space objects, 2*f*
 - events of LEO satellites, 7*t*
 - minimum distance calculation, 161–165
 - orbit calculation method
 - cataloged orbit calculation method, 131–154
 - orbital calculation method, 124–130
 - probability of collision, 166
 - risky object screening, 156–160
 - for spacecraft safety operation, 177–185
 - approaching events screening, 179*t*, 180*t*, 181*t*, 182*t*
 - avoidance control, 185
 - daily warning analysis, 183–184
 - precision collision warning, 184–185
 - risky objects screening, 178–183
 - statistical data of collision avoidance maneuver of ISS, 6*t*
 - Spacecraft flight safety, 123
 - Special perturbation, 123
 - Speed measurement systematic error, 44
 - SSN. *See* Space surveillance network (SSN)
 - Star catalog selection, 53–54
 - Star image's centroid calculation, 54
 - Star pattern
 - fast matching algorithm of, 54
 - matching, 53–54
 - matching algorithm, 53–54
 - recognition database establishment, 54
 - State transition matrix, 140, 146
 - Statics equation, 76
 - Step stretching factor, 128
 - Surveillance Network of United States Space, 77
 - System error, 39–41
 - Systematic error, 62, 115–116
 - of atmospheric density models, 106–109
 - mathematical model of, 44–45
- T**
- TAI system. *See* International Atomic Time system (TAI system)
 - Taylor expansion, 143
 - Telescope angle measurement error, 59
 - Telescope systematic error correction, 64
 - Temperature calculation, 95–106
 - Theoretical observations precision, 130
 - Thermal noise error, 40, 44
 - Thermosphere composition, 75–76
 - Time avoidance method, 176–177, 185
 - Time system
 - conversion, 17–18
 - and transformation formula, 14–18
 - atomic time, 16
 - BeiDou time, 17
 - coordinated universal time, 16
 - ephemeris time, 15–16
 - GPST, 16–17
 - sidereal time, 14–15
 - solar time, 15
 - universal time, 15
 - TLE. *See* Two-line element (TLE)
 - Topocentric coordinate system, 20
 - Topocentric equatorial Cartesian coordinate system, 51
 - Trackable space objects, increment of, 1, 2*f*
 - Tracking direction, 163
 - Tracking errors, 40–41
 - Transformation matrix, 51

- Transmit pulse width variation error, 40
 - Tropospheric refraction error correction, 65–66
 - True sidereal time, 14–15
 - True solar time, 15
 - TV miss distance pure lag error, 57
 - TV static miss distance measurement error, 57
 - 24-Hour orbit error for orbital height prediction, 74–75, 75*t*
 - Two-body motion. *See* Two-body problem
 - Two-body problem, 22
 - integration of, 22–25
 - partial derivative of acceleration with respect to position/velocity in, 28–29
 - Two-constant model, 55
 - 2D Gaussian PDF, 166
 - 2D normal distribution PDF, 167
 - Two-line element (TLE), 131–134
 - cataloging orbit calculation with, 131–142
 - data, 1
 - orbital elements, 77
 - US two-line elements, 132–134, 133*t*
 - 2000 China Geodetic Coordinate System.
 - See* China Geodesic Coordinate System 2000 (CGCS2000)
 - 2000.0 inertial coordinate system, 18
- U**
- Uncertainty of atmospheric density, 74
 - Unit vector of Sun in Earth-fixed coordinate system, 83–84
- United States (US)
 - cataloging precision analysis, 148–150
 - cataloging system, 131–132
 - two-line elements, 132–134
 - US Standard Atmosphere, 75–76
 - United States Space Command (USSPACECOM), 37
 - Universal time, 15
 - UNW coordinate system, 20–21
 - Upper atmosphere, 76
 - US Department of Defense (DOD), 131–132
 - US Global Observation Network, 131–132
 - USSPACECOM. *See* United States Space Command (USSPACECOM)
 - UTC. *See* Coordinated universal time (UTC)
- V**
- Variational equation, 129
 - Velocity measurement error, 44
 - Vernal equinox, 12
 - Vertical deflection correction, 70
- W**
- Winter helium outstanding, 93
 - World Geodesic System 1984 (WGS-84), 19
- Z**
- Zero error, 41–43
 - Zero value error of discriminator, 44

Spacecraft Collision Avoidance Technology

ZHANG RONGZHI & YANG KAIZHONG

The large number of objects now in orbit has created a risky operating environment for satellites. Satellite collision avoidance has consequently emerged as an important concern for space security and for cooperation between nation states involved with space, particularly the United States and China.

Spacecraft Collision Avoidance Technology presents the theory and practice of space collision avoidance. The book gives models of time and space environment, and their impact on high-precision orbit prediction; considers optimal orbit determination methods and models in different warning stages; and establishes basic models for warning and avoidance. Six chapters present an outline of spacecraft collision warning strategy; elaborate on the basics of orbital calculation for collision avoidance; consider space object detection technology; detail space environment and object orbit; give a method for spacecraft collision warning orbit calculation; and finally demonstrate a strategy for spacecraft collision warning and avoidance.

Key features:

- Presents strategies, methods, and real-world examples relating to space collision avoidance
- Considers time and space environment models in orbit prediction
- Gives optimal orbit determination methods and models for various warning stages
- Establishes and elaborates basic models for warning and avoidance
- Takes note of the current space environment for object detection and collision avoidance



ACADEMIC PRESS

An imprint of Elsevier
elsevier.com/books-and-journals

ISBN 978-0-12-818011-2



9 780128 180112